Collège Doctoral du Languedoc-Roussillon

THÈSE

Pour obtenir le grade de

Docteur

Délivré par l'**Université de Montpellier**

Préparée au sein de l'école doctorale **I2S***
Et de l'unité de recherche **UMR 5299**

Spécialité : **Physique**

Présentée par **Stefano Magni**

Astrophysical aspects of dark matter direct detection

Soutenue le 13 novembre 2015 devant le jury composé de :

M.	Julien Lavalle	Chargé de recherche, Université de Montpellier, LUPM	**Directeur**
M.	Thomas Schwetz	Professeur, Université de Karlsruhe	**Rapporteur**
M.	Benoit Famaey	Chargé de recherche, Observatoire de Strasbourg	**Rapporteur**
M.	Jules Gascon	Professeur, Université de Lyon, IPNL	**Examinateur**
M.	Jean Orloff	Professeur, Université Blaise Pascal, LPC	**Examinateur**
M.	Nicolao Fornengo	Professeur, Université de Torino, CNRS	**Examinateur**
M.	Denis Puy	Professeur, Université de Montpellier, LUPM	**Examinateur**

Université Montpellier

* **I2S :** école doctorale Information Structures Systémes

Contents

List of Figures

List of Tables

Introduction

The dark matter problem is an important open question in modern-day physics. Originally, it arose as the problem of the missing mass on the scale of galaxies and clusters of galaxies. This topic, born as an astrophysical one, encompasses nowadays many other domains, for instances particle physics, cosmology and the physics of detectors. Among many possible solutions to this problem that have been proposed, Weakly Interacting Massive Particles (WIMPs) are among the most promising and well studied objects.

WIMPs are particularly appealing also because of the possibilities of detecting such particles, which make them an experimentally testable class of candidates. One of the main strategies to look for them is dark matter direct detection, which aims at detecting WIMPs via their scattering off the nuclei in a detector. This thesis focuses on WIMP dark matter, and in particular on the direct detection of WIMPs.

Astrophysical quantities play an important role in direct detection, because they enter in the computation of direct detection limits from experimental results. Among these quantities, we have the escape speed from the Milky Way, the circular speed at the location of the Sun and the local dark matter density.

Often a standard set of assumptions for the astrophysics involved in dark matter direct detection is used, the Standard Halo Model (SHM), where a Maxwell-Boltzmann speed distribution is assumed for the dark matter. Anyway, the Maxwell-Boltzmann is an approximation, and the astrophysical quantities fixed at standard values by the SHM are determined from observations which relie on assumptions that is important to take into account.

These quantities are intimately related, and these relations become evident when a mass model for the Milky Way is considered. Under assumptions on the symmetry of the Galactic gravitational potential and on the distribution of the velocities of the dark matter particles, we can relate to such a mass model also the phase-space distribution of the dark matter, which influences the interpretation of the experimental results in direct detection. Moreover, the determinations of the

above astrophysical quantities from observations are affected by uncertainties, which translate on the direct detection limits. In the present-day scenario, understanding these uncertainties would be useful in the case of a discovery in correctly reconstruct the properties of the detected dark matter candidate.

In this work, we review the formalism of dark matter direct detection, putting particular emphasis on the astrophysics that enters therein. We thus otuline the main experimental facts that should be taken into account, explaining some of the statistical methods usually employed to interpret the data, and we describe some of the main experiments carried out in this domain. We then outline the main concepts of the dynamics of our galaxy that allow to put the astrophysics related to direct detection in a wider framework.

In the main part of this thesis, we focus on the recent estimates of the local Galactic escape speed, published by the RAVE collaboration in 2014. We have studied in detail which are the implications of these results for dark matter direct detection, in particular focusing on the exclusion curves of the most constraining and representative experimental results at the moment of writing. We have seen how these estimates impact on the direct detection limits, and how the assumed mass model for the Milky Way induces correlations between the astrophysical quantities relevant for dark matter direct detection, that we have taken into account.

In order to make the picture more general, we finally attempt to review the main estimates present in the literature for the astrophysical quantities relevant for direct detection, pointing out the main results and assumptions.

Let us briefly summarize how this work is structured.

Chapter 1: Dark matter direct detection: formalism and general aspects. In this chapter we explain the principles of dark matter direct detection, reviewing the basic formalism. We will focus in particular on how astrophysics enters in the computations, and on the standard set of assumptions employed (the so-called Standard Halo Model). We will thus describe how the velocity distribution of the dark matter particles is taken into account, as well as the transformation of this distribution from the Galactic to the Earth reference frame, and the annual modulation of the WIMP signal expected in a detector that this change of reference induces.

Chapter 2: Understanding the experimental results. In this chapter we are going to present the DMDD experiments which we consider in the following, and some other representative ones, the statistical procedures that we have applied to compute limits (and regions), and the impact of the astrophysical parameters of the Standard Halo Model on such limits.

Chapter 3: Galactic dynamics and the dark halo, from Milky Way mass models to the WIMPs phase space. In this chapter we are going to present the elements of Galactic dynamics which allow us to place the astrophysical

quantities related to direct detection in a more general framewok. We will present particular Milky Way mass models. This treatment enlightens the relations among the astrophysical quantities (like the local circular velocity, the local dark matter density, distance to the Galactic center, the local Galactic escape speed, etc.) that enter the computation of direct detection predictions and limits, and with the underlying mass model.

Chapter 4: the impact of the local Galactic escape speed estimates on dark matter direct detection. In this chapter we will concentrate on the recent estimate of the local Galactic escape speed published by the RAVE collaboration [1], which relies on the assumption of a particular Milky Way mass model. This induces correlations among the astrophysical quantities that enter the computation of direct detection limits.

We will go beyond the Maxwell-Boltzmann approximation by inferring the WIMP phase-space distribution from the Galactic mass model components thanks to the Eddington equation. This procedure self-consistently accounts for the dynamical correlations among the astrophysical parameters.

We will show that a treatment which implements the RAVE results on the escape speed by consistently correlating all relevant parameters leads to more constraining exclusion curves with respect to the standard ones, and to moderate uncertainties. These results are contained in our paper [2] that has recently been published in the journal Physical Review D.

To accomplish this project we have developed a C/C++ code which allows to compute DMDD exclusion curves and contours for certain direct detection experiments, and a code to numerically solve Eddington equation for certain different mass models of the Galaxy.

Chapter 5: a review of estimates of the astrophysical quantities relevant to dark matter direct detection. In this chapter we complete the picture by attempting a review of the main estimates present in the literature for the astrophysical quantities relevant for direct detection, and those characterizing the mass models involved in the description of our Galaxy, pointing out the main results and assumptions. This is meant to provide complementary information on many of the astrophysical quantities that have been encountered in the rest of the manuscript, and represents an opening toward possible generalizations of the work done in this thesis.

Conclusions. We will finally draw our conclusions.

CHAPTER 1

Direct detection: formalism and general aspects

Contents

1.1 Introduction

The dark matter problem is an important open question in modern-day physics. Originally, it arose as the problem of the missing mass on the scale of galaxies and clusters of galaxies, so as a purely gravitational issue.

This problem dates back to observations in 1933 by Fritz Zwicky, who proposed the existence of dark matter as a source of gravitational potential to explain the motions of galaxies in the Coma Cluster [3].

Subsequently, others discovered flat rotation curves in disk galaxies, Babcock already in 1939 [4], and Rubin and Ford [5] and Roberts and Whitehurst [6] with more convincing data in the seventies, which could be explained by non luminous matter to be the predominant constituent of mass inside galaxies. Even today, the most convincing evidences for the presence of missing mass in the universe are from spiral galaxies. There is simply not enough luminous matter observed in spiral galaxies to account for their observed rotation curves.

The Planck data on the cosmic microwave background, once interpreted in the framework of the standard model of cosmology (the ΛCDM), provide a Universe which consists for the 26.8% of dark matter (and only for the 4.9% of ordinary matter, while the remaining 68.3% is supposed to be made of dark energy).

It is important to remind that different approaches to solve the missing mass problem can be considered. In particular, an alternative possibility is that the observations indicate a breakdown of our understanding of gravitational dynamics on certain scales, which leads to theories where modifications of gravity are considered. One particular such theory is MOND (MOdified Newtonian Dynamics), which considers a modification of Newtonian dynamics on galactic scales. A review of the current observational successes and problems of this alternative paradigm can be found in [7].

In particle physics, the Standard Model provides a very good description of processes related to three of the four known fundamental interactions (electromagnetic, weak and strong) up to the energies thus far probed by experiments. However, this model has some issues, like the explanation of the origin of mass, the neutrino oscillations, the naturalness problem, the matter-antimatter asymmetry and others. Moreover, there is the question of a more fundamental theory which would include

gravitational interaction. Thus, it seems quite possible for the Standard Model of particle physics to be just an approximation of some bigger underlying theory [8].

Extensions of the Standard Model which aims at dealing with one or more of these issues are called theories Beyond the Standard Model (BSM theories). Some of them rely on supersimmetry (SUSY), which roughly speaking introuces a doubling of the number of particles (w.r.t. those of the Standard Model) which relates bosonic integral-spin particles to fermionic half-integral-spin superpartners.

While observations on the scales of galaxies, clusters of galaxies and on the cosmological scale indicate the presence of dark matter in the universe and allow to quantify its cosmological abundance, Big Bang nucleosynthesis provides upper limits on the cosmological density of baryons. Such abundances tell us that the majority of the dark matter in the universe cannot be of a baryonic nature. If the dark matter is made of non baryonic matter, then particle physics can provide candidates in abundance in the form of new elementary particles [8]. For instance, in many supersymmetric models the lightest supersymmetric particle, often the neutralino, is stable and massive and it undergoes week interaction with ordinary matter.[1]

Such massive new elementary particles wich undergo weak interaction, predicted by BSM theories, are in general called Weakly Interacting Massive Particles (WIMPs). Their name refers to the fact that these particles undergo weak interaction and feel the effects of gravity, while do not participate in electromagnetic or strong interactions. Nowadays, WIMPs are among the most promising and well studied classes of dark matter candidates.

Since WIMP-like particles are predicted in many BSM theories, they potentially rely on theoretically motivated grounds. Moreover, the fractional contribution of WIMPs to the energy density of the Universe is such that, with an annihilation cross section of weak interaction strength, they could provide a cosmological abundance near the value measured by Planck. This coincidence is known as the "WIMP miracle", and it is one of the reasons because of WIMPs have received a lot of attention as a dark matter candidate [8]. Thus, WIMPs are a class of candidates which might have the right properties to represent the dark matter.

WIMPs are particularly appealing also because of the possibility of detecting such particles, which makes them an experimentally testable class of candidates. A multitude of experimental efforts are currently underway to detect WIMPs. Three are the main strategies to detect them: production at colliders, indirect detection and direct detection.

Searches for WIMP dark matter are ongoing at colliders, for instance at the Large Hadron Collider. An example is the search for missing energy events, i.e. roughly speaking collisons in which a part of the energy goes to an undetected particle, which could be a WIMP.

[1] More about this will be said in section 1.5, while an extensive review of supersymmetric dark matter can be found in [8]. Let us remark that we quote supersymmetry only as an example, while the content of this thesis is more general and it is not related to a particular BSM theory.

Indirect detection of dark matter is based on the idea that WIMPs can annihilate into Standard Model particles, which can then propagate through space till the Earth. Here, cosmic rays detectors (as for instance the AMS experiment), gamma ray telescopes (as Fermi) or neutrino observatories (like Ice Cube) should be able to detect them as an excess with respect to standard astrophysics backgrounds.[2]

The third strategy is dark matter direct detection, on which we will focus in this work. This field began thirty years ago with the work of Drukier and Stodolsky [9], who proposed to search for neutrinos by observing the nuclear recoil caused by their weak interactions with nuclei in detectors. Subsequently, Goodman and Witten [10] pointed out that this approach could be used to search not just for neutrinos, but also for WIMPs, again via their week interaction with detectors. Soon after, Drukier, Freese and Spergel [11] extended this work by taking into account the halo distribution of WIMPs in the Milky Way, as well as proposing the presence of an annual modulation in the signal.

Dark matter direct detection (DMDD) experiments aim at detecting WIMPs via the nuclear recoils expected in underground detectors and triggered by the predicted elastic scatterings of WIMPs off target nuclei. These detectors employ different target materials (for instance germanium or xenon) and are placed underground to shield them from the cosmic-ray background. In the standard cosmological picture, the Galaxy is embedded in a dark matter halo, and weakly interacting massive particles (WIMPs) are one of the most studied classes of candidates to constitute such a halo. In the reference frame w.r.t which the halo has no global motion, the positions and motion of these particles can be described through their phase-space distribution. Detectors involved in DMDD experiments are located on Earth, which is orbiting around the Sun, and the Sun is orbiting around the Galactic center. If the WIMP velocity distribution is isotropic in the Galaxy, than DMDD experiments are therefore hit by a flux of DM particles, and this flux varies with a periodicity of one year, as the Earth's orbital period. A comprehensive review of these facts can be found in [12].

As the name suggests, WIMPs can interact with matter through weak interaction. In particular, they can interact with the nuclei of the target material in a detector.[3] Elastic as well as inelastic scattering between a WIMP and a nucleus can be considered (the latter only when the WIMP has excited states). After the collision the hit nucleus will recoil having acquired kinetic energy, the so called recoil energy.

In this chapter we present in detail the standard formalism which allows one a description of these issues. For a review, see for instance [13]. We start by introducing the recoil energy and its relation with the velocity of the incoming WIMP. We then describe how to compute the rate of events in a DMDD experiment and the cross section of the elastic scattering for spin-dependent and spin-independent

[2] It is important to remember, anyway, that the modelling of such astrophysical backgrounds is rather uncertain.

[3] More precisely, WIMPs can interact with quarks, which are the constituents of nucleons, and nucleons themselves are the constituents of nuclei, so the interaction of a WIMP on a nucleus in a detector is studied in three different steps, as we will see later on.

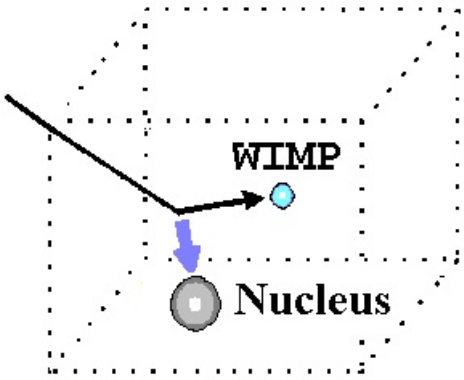

Figure 1.1: A schematic representation of how DMDD works: a WIMP hits a nucleus inside the detector, and the nucleus acquires a recoil energy that we can measure. Figure from http://inpac.physics.sjtu.edu.cn.

WIMP-nucleon interaction. We then focus on the astrophysics that directly enters in the computation of the rate of events, mainly the dark matter velocity distribution. We introduce the Maxwell-Boltzmann distribution, with its variants including a cut-off at high velocity. We describe in detail the velocity transformation necessary to translate these distributions into the Earth reference frame, and the annual modulation of the expected WIMP signal that arises from such transformation. We finally specify the standard set of assumptions on the astrophysics involved commonly employed to compare the results of different experiments.

We will describe in detail in chapter 2 the issues that must be taken into account when dealing with real experiments. We will explore more in details the astrophysical aspects involved in DMDD, in particular in relation to the dynamics of the Galaxy, in chapter 3.

1.2 Relations between velocity and recoil energy in an elastic scattering process

In this section we would like to introduce the recoil energy that a target nucleus acquires from the scattering of a WIMP.

In an elastic scattering process between two generic particles, the relative velocity between the particles and the energy exchange among them are related. The relation involves also the masses of the particles and the scattering angle. In the following section we will derive from kinematics the relation between these quantities. In the subsequent section we will use this equation in order to obtain a relation between the relative WIMP-nucleus velocity, and the corresponding maximal recoil energy of the nucleus.

1.2.1 General relation between relative velocity and recoil energy

We start by studying the elastic scattering between two particles, which we denote χ and A (that will represent respectively a WIMP and a target nucleus). We use non-relativistic kinematics, which is a good approximation for our purposes since we want to apply this relation to the case of a WIMP which scatters over a nucleus, which is a highly non-relativistic process since WIMPs are expected to have speeds of order $\sim 0.001 \times c$ at the Solar location. The nucleus is assumed to be initially at rest.

The *recoil energy E_r of the nucleus* is given by

$$E_r = \frac{|\vec{p}_{Af}|^2}{2m_A} = \frac{|\vec{q}|^2}{2m_A} \ , \tag{1.1}$$

where $\vec{p}_{Af}$ is the *momentum of the nucleus after the collision* (in the Laboratory frame[4]), $\vec{q}$ is the *momentum transferred* between the two particles and m_A is the *mass of the nucleus A*. Note that the second equality is valid since the initial momentum of the nucleus is assumed to be zero.

Now we can place ourself in the Center of Mass (CM) frame of reference, and calculate the transferred momentum, which has the same value in any reference frame. We have:

$$\begin{aligned} |\vec{q}|^2 &= \left|\vec{p'}_{\chi f} - \vec{p'}_{\chi 0}\right|^2 \\ &= \left|\vec{p'}_{\chi f}\right|^2 + \left|\vec{p'}_{\chi 0}\right|^2 - 2\left|\vec{p'}_{\chi f}\right|\left|\vec{p'}_{\chi 0}\right|\cos\vartheta_{CM} \ , \end{aligned} \tag{1.2}$$

where $\vec{p'}_{\chi f}$ and $\vec{p'}_{\chi 0}$ are the momenta of χ in the CM frame respectively after and before the collision, and ϑ_{CM} is the *scattering angle in the CM frame* (we mark with a prime $'$ the quantities calculated in the CM frame).

Since by assumption the scattering is elastic, we have that $\left|\vec{p'}_{\chi f}\right| = \left|\vec{p'}_{\chi 0}\right|$, so the above equation becomes:

$$|\vec{q}|^2 = 2\left|\vec{p'}_{\chi 0}\right|^2 (1 - \cos\vartheta_{CM}) \ . \tag{1.3}$$

With simple kinematics we can demonstrate the relation

$$\vec{p'}_{\chi 0} = -\vec{p'}_{A0} = m_{red}\vec{v}_{rel} \ , \tag{1.4}$$

where

$$m_{red} \doteq \frac{m_\chi m_A}{m_\chi + m_A} \ , \tag{1.5}$$

is the *WIMP-nucleon reduced mass* and $\vec{v}_{rel}$ is the *relative velocity* between the nucleus and the WIMP in the Laboratory frame. Inserting equation (1.4) in equation (1.3) we obtain

$$|\vec{q}|^2 = 2m_{red}^2 v_{rel}^2 (1 - \cos\vartheta_{CM}) \ . \tag{1.6}$$

[4]The Laboratory frame is the one where the nucleus is initially at rest.

Eventually from (1.1) we get:

$$E_r = \frac{m_{red}^2 v_{rel}^2 \left(1 - \cos\vartheta_{CM}\right)}{m_A} \ , \tag{1.7}$$

which provides the recoil energy of a nucleus as a function of the relative velocity.

1.2.2 Relation between velocity and maximal recoil energy

Now we want to see what (1.7) can tell us in the case of our interest, the elastic scattering between a WIMP and a nucleus. Its meaning is that when a WIMP of a given velocity[5] v_{rel} scatters on a nucleus, it transfers to the nucleus a certain amount of energy E_r. This amount of energy depends on the masses and, in particular, depends on the scattering angle in the CM frame ϑ_{CM} which varies from 0 to π. A vanishing scattering angle means that the WIMP passes without interaction, so there is no transferred energy. On the other hand the WIMP can backscatter, i.e. $\vartheta_{CM} = \pi$. This is the case which corresponds to the maximum transfer of energy, for a given v_{rel}. Thus, inserting in equation (1.7) the value $\vartheta_{CM} = \pi$, we obtain that the *maximal recoil energy* of a nucleus (initially at rest) hit by a WIMP of velocity v is:

$$E_{max}\left(v\right) = \frac{2m_{red}^2 v^2}{m_A} \ . \tag{1.8}$$

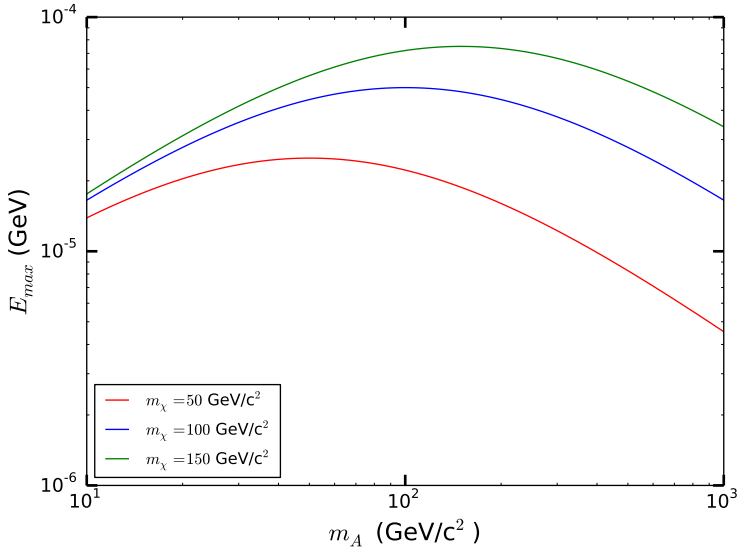

Figure 1.2: Maximal recoil energy E_{max} as a function of the mass of the target nucleus m_A, for three different values of m_χ. The relative velocity between the WIMP and the nucleus has been fixed to 300 km/s.

[5]The nucleus is considered to be initially at rest in the Laboratory, so the relative velocity between the nucleus and the WIMP is equal to the WIMP velocity in the Laboratory frame.

Inverting this relation we obtain the *minimal velocity* v_{min} necessary for a WIMP of mass m_χ to transfer to a nucleus of mass m_A the recoil energy E_r, which reads:[6]

$$v_{min}\left(E_r\right) \doteq \sqrt{\frac{E_r m_A}{2m_{red}^2}} \ . \tag{1.9}$$

In figure 1.2 we have plotted the maximal recoil energy E_{max} as a function of the mass of the target nucleus m_A, for three different values of m_χ. As we can clearly see, every curve presents a maximum. The positions of these maxima coincide with masses such that $m_A = m_\chi$. This can be easily proven finding the values of m_A for which the equation $\partial E_r/\partial m_A = 0$ is satisfied. This tells us that the maximal transfer of energy (so the maximum recoil energy) for a given WIMP occurs when using a target nucleus of roughly the same mass, so the choice of the nucleus to be used as a target in a detector determines which WIMP masses the detector will be more sensitive to. Lower mass nuclei will give a detector more sensitive to lower mass WIMPs.

1.3 The event rate

We now want to compute the expected rate of events in a DMDD experiment.

Our physical intuition can drive us toward a simple form for this quantity, but there are many subtle facts which must be taken into account, most of them related to the experimental issues that we will discuss in chapter 2.

Before starting let us remark that in this section we are dealing with $\vec{v'}$, which is the *velocity of the WIMP w.r.t. the target nucleus*, i.e. the velocity of the WIMP in the frame of reference comoving with the Earth. However, the dark matter halo around our Galaxy is not comoving with the Earth. So we can define another velocity $\vec{v}$ which is the *velocity of the WIMP in the Galactic frame of reference*, i.e. the frame of reference w.r.t. which the dark matter halo has no global motion. The two velocities are related by a Galilean transformation, as we will see in the following sections.

1.3.1 The total event rate

We can write the *total event rate per unit detector mass* R expected in a dark matter direct detection experiment as:[7]

$$R = \frac{n_{\chi\odot}}{m_A}\left\langle v'\sigma\left(v'\right)\right\rangle = \frac{n_{\chi\odot}}{m_A}\left\langle v'\int_{E_T}^{E_{max}(v')} dE_r \frac{d\sigma}{dE_r}\left(E_r, v'\right)\right\rangle \ , \tag{1.10}$$

[6] Since for the rest of this work we will focus on elastic scattering, we will not discuss inelastic scattering further. Anyway, let us just mention that in the case of an inelastic scattering interaction the minimal velocity becomes $v_{min} = \frac{1}{\sqrt{2m_A E_r}}\left(\frac{m_A E_r}{m_{red}} + \delta\right)$, where δ is the *mass splitting* between the lightest and next-to-lightest states in the spectrum (see for instance [12]).

[7] In this chapter we neglect the corrections due to the experimental setup, like the energy resolution, that we will introduce in the next chapter.

where $n_{\chi\odot} = \varrho_\odot / m_\chi$ is the *number density of WIMPs at the location of the Sun* (and so of the Earth), $\varrho_\odot$ is the *dark matter density at the location of the Sun* (*local dark matter density* from now on), m_χ is the *mass of the WIMP* considered, m_A is the *mass of the nucleus* and $\frac{d\sigma}{dE_r}(E_r, v')$ is the *differential cross section for the process*. The integration goes from the *threshold energy* E_T, i.e. the minimal recoil energy which is considered for the analysis of the data of a given experiment, to the maximal recoil energy E_{max} that has been defined in the previous section.

The symbol $\langle \ldots \rangle$ stands for *average over velocities* $\vec{v'}$, and for any function $h(\vec{v'})$ it is defined as

$$\left\langle h(\vec{v'}) \right\rangle \doteq \int d^3\vec{v'} h(\vec{v'}) f_{\vec{v'}}(\vec{v'}) = \int_0^{2\pi} d\varphi \int_0^{\pi} \sin\vartheta d\vartheta \int_0^{+\infty} dv' v'^2 h(\vec{v'}) f_{\vec{v'}}(\vec{v'}) \ . \quad (1.11)$$

The variable $\vec{v'}$ is the *velocity of a WIMP in the rest frame of the detector*, i.e. any frame of reference comoving with the Earth. $f_{\vec{v'}}(\vec{v'})$ is the *distribution of the WIMP's velocities in the Eath reference frame* (normalized by definition). It is of fundamental importance not to misinterpret $f_{\vec{v'}}(\vec{v'})$ nor $\vec{v'}$. In section 1.6 we will provide some different forms for the distribution of the WIMPs velocities expressed in the Galactic reference frame, and soon after we will show how to transform them into $f_{\vec{v'}}(\vec{v'})$.

We can rewrite equation (1.10) as

$$R = \frac{n_{\chi\odot}}{m_A} \int_0^{2\pi} d\varphi \int_0^{\pi} \sin\vartheta d\vartheta \int_0^{+\infty} dv' v'^3 f_{\vec{v'}}(\vec{v'}) \int_{E_T}^{E_{max}(v')} dE_r \frac{d\sigma}{dE_r}(E_r, v') \ . \quad (1.12)$$

Using the *Heaviside step function* $\Theta(x)$, we can rewrite the integral over E_r as

$$\int_{E_T}^{E_{max}(v')} dE_r \ldots = \int_{E_T}^{\infty} dE_r \ldots \Theta\left(E_{max}(v') - E_r\right) \ , \quad (1.13)$$

and so the event rate becomes:

$$R = \frac{n_{\chi\odot}}{m_A} \int_{E_T}^{\infty} dE_r \int_0^{2\pi} d\varphi \int_0^{\pi} \sin\vartheta d\vartheta \int_0^{+\infty} dv' v'^3 f_{\vec{v'}}(\vec{v'}) \Theta\left(E_{max}(v') - E_r\right) \frac{d\sigma}{dE_r}(E_r, v') \ . \quad (1.14)$$

Now it is interesting to observe in detail the boundaries of the integration over E_r and v'. What we note is that we are integrating over an area that, in the plane E_r, v', is defined by the value E_T and by the curve $E_{max}(v') = \frac{2m_{red}^2 v'^2}{m_A}$. Under these integrals we can rewrite the Heaviside function as

$$\Theta\left(E_{max}(v') - E_r\right) = \Theta\left(\frac{2m_{red}^2 v'^2}{m_A} - E_r\right) = \Theta\left(v' - \sqrt{\frac{E_r m_A}{2m_{red}}}\right) = \Theta\left(v' - v'_{min}\right) \ , \quad (1.15)$$

where as we have seen v'_{min} is defined as

$$v'_{min}(E_r) \doteq \sqrt{\frac{E_r m_A}{2m_{red}^2}} \ . \quad (1.16)$$

This allows us to write

$$R = \int_{E_T}^{\infty} dE_r \frac{n_{\chi\odot}}{m_A} \int_0^{2\pi} d\varphi \int_0^{\pi} \sin\vartheta d\vartheta \int_{v'_{min}}^{+\infty} dv' v'^3 f_{\vec{v'}}(\vec{v'}) \frac{d\sigma}{dE_r}(E_r, v') \ , \tag{1.17}$$

and eventually:

$$R = \int_{E_T}^{\infty} dE_r \frac{dR}{dE_r}(E_r) \ , \tag{1.18}$$

$$\frac{dR}{dE_r}(E_r) \doteq \frac{n_{\chi\odot}}{m_A} \int_{|\vec{v'}|>v'_{min}(E_r)} d^3\vec{v'} v' f_{\vec{v'}}(\vec{v'}) \frac{d\sigma}{dE_r}(E_r, v') \ , \tag{1.19}$$

$$\tag{1.20}$$

where we have defined the *differential event rate* $\frac{dR}{dE_r}$.

1.4 The scattering cross section

Let us now focus on the differential scattering cross section which appears in equation (1.19).

1.4.1 Split of the differential event rate into particle physics and astrophysics

In the case of elastic scattering, either if we are interested in a *spin-dependent interaction* (*SD*), or in a *spin-independent interaction* (*SI*), we can use for the differential cross section the expression (see for instance [8, pages 265, 272])

$$\frac{d\sigma}{dq^2}\left(q^2, v\right) = \frac{\sigma_0}{4m_{red}^2 v^2} F^2(q) \ , \tag{1.21}$$

where σ_0 is a *"standard" cross section at zero momentum transfer*, $F(q)$ is the *form factor* which accounts for the non-null dimension of the nucleus and its shape, and q is the transferred momentum as before. We will justify this equation in the next section.

Recalling that the recoil energy and the transferred momentum are related by $E_r = q^2/2m_A$, we obtain that

$$\frac{d\sigma}{dE_r}(E_r, v) = \frac{\sigma_0 m_A}{2m_{red}^2 v^2} F^2(E_r) \ . \tag{1.22}$$

Inserting this expression in equation (1.19), and recalling that $n_{\chi\odot} = \varrho_\odot/m_\chi$, we can write

$$\frac{dR}{dE_r}(E_r) = \frac{\varrho_\odot \sigma_0}{2m_\chi m_{red}^2} F^2(E_r)\, \tilde{\eta}(E_r, t) \tag{1.23}$$

$$\tilde{\eta}(E_r) \doteq \int_{|\vec{v'}|>v'_{min}(E_r)} d^3\vec{v'} \frac{1}{v'} f_{\vec{v'}}(\vec{v'}) \ . \tag{1.24}$$

Note that when we will make the standard assumption of a Maxwell-Boltzmann form for the speed distribution in the Galactic frame, we will use the adimensional quantity η, defined as

$$\eta \doteq v_0 \tilde{\eta} \ , \tag{1.25}$$

where v_0 is the *most probable speed* of the Maxwell-Boltzmann distribution (the one at which the maximum of the distribution occurs).

Writing the differential event rate in the above way hallows us to separate it in two parts: $\varrho_\odot \tilde{\eta}$, which contains all the astrophysical dependences, and the other terms which contain all the description of the WIMP-nucleus interaction from the point of view of particle and nuclear physics.

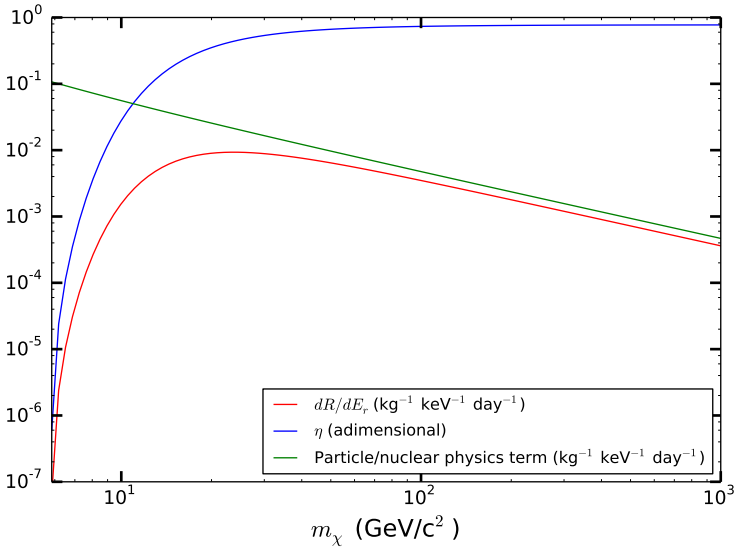

Figure 1.3: Contributions to dR/dE_r from astrophysics and from particle/nuclear physics as functions of the WIMP mass m_χ, for a xenon target nucleus.

Figure 1.3 gives an idea of the impact on the differential rate dR/dE_r of the two contributions, the particle physics one and the astrophysics one, as a function of the mass. In particular we can remark that the astrophysics dominates the behavior of $dR/dE_r\,(m_\chi)$ at small m_χ, while at big m_χ the other part dominates.

1.4.2 Spin-dependent and spin-independent interactions

The "standard" cross section at zero momentum transfer σ_0 can be used to describe either a spin-dependent (SD) or a spin-independent (SI) interaction, so we will write it as:

$$\sigma_0 = \begin{cases} \sigma_{SI} & \text{for SI interactions,} \\ \sigma_{SD} & \text{for SD interactions.} \end{cases}$$

Spin-independent interaction

For SI interactions, i.e. for the case on which we will focus the most in the following chapters, we have

$$\sigma_{SI} = \frac{4}{\pi} m_{red}^2 \left(Z f_p + (A - Z) f_n \right)^2 \ , \tag{1.26}$$

where A is the *mass number* of the nucleus considered, Z is the *number of protons* (so $(A - Z)$ is the *number of neutrons*), and f_p and f_n are the *effective couplings of the WIMPs to protons and neutrons* (see for instance [8, page 271]). We will show in the next section how this equation arises. In many cases (for instance for the *neutralino*, but also for many other WIMP candidates) the two couplings are comparable, i.e. $f_p \approx f_n$ (see for instance [14]). In these cases we can write (see [12]):

$$\sigma_{SI} \approx \frac{m_{red}^2}{m_{red,p}^2} A^2 \sigma_{p,SI} \ , \tag{1.27}$$

where $m_{red,p}$ is the *reduced mass between the WIMP and the proton*, and $\sigma_{p,SI}$ is the *WIMP-nucleon cross section*. This equation becomes exact if $f_p = f_n$.

Inserting this approximation in equation (1.23) we obtain

$$\frac{dR}{dE_r}(E_r) = \frac{\varrho_\odot A^2 \sigma_{p,SI}}{2 m_\chi m_{red,p}^2} F^2(E_r) \, \tilde{\eta}(E_r, t) \ . \tag{1.28}$$

To give an idea of the orders of magnitude and units of measure involved, equation (1.28) with the expression (1.86) for η and the values of $m_\chi = 100$ GeV/c^2, $A = 131$ (a xenon nucleus), $E_r = 1$ keV and $\sigma_{p,SI} = 4 \times 10^{-43}$ cm^2 has the value of $\frac{dR}{dE_r} \approx 10^{-2}$ kg^{-1} keV^{-1} days^{-1}.

1.5 Computation of the elastic scattering cross sections

The aim of this section is to justify equations (1.21) and (1.26) in the framework of a particular class of models. The WIMP-nucleus elastic scattering cross section depends mainly on the WIMP-quark interaction strength. Anyway, the scattering rate is computed from the WIMP-nucleus cross section, so a very important role is played by the distribution of nucleons inside the nucleus and that of quarks inside the nucleons. Thus the computation of the WIMP-nucleus cross section should be worked out in three main steps.

For illustrative purposes, let us now consider the case of cold dark matter to be represented by a supersymmetric neutralino.[8] This case is considered for instance in [8] or [15].

[8] A similar description holds for most other WIMP candidates with a SI interaction arising through scalar couplings. The neutralino is usually used for illustrative purposes because it is among the favored WIMP candidates (see for instance [8]) and because it represents a useful benchmark in which working out computations. In the framework of the minimal supersymmetric

The first step consists in determining the interaction of WIMPs with quarks and gluons. The effective interactions of neutralinos at the microscopic level are in practice inferred from diagrammatic calculations.[9] The relevant quantities like the couplings are determined by the supersymmetric model. Thus, the fundamental elastic scattering cross section is strongly model dependent.

The second step is the translation of the microscopic interactions into interactions with nucleons, making use of the matrix elements of the quark and gluon operators in a nucleon state. There are several quantitatively different types of interactions: vector, axial-vector, scalar, pseudoscalar and tensor, which add very differently inside the nucleon. All this implies additional uncertainties in the final elastic-scattering cross section, for instance coming from experimental constraints on the nucleon quark content, or from those coming from Lattice-QCD computations.

The third step finally consists of adding coherently the spin and scalar components of the nucleons, using nuclear wave functions, to give the WIMP-nucleus cross section as a function of momentum transfer. This is obtained by sandwiching the nucleon operators from the previous step in a nuclear state. This step introduces a form-factor suppression, which reduces the cross section for heavy WIMPs and heavy nuclei.

Anyway, an important simplification in the above calculations occurs because the elastic scattering of WIMPs takes place in the extreme non-relativistic limit. In particular, the axial-vector current becomes an interaction between the spin of the quark and the spin of the WIMP, while the vector and tensor currents assume the same form of the scalar interaction. Because of this reason, only two cases needs to be considered: scalar interaction and spin-spin interaction. In the latter, the WIMP couples to the spin of the nucleus, while in the former it couples to the mass of the nucleus. The complete elastic-scattering cross section is the sum of these two pieces.

standard model (MSSM), the neutralino is the lightest of the four mass eigenstates arising from linear combinations of the Bino $\tilde{B}$, the Wino $\tilde{W}^3$ and the Higgsinos $\tilde{H}_1^0$ and $\tilde{H}_2^0$, which are the superpartners of the photon, Z^0 boson and the neutral Higgs bosons. The neutralino is usually stable and in many supersymmetric models it is the lightest supersymmetric particle (LSP).

[9] An effective-Lagrangian approach is usually possible because the momentum exchanged between for instance the neutralino and a quark is small compared to the mass of the mediator. In fact, as we have seen the WIMP velocities are non relativistic, and thus the transferred energy (and so the momentum) are small, when compared to the masses of the mediator that for the scalar interaction can be for instance an Higgs Boson. This approach is no more valid if a mediator lighter w.r.t. the exchanged momentum is taken into account.

1.5.1 Spin-Independent cross section

Microscopic level

Microscopic interactions other than the axial-vector one can be very important and will often dominate over the spin interaction in heavy nuclei, so it is of fundamental importance to evaluate this contribution accurately. The scalar neutralino-nucleon interaction arises from several sources. There are contributions from squark exchange and Higgs exchange which give rise to couplings to quark currents, and there are one-loop amplitudes for interactions of neutralinos with gluons. An effective Lagrangian for scalar and tensor neutralino-quark and neutralino-gluon interactions can be found in [8, page 267]. Here we consider as in [15] the Lagrangian

$$\mathcal{L} = \alpha_i \overline{\chi}\chi\overline{q_i}q_i \ , \tag{1.29}$$

that has to be summed over quark generations, with i labeling the u-type and d-type generations, and the full expression for the coefficients α_i provided in [15] or [8].

Nucleonic matrix elements

The next step is to evaluate the matrix elements of the quark and gluon operators in a nucleon state. Those of the light-quark current are obtained in chiral perturbation theory from measurements of the *pion-nucleon sigma term* $\sigma_{\pi N}$. For each of the three light quarks (q = u, d, s) we can define the quantities $f_{Tq}^{(N)}$ by:

$$M_N f_{Tq}^{(N)} \doteq \langle N| \, m_q \overline{q}q \, |N\rangle \ , \tag{1.30}$$

where $N = p$ (for protons) or $N = n$ (for neutrons). We can also define the quantities

$$m_q B_b^{(N)} \doteq \langle N| \, m_q \overline{q}q \, |N\rangle \ , \tag{1.31}$$

in terms of which the the pion-nucleon sigma term $\sigma_{\pi N}$ may be written as

$$\sigma_{\pi N} = m_{ud}\left(B_u^{(N)} + B_d^{(N)}\right) \quad \text{and} \tag{1.32}$$

$$\sigma_{\overline{s}sN} = 2m_s \langle N| \, \overline{s}s \, |N\rangle \ , \tag{1.33}$$

where $m_{ud} \doteq \frac{1}{2}(m_u + m_d)$.

For the heavy quarks we can define instead

$$f_{TG}^{(N)} \doteq 1 - \sum_{q=u,d,s} f_{Tq}^{N} \ , \tag{1.34}$$

and it is found [8] that (for Q = c,t,b)

$$\langle N| \, m_Q \overline{Q}Q \, |N\rangle = \frac{2}{27} M_N f_{TG}^{(N)} \ . \tag{1.35}$$

In the limit of large squark masses, i.e. $m_\chi \ll m_{\tilde{q}}$ and $m_q \ll m_{\tilde{q}}$, to lowest order in $m_{\tilde{q}}^{-1}$ the effective couplings of neutralinos to protons and neutrons f_p and f_n can be approximated as (see [15] and [8])

$$\frac{f_N}{M_N} \approx \sum_{q=u,d,s} f_{Tq}^N \frac{\alpha_q}{m_q} + \sum \frac{2}{27} f_{TG}^{(N)} \sum_{q=c,b,t} \frac{\alpha_q}{m_q} \ , \tag{1.36}$$

where the coefficients α_q are those of the Lagrangian (1.42).

The determination of the pion-nucleon sigma term $\sigma_{\pi N}$ from data is plagued by significant uncertainties, which in turns affect the parameter $f_{Tq}^{(N)}$, and eventually the cross section for spin-independent interaction. The uncertainty in the pion-nucleon sigma term is perhaps the biggest one in the calculation of this subsection (see for instance [15]). This uncertainty impacts on the interpretation of experimental searches for cold dark matter, and (particularly interesting for us) DMDD. To properly evaluate the impact of the results of such experiments on (for instance) supersymmetric models, it is important to understand and minimize the hadronic uncertainties in the elastic scattering matrix elements. For certain models, the allowed values of the spin-independent cross section can nowadays be reached by the experimental sensitivities, but these cross sections are affected by the above mentioned uncertainties. [15] appeals for a dedicated effort to reduce the experimental uncertainties in the pion-nucleon sigma term since this quantity can be crucial to the understanding of new physics beyond the Standard Model.

Lattice-QCD calculations are nowadays able to estimate this quantity with uncertainties that are considerably reduced w.r.t. the past. Thus, they provide an alternative to the experimental efforts to reduce the above mentioned uncertainties, and they are complementary to them. To give an idea of the estimates provided by Lattice-QCD, we report here the values of $\sigma_{\pi N}$ and $\sigma_{\bar{s}sN}$ evaluated by our colleagues[10] using Lattice-QCD calculations. These values are $\sigma_{\pi N} = 41.8\,(3.2)\,(4.4)$ MeV and $\sigma_{\bar{s}sN} = 235\,(113)\,(20)$ MeV, where the first brackets provide statistical uncertainties, and the second ones systematic uncertainties.[11]

Nuclear matrix elements

We finally have to evaluate the effective interaction with the nuclei by evaluating the matrix elements of the nucleon operators in a nuclear state. Since no spin is involved here, the nuclear physics is simplified, because in fact the operators simply count the nucleons, so that the amplitude is proportional to the nucleon number. This gives a substantial enhancement for heavy nuclei.

[10] We warmly thanks L. Lellouche and C. Torrero for providing us with their preliminary results quoted above.

[11] The same results can be rewritten in terms of other useful quantities as $f_{udN} \doteq \sigma_{\pi N}/M_N = 0.0449\,(42)\,(48)$ and $f_{sN} \doteq \sigma_{\bar{s}sN}/2M_N = 0.126\,(60)\,(11)$. Let us remark that these Lattice-QCD computations are worked out assuming no difference between the masses of the up and down quarks, so that the proton and neutron have the same mass, here indicated with M_N.

At non-zero momentum transfer, the form factor associated with the nucleon-number operator is simply the Fourier transform of the nucleon density, which has a well-determined form. We denote the form factor as $F(E_r)$, where E_r is the energy that is transferred from the WIMP to the nucleus. The most commonly used forms of the nuclear form factor are given in the next subsection.

The differential cross section for the scalar interaction can now be written

$$\frac{d\sigma}{dq} = \frac{F^2(q)}{\pi v^2}\left[Zf_p + (A-Z)f_n\right]^2 = \frac{\sigma_{SI}}{4m_{red}^2 v^2}F^2(q) \ , \tag{1.37}$$

where $q \doteq |\vec{q}|$ is the modulus of the transfered momentum, and to obtain the second equality we have defined the *standard cross section at zero momentum transfer* as

$$\sigma_{SI} \doteq \int_0^{4m_{red}^2 v^2} dq \frac{d\sigma(q=0)}{dq} = \frac{4}{\pi}m_{red}^2\left[Zf_p + (A-Z)f_n\right]^2 \ . \tag{1.38}$$

Nuclear form factors

The nuclear form factor $F(E_r)$ is a function of the transferred energy E_r, so it is implicitly a function of the transferred momentum $q = \sqrt{2m_A E_r}$. It is normalized to 1 at zero energy transfer and it decreases while increasing E_r.

No form factor. As a first approximation we can neglect the form factor $F(E_r)$, i.e. put $F(E_r) = 1$.

Exponential form factor. A better but still oversimplified approximation is to use an exponential form (see [8, page 272]), i.e.

$$F(E_r) = \exp\left(-\frac{E_r m_\chi r_0^2}{3}\right) \ , \tag{1.39}$$

where $r_0 = 10^{-13}cm \times \left(0.3 + 0.91\left(m_A/GeV\right)^{1/3}\right)$ is the *nuclear radius*. It corresponds to a radial density profile of the nucleus with a Gaussian form.

Woods-Saxon form factor. A more accurate form factor is (see for instance [8])

$$F(E_r) = \left[\frac{3j_1(qR_1)}{qR_1}\right]^2 \exp\left(-(qs)^2\right) \ , \tag{1.40}$$

where $q = \sqrt{2m_A E_r}$ is the transferred momentum, $R_1 = \sqrt{R^2 - 5s^2}$ with $R \approx 1.2\ fm \times A^{1/3}$, j_1 is a spherical Bessel function and $s \approx 1\ fm$. This form factor is not that obtained from the Fourier transform of the Woods-Saxon density distribution, but it is very similar to it so it bears the same name.

Helm form factor. A reasonably good approximation for the nuclear form factor, which is widely used nowadays, is (see [12]) the *Helm form factor*

$$F(q) = 3e^{-q^2 s^2/2} \frac{\sin(qr_n) - qr_n \cos(qr_n)}{(qr_n)^3} \ , \tag{1.41}$$

where $s \approx 0.9\ fm$ and $r_n^2 = c^2 + \frac{7}{3}\pi^2 a^2 - 5s^2$ is an effective nuclear radius with $a \approx 0.52\ fm$ and $c \approx 1.23A^{1/3} - 0.60\ fm$. This is the form factor more often used in the literature of DMDD, and we have used it in our implementation as well.

More realistic form factors. Even though the Helm form factor is a common choice in the literature, studies dedicated to the development of more realistic form factors to be used for SI interaction in the framework of DMDD exist. For instance, in [16] model independent, analytic form factors for SI neutralino-nucleon scattering are derived, mainly on the basis of experimental data of elastic electron scattering, which allows a more careful determination of these factors. Significant differences may exist even at relatively low momentum transfers between generic Helm form factors and these more realistic ones, particularly for large A nuclei. Two of these proposed form factors are the *Fourier Bessel* and the *Sum of Gaussian*. The authors of [16] warmly suggest their use in computing limits on neutralino-nucleon cross sections and detection rates in direct dark matter searches.

1.5.2 Spin-Dependent cross section

The SD scattering is due to the interaction of a WIMP with the spin of the nucleus through the part of the Lagrangian given by operators such as

$$\mathcal{L} = \beta_i \overline{\chi}\gamma^\mu\gamma^5\chi\overline{q_i}\gamma_\mu\gamma^5 q_i \ , \tag{1.42}$$

that has to be summed over quark generations, with i labeling the u-type and d-type generations, and the expression for the coefficients β_i provided in [15] or [8]. This interaction takes place only in those detector isotopes with an unpaired proton and/or an unpaired neutron.

The spin-dependent part of the elastic WIMP-nucleus cross section can be written as

$$\sigma_{SD} = \frac{32}{\pi} G_F^2 m_{red}^2 \Lambda^2 J(J+1) \ , \tag{1.43}$$

where m_{red} is the *reduced neutralino mass*, J is the *spin of the nucleus* and

$$\Lambda \doteq \frac{1}{J}\left(a_p\langle S_p\rangle + a_n\langle S_n\rangle\right) \ . \tag{1.44}$$

In the above equation, $\langle S_p\rangle$ and $\langle S_n\rangle$ are the *average spin contributions from the proton and neutron groups*, and a_p and a_n are the *effective couplings to the proton and neutron* respectively, given by

$$a_p = \sum_q \frac{\beta_q}{\sqrt{2}G_F}\Delta_q^{(p)} \qquad \text{and} \qquad a_n = \sum_q \frac{\beta_q}{\sqrt{2}G_F}\Delta_q^{(n)} \ . \tag{1.45}$$

The factors Δ_q parametrize the *quark spin content of the nucleon* and are only significant for the light (u,d,s) quarks.

Let us remark that (see for instance [12]) SD scattering is often less important than SI scattering in DMDD experiments for two reasons. First, $\sigma_{SI} \propto A^4$ for heavy WIMPs, while $\sigma_{SD} \propto A^2$. Second, spin-zero isotopes do not contribute to SD scattering, which is thus reduced in elements where non-zero-spin nuclei represent only a small fraction of the naturally occurring isotopes within a detector's target mass. The fact that SD couplings may often be larger than SI couplings is not enough to make the SD dominant ([12]).

Let us remark that also in the SD case a nuclear form factor should be taken into account. Anyway, the SD form factor depends on the spin structure of a nucleus and thus it is different between individual elements.

1.6 The dark matter's velocity distribution

Galactic dark matter should be distributed in a halo which encompasses our galaxy. In the study of the dynamics of our galaxy, we can model the dark matter in the Milky Way as a gas of particles which can be described via its phase-space distribution $f(\vec{x}, \vec{v})$. The phase-space distribution contains all information about the spatial and velocity distributions, which can be specified individually by integrating out the conjugate quantity. However, we will use that approach in chapter 3, while here we use a more simple approach, starting from the study of $f(\vec{v})$ only, because this is the quantity that directly enters in the above computations.

We will start from the simplest picture, and after we will try to make it more complex. Let us assume that the DM halo presents no global motion, so it is not rotating with the stars of the Galactic disk. We can call the rest frame of the halo the *Galactic reference frame*, which does not rotate, and has the center of the Galaxy at the origin. So the *Galactic reference frame* is defined as the reference frame where the dark matter particles of the halo present no global motion, thus we have $\langle \vec{v} \rangle \doteq \int d^3v \vec{v} f_{\vec{v}}(\vec{v}) = \vec{0}$. Note that while by definition the average velocity of the dark matter particles is zero, of course the velocity of a single dark matter particle should not.

For dark matter direct detection experiments it is necessary to take into account the motion of the Sun throughout the Galaxy, and that of the Earth around the Sun.[12] The Sun is orbiting around the center of the Galaxy, and in particular it is moving with respect to the above mentioned frame. The Earth has a motion in that frame that is the composition of the motion of the Solar System, and Earth's peculiar motion around the Sun. Since experiments of direct detection are worked out on the Earth, the distribution of dark matter velocities that they are sensitive to is not the one of the dark matter particles in their rest frame, i.e. the *Galactic reference frame*, but rather the one in the Earth frame, $f_{\vec{v}'}(\vec{v'})$.

[12] In this work we neglect the rotation of the Earth around itself, because the daily modulation of the WIMP signal that it would induce is not detectable by current experiments.

In order to work out the integral in (1.24), and so to be able to calculate the event rate we expect to see in a dark matter direct detection experiment, we need to know the *distribution of the WIMPs' velocities in the frame of reference of the Earth* $f_{\vec{v}'}(\vec{v'})$.

This distribution is related to the one in the Galactic frame $f_{\vec{v}}(\vec{v})$ by a Galilean transformation, which is independent from the functional form of $f_{\vec{v}}(\vec{v})$.

One thus assumes a particular form for $f_{\vec{v}}(\vec{v})$, the *distribution of the WIMP's velocities* $\vec{v}$ *in the Galactic reference frame*, and converts it via that transformation into the corresponding $f_{\vec{v}'}(\vec{v'})$.

In subsection 1.6.1 we will provide the standard forms most commonly used for $f_{\vec{v}}(\vec{v})$. More realistic forms will be studied in the subsequent chapters. We present the above mentioned Galilean transformation in a crude thought intuitive way in section 1.6.2, and in a detailed manner in section 1.6.3. We show the impact of the different steps on η in section 1.6.4 and we provide the transformed forms of the above mentioned distributions in section 1.6.5.

1.6.1 Velocity distributions in the dark matter rest frame

The standard assumption corresponds to chose for the velocity distribution in the Galactic frame a Maxwell-Boltzmann shape. We will study more realistic configurations in the following chapters.

Any object (stars, WIMPs, etc.) remains gravitationally bound to the Milky Way only up to a maximum value of its speed which is called the *escape speed* v_{esc}.[13] This can be taken into account adding a cut-off to the high velocity tail of the Maxwell-Boltzmann distribution. We present these possibilities in the following sections.

Pure Maxwell-Boltzmann distribution

For illustrative purposes, we will first introduce some general features of the Maxwell-Boltzmann distribution, before considering it in an astrophysical framework.

In statistical thermodynamics, the Maxwell-Boltzmann distribution describes the velocity of the particles of a classical ideal gas, in which the particles move freely without interacting with one another (except for very brief elastic collisions in which they may only exchange momentum and kinetic energy), when the system has reached the thermodynamical equilibrium.

The *Maxwell-Boltzmann distribution for the velocity vector* $\vec{v}$ is:

$$f_{\vec{v}}(\vec{v}) = \left(\frac{m}{2\pi k_B T}\right)^{\frac{3}{2}} \exp\left(-\frac{m\,|\vec{v}|}{2k_B T}\right) , \tag{1.46}$$

[13] This quantity is often referred to as *escape velocity*, but for coherence with the terminology that we use in the following sections we will not use this term (we will use the term *velocity* for vectors such as $\vec{v}$, and the term *speed* for moduli such as v).

where m is the mass of a gas particle, T is the temperature of the gas and k_B is the *Boltzmann constant*. This distribution has a mean of $\mu_{\vec{v}} = \vec{0}$ and a *root mean square speed* of: $\sigma_{\vec{v}} = \sqrt{\frac{3k_BT}{m}}$.

We can see this distribution in terms of the distributions of the three components of the velocity vector v_x, v_y and v_z. Let $\vec{v} = (v_x, v_y, v_z)$ be the *velocity vector* of the gas particles in the reference frame of null bulk motion. Let the components of $\vec{v}$ be normally distributed (i.e. they follow *Gaussian distributions*), and these distributions have *mean* $\mu_i = 0$ because there is no global motion, and *root mean square speed* $\sigma_i = \sqrt{\frac{k_BT}{m}}$ (with $i = x, y, z$), i.e. they follow the distribution:

$$f(v_i) = \sqrt{\frac{m}{2\pi k_B T}} \exp\left(-\frac{mv_i^2}{2k_BT}\right) . \tag{1.47}$$

Considering then the distribution for the random variable velocity vector $\vec{v}$, which is simply the product of the distributions for the three components, we have:

$$f_{\vec{v}}(v_x, v_y, v_z) = f(v_x) f(v_y) f(v_z) \tag{1.48}$$

$$= \left(\frac{m}{2\pi k_B T}\right)^{\frac{3}{2}} \exp\left(-\frac{m\left(v_x^2 + v_y^2 + v_z^2\right)}{2k_BT}\right) = f_{\vec{v}}(|\vec{v}|) \ , \tag{1.49}$$

i.e. a *three-dimensional normal distribution* (*multinomial distribution*), with a mean of $\mu_{\vec{v}} = \vec{0}$ and a *root mean square speed* of: $\sigma_{\vec{v}} = \sqrt{\frac{3k_BT}{m}}$. As we can see, this is simply the Maxwell-Boltzmann distribution for the velocity vector $\vec{v}$ just introduced above.

While equation (1.46) gives the distribution for the three-dimensional velocity vector, we are also interested in the distribution of the *speed* v (defined as $v \doteq |\vec{v}|$). In order to achieve this let us integrate $f_{\vec{v}}(\vec{v})$ over the angles:

$$\begin{aligned} \int d^3\vec{v} f_{\vec{v}}(\vec{v}) &= \int_{-\infty}^{+\infty} dv_x \int_{-\infty}^{+\infty} dv_y \int_{-\infty}^{+\infty} dv_z f_{\vec{v}}(\vec{v}) \\ &= \int_0^{2\pi} d\varphi \int_0^{\pi} \sin\vartheta d\vartheta \int_0^{+\infty} dv v^2 f_{\vec{v}}(\vec{v}) \\ &= \int_0^{+\infty} dv 4\pi v^2 f_{\vec{v}}(\vec{v}) \ , \end{aligned} \tag{1.50}$$

so we see that the *Maxwell-Boltzmann distribution for the speed* v is

$$f_v(v) = 4\pi v^2 f_{\vec{v}}(\vec{v}) \ . \tag{1.51}$$

The distribution $f_v(v)$ and $f_{\vec{v}}(\vec{v})$ are normalized to unity by definition, as can be trivially shown by directly computing the normalization.

We can rewrite the above distributions in a more convenient form. As we can argue from its expression, the distribution for the speed will increase from $v = 0$ to a certain value v_0 of v, and it will be decreasing toward zero for higher speeds.

The most probable speed v_0 is thus defined to be the speed at which the speed distribution (1.51) will have its maximum. Deriving this distribution w.r.t. v and imposing the derivative to vanish we get

$$v_0 = \sqrt{\frac{2k_BT}{m}} = \sqrt{\frac{2}{3}}\sigma_{\vec{v}} \ . \tag{1.52}$$

The relation between v_0 and $\sigma_{\vec{v}}$ will be useful in the sequel. Using this we can rewrite the above distributions in their usual form:

$$f_{\vec{v}}\left(\vec{v}\right) = \frac{1}{v_0^3\pi^{3/2}} \exp\left(-\frac{\left|\vec{v}\right|^2}{v_0^2}\right) \tag{1.53}$$

and

$$f_v\left(v\right) = \frac{4}{v_0^3\pi^{1/2}} v^2 \exp\left(-\frac{v^2}{v_0^2}\right) \ . \tag{1.54}$$

As we will show in section 3.4.3 (see also [17, page 304]), the Maxwell-Boltzmann velocity distribution is the distribution of a self-gravitating isothermal sphere of ideal gas, which corresponds to a collisionless system of stars described by the isothermal sphere profile (that we will introduce in chapter 3). This profile is sometimes used in astrophysics to describe a stellar system, the stars belonging to which thus have velocities distributed following the Maxwell-Boltzmann distribution. Also the velocities of an infinite homogeneous stellar system follow a Maxwell-Boltzmann distribution (see [17]).

The Maxwell-Boltzmann is also usually assumed for the velocity and speed distributions of the dark matter particles in the Galactic reference frame, where they have no global motion.[14] In DMDD the velocity distribution considered is the one at the position of the Solar system, which is assumed to have this form.

Cut Maxwell-Boltzmann distribution

Unfortunately, a pure Maxwell-Boltzmann distribution gives only a very approximate description of the real distribution of the WIMP's velocities. In fact there are many aspects that it does not take into account. The most important is that WIMPs with a speed higher than the escape speed v_{esc} will be no more gravitationally bound to the Galaxy, and so they will escape the halo. This can be taken into account by considering a Maxwell-Boltzmann distribution with a cut-off in the high-velocity tail.

Adding a cut-off has the effect of removing all the particles with a speed higher than the escape speed, while the pure Maxwell-Boltzmann contains particles with velocities that can be higher. Let us anticipate that the high velocity tail of the speed distribution is particularly important for the direct detection of light WIMPs, because among them only those that are sufficiently fast can provide a detectable

[14] We will see in chapter 3 how this distribution is related to the spatial distribution of the dark matter particles.

recoil energy to a target nucleus in the detector. Thus, adding a cut-off allows a more realistic interpretation of the experimental results in particular at low WIMP masses.

The simplest cut-off that we can use is a sharp one, so we can define a *cut Maxwell-Boltzmann distribution* as

$$f_{\vec{v}}^{esc}\left(\vec{v}\right) \doteq \frac{1}{N_{esc}} f_{\vec{v}}\left(\vec{v}\right) \Theta\left(v_{esc} - |\vec{v}|\right) = \begin{cases} \frac{1}{N_{esc}} f_{\vec{v}}\left(\vec{v}\right) & \text{if } |\vec{v}| < v_{esc} \ , \\ 0 & \text{if } |\vec{v}| \geqslant v_{esc} \ , \end{cases} \tag{1.55}$$

where N_{esc} is a normalization constant, $\Theta\left(x\right)$ is the Heaviside distribution[15] which is equal to zero for negative x and equal to 1 for positive x, and $f_{\vec{v}}\left(\vec{v}\right)$ is the Maxwell-Boltzmann distribution for the velocity given in equation (1.53).

As we did in the previous section, we can obtain the corresponding distribution for the speed $f_v^{esc}\left(v\right)$ as

$$f_v^{esc}\left(v\right) = 4\pi v^2 f_{\vec{v}}^{esc}\left(\vec{v}\right) \ , \tag{1.56}$$

which means that:

$$f_v^{esc}\left(v\right) = \frac{1}{N_{esc}} f_v\left(v\right) \Theta\left(v_{esc} - v\right) = \begin{cases} \frac{1}{N_{esc}} f_v\left(v\right) & \text{if } v < v_{esc} \ , \\ 0 & \text{if } v \geqslant v_{esc} \ . \end{cases} \tag{1.57}$$

Now we can normalize the two distributions by imposing

$$\int_{|\vec{v}|<v_{esc}} d^3\vec{v} f_{\vec{v}}^{esc}\left(\vec{v}\right) = \int_0^{v_{esc}} dv f_v^{esc}\left(v\right) = 1 \ , \tag{1.58}$$

which, in order to be satisfied, fixes the normalization constant at:

$$N_{esc} = \mathrm{erf}\left(z\right) - \frac{2}{\sqrt{\pi}} z \exp\left(-z^2\right) \ , \tag{1.59}$$

where $z \doteq \frac{v_{esc}}{v_0}$ and we remind that the *error function* is defined as:

$$\mathrm{erf}\left(t\right) \doteq \frac{2}{\sqrt{\pi}} \int_0^t exp\left(-x^2\right) dx \ . \tag{1.60}$$

Smoothly cut Maxwell-Boltzmann distribution

The cut-off that is present in equation (1.55) is sharp, so it is not physical. To smoothen the transition near the escape speed, one may use a (still ad hoc) version of the cut Maxwell-Boltzmann distribution which presents a smooth (exponential) cut-off. This distribution can be found for instance in [12] and it reads:

$$f_{\vec{v}}^{esc*}\left(\vec{v}\right) \doteq \begin{cases} \frac{1}{N_{esc}^*} \left(\frac{1}{\pi v_0^2}\right)^{3/2} \left[e^{-|\vec{v}|^2/v_0^2} - e^{-v_{esc}^2/v_0^2}\right] & \text{if } |\vec{v}| < v_{esc} \ , \\ 0 & \text{if } |\vec{v}| \geqslant v_{esc} \ , \end{cases} \tag{1.61}$$

[15] Let us remark that in this work we speak about distributions, but we treat them as functions and not as proper distributions in the mathematical sense of the term.

where

$$N^*_{esc} \doteq \mathrm{erf}\,(z) - \frac{2}{\sqrt{\pi}} z \left(1 + \frac{2}{3} z^2\right) e^{-z^2} \ . \tag{1.62}$$

The standard assumption for the dark matter velocity distribution is a Maxwell-Boltzmann, but often a smooth cut-off of this kind is used also in the standard picture.

The η function

Now that we have presented the velocity distributions which is used as a standard assumption, we want to redefine the term that contains the majority of the astrophysical information in the expression of the scattering rate.

This information is contained in $\tilde{\eta}$, defined in equation (1.24), but we may also use an adimensional quantity, so we define the *function* η as:

$$\eta \doteq v_0 \tilde{\eta} = v_0 \int_{|\vec{v}'| > v'_{min}(E_r)} d^3\vec{v}' \frac{1}{v'} f_{\vec{v}'}\left(\vec{v}'\right) \ . \tag{1.63}$$

Note that many authors define their η as our dimensionful $\tilde{\eta}$.

1.6.2 Velocity transformation: the basic picture

While the distribution of the velocity of the WIMPs in the Galactic reference frame is assumed to follow a Maxwell-Boltzmann distribution, the computation of the event rate relies on the velocity relative to the detector. The two distributions are related by a Galilean transformation, and there are two superimposed motions which must be considered separately. The first one is the motion of the Sun around the Galactic center, the second one is that of the Earth around the Sun.[16]

Motion of the Sun around the Galactic center

The Sun is orbiting the Galactic center and this orbit is approximately contained in the Galactic plane. This orbit is expected to be roughly elliptical, and because of this reason the velocity of the Sun forms an angle with the direction of the Galactic center (i.e. the line which connect the sun and the Galactic center) which is not 90°, as expected if the orbit would have been circular, but rather $\approx 60°$. The situation is sketched in figure 1.4.

In principle the velocity of the Sun is a time-dependent vector, but since the time-scale of its changes is by far bigger than the duration of a direct detection experiment, we consider it as a constant vector, only approximatively lying in the Galactic plane.

[16] As already said, in this work we neglect the rotation of the Earth around itself.

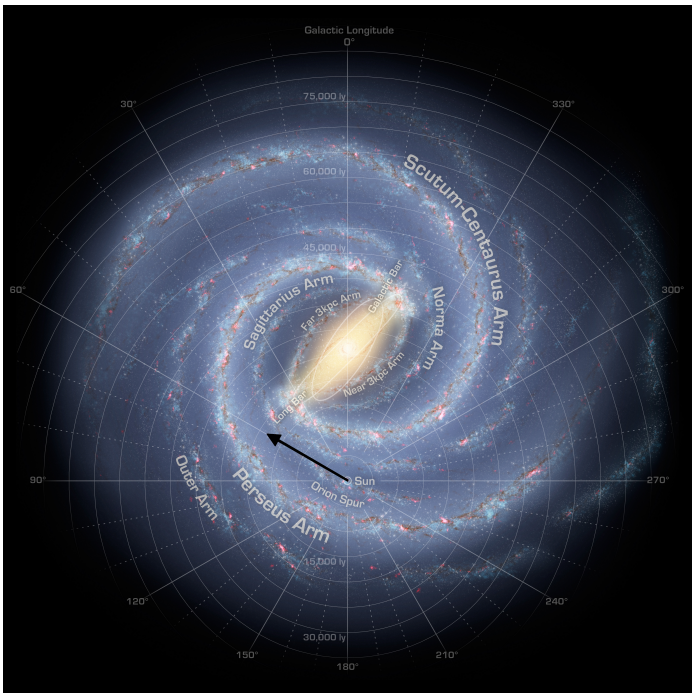

Figure 1.4: Artist's view of the Milky Way, with the position of the Sun in the Galactic plane, the projection of the Sun velocity and the Galactic longitude. Figure adapted from https://en.wikipedia.org.

Motion of the Earth around the Sun

The Earth is orbiting the Sun, the rotation's timescale of this motion can no longer be neglected with respect to the lifetime of DMDD experiments, thus Earth's velocity will be a time-dependent vector.

As illustrated by figure 1.5, the Plane of the Ecliptic is inclined with respect to the Galactic plane of an angle of roughly 60°.

Annual modulation

Here we encounter a very important characteristic of the event rate. The Earth is orbiting around the Sun, so in one year there will be a moment when the velocity of the Earth will be maximally aligned with that of the Sun (not parallel, see the following sections), as shown by figure 1.6. When this will happen, of course the flux of WIMPs hitting the Earth (and thus any DMDD detector) will be enhanced, and as a consequence the collision rate will have a maximum. Roughly six months later the situation will be inverted, and the collision rate will then have a minimum. This means that the collision rate will have an annual modulation, with one maximum and one minimum during the year. If the Maxwell-Boltzmann is assumed, with the standard values of the parameters, the maximum happens in June the 1st, and the minimum in December the 1st (see for instance [18]).

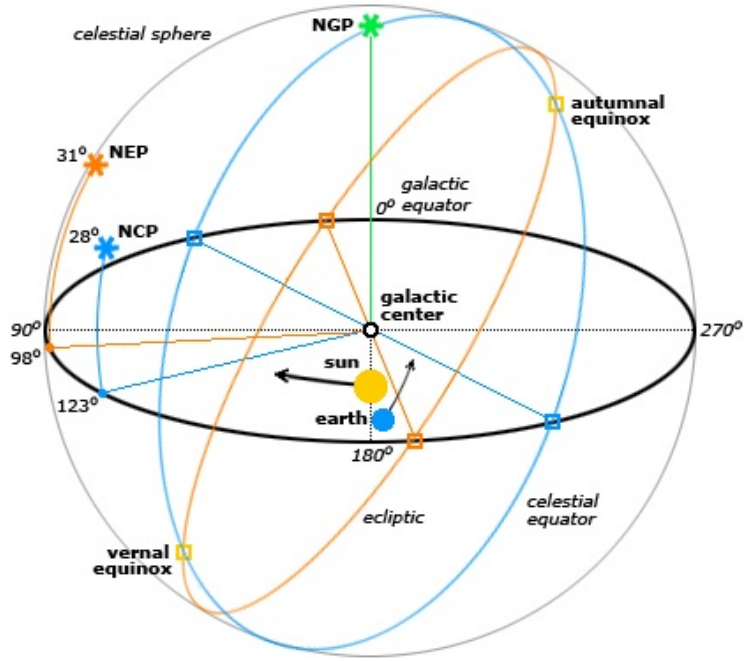

Figure 1.5: The relative position between the Ecliptic plane and the Galactic plane. Note that in reality the Ecliptic plane does not pass through the Galactic center. Note also that the diameter of the Ecliptic shown in the figure should point in a direction which lies in the Galactic plane, but 8° far away from the Galactic center, so the *Galactic longitude of the North Ecliptic Pole* is not 90°, but instead it is $l_{NEP} \approx 98°$. Figure from http://atomictoasters.com.

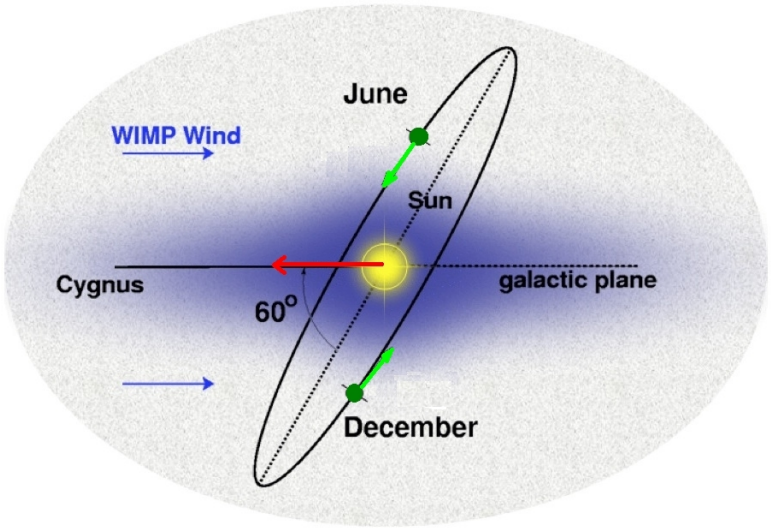

Figure 1.6: Relative motion of the Earth around the Sun, showing the maximum and the minimum alignment of the velocities of these two objects. Figure adapted from www.hep.shef.ac.uk.

1.6.3 Velocity transformation: rigorous calculation

Now we want to understand how to transform $f_{\vec{v}}(\vec{v})$ into $f_{\vec{v}'}(\vec{v'})$. For this purpose we need to understand how the velocities $\vec{v'}$ and $\vec{v}$ are related, and to insert this relation into $f_{\vec{v}}(\vec{v})$ (that we assume a priori) in order to obtain $f_{\vec{v}'}(\vec{v'})$.

The relation between the velocity of a WIMP in the Earth reference frame $\vec{v'}$ and the one in the Galactic reference frame $\vec{v}$ is given by the Galilean transformation:

$$\vec{v'} = \vec{v} - \vec{v}_{\oplus}(t) \ , \tag{1.64}$$

where $\vec{v}_{\oplus}(t)$ is the *velocity of the Earth reference frame* (i.e. any reference frame in which the Earth is at rest) *w.r.t. the Galactic reference frame*. Now the distribution $f_{\vec{v'}}\left(\vec{v'}_{\chi}\right)$ is simply obtained inserting (1.64) in $f_{\vec{v}}(\vec{v})$:

$$f_{\vec{v'}}(\vec{v'}) = f_{\vec{v}}(\vec{v}_{\oplus}(t) + \vec{v'}) \ . \tag{1.65}$$

We can also calculate $|\vec{v}|^2$:

$$|\vec{v}|^2 = \left|\vec{v}_{\oplus}(t) + \vec{v'}\right|^2 = \left|\vec{v'}\right|^2 + |\vec{v}_{\oplus}(t)|^2 + 2\left|\vec{v'}\right| |\vec{v}_{\oplus}(t)| \cos\vartheta \ , \tag{1.66}$$

where for every $\vec{v}$ the angle ϑ is the angle between $\vec{v}_{\oplus}$ and $\vec{v}$.

The motion of the Earth w.r.t. the Galactic frame

Before studying how the velocity distribution of dark matter changes, let us compute $\vec{v}_{\oplus}$. The velocity of the Earth w.r.t. the Galactic frame is constituted by two components:

$$\vec{v}_{\oplus}(t) = \vec{v}_{\oplus/\odot}(t) + \vec{v}_{\odot} \ , \tag{1.67}$$

where $\vec{v}_{\odot}$ is the velocity of the Sun w.r.t. the Galactic frame, detailed in the following paragraph, while $\vec{v}_{\oplus/\odot}(t)$ is the velocity of the Earth w.r.t. the Sun, described in the next-to-following one.

The motion of the Sun w.r.t. the Galactic frame

The velocity of the Sun in the Galactic frame can be separated itself into two components:

$$\vec{v}_{\odot} = \vec{v}_{LSR} + \vec{v}_{\odot pec} \ , \tag{1.68}$$

where $\vec{v}_{LSR}$ is the *velocity of the Local Standard of Rest*[17] (LSR), while $\vec{v}_{\odot pec}$ is the velocity of the Sun w.r.t. the LSR, called the *peculiar velocity of the Sun*.

Galactic coordinates are defined as the coordinates in the Cartesian frame aligned with the x axis in the direction which connects the center of the Galaxy

[17]The LSR is defined as the rest frame at the location of the Sun of a star that would be on a circular orbit in the gravitational potential one would obtain by azimuthally averaging away non-axisymmetric features in the actual Galactic potential.

and the Sun, directed toward the center of the Galaxy, the y axis lying in the plane of the disk, and directed as the rotation of the stars of the disk, and thus the z axis perpendicular to the Galactic plane, see figure 1.4. The components of the velocity vectors in this section are given in the Galactic reference frame.

The velocity of the LSR is defined as:

$$\vec{v}_{LSR} \doteq (0, v_c, 0) \ , \tag{1.69}$$

where v_c is the *Galactic circular speed* at the position of the Sun. The peculiar velocity of the Sun is defined as:

$$\vec{v}_{\odot pec} \doteq (U_\odot, V_\odot, W_\odot) \ , \tag{1.70}$$

so the velocity of the Sun turns out to be:

$$\vec{v}_\odot = (U_\odot, v_c + V_\odot, W_\odot) \ . \tag{1.71}$$

For the peculiar velocity of the Sun, in this work we use the values most commonly used in the literature at the moment of writing, which have been determined in [19] and reads

$$\vec{v}_{\odot pec} = \left(11.1^{+0.69}_{-0.75}, 12.24^{+0.47}_{-0.47}, 7.25^{+0.37}_{-0.36}\right) \text{km/s} \tag{1.72}$$

with additional systematic uncertainties of $\approx (1, 2, 0.5)$ km/s.

Let us note that the values of $U_\odot$, $V_\odot$ and $W_\odot$ as well as v_c are determined via observations, and the results of such studies in the literature are affected by uncertainties and present some contrast between each others, as we will see in chapters 4 and 5.

The motion of the Earth in the Solar system

The velocity of the Earth w.r.t. the Sun, in Galactic coordinates, can be written as (see for instance [12], but also [20] where a slightly different notation is used[18]):

$$\vec{v}_{\oplus/\odot}(t) = v_{\oplus/\odot}\left[\hat{\varepsilon}_1 \cos\left(\frac{2\pi}{T}\left(t - \tilde{t}\right)\right) + \hat{\varepsilon}_2 \sin\left(\frac{2\pi}{T}\left(t - \tilde{t}\right)\right)\right] \ , \tag{1.73}$$

where $v_{\oplus/\odot} = 29.8\ km/s$, and the two unitary vectors $\hat{\varepsilon}_1$ and $\hat{\varepsilon}_2$ have the components:

$$\hat{\varepsilon}_1 = (0.9931, 0.1170, -0.01032) \quad \text{and} \quad \hat{\varepsilon}_2 = (-0.0670, 0.4927, -0.8676) \ , \tag{1.74}$$

and are the directions of the Earth's motion at the Spring equinox (March 21, $t = \tilde{t} = 80\ days$) and Summer solstice (June 21, $t = \tilde{t} + 0.25\ years$), respectively.

[18] A most recent and accurate determination of these quantities can be found in [21]. In our work anyway we stick to the standard values presented above.

The value of $\tilde{t} = 80\ days$ corresponds to 21 March, i.e. the Spring Equinox, and it is the time at which the direction of the Earth's motion is $\hat{\varepsilon}_1$; so we choose the value of $\tilde{t}$ by construction, i.e. because of the definitions (1.73) and (1.74). With this value for the phase $\tilde{t}$, we can compute the maxima/minima of $|\vec{v}_\oplus|$. We get $t = 152\ days$ (i.e. the 1st of June) and $t = 152 + \frac{365}{2}\ days \approx 335\ days$, i.e. the 1st of December.

Note anyway that the expected event rate in a DMDD experiment can have different minima/maxima. In particular an exchange of the times at which maximum and minimum occur is possible, and it occurs for combinations of m_χ and m_A corresponding to a low enough v_{min}, as we will see in the next sections.

Also other changes in the shape of the modulation and in the time at which the maximum and the minimum occur are possible, as detailed in [12]. For instance, [12] considers (among others) the addition of another component to the smooth dark matter halo following a Maxwell-Boltzmann distribution, a stream of dark matter particles modeled on the base of the Sagittarius stream, which originates from the Sagittarius galaxy which is a satellite of the Milky Way. This stream has a very different velocity distribution, and thus originates a DMDD signal which has a maximum on December the 29th, and a minimum on June the 30th. The resulting modulation spectrum is a linear combination of the spectrum for the smooth halo component and that for the stream, appropriately weighted; it is no longer sinusoidal, is not even symmetric in time and has a maximum which occurs several months from each maximum of the two separate components.

The velocity of the Earth w.r.t. the Galaxy

Inserting equations (1.73) and (1.68) into (1.67) we obtain:

$$\vec{v}_\oplus(t) = \begin{pmatrix} v_{\oplus/\odot}\varepsilon_{1x}\cos\left(\frac{2\pi}{T}\left(t-\tilde{t}\right)\right) + v_{\oplus/\odot}\varepsilon_{2x}\sin\left(\frac{2\pi}{T}\left(t-\tilde{t}\right)\right) + U_\odot \\ v_{\oplus/\odot}\varepsilon_{1y}\cos\left(\frac{2\pi}{T}\left(t-\tilde{t}\right)\right) + v_{\oplus/\odot}\varepsilon_{2y}\sin\left(\frac{2\pi}{T}\left(t-\tilde{t}\right)\right) + v_c + V_\odot \\ v_{\oplus/\odot}\varepsilon_{1z}\cos\left(\frac{2\pi}{T}\left(t-\tilde{t}\right)\right) + v_{\oplus/\odot}\varepsilon_{2z}\sin\left(\frac{2\pi}{T}\left(t-\tilde{t}\right)\right) + W_\odot \end{pmatrix} . \quad (1.75)$$

From this we can easily calculate the modulus that appears in equation (1.66):

$$\begin{aligned} |\vec{v}_\oplus(t)|^2 =& v_{\oplus/\odot}^2 + U_\odot^2 + (v_c + V_\odot)^2 + W_\odot^2 \\ &+ 2v_{\oplus/\odot}\sin\left(\frac{2\pi}{T}\left(t-\tilde{t}\right)\right)\left[\varepsilon_{2x}U_\odot + \varepsilon_{2y}(v_c + V_\odot) + \varepsilon_{2z}W_\odot\right] \\ &+ 2v_{\oplus/\odot}\cos\left(\frac{2\pi}{T}\left(t-\tilde{t}\right)\right)\left[\varepsilon_{1x}U_\odot + \varepsilon_{1y}(v_c + V_\odot) + \varepsilon_{1z}W_\odot\right] \\ &+ 2v_{\oplus/\odot}^2\cos\left(\frac{2\pi}{T}\left(t-\tilde{t}\right)\right)\sin\left(\frac{2\pi}{T}\left(t-\tilde{t}\right)\right)\left[\varepsilon_{1x}\varepsilon_{2x} + \varepsilon_{1y}\varepsilon_{2y} + \varepsilon_{1z}\varepsilon_{2z}\right] . \end{aligned} \quad (1.76)$$

1.6.4 Approximated expressions for the η term

Now that we know how to write the distribution in terms of the velocities in the Earth's frame, we can work out the calculation of the collision rate.

We look at it in three different cases: 1) neglecting the motion of the Earth and the motion of the Sun, 2) neglecting only the motion of the Earth around the Sun, and finally 3) with all the terms.

We express our results in terms of η, which is a function of many physical variables, but in the sequel we will write it as a function of few or none of them only, for simplicity.

We recall here equation (1.28), which tells us that for the spin-independent interaction we have:

$$\frac{dR}{dE_r} \approx \frac{\sigma_{p,SI} F^2}{2 m_{red}^2 m_\chi} \varrho_\odot \tilde{\eta} \ . \tag{1.77}$$

(1.78)

Neglecting the motion of the Earth and the motion of the Sun

If we could neglect the motion of the Sun through the Galaxy, and that of the Earth around the Sun, we would have simply $\vec{v'} \approx \vec{v}$, and then at this point in order to get η we would just need to choose a form for the velocity distribution of dark matter, which appears in equation (1.63), and solve the integral therein. In the case of the smoothly cut Maxwell-Boltzmann distribution of equation (1.61), the calculation is straightforward, and $\tilde{\eta}$ turns out to be:

$$\tilde{\eta}\left(v_{min}\left(E_r, m_\chi, m_A\right), v_0\right) = \frac{2}{v_0 \sqrt{\pi} N_{esc}^*} \left(\exp\left(-\frac{v_{min}}{v_0} \right)^2 - \exp\left(-\frac{v_{esc}}{v_0} \right)^2 \right) \tag{1.79}$$

$$= \frac{2}{v_0 \sqrt{\pi} N_{esc}^*} \left(\exp\left(-\frac{E_r m_A}{2 m_{red}^2 v_0^2} \right) - \exp\left(-\frac{v_{esc}}{v_0} \right)^2 \right) \ , \tag{1.80}$$

where we recall that v_0 is the most probable speed of the Maxwell-Boltzmann distribution.

We can clearly see that because of (1.80) the differential event rate (1.77) is exponentially decreasing with the recoil energy E_r. This feature, present already at this very approximate stage, will remain present also in the subsequent approximations.

η has here lost its time-dependence because the time-dependent part of the velocity has been neglected. Anyway, for the purposes of direct detection experiments we cannot neglect the above mentioned motions.

Neglecting only the motion of the Earth around the Sun

With the approximation

$$\vec{v'} \approx \vec{v} - \vec{v}_\odot \ , \tag{1.81}$$

we obtain (again for a smoothly cut Maxwell-Boltzmann and for SI interaction):

$$\tilde{\eta} = \begin{cases} \frac{\mathrm{erf}\left(x+\frac{v_\odot}{v_0}\right)-\mathrm{erf}\left(x-\frac{v_\odot}{v_0}\right)-\frac{4}{\sqrt{\pi}}\left(1-\left(x^2+\frac{\left(\frac{v_\odot}{v_0}\right)^2}{3}-z^2\right)\right)\frac{v_\odot}{v_0}e^{-z^2}}{2N^*_{esc}v_\odot} & \\ & \text{for } v_{min} < |v_\odot - v_{esc}|, \\ \frac{\mathrm{erf}(z)-\mathrm{erf}\left(x-\frac{v_\odot}{v_0}\right)-\frac{2}{\sqrt{\pi}}\left(\frac{v_\odot}{v_0}+z-x-\frac{1}{3}\left(\frac{v_\odot}{v_0}-2z-x\left(\frac{v_\odot}{v_0}+z-x\right)^2\right)\right)e^{-z^2}}{2N^*_{esc}v_\odot} & \\ & \text{for } |v_\odot - v_{esc}| < v_{min} < v_\odot + v_{esc}\ , \\ 0 & \text{for } v_\odot + v_{esc} < v_{min} \end{cases} \tag{1.82}$$

where $x = v_{min}/v_0$ and $z = v_{esc}/v_0$, and again there is no time-dependence in η.

Exact calculation

Finally, without approximations, i.e. with

$$\vec{v'} = \vec{v} - \vec{v}_\oplus(t) = \vec{v} - \vec{v}_\odot - \vec{v}_{\oplus/\odot}(t)\ , \tag{1.83}$$

we have the full solution, that we will give in equation (1.96).

Now η has acquired a time dependence, through the time dependent $\vec{v}_\oplus(t)$.

In the next section we will provide the analytic forms for η computed for the pure, cut and smoothly cut Maxwell-Boltzmann distributions.

1.6.5 Velocity distributions in the Earth reference frame

Transformed pure Maxwell-Boltzmann distribution

If we have assumed for the distribution of the dark matter in the Galactic rest frame a pure Maxwell-Boltzmann shape, inserting (1.66) in the distribution (1.46) we obtain the corresponding $f_{\vec{v'}}\left(\vec{v'}_\chi\right)$ holding for the velocities in the Earth's reference frame which is:

$$f_{\vec{v'}}(\vec{v'}) = f_{\vec{v}}\left(\vec{v}_\oplus(t) + \vec{v'}\right) = \frac{1}{v_0^3\pi^{\frac{3}{2}}}\exp\left(-\frac{\left|\vec{v}_\oplus(t)+\vec{v'}\right|^2}{v_0^2}\right). \tag{1.84}$$

Using this result and equation (1.63) we can rewrite η as:

$$\eta^{MB}\left(t, v_{min}\left(E_r, m_\chi, m_A\right), v_0\right) = v_0\int_{|\vec{v'}|>v'_{min}} d^3\vec{v'}\frac{1}{v'}\frac{1}{v_0^3\pi^{\frac{3}{2}}}\exp\left(-\frac{\left|\vec{v}_\oplus(t)+\vec{v'}\right|^2}{v_0^2}\right) \tag{1.85}$$

We can solve this integral and we obtain:[19]

$$\eta^{MB}\left(t, v_{min}\left(E_r, m_\chi, m_A\right), v_0\right) = \frac{v_0}{2v_\oplus\left(t\right)}\left[\mathrm{erf}\left(\frac{v_{min}}{v_0}+\frac{v_\oplus\left(t\right)}{v_0}\right)-\mathrm{erf}\left(\frac{v_{min}}{v_0}-\frac{v_\oplus\left(t\right)}{v_0}\right)\right]. \tag{1.86}$$

Note that the escape speed do not appear here because we are considering the pure Maxwell-Boltzmann without any cut-off.

Applying now the same definition and procedure that we used in deriving equation (1.54) from equation (1.53), we obtain that the speed distribution associated with a pure Maxwell-Boltzmann velocity distribution, in the Earth reference frame, is:

$$f_{v'}\left(v'\right) = \frac{v'\exp\left[-\left(\frac{v'}{v_0}\right)^2-\left(\frac{|\vec{v_\oplus}|}{v_0}\right)^2\right]}{v_0\sqrt{\pi}\,|\vec{v_\oplus}|}\left[\exp\left(2\frac{v'\,|\vec{v_\oplus}|}{v_0^2}\right)-\exp\left(-2\frac{v'\,|\vec{v_\oplus}|}{v_0^2}\right)\right] \tag{1.87}$$

This speed distribution is shown in figure 1.7 for two different times of the year, $t = 152\ days$ and $t = 335\ days$. These times correspond to June the 1st and December the 1st, i.e. they correspond to the minimum and maximum alignment of the velocity of the Earth with the Sun's one. In the same figure we plotted the pure Maxwell-Boltzmann speed distribution in the Galactic reference frame, i.e. equation (1.54).

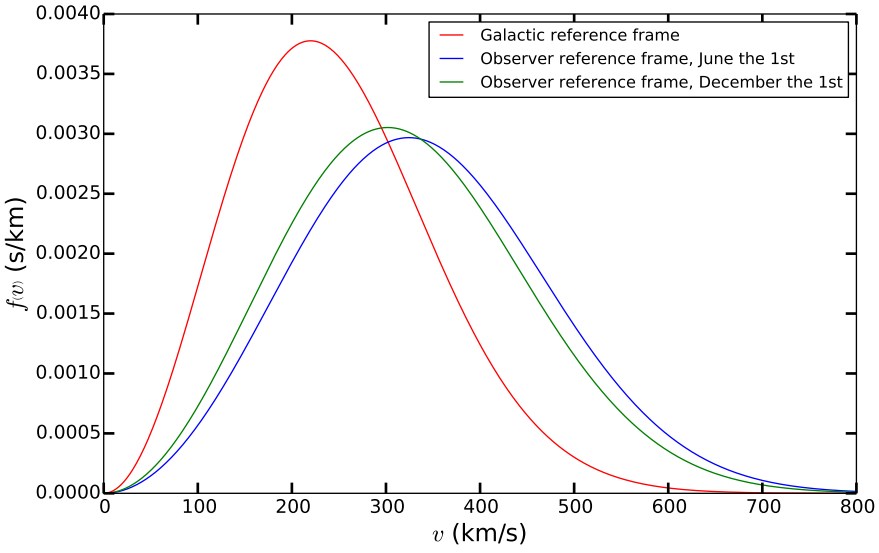

Figure 1.7: An example of a pure Maxwell-Boltzmann speed distribution in the Galactic frame and in the Earth frame at two different times of the year.

[19]The same result is obtained in [12, page 30], but note that their η is defined as our $\tilde{\eta}$.

Transformed cut Maxwell-Boltzmann distribution

If we assume as distribution for the WIMP's velocities the cut Maxwell-Boltzmann distribution of equation (1.55), η will be a function of the following variables:

$$\eta = \eta\left(t, v_{min}\left(E_r, m_\chi, m_A\right), v_{esc}, v_0\right) \ . \tag{1.88}$$

For the velocities in the Earth's reference frame we obtain:

$$\begin{aligned} f_{\vec{v}'}^{esc}\left(\vec{v'}_\chi\right) =& \frac{1}{N_{esc}} f_{\vec{v}}\left(\vec{v}_\oplus\left(t\right) + \vec{v'}_\chi\right) \Theta\left(v_{esc} - \left|\vec{v}_\oplus\left(t\right) + \vec{v'}_\chi\right|\right) \\ =& \begin{cases} \frac{1}{N_{esc}} f_{\vec{v}}\left(\vec{v}_\oplus\left(t\right) + \vec{v'}_\chi\right) & \text{if } \left|\vec{v}_\oplus\left(t\right) + \vec{v'}_\chi\right| < v_{esc} \ , \\ 0 & \text{if } \left|\vec{v}_\oplus\left(t\right) + \vec{v'}_\chi\right| > v_{esc} \ . \end{cases} \end{aligned} \tag{1.89}$$

Using this result we can rewrite η as:

$$\eta\left(t, v_{min}\left(E_r, m_\chi, m_A\right), v_{esc}, v_0\right) \tag{1.90}$$

$$= \int_{|\vec{v'}|>v'_{min}} d^3\vec{v'} \frac{\Theta\left(v_{esc} - \left|\vec{v}_\oplus\left(t\right) + \vec{v'}_\chi\right|\right)}{v' N_{esc} v_0^2 \pi^{\frac{3}{2}}} \exp\left(-\frac{\left|\vec{v}_\oplus\left(t\right) + \vec{v'}_\chi\right|^2}{v_0^2}\right) . \tag{1.91}$$

This integral can be solved analytically, and the result is provided by equation (1.96) taking $\beta = 0$.

Transformed smoothly cut Maxwell-Boltzmann distribution

Assuming as distribution for the WIMP's velocities the smoothly cut Maxwell-Boltzmann distribution of equation (1.61), η will be again a function of the following variables:

$$\eta = \eta\left(t, v_{min}\left(E_r, m_\chi, m_A\right), v_{esc}, v_0\right) \ . \tag{1.92}$$

For the velocities in the Earth's reference frame we obtain:

$$f_{\vec{v}'}^{esc*}\left(\vec{v'}\right) \doteq \begin{cases} \frac{1}{N^*_{esc}} \left(\frac{1}{\pi v_0^2}\right)^{3/2} \left[e^{-\left|\vec{v}_\oplus(t)+\vec{v'}\right|^2/v_0^2} - e^{-v_{esc}^2/v_0^2}\right] & \text{if } \left|\vec{v}_\oplus\left(t\right) + \vec{v'}\right| < v_{esc} \ , \\ 0 & \text{if } \left|\vec{v}_\oplus\left(t\right) + \vec{v'}\right| > v_{esc} \ . \end{cases} \tag{1.93}$$

Using this result we can rewrite η as:

$$\eta\left(t, v_{min}\left(E_r, m_\chi, m_A\right), v_{esc}, v_0\right) \tag{1.94}$$

$$= \int_{|\vec{v'}|>v'_{min}} d^3\vec{v'} \frac{\Theta\left(v_{esc} - \left|\vec{v}_\oplus\left(t\right) + \vec{v'}_\chi\right|\right)}{v' N^*_{esc} v_0^2 \pi^{\frac{3}{2}}} \left[e^{-\left|\vec{v}_\oplus(t)+\vec{v'}\right|^2/v_0^2} - e^{-v_{esc}^2/v_0^2}\right] . \tag{1.95}$$

This integral can be solved analytically, and the result can be found in [12, page 30] (where their η is defined as our $\tilde{\eta}$). We report here the solution corresponding to (1.89) (obtained for $\beta = 0$) and the one for (1.93) (obtained for $\beta = 1$). They read:

$$\tilde{\eta} = \begin{cases} \frac{1}{|\vec{v}_\oplus(t)|} & \text{for } z < y, x < |y-z| \ , \\ \frac{\mathrm{erf}(x+y) - \mathrm{erf}(x-y) - \frac{4}{\sqrt{\pi}}\left(1-\beta\left(x^2+\frac{y^2}{3}-z^2\right)\right)ye^{-z^2}}{2N_{esc,\beta}|\vec{v}_\oplus(t)|} & \text{for } z > y, \ x < |y-z| \ , \\ \frac{\mathrm{erf}(z) - \mathrm{erf}(x-y) - \frac{2}{\sqrt{\pi}}\left(y+z-x-\frac{\beta}{3}(y-2z-x)(y+z-x)^2\right)e^{-z^2}}{2N_{esc,\beta}|\vec{v}_\oplus(t)|} & \text{for } |y-z| < x < y+z \ , \\ 0 & \text{for } y+z < x \ , \end{cases} \tag{1.96}$$

where $x \doteq v_{min}/v_0$, $y \doteq |\vec{v}_\oplus(t)|/v_0$ and $z \doteq v_{esc}/v_0$. Note that the normalization is different for the two distributions, so we have $N_{esc,0} \doteq N_{esc}$ and $N_{esc,1} \doteq N^*_{esc}$.

1.7 Annual modulation

In the previous section we have seen that the velocity of the Earth changes with time, because our planet orbits around the Sun and this motion, unlike the motion of the Sun throughout the Galaxy, has a timescale comparable with that of the direct detection experiments.

Once we have expressed $\vec{v}_\oplus(t)$ as in equation (1.67), we are interested in discussing its variation over time. It is important to remind that this velocity arises from the composition of the constant term $\vec{v}_\odot$ and the time-dependent term $\vec{v}_{\oplus/\odot}(t)$. As time changes, $\vec{v}_\oplus(t)$ changes too, and in particular $|\vec{v}_\oplus(t)|$ varies through a maximum and a minimum. Anyway, due to the inclination of the plane of the ecliptic w.r.t. the Galactic plane, these extreme values are not $|\vec{v}_\odot| + |\vec{v}_{\oplus/\odot}|$ and $|\vec{v}_\odot| - |\vec{v}_{\oplus/\odot}|$, as can be seen from figure 1.8.

Note also that, as can be seen from the figure, the curve which describes $|\vec{v}_\oplus(t)|$ is slightly translated to higher velocity values w.r.t. $|\vec{v}_\odot|$. This is due to the fact that the axis of inclination of the Ecliptic w.r.t the Galactic plane is not passing through the center of the Galaxy, but 8° further away.

Once we take into account the motion of the Earth around the Sun, we have a time dependence of the velocity distribution of the dark matter particles in the Earth frame. As a consequence, also η, and so the differential scattering rate dR/dE_r of equation (1.28), and the scattering rate R itself, will present a time dependence (in particular they will have a periodic behavior with a period of one year). The precise behavior with time of these quantities depends on which velocity distribution we consider for the dark matter. In the case of a pure Maxwell-Boltzmann distribution (1.53), $\eta(t)$ assumes the form (1.86), and its behavior with time can be well approximated by a cosinusoidal function plus a constant, so does the event rate. In this section we want to show this in detail. Similar behavior is expected for a cut Maxwell-Boltzmann distribution with v_{esc}, as that in equation (1.55). Behaviors which differ by far from the cosinusoidal one are typical of certain velocity distributions, for instance those presented in [12, figure 4].

1.7.1 Approximated expression for the velocity of the Earth

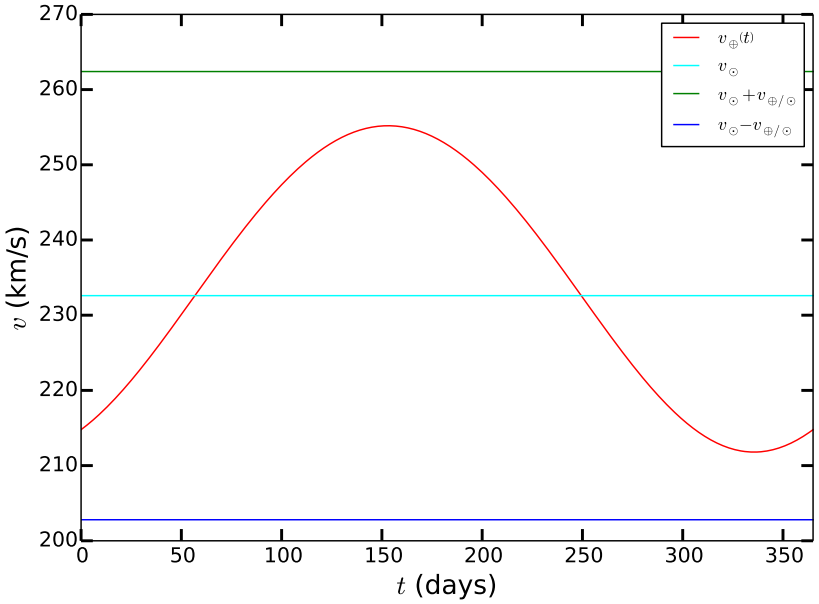

Figure 1.8: Yearly variation of the modulus of the velocity of the Earth w.r.t. the Galactic frame. For this illustration we have assumed $v_\odot \approx 232.6$ km/s, $v_{\oplus/\odot} = 29.8$ km/s, and $v_\odot(t)$ as in the text.

We can calculate $v_\oplus \doteq \sqrt{|\vec{v}_\oplus|}$ using (1.76), and considering that $v_{\oplus/\odot} \ll v_\odot$ we obtain to first order the approximated expression:

$$v_\oplus(t) \approx v_\odot + b v_{\oplus/\odot} \cos\left(\frac{2\pi}{T}(t - t_0)\right) \ , \tag{1.97}$$

where $b_i \doteq \hat{\varepsilon}_i \cdot \hat{v}_\odot$, $b \doteq \sqrt{b_1^2 + b_2^2}$ and t_0 is the time at which the maximum of $v_\oplus(t)$ occurs, i.e. $t_0 \approx 152$ *days* with the above mentioned assumptions on the motion of the Sun and the Earth.

1.7.2 Approximated expression for the η term

We are now going to show that the function $\eta(t)$ in the case of a pure Maxwell-Boltzmann distribution is well approximated by a cosine plus a constant. We start from the expression (1.86), and defining $x_{min} \doteq \frac{v_{min}}{v_0}$ and $y(t) \doteq \frac{v_\oplus(t)}{v_0}$ we can rewrite it as:

$$\eta(y(t)) = \frac{1}{2y(t)}\left[\mathrm{erf}(x_{min} + y(t)) - \mathrm{erf}(x_{min} - y(t))\right] \ . \tag{1.98}$$

Using the approximation (1.97) we get for $y(t)$ the approximation

$$y(t) \approx \frac{1}{v_0}\left(v_\odot + b v_{\oplus/\odot}\cos\left(\frac{2\pi}{T}(t - t_0)\right)\right) = y_0 + \delta y \cos\left(\frac{2\pi}{T}(t - t_0)\right) \ , \tag{1.99}$$

where $y_0 \doteq \frac{v_\odot}{v_0} \sim 1$ and $\delta y \doteq \frac{b v_{\oplus/\odot}}{v_0} \sim 10^{-1}$, i.e. we can see that $\delta y \ll y_0$ because $v_{\oplus/\odot} \ll v_\odot$.

Now we can develop $\eta(t)$ in Taylor series, i.e. we can write:

$$\eta(y(t)) = \sum_{n=0}^{\infty} \frac{\eta^{(n)}(y_0)}{n!} (y(t) - y_0)^n \ , \tag{1.100}$$

and keep only the first two terms, those with $n = 0$ and $n = 1$ respectively, and neglect all the subsequents. In fact, since $|y(t) - y_0| \leq \delta y \approx 10^{-1}$, it turns out that $|y(t) - y_0| \gg (y(t) - y_0)^2$.

Inserting the explicit form of η (1.98) in the development (1.100) and neglecting the terms of order higher than $n = 1$ we get:

$$\eta(y(t)) \approx \eta(y_0) + M_\eta \cos\left(\frac{2\pi}{T}(t - t_0)\right) \ , \tag{1.101}$$

with

$$M_\eta \doteq \frac{\delta y}{y_0}\left[\frac{1}{\sqrt{\pi}}\left(e^{-(x_{min}+y_0)^2} - e^{-(x_{min}-y_0)^2}\right) - \eta(y_0)\right] \ . \tag{1.102}$$

1.7.3 Approximated expressions of the event rate

Now, inserting the expression (1.101) in the equation for the differential event rate (1.28), we obtain

$$\frac{dR}{dE_r}(E_r, t) \approx \frac{dR_0}{dE_r}(E_r) + \frac{dR_{mod}}{dE_r}(E_r) \cos\left(\frac{2\pi}{T}(t - t_0)\right) \ , \tag{1.103}$$

with

$$\frac{dR_0}{dE_r}(E_r) \doteq \frac{\varrho_\odot A^2 \sigma_{p,SI} F^2(E_r)}{2 v_0 m_\chi m_{red,p}^2(m_\chi)} \eta(y_0) \quad \text{and} \quad \frac{dR_{mod}}{dE_r}(E_r) \doteq \frac{\varrho_\odot A^2 \sigma_{p,SI} F^2(E_r)}{2 v_0 m_\chi m_{red,p}^2(m_\chi)} M_\eta \ . \tag{1.104}$$

Experiments collect events that they often must put into energy bins before performing statistical analyses. A bin has a finite width, in which the total rate reads

$$R(t) = \int_{E_1}^{E_2} dE_r \frac{dR}{dE_r}(E_r, t) \ , \tag{1.105}$$

so using the approximation (1.103) we obtain

$$R(t, m_\chi, \sigma_{p,SI}) \approx R_0(m_\chi, \sigma_{p,SI}) + R_{mod}(m_\chi, \sigma_{p,SI}) \cos\left(\frac{2\pi}{T}(t - t_0)\right) \ , \tag{1.106}$$

with

$$R_0(m_\chi, \sigma_{p,SI}) \doteq \frac{\varrho_\odot A^2 \sigma_{p,SI}}{2 v_0 m_\chi m_{red,p}^2(m_\chi)} \int_{E_1}^{E_2} dE_r F^2(E_r) \eta(y_0) \tag{1.107}$$

and

$$R_{mod}(m_\chi, \sigma_{p,SI}) \doteq \frac{\varrho_\odot A^2 \sigma_{p,SI}}{2 v_0 m_\chi m_{red,p}^2(m_\chi)} \int_{E_1}^{E_2} dE_r F^2(E_r) M_\eta(E_r) \ . \tag{1.108}$$

1.7.4 The recoil spectra, the amplitude of the modulation and the phase inversion

As we have seen, the time dependence of the differential event rate comes entirely from the time dependence of the term η. This term undergoes a small (but crucial in this section) variation during the year, and this variation reflect on a similar variation on the differential event rate. We show in figure 1.9 the differential event rate (also called *recoil spectrum*) computed at $t = 152$ days (June the 1st) and $t = 335$ days (December the 1st), which correspond to the time of the maximum and minimum of the differential event rate. We can see from the figure that the differential event rate at $t = 335$ days is greater than that at $t = 152$ days for low values of the recoil energy E_r, while the converse occurs for high E_r values.

For illustrative purposes the figures of this section have been obtained considering a WIMP of $m_\chi = 100$ GeV scattering off a xenon nucleus with a WIMP-proton SI cross section of $\sigma_{p,SI} = 10^{-45}$ cm^2, assuming the smoothly cut MB distribution, the SHM values for the astrophysical parameters (see next section) and the Helm form factor. We recall that features similar to those illustrated in this section for the differential event rate as a function of the recoil energy are present also in the term η as a function of the minimal velocity v_{min} (a part from the effect of the form factor), since the two are related by (1.28).

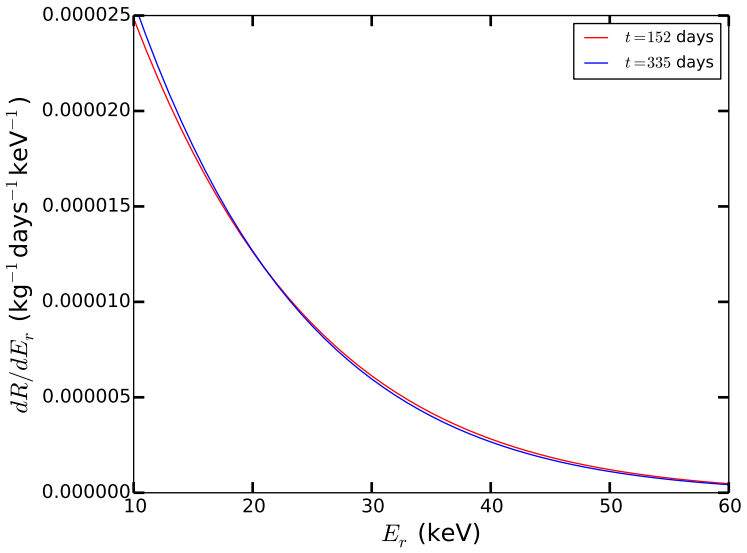

Figure 1.9: We compare the differential event rates at $t = 152$ days and $t = 335$ days, for a WIMP of $m_\chi = 100$ GeV scattering off a xenon nucleus with a WIMP-proton SI cross section of $\sigma_{p,SI} = 10^{-45}$ cm^2, assuming the smoothly cut MB distribution, the SHM values for the astrophysical parameters and the Helm form factor.

Let us recall that the average differential event rate is approximately given by

$$\langle dR/dE_r \rangle \approx \frac{1}{2}\left(\frac{dR}{dE_r}(E_r, 152) + \frac{dR}{dE_r}(E_r, 335)\right) , \tag{1.109}$$

and the amplitude of the modulation is given by

$$\Delta \frac{dR}{dE_r}(E_r) \approx \frac{1}{2}\left(\frac{dR}{dE_r}(E_r, 152) - \frac{dR}{dE_r}(E_r, 335)\right) . \tag{1.110}$$

Two important features of the modulation should be pointed out. First, the amplitude of the modulation is usually small relative to the average rate, in particular it is in general of order 1% to 10% of the average rate. Second, the amplitude of the modulation changes sign at low recoil energies (small v_{min}).

These two features are evident in figure 1.10, where we compare the average differential event rate with the modulus of the amplitude of the modulation of the differential event rate. This figure has been obtained with the above mentioned assumptions, but the described features occur in general, not only in this particular case. We remark that in the figure the modulus of the amplitude is shown, so that the sign change of the modulation appears as the fall of the blue curve at around $E_r \approx 20$ keV.

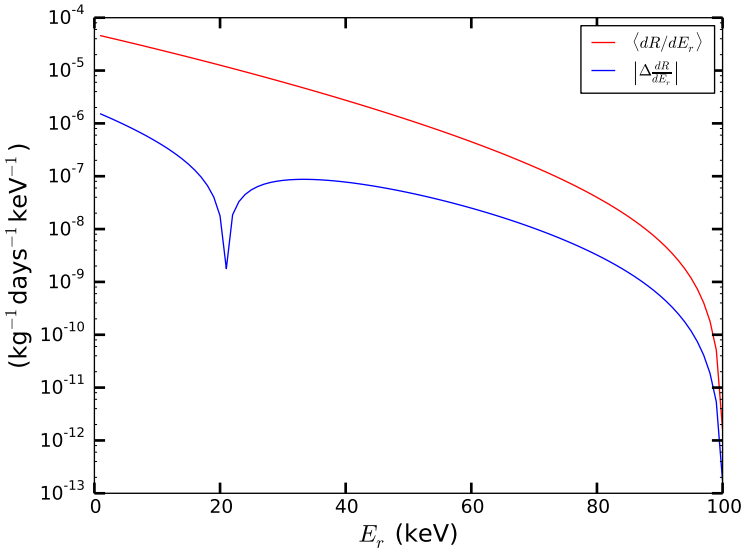

Figure 1.10: The average differential event rate is shown together with the associated modulation (definitions are given in the text), for a WIMP of $m_\chi = 100$ GeV scattering off a xenon nucleus with a WIMP-proton SI cross section of $\sigma_{p,SI} = 10^{-45}$ cm^2, assuming the smoothly cut MB distribution, the SHM values for the astrophysical parameters and the Helm form factor.

The amplitude of the modulation is positive when $\frac{dR}{dE_r}(E_r, 152) > \frac{dR}{dE_r}(E_r, 335)$ (so $t_{max} = 152$ days and $t_{min} = 335$ days) and negative when $\frac{dR}{dE_r}(E_r, 152) < \frac{dR}{dE_r}(E_r, 335)$ (so $t_{max} = 335$ days and $t_{min} = 152$ days). Thus, the change in sign of the modulation tells us that the times at which maximum and minimum occur can exchange. As we can see from figure 1.11, the amplitude of the modulation

is negative for low recoil energies (small v_{min}), where thus $t_{max} = 335$ days, and positive for high recoil energies (large v_{min}), where thus $t_{max} = 152$ days.

The phase reversal of the annual modulation that we have shown in figure 1.11 provides a way to determine the WIMP mass (see for instance [12]). In fact, while the phase of the modulation is fixed for a given v_{min}, regardless of the WIMP mass, the phase of the modulation for a given recoil energy is not. This occurs because, due to the relation (1.16), to compute the recoil energy associated with a given v_{min} one also must specify the mass of the WIMP (and the mass of the target nucleus). Thus the WIMP mass can be constrained trough an experimental determination of the recoil energy at which the phase reverses. Moreover, the detection of this phase reversal could constitute an important signature of WIMPs, because known backgrounds are not expected to provide such an effect.

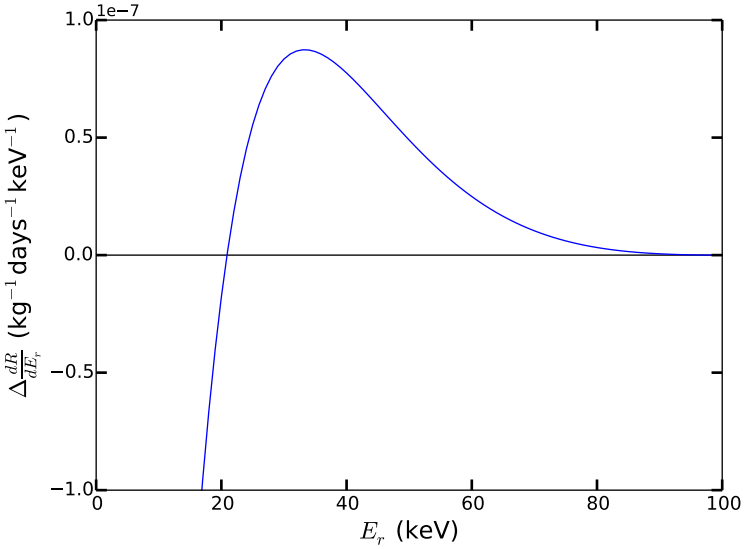

Figure 1.11: We show the amplitude of the modulation of the differential event rate for a WIMP of $m_\chi = 100$ GeV scattering off a xenon nucleus with a WIMP-proton SI cross section of $\sigma_{p,SI} = 10^{-45}$ cm^2, assuming the smoothly cut MB distribution, the SHM values for the astrophysical parameters and the Helm form factor.

1.8 The standard halo model (SHM)

The so called standard halo model is a sort of industry agreed standard used in interpreting the results of DMDD experiments. It consists of a set of assumptions about the astrophysics entering the calculation of quantities related to DMDD experiments (for instance the scattering rate (1.23)). The advantage of this model is that it allows the comparison between the results of different experiments.

Let us now fix what we will call from now on the Standard Halo Model (SHM).[20]

[20] Note that, even if this model is rather standard, some variations are possible depending on

This model assumes for the velocity distribution of the dark matter at the position of the Sun a Maxwell-Boltzmann form. Usually this distribution is cut in such a way that no particle is present at $|\vec{v}| > v_{esc}$. This can be obtained with a sharp cut-off like in (1.55), but in our computations we prefer to use the more physical smooth cut-off of (1.61).

The values assumed by the SHM are:

$$v_{esc} = 544 \text{ km/s}, \quad v_c = 220 \text{ km/s}, \quad v_0 = v_c \quad \text{and} \quad \varrho_\odot = 0.3 \text{ GeV/cm}^3, \quad (1.111)$$

where we recall that v_{esc} is the local Galactic escape speed, v_c is the circular speed at the position of the Sun, v_0 is the most probable speed of the Maxwell-Boltzmann distribution (which gives also a measure of the dispersion of the speeds around the mean value), and $\varrho_\odot$ is the local dark matter density. The values above are employed for instance in the interpretation of the experiments XENON100 ([22]), CDMSII ([23]) and LUX ([24]).

Some papers using the SHM specify also that they assume a *mean circular velocity of the Earth with respect to the galactic center of* 232 km/s (like for instance [23]).[21] This quantity is equivalent to the average (over time) of our equation (1.97), i.e. (for sufficiently long time) to the modulus of $\vec{v}_\odot$, the velocity of the Sun in the galactic rest frame, given in equation (1.71). It is straightforward to see from that equation that the values we employed for the peculiar motion of the Sun, equation (1.72), used with the above value of v_c give precisely the value of 232 km/s.[22]

the author and the collaboration. Moreover, the value of some of the quantities of the SHM has slightly changed over time, so we try to provide the most recent values assumed under this name.

[21] Note that sometimes the authors do not specify which value has been assumed for such a quantity (for instance [22]), while others use different values (for instance 245 km/s in [24]).

[22] Note anyway that, instead of using the approximated equation (1.97), we fully implemented in our code the peculiar motion of the Sun and the motion of the Earth around it, see section 1.6.3.

CHAPTER 2

Understanding the experimental results

Contents

2.1 Introduction

Many tens of experiments which aim at detecting WIMPs (and/or other dark matter candidates, for instance axions) via their scattering off nuclei in a detector are currently operating, and the next generation (under construction) is about to reach the ton scale.

In this chapter we explain how we can use the data taken by such DMDD experiments to obtain limits or signal regions in the relevant parameter space. We will focus on the interpretation of such results in terms of spin-independent elastic scattering of WIMPs off nuclei (and we will present only some of the existing experiments and statistical methods, among which those that we are going to consider in the rest of this work).

We start by presenting some experimental facts that must be taken into account, and enter in the computation of the total event rate R, and then we present the statistical methods that we have applied to compute upper limits. We then introduce a certain number of DMDD experiments, some of which are relevant for our work and will be used in the following chapters. We will focus in particular on the quantities that we can use to recompute the associated limits or regions. We will present a number of experiments which allow to put upper limits in the parameter space σ_{pSI}, m_χ, as well as the DAMA experiment with its long standing detected modulated signal, and its interpretation in terms of SI elastic scattering of WIMPs off nuclei. We will conclude by presenting the prospects for future experiments.

2.2 Experimental features that must be taken into account

In chapter 1 we have presented the total event rate R (i.e. the number of events per unit time per unit detector mass) of a DMDD experiment, that we have finally written as an integral over energies of the differential event rate dR/dE_r, equation (1.18). When we deal with real detectors, we must also account for the precise composition and response of the detector to predict the recoil event rate for a given experiment; this is what we are going to present in this section.

In particular, we need to take into account that in some experiments the measured recoil energy is just a part of the actual recoil energy (this is called *quenching*), that experiments introduce cuts in the data to reduce the background, so an energy-dependent *experimental efficiency* must be included, and that the experimental apparatus cannot determine energies with a perfect precision, so an *energy resolution* must be taken into account. Moreover, real experiments sometimes use as targets more than one nuclear species, and/or the target element exists in nature with more than one isotope. Finally, to obtain the number of expected events we need to multiply the event rate by the mass of the detector and the exposure time, and for experiments which run for a certain period of time but for which the number of detected events (thanks to efficient background discrimination) is very small, we need to take the average over time of the time-dependent total event rate. These points are reviewed for instance in [13], and more recently in [25] and [26].

2.2.1 Quenching

The recoiling nucleus transfers its energy to either the electrons, in which case this energy may be observed as ionization or scintillation in the detector, or to other nuclei, producing phonons or heat. Experiments that do not measure the phonons/heat can only directly measure the fraction of energy Q that goes into the channel that is observed (such as scintillation); we refer to this as the observed nuclear recoil energy E_{obs}. Observed energies for experiments that measure only from the electron channel are usually quoted in keV_{ee}, where ee stands for "electron equivalent".[1] These differ from the actual nuclear recoil energy E_r (sometimes quoted in keV_{nr}, where nr stands for "nuclear recoil"), and they are related through the so-called *quenching factor* Q, via the relation

$$E_{obs} = QE_r \ . \tag{2.1}$$

Some detectors can calibrate their energy scale to $E_{obs} = E_r$, in which case the quenching factor can be ignored ($Q = 1$) in the above formulation (this is the case

[1] Let us note that, on the other hand, for experiments which measure phonons, the phonon energy can be labeled as well in electron equivalent units, as it is the case for CDMSLite [27], which calibrates the phonon energy w.r.t. electron recoils; a conversion to nuclear recoil energies is thus necessary, as explained in detail in section 2.5.7.

for instance of XENON10 [28] and CDMSII [23], as pointed out also in [25]).

Often we will not be interested in the event rate over the full energy spectrum to which the experiment is sensitive (1.18), but instead we will need to compute the total event rate within a particular *detected energy interval* $[E_1, E_2]$, which reads:

$$R_{[E_1,E_2]}(t) = \int_{E_1/Q}^{E_2/Q} dE_r \frac{dR}{dE_r}(E_r, t) = \int_{E_1}^{E_2} dE_{obs} \frac{dR}{dE_{obs}}(E_{obs}, t) \ , \tag{2.2}$$

where the last equality simply follows via a trivial substitution. This form is relevant when dealing with binned events, or when applying the maximum gap method presented in section 2.3.2.

2.2.2 Experimental efficiency

Due to e.g. data cuts designed to reduce backgrounds, an energy dependent experimental efficiency $\varepsilon(E_{obs})$ must be taken into account, so the above equation becomes:

$$R_{[E_1,E_2]}(t) = \int_{E_1}^{E_2} dE_{obs} \varepsilon(E_{obs}) \frac{dR}{dE_{obs}}(E_{obs}, t) = \int_{E_1/Q}^{E_2/Q} dE_r \varepsilon(QE_r) \frac{dR}{dE_r}(E_r, t) \ . \tag{2.3}$$

2.2.3 Energy resolution

Detectors cannot determine the event energies with perfect precision. If the expected amount of energy in the channel an experiment observes due to a nuclear recoil is E_{obs}, the measured energy will be distributed about E_{obs}, and we will indicate it as E'. The previous formula applies only for a perfect energy resolution and must be corrected for this finite resolution. To take it into account, the differential event rate in the previous equation has to be replaced by a convolution of the differential event rate with a function $G(E_{obs}, E')$ which describes the energy resolution (and in particular the dispersion of the value of the measured energy E' around the actual value E_{obs}), so instead of equation (2.3) we will use[2]

$$\begin{aligned} R_{[E_1,E_2]}(t) &= \int_{E_1}^{E_2} dE' \int_0^{\infty} dE_{obs} \varepsilon(E_{obs}) \frac{dR}{dE_{obs}}(E_{obs}, t) G(E_{obs}, E') \\ &= \int_0^{\infty} dE_{obs} \varepsilon(E_{obs}) \frac{dR}{dE_{obs}}(E_{obs}, t) \int_{E_1}^{E_2} dE' G(E_{obs}, E') \ . \end{aligned} \tag{2.4}$$

Usually a Gaussian energy resolution is assumed, the form of which is given by

$$G(E_{obs}, E') = \frac{1}{\sigma(E_{obs})\sqrt{2\pi}} \exp\left[-\frac{(E' - E_{obs})^2}{2\sigma^2(E_{obs})}\right] \tag{2.5}$$

[2] Note that sometimes, as for instance in [26], a second experimental efficiency $\varepsilon(E')$ is used, in which case equations (2.6) and (2.7) are no more valid.

where $\sigma\left(E_{obs}\right)$ is the standard deviation of the above Gaussian distribution of mean E_{obs}, but it is often referred to as "the energy resolution" tout court.

If such an energy resolution is assumed, the integration over E' in equation (2.4) can be solved providing a result in terms of the error function. So we can rewrite equation (2.4) with the integral in E_{obs} only, as

$$R_{[E_1,E_2]}\left(t\right) = \int_0^\infty dE_r \varepsilon\left(QE_r\right) \Phi\left(QE_r, E_1, E_2\right) \frac{dR}{dE_r}\left(E_r, t\right) \ , \tag{2.6}$$

where we have defined the so-called *energy response function* as

$$\begin{aligned} \Phi\left(E_{obs}, E_1, E_2\right) &\doteq \int_{E_1}^{E_2} dE' G\left(E_{obs}, E'\right) \\ &= \frac{1}{2}\left[\mathrm{erf}\left(\frac{E_2 - E_{obs}}{\sqrt{2}\sigma\left(E_{obs}\right)}\right) - \mathrm{erf}\left(\frac{E_1 - E_{obs}}{\sqrt{2}\sigma\left(E_{obs}\right)}\right)\right] \ . \end{aligned} \tag{2.7}$$

It should be noticed that the energy resolution becomes particularly important at low WIMP masses, so particular care should be employed in this regime. Let us consider for instance dual phase detectors (as those using xenon as a target material), for which as we will see the number of detected photoelectrons (of the primary scintillation signal $S1$, see the following sections) is then converted into nuclear recoil energy. Close to the energy threshold, the number of detected photoelectrons is small. For this reason, one could reasonably expect the detector resolution for nuclear recoils (as a function of E_r) to be governed by Poisson statistics for the number of detected photoelectrons.[3]

2.2.4 More than one target nucleus and isotopic composition

The above equations are related to the interaction between a WIMP and a particular nucleus, but in detectors there may be several different nuclei and several isotopes per nucleus. The *mass number* A is the total number of nucleons in a single nucleus, i.e. the number of protons plus neutrons, so it is a dimensionless integer. Since in nature for the majority of the elements there exist many different isotopes for each element, and different isotopes of the same element differ because of their number of neutrons, the mass number is not characteristic of a certain element, but rather of a certain isotope of a certain element.[4] So detectors based on elements which

[3] Moreover, as pointed out by [29], reality is more complicated, and the observed distribution is at best quasi Poisson. Thus, [29] concludes that the detector resolution can unlikely be summarized with a simple statistical model, in particular at low recoil energies where it is more relevant. For light WIMP masses (below ~ 10 GeV), regime in which the detector sensitivity is dominated by Poisson fluctuations above the threshold in the $S1$ signal, a correct model of the detector resolution becomes essential, and it seems preferable to use the discrete resolution distributions directly obtained from Monte Carlo simulations.

[4] A quantity which is characteristic of a certain element is instead the *relative atomic mass* which is the mass of a nucleus of a certain element averaged over the population of different isotopes, and expressed in *atomic mass units*.

are present in nature with many isotopes (for example the element xenon, used for instance by the experiments LUX, XENON100 and XENON10), contain nuclei of the same element but with different mass numbers.

Moreover, some experiments use targets which contain more than one species of elements (an example is given by the experiment DAMA, which uses crystals of NaI).

These effects can be taken into account by calculating the total event rate as a weighted average of the individual rates for the different elements/isotopes, which can be written as:

$$R(t) = \sum_{i=1}^{N} h_i R_i(t) \ , \tag{2.8}$$

where i is an index which enumerates the different isotopes/elements, N is the number of different isotopes/elements present in the detector and $R_i(t)$ is computed for each isotope/element i from equation (1.18). h_i is the *mass fraction* of the i-th isotope/element given by

$$h_i = \frac{n_i m_{A_i}}{\sum_{j=1}^{N} n_j m_{Aj}} \ , \tag{2.9}$$

where m_{A_i} is the mass of a nucleus of the isotope/element i and n_i is the number fraction of the i-th species, i.e. the number of nuclei of the i-th species divided by the total number of nuclei.

In our numerical implementation of these computations we have assumed that for every experiment the isotopic composition of its target material is the same as the natural isotopic composition of the corresponding element (apart for elements for which the most common isotope has a natural abundance of at least 99%, for which we neglected rare isotopes). In the case of more isotopes, for every isotope n_i is given by its *natural abundance*, while for the case of many elements it is given by the ratio between the number of the atoms of the species i in a molecule of the target material, and the number of atoms that composes such molecule.

In table 2.1 we provide the values of the useful quantities associated with the elements used by the DMDD experiments that we will present in this chapter, while in table 2.2 we provide the isotopic composition of those elements (among the above ones) for which no single isotope has a natural abundance of more than 99%.

Element	Atomic number Z	Mass number A	Atomic weight (u.m.a.)	Mass (average) (GeV)
O	8	16	15.999	14.90
Na	11	23	22.990	21.41
Si	14	–	28.085	26.16
Ar	18	40	39.948	37.21
Ca	20	–	40.078	37.33
Ge	32	–	72.630	67.65
I	53	127	126.904	118.21
Xe	54	–	131.293	122.29
W	74	–	183.840	171.25

Table 2.1: The main properties of the elements used in the DMDD experiments described in this chapter. The mass numbers reported are those of the more frequent isotope. For elements with the symbol – in the column of the mass number, there is no isotope which constitutes at least the 99% of all atoms of that material. As a consequence,we took into account the isotopic composition of that material using equation (2.8) to calculate the total rate. The isotopic compositions of those elements are listed in table 2.2.

Si		Ca		Ge		Xe		W	
A	n.a.	A	n.a.	A	n.a.	A	n.a.	A	n.a.
28	0.9223	40	0.96941	70	0.2123	128	0.019	180	0.0012
29	0.0467	42	0.00647	72	0.2766	129	0.264	182	0.2650
30	0.0310	43	0.00135	73	0.0773	130	0.041	183	0.1431
		44	0.02086	74	0.3594	131	0.212	184	0.3064
		46	0.00004	76	0.0744	132	0.269	186	0.2843
		48	0.00187			134	0.104		
						136	0.886		

Table 2.2: The isotopic composition of some elements used in DMDD experiments; A is the mass number, $n.a.$ stands for natural abundance.

2.2.5 Detector mass and exposure time, average over time

Finally, let us remark that all the experiments presented in this section, apart from the DAMA experiment, run for a period of time of the order of many months, but the number of detected events, thanks to efficient background discrimination, is very small. For such experiments we need to consider the average over time of the time-dependent total event rate. Since the information on which are the

actual days of activity of the detector is in general not available, we simply take the average between the maximum and the minimum event rate over one year

$$\overline{R}_{[E_1,E_2]} = \frac{R_{[E_1,E_2](t_{max}\simeq 152 \text{ days})} + R_{[E_1,E_2](t_{min}\simeq 335 \text{ days})}}{2} \ , \tag{2.10}$$

where $R_{[E_1,E_2]}(t)$ is given in equation (2.4), while t_{min} and t_{max} are discussed in section 1.7.

Often we will need to compute the number of recoil events expected by a detector in the energy window $[E_1, E_2]$. This is obtained by multiplying the average event rate per unit detector mass in the same energy window, provided by equation (2.4), by the total mass of the detector ΔM and by the exposure time ΔT:

$$N_{[E_1,E_2]} = \Delta M \Delta T \overline{R}_{[E_1,E_2]} \ . \tag{2.11}$$

Note that usually experimental papers provide both the total $\Delta M \times \Delta T$ of the experiment, and the same quantity after cuts. If the cuts have properly been taken into account using the experimental efficiency as in equation (2.3) and subsequent, then the total $\Delta M \times \Delta T$ must be used.

2.3 Statistical methods to extract upper limits from data

In this section we describe how to extract limits from DMDD data using Poisson statistics, and two of the methods often employed in the direct detection community.

2.3.1 Poisson statistics

In the DMDD experiments presented in this section, the number of detected events is usually small enough for the Poisson statistics to apply.

Poisson statistics allows to exclude some part of the parameter space as follows: parameters that predict an average number of events N_{th} (in the energy range under consideration) are excluded at a confidence level $1 - \alpha$ if the probability of seeing as few as the observed number of events is less than α. For zero event, that corresponds to upper limits on N_{th} of 2.3 at a 90% CL, 5.9 at 3σ and 14.4 at 5σ. We provide the proof of this in the following subsections.

The case of N_{obs} detected events

A discrete non negative random variable $\mathcal{X}$ is said to follow a Poisson distribution of expected value μ when the probability of $\mathcal{X}$ being equal to a discrete value x is

$$P(\mathcal{X} = x) = \frac{\mu^x}{x!} e^{-\mu} \ . \tag{2.12}$$

So, assuming that in a detector the number of observed events $\mathcal{N}_{obs}$ is a random variable Poissonianly distributed with expected value N_{th} predicted by the theory, the probability that in a given experiment the random variable $\mathcal{N}_{obs}$ will assume the value N_{obs} (i.e. that we will observe a number of events N_{obs}) is:

$$P\left(\mathcal{N}_{obs} = N_{obs}|N_{th}\right) = \frac{N_{th}^{N_{obs}}}{N_{obs}!}e^{-N_{th}} = 1 - P\left(\mathcal{N}_{obs} \neq N_{obs}|N_{th}\right) \ . \tag{2.13}$$

Now, when in a real experiment we observe N_{obs} events, in order to put a conservative limit on the value of N_{th} we can allow all the N_{th} for which $\mathcal{N}_{obs} = N_{obs}$ is as improbable as occurring in only a fraction α (for instance 10%) of the repetitions of the experiment, and discard at an $1-\alpha$ CL (for instance 90%) the N_{th} for which this is more improbable, because they are assumed to be "too unlikely". So we want to find the N_{th} associated with a probability of

$$\alpha \leq P\left(\mathcal{N}_{obs} = N_{obs}|N_{th}\right) = \frac{N_{th}^{N_{obs}}}{N_{obs}!}e^{-N_{th}} \ . \tag{2.14}$$

Since this means that

$$P\left(\mathcal{N}_{obs} \neq N_{obs}|N_{th}\right) \leq 1 - \alpha \ , \tag{2.15}$$

we will say that we are excluding the above mentioned values of N_{th} at $1-\alpha$ CL (for instance 90% CL). This means that we have excluded all the N_{th} which give $\mathcal{N}_{obs} = N_{obs}$ in less than a fraction α of the cases.

In our case, since $N_{th} = N_{th}\left(\sigma_{pSI}, m_\chi\right)$, we can invert the above relation and obtain an exclusion curve (giving an upper limit) in the plane σ_{pSI},m_χ in the form of a function $\sigma_{pSI}\left(m_\chi\right)$.

The case of 0 detected event

When we are interested in the particular case of 0 detected event, inserting the value $N_{obs} = 0$ in equation (2.14), we get that we exclude at 90% CL all the N_{th} which do not satisfy the condition

$$N_{th} \leq 2.30 \ . \tag{2.16}$$

In the same way we obtain $N_{th} \lesssim 5.9$ for 3σ (which means a CL of 99.73002%) and $N_{th} \lesssim 14.4$ for 5σ (which means a CL of 99.99994%).

Another way to obtain the same result is the following. The standard "Poisson" confidence level C upper limit N_{th} is the one which would result in a fraction C of random experiments having more events in the entire experimental range than the N_{obs} actually observed. This fraction C is simply the sum of the probability of $\mathcal{N}_{obs} = N_{obs} + 1$ plus the probability of $\mathcal{N}_{obs} = N_{obs} + 2$, etc., i.e.:

$$P\left(\mathcal{N}_{obs} > N_{obs}|N_{th}\right) = \sum_{k=N_{obs}+1}^{\infty} \frac{N_{th}^k}{k!}e^{-N_{th}} = \int_0^{N_{th}} dt \frac{t^{N_{obs}}}{N_{obs}!}e^{-t} \ , \tag{2.17}$$

where the last equality is justified in [30].

If we require a C.L. of $C = 90\%$, and we are in the particular case of $N_{obs} = 0$, the above equation becomes

$$0.90 = 1 - e^{-N_{th}} \ , \tag{2.18}$$

from which it follows that the exclusion curve for a 90% CL is defined by $N_{th} = 2.3$.

The limits obtained using Poisson statistics as presented above, both in the case of 0 and of N_{obs} detected events, always exclude less parameter space then naively imposing $N_{th}\left(m_\chi, \sigma_{pSI}\right) < N_{obs}$.[5] This is due to the fact that they take into account statistical fluctuations, which are governed by Poisson statistics, of the number of observed events.

2.3.2 Maximum Gap Method

The maximum gap method (MGM) was originally presented in [30] and has been largely employed to extract upper limits from the data of DMDD experiments (for instance in [28], [22] and [26]). Here we present it showing how we apply it to the case of our interest, i.e. DMDD experiments (even though its formulation in [30] allows more general applications). We will use it to extract upper limits from all the experiments with no or few events detected presented in this chapter, taking into account some subtleties related to some particular experiments.

Motivation

In DMDD experiments the detected events can be seen as distributed along a one dimensional axis (the one of the recoil energy E_r, see figure 2.1). In addition to the events coming from WIMPs scattering off nuclei (signal events) there can be a background of which the expectation can be computed, but one cannot exclude (or might not want to exclude) the presence of an additional unknown (non-negative) background. If it cannot be excluded that the unknown background could account for all the detected events, then only an upper limit on the signal can be reported.

Since the likelihood associated with an unknown background is unknown, methods based on likelihood, like that of Feldman-Cousins [31] or the Bayesian approach, cannot be applied (see [30]). For a given WIMP mass m_χ, the distribution of events in the variable E_r (i.e. the differential event rate times the fiducial mass

[5] For a given experiment we expect the number of observed events N_{obs} to be given by the sum of the events produced by WIMPs, and those produced by the possible presence of an unknown background (a part of which is estimated by the experimental collaborations and presented as expected background). Thus a naive way to extract an upper limit on σ_{pSI} from the data of experiments which detect a non-zero (but small) number of events N_{obs} consists in excluding all the points in the plane m_χ, σ_{pSI} for which the theoretical expectation for the events produced by WIMPs is $N_{th}\left(m_\chi, \sigma_{pSI}\right) \geq N_{obs}$. Of course this method provides just an approximated exclusion limit, but it can be used for rapid estimations; the exclusion curves shown in figure 2.2 are computed in this way.

times the total exposure) can be computed, but the WIMP-nucleon cross section σ_{pSI} is unknown. The simplest thing that one could do would be to select an interval in recoil energy and apply the method from Poissonian statistics (described in the previous section) to that energy interval. Usually, the bottom of the range of energies to which the detector is sensitive is limited by noise or other backgrounds. Thus if there are many events at such low energies, the limit will be weaker than required by the data. On the other hand, the experimenter could inadvertently bias the result by choosing the interval endpoints to give particularly few events, and thus obtaining an upper limit which is stronger than required by the data. In order to avoid such a bias, it might be safer to avoid using the observed events to select the interval used. Anyway this method follows the opposite strategy, i.e. the range is carefully chosen to have especially few observed events with respect to the predicted number of events in the same interval. This approach is meant to make the method particularly insensitive to background, because the background is likely to be higher in regions where more events are found. The maximum gap method cannot be used to identify a positive detection, but instead it is appropriate to extract limits from experiments with a very low, but not zero, background (in the case where we cannot exclude that all the events are due to background).

The maximum gap

The lower part of figure 2.1 (adapted from [30]) represents as the continuous line the predicted number of events as a function of energy dN/dE (for a given proposed σ_{pSI}), and the actually detected events (black rectangles).

If an expected background is present, it can be included in dN/dE, even though usually it is not (and we thus say that there is no background subtraction). In any case, we assume that also an unknown background could be present, which could in principle account for all the detected events.

To set an upper limit, for every value of the WIMP mass m_χ we augment the value of σ_{pSI} until we reach a value that is just "too high" to be accepted. We need to specify which is the criterion for considering a value of σ_{pSI} as "too high". Note that to find the strongest possible upper limit we should look at energies where there is a small number of events, and thus a small background.

Let us consider the *gap* between two events occurring at energies E_i and E_{i+1}. The *size of the gap* (for a given couple of values of m_χ and σ_{pSI}) can be characterized by the value of the expected number of events within the gap, given by:

$$x_i = N_{[E_i,E_{i+1}]} = \int_{E_i}^{E_{i+1}} \frac{dN}{dE_r}\,(m_\chi, \sigma_{pSI})\,dE_r \ , \tag{2.19}$$

where $N_{[E_i,E_{i+1}]}$ is the one of equation (2.11), that as we have seen can be computed from the differential scattering event rate.[6]

[6] Note that here we are considering a time averaged number of events (so the variation over time is neglected).

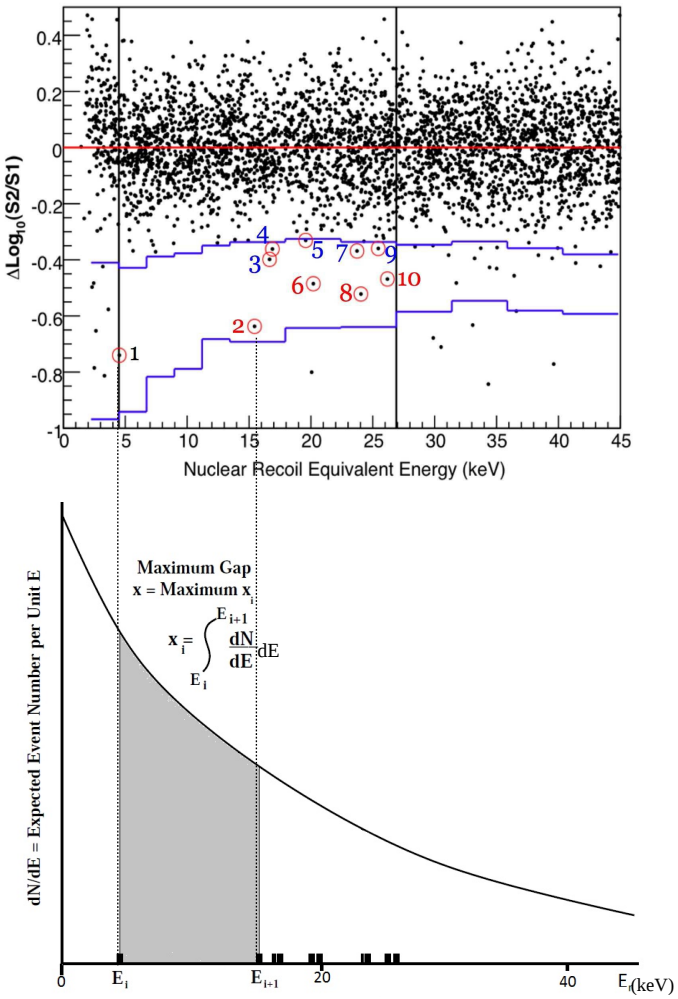

Figure 2.1: Sketch of how we apply the maximum gap method to a concrete case (in this figure, the data of the XENON10 experiment published in [28]. The upper part of the figure (adapted from [28]) represents the distribution of the events as usually presented by the experimental papers, i.e. as a function of the recoil energy and of a function of the ratio of the two measured quantities $S1$ (scintillation of the hit xenon nucleus) and $S2$ (scintillation light emitted in the top xenon gaseous phase from ionization electrons that drifted upward from the hit nucleus). For a more detailed description of the quantities $S1$ and $S2$, see section 2.5.1. Note that only events following in a particular area of this plane, namely the one identified by the blue and the black lines, are considered candidate events, i.e. events that might come from WIMP scattering off nuclei. The lower part of the figure (adapted from [30]) represents as the continuous line the predicted number of events as a function of energy dN/dE (for a given proposed σ_{pSI}), and the actually detected events as black rectangles corresponding to the events in the signal region which are surrounded by a red circle in the upper part of the figure.

We will thus call the *maximum gap* the one which corresponds to the maximum among all the gap sizes x_i.

The criterion which defines the upper limit

The bigger the σ_{pSI} we consider, the bigger the value of the gap size of the corresponding maximum gap,[7] and we will have to reject those σ_{pSI} that give a too big value of x w.r.t. the data. The criterion for "too big" is that if the choice of σ_{pSI} would be correct, a random experiment would almost always give fewer expected events in its maximum gap. Call x the maximum gap size of such a random experiment. If the random variable x is lower than the observed maximum gap size with probability C_0, the assumed value of σ_{pSI} is rejected as too high with confidence level C_0.

Obviously we can make a substitution of the variable of integration in equation (2.19) without varying x, which means that x is unchanged under a transformation of the variable in which events are distributed. So we can make a substitution such that every point of the E_r axis is transformed to a variable equal to the total number of events expected in the interval between that E_r point and the lowest allowed value of E_r (which is E_T). Irrespective of how events were expected to be distributed in the original variable, they will be distributed uniformly with unit density in the new variable. So any event distribution can be transformed to an equivalent uniform distribution of unit density. The new probability distribution of x depends on the total length of this uniform unit density distribution, and in this new variable the total length of the distribution is equal to the total expected number of events μ (which in our case can be computed using equation (2.11) as $\mu = N_{[E_T, E_{max}]}$), but it does not depend on the shape of the original event distribution.

The probability C_0 (given a total number of events predicted μ) of the maximum gap size being smaller than a particular value of x is a function only of x and μ:

$$C_0(x, \mu) = \sum_{k=0}^{m} \frac{(kx - \mu)^k \exp(-kx)}{k!} \left(1 + \frac{k}{\mu - kx}\right) , \tag{2.20}$$

where m is the greatest integer $\leq \mu/x$. For a $1 - \alpha$ CL upper limit (for instance 90%) we have to increase σ_{pSI} until μ and the observed x are such that C_0 reaches $1 - \alpha$ (which means $C_0 = 0.90$ in the case of a 90% CL). Equation (2.20) is derived in [30]. This method is most appropriate when there are only a few events in the part of the range that seems relatively free of background (small μ), even though this method can be used with an arbitrary number of events in the data. The result is a conservative upper limit that is not too badly weakened by a large unknown background in part of the considered region because it excludes regions where a

[7] Since x scales linearly with σ_{pSI}, in our numerical implementation we have used this fact to reduce the computation time by computing x only once for a given σ_{pSI} of reference, and than rescaling this value by the ratio between the new σ_{pSI} and the reference value of σ_{pSI} used.

large unknown background causes events to be too close together for the maximum gap to be there.

Let us just remark a couple of facts. First, in our numerical implementation of the MGM, in order to optimize the computation time, we first used the (very fast) Poisson method to look for a naive limit, and we started from that value to look for the upper limit with the MGM. Secondly, let us remark that, when scanning the parameter space σ_{pSI},m_χ the max gap interval (in E_r) not necessary need to be the same for all the tested values of m_χ. For instance, this occurs for CDMSLite.

2.3.3 Optimum Interval Method

The *optimum interval method* (OIM) was originally introduced by [30]. It has been used, in the framework of DMDD experiments, for instance by the CDMS collaboration in [23], [32] and [27], by the Edelweiss collaboration in [33] and by the CRESST2 collaboration in [34]. This method is a generalization of the maximum gap method.

Instead of considering the interval with 0 events detected in it, corresponding to the maximum gap, as done with the maximum gap method, if there is a relatively high density of events in the data we may want instead to consider the "maximum" interval over which there is 1 event detected, or 2 events, or n events. This is precisely what the OIM does, with an automatic selection of which interval to use.

Let us shortly review how does the method work. Let us take $C_n(x, \mu)$ to be the probability, for a given cross section and no background, that all intervals with $\leq n$ events have their expected number of events $\leq x$. This quantity can be computed via equation (2.20) for the particular case of $n = 0$, and can be tabulated via a Monte Carlo for the other values of n. Then C_n can be used in the same way as C_0 to obtain an upper limit: for x equal to the maximum expected number of events taken over all intervals with $\leq n$ events, $C_n(x, \mu)$ is the confidence level with which the assumed cross section is excluded as being too high.

To avoid biasing the result by choosing a particular interval influenced by our prejudices, the method implements an automatic selection of which interval to use. C_n is computed for each interval within the total range of an actual experiment, for the observed number of events n and the expected number of events x in the interval. The bigger C_n, the stronger the evidence that the assumed cross section is too high. The "optimum interval" will then be the one that will most strongly indicate that the proposed cross section is too high (we will call C_{max} the corresponding value of $C_n(x, \mu)$).

Thus, a 90% confidence level upper limit on the cross section (this is the value usually chosen when computing limits from DMDD results) is one for which the observed C_{max} is higher than would be expected from 90% of random experiments with that cross section and no unknown background.

Even though the definition of C_{max} seems to imply that its determination requires to check an infinite number of intervals, this is not case. In fact, to determine C_{max} one only needs to consider those intervals that are terminated by

an event or by an endpoint of the total experimental range, because sub-intervals of these would necessarily have a smaller $C_n(x, \mu)$ than the corresponding original ones.

In [30] also a comparison of the above methods is worked out, with the following main conclusions. When there is no background, or the background is distributed the same as the signal, then OIM gives a stronger limit than the MGM, and for some values of μ also a stronger limit than the Poisson statistics. When the background, unknown to the experimenters, is distributed in a different way w.r.t. the expected signal, than the MGM produces a limit weaker than that of the OIM, and Poisson statistics provides the weakest limit of all.

2.3.4 Impact of the nucleus mass on the exclusion curves

In figure 2.2 we have plotted many exclusion curves (computed with the naive $N_{th} < N_{obs}$ method) for different target nuclei. For all curves we used $E_r = 5$ keV, the SHM, the Helm form factor and an exposure of 200 kg×day. The shape of these curves is due to the predominance of the astrophysical part in the expression of the scattering rate at low m_χ, and the predominance of the particle physics part at high m_χ, as we already pointed out with figure 1.3.

One thing that is important to underline is that, as we can see from the figure, different materials (which have different atomic masses m_A) give exclusion curves with a minimum at different values of m_χ. The higher the value of m_A, the higher the value of m_χ at which the curve has its minimum. This is due to the fact that, as shown in figure 1.2, the recoil energy transferred from a WIMP colliding with a nucleus as a function of m_A has a maximum at $m_i = m_\chi$. Since the minimum in the exclusion curve indicates on which values of m_χ the detector is able to put the strongest constraint, it is evident that the choice of the material used in a particular detector will depend also on which is the range of WIMP masses that the experiment wants to study more carefully.

2.4 How the astrophysics fixed by the SHM affects the exclusion curves

Now that we have explained how we can obtain limits on the relevant parameter space from the data of DMDD experiments, we want to show how variations in the values of the astrophysical quantities fixed by the SHM impact on the exclusion curves. We will first point out the role of the SHM in comparing different experimental results. We will thus briefly discuss the astrophysical uncertainties that affect the quantities fixed by the SHM. Finally, we will describe the impact of variations in the values of the astrophysical parameters of the SHM on the exclusion curves, both with qualitative and quantitative illustrations.

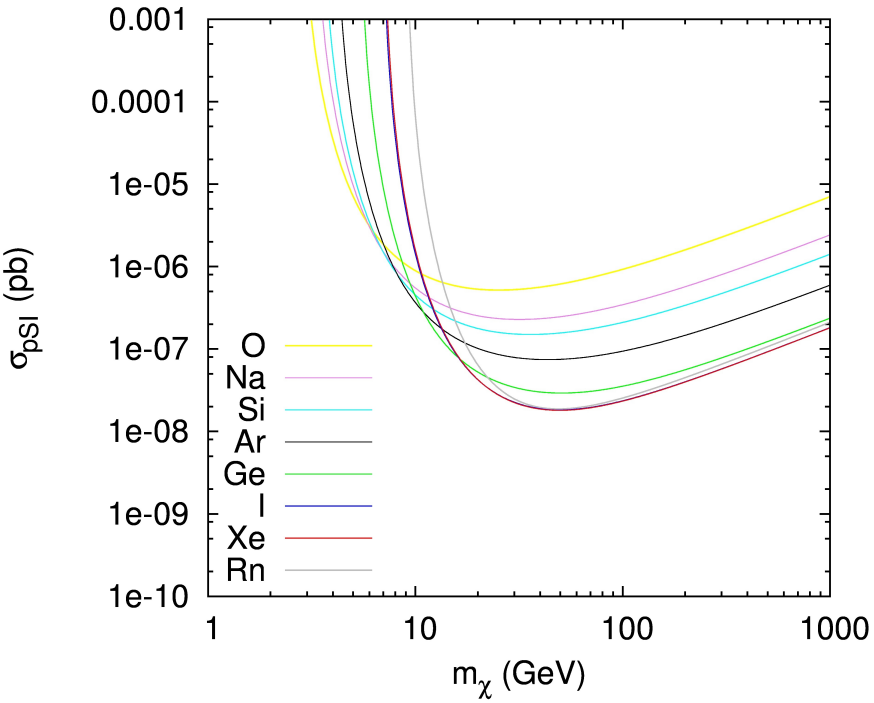

Figure 2.2: We illustrate the impact of the target nucleus mass on the exclusion curves, which have been computed with the naive method $N_{th} < N_{obs}$. We consider for illustration a recoil energy of $E_r = 5$ keV and an exposure of 200 kg×days. The SHM and the Helm form factor are assumed.

2.4.1 The role of the SHM in comparing different experimental results

As we have extensively discussed in chapter 1, DMDD aims at detecting WIMPs via their scattering off nuclei. In this chapter we describe some of the experimental techniques employed in this domain, together with the details and results of some of the most sensitive experiments carried out until now. As we have seen in the previous section, to extract limits from the experimental data, statistical methods (like for instance the maximum gap method or, in the case of signal regions, a χ^2 test, as we will see later on in this chapter) are employed. Roughly speaking, the underlying principle of all these methods is to compare the theoretical prediction associated with a certain set of parameter values with the experimental data, and thus to associate to these parameter values a probability of being excluded/favored accordingly. In particular, in the case of DMDD the theoretical predicted quantities that are compared with the experimental findings are all computed from the differential event rate given for instance in equation (1.23) (which has to be modified to take into account general or particular experimental subtleties, as

explained in this chapter).

As we can see from that equation, a central role in computing this quantity is played by the astrophysical properties of dark matter, in particular its velocity distribution $f_{\vec{v}}(\vec{v})$, for which also the local circular speed v_c and the local Galactic escape speed v_{esc} play an important role, and its local mass density $\varrho_\odot$. A standard set of assumptions is usually employed to fix these quantities, the so-called standard halo model (SHM), which assumes a Maxwell-Boltzmann speed distribution for the dark matter, and which we have already described in detail in section 1.8 (most of the ingredients used below are explained there).

A common setup is useful because it allows to compare among each others the experimental results presented by different collaborations, nevertheless, it represents an oversimplified point of view which neglects many facts. To start with, it assumes fixed values for the above mentioned quantities, but those quantities are determined through astrophysical observations, so different studies exist in the literature, providing different results, and each result is affected by statistical and/or systematic uncertainties. We outline this issue in the following section, and we will explore it in more detail in chapter 5. We then illustrate at a qualitative level in the subsequent section how variations in the values of these parameters affect the limits set by DMDD experiments.

Moreover, as we will see in chapter 3 the above mentioned astrophysical quantities can be related by an underlying mass model. This is of particular importance because often measures of such quantities rely on particular assumptions on the Milky Way mass model.

As we will see in section 3.4.3, the density profile corresponding to a Maxwell-Boltzmann speed distribution is the singular isothermal sphere of equation (3.33). Anyway, N-body simulations suggest that the dark matter density may not follow such a profile.

It is important to understand the level of error induced by the SHM assumptions. In the following section we briefly summarize some of the estimates of the astrophysical parameters of the SHM that are currently available in the literature, than focusing on the effects that varying these parameters has on the DMDD limits.

In chapter 4 we will present as a case study the impact on DMDD limits of the most recent estimate of the escape speed. This will also give us the opportunity to drop the assumption of a Maxwell-Boltzmann speed distribution and to consider speed distributions arising from the assumed mass model.

2.4.2 Astrophysical uncertainties

Let us now briefly outline some of the different estimates present in the literature for the parameters of the SHM, and the associated uncertainties, in order to give to the reader an idea on which are the ranges of variation to expect for the values of these astrophysical quantities w.r.t. those fixed by the SHM. We will explore more in detail in chapter 5 the different estimates present in the literature, the methods used to obtain them and the associated uncertainties.

The distance of the Sun from the Galactic center

When we consider quantities as the local circular speed, the local Galactic escape speed, the local dark matter density, we are talking about local quantities in the sense that they are evaluated at the location of the Sun.[8] So, when we talk about the local Galactic escape speed, the local circular speed and the local dark matter density, we mean respectively $v_{esc}(\vec{r}_\odot)$, $v_c(\vec{r}_\odot)$ and $\varrho_{DM}(\vec{r}_\odot)$.

The statements above mean that all these quantities contain in their definition the distance $r_\odot$ of the Sun from the Galactic center (where we indicate $r_\odot \doteq |\vec{r}_\odot|$). There is some debate on the value of $r_\odot$, anyway the standard value reported in [35] is $r_\odot = 8.4 \pm 0.6$ kpc.

The local dark matter density

The local dark matter density $\varrho_\odot$ is the dark matter density evaluated at the position of the Solar System, i.e. where the DMDD experiments are carried out. The value assumed by the SHM is $\varrho_\odot = 0.3$ GeV/c^2 cm^{-3}. This is the "canonical value" reported in [36] and in [35], where it is also reported that this number has to be considered correct within a factor of 2 or 3 ([35] reports that these values arise from a sampling of many references).

In the recent years, anyway, there has been a tendency to consider higher values, somewhat around $\varrho_\odot \approx 0.4$ GeV/c^2 cm^{-3}, as noticed for instance by [12]. In [37] it is reported that, even if the commonly used value is the one above, the authors found in their simulation $\varrho_\odot = 0.39$ GeV/c^2 cm^{-3}.[9]

The work of [38] employs a model for the local (i.e. in the Solar neighborhood) Galactic potential applied to the data from the observations worked out by the RAVE collaboration. The value of $\varrho_\odot = 0.542 \pm 0.042$ GeV/c^2 cm^{-3} is then determined, considerably higher the standard one.

We can basically conclude by saying that recent estimates of the local dark matter density are pointing toward values higher than the standard one, but the uncertainties on each individual measure and especially the differences among the methods employed by these different studies are still very important.

The ratio between the local circular speed and the distance from the Sun to the Galactic center

In [39] the authors investigate the distance of the Sun from the Galactic center, the rotational speed of the local standard of rest (to which in this thesis we refer as the local circular speed at the position of the Sun v_c, see equation (1.69)) and the peculiar velocity of the Sun. They find out that the value of the ratio $v_c/r_\odot$ is better

[8] Let us remark that sometimes we do not explicitly write the word local, which is left understood.

[9] For the spherical halo, at a radius roughly equal to the Sun's distance from the Galactic center, [37] finds $\langle\varrho_\odot\rangle = 0.30$ GeV/c^2 cm^{-3}, but this value increase to $\langle\varrho_\odot\rangle = 0.37$ GeV/c^2 cm^{-3} for a thick disk, and to $\langle\varrho_\odot\rangle = 0.39$ GeV/c^2 cm^{-3} for the thin disk containing Sun's position.

constrained than the two quantities considered independently. In particular, they find $v_c/r_\odot = 29.9 \pm 1.7$ km s^{-1} kpc^{-1} to $v_c/r_\odot = 31.6 \pm 1.7$ km s^{-1} kpc^{-1}. This is particularly important, because it points out that an important correlation in the measured values of v_c and $r_\odot$ is present, as it is clearly shown by figure 2 of [39]. It would be good to try to keep in mind similar correlations when using this or similar estimates in computing DMDD limits.

The local circular speed

The value assumed for the circular speed at the position of the Sun in the SHM is $v_c = 220$ km/s.

This value, anyway, has been for long time subject to big uncertainties, for instance the study of [39] reports that the best fit values they find range from $v_c = 200 \pm 20$ to $v_c = 279 \pm 33$, and that the value of $v_c/r_\odot$ is better constrained than the two quantities separately, as already discussed.

The recent estimate of [40] reports a value, higher than the standard one, of $v_c = 240 \pm 8$ km/s, and specifies that with the large data set they have the values of v_c and $r_\odot$ are no more tightly correlated.

The local Galactic escape speed

The value of the local Galactic escape speed assumed in the SHM is $v_{esc} = 544$ km/s. This value was estimated by the RAVE collaboration in [41] in 2007. In particular, the result of that study was the range 498 km/s $< v_{\rm esc} <$ 608 km/s at 90% confidence level, with 544 km/s as a median likelihood.

A new estimate of this quantity was published in 2014 by the RAVE collaboration in [1], providing the result of 533^{+54}_{-41} km/s at 90% confidence level, with an additional 4% of systematic uncertainty. This is the estimate on which we will focus in chapter 4, so a detailed description of it will be provided therein.

2.4.3 Impact of the astrophysical parameters of the SHM on the exclusion curves

Even tough the SHM fixes the values of the Galactic escape speed, of the circular speed and of the local dark matter density, these values are just conventional ones. Because of this, it is interesting to recall which are the effects of variations of these parameters on the DMDD exclusion curves. These effects are schematically illustrated in figure 2.3, where two reference target nuclei are considered (silicon and xenon). We consider variations of $\varrho_\odot$ of a factor of two, and variations of the escape speed, of the circular speed and of the most probable speed of the assumed Maxwell-Boltzmann distribution of ± 50 km/s (the values assumed for the analysis are provided in the caption).

A qualitative representation of the variation of these quantities is illustrated in figure 2.4 where we illustrate the changes by flashes, rather than by using different

values of the parameters.

Let us recall that in this chapter we are focusing on the spin-independent interpretation of the elastic scattering of a WIMP (of mass m_χ) off a nucleus (atomic number A, mass m_A), and no isospin violation. To understand the impact of the above parameters on DMDD limits, we need to recall equation (1.23), from which we have that the differential event rate per atomic target mass in an experiment is:

$$\frac{dR}{dE_r}(E_r) = \frac{\varrho_\odot \sigma_{pSI} A^2}{2 m_\chi \mu_{\rm p}^2} F^2(E_r) \int_{|\vec{v}|>v_{\rm min}(E_r)} d^3\vec{v} \frac{f_\oplus(\vec{v},t)}{|\vec{v}|} \ , \tag{2.21}$$

with $\mu_{\rm p}$ the WIMP-proton reduced mass, E_r the recoil energy, σ_p the WIMP-nucleon cross section, $F(E_r)$ the nuclear form factor (assumed of the Helm type), and $v_{\rm min} = \sqrt{m_A E_r/(2\mu_{\rm p})}$ the minimal velocity that a WIMP needs to transfer to a nucleus the recoil energy E_r; we take the time average of Eq. 2.21. $f_\oplus(\vec{v},t)$ is the dark matter velocity distribution in the Earth reference frame obtained from the one in the Galactic frame via a Galilean transformation.[10]

From the above equation (2.21), and recalling the velocity transformations described in chapter 1, we can remark that the effects of variations in the parameters fixed by the SHM are the following.

- Both $v_{\rm esc}$ and $v_{\rm c}$ impact on the position of the asymptote of the limit at low WIMP mass. In fact, $v_{\rm esc} + v_{\rm c} + V_\odot$ defines the average WIMP mass threshold $m_{\chi{\rm min}}$ given an atomic target and a recoil energy threshold, by solving $v_{\rm min}(E_T, m_{\chi{\rm min}}, m_A) = v_{\rm esc} + v_c + V_\odot$, see equation (1.16). This corresponds to the position on the mass axis of the asymptote of the upper limit on the spin-independent cross section (the larger $v_{\rm esc}$ and/or $v_{\rm c}$, the lower the mass threshold).

- $v_{\rm c}$ impacts on the relative position of the maximum sensitivity of a DMDD experiment on the m_χ axis (for a given atomic target); a larger $v_{\rm c}$ globally shifts the cross section limit curve to the left while not fully affecting the asymptote at the mass threshold, for which $v_{\rm esc}$ is also relevant.

- The larger the velocity dispersion, the larger the sensitivity peak (in the SHM, it is fixed by the most probable speed of the Maxwell-Boltzmann which is $v_0 = v_{\rm c}$).

- The local dark matter density $\varrho_\odot$ produces a global linear vertical translation of the entire exclusion curve.

[10] As explained in this chapter, when computing DMDD limits for real experiments we also take into account the experimental efficiency, the energy resolution of the detector, the fractions of atomic targets and the isotopic compositions for each target element. Anyway, in the illustrative plots of figures 2.3 and 2.4 these effects are not included.

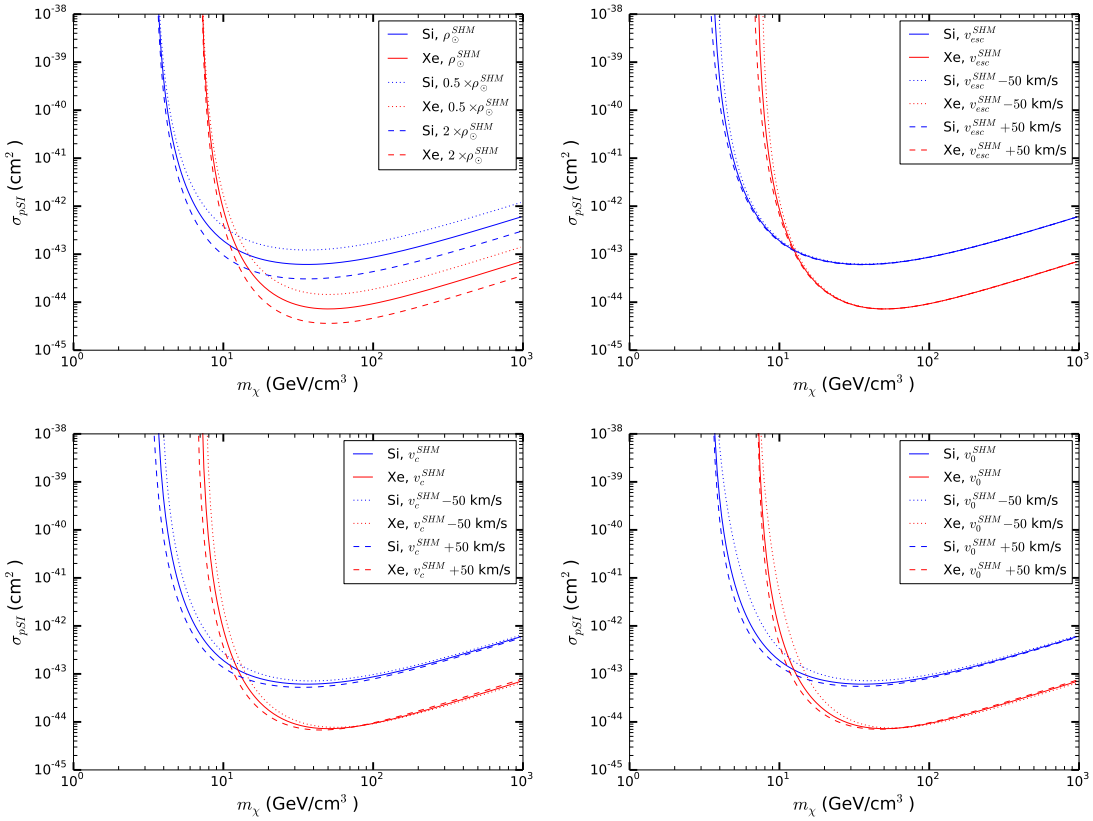

Figure 2.3: The figure shows the impact on DMDD exclusion curves of variations in the astrophysical parameters usually fixed by the SHM, $\varrho_\odot$, $v_{\rm esc}$, $v_{\rm c}$ and v_0 (see section 1.8). The limits are computed for illustration using Poisson statistics assuming 0 events detected (thus applying $N_{th} \leq 2.30$ to obtain a 90% C.L. limit) in a recoil energy range comprised between $E_T = 5$ keV and $E_{\rm max} = 100$ keV, with a total exposure of 500 kg×day. We consider two different target nuclei, silicon (lighter) and xenon (heavyer). Top left panel: the local dark matter density $\varrho_\odot$. Top right panel: the local Galactic escape speed $v_{\rm esc}$. Bottom left panel: the local circular speed $v_{\rm c}$. Bottom right panel: the most probable speed v_0 (which gives also the velocity dispersion) of the cut Maxwell-Boltzmann velocity distribution assumed.

2.5 DMDD experiments

In this section we describe some DMDD experiments, among which those that we will use in chapter 4.[11] For every experiment, we briefly summarize the most important quantities that allow to reproduce their data analysis, and how we can work it out (as we did for instance to produce the exclusion curves presented in figure 2.5). Some of these properties, along with other experiment-related quantities,

[11]The list of experiments presented here is not meant to be complete, but only to describe those experiments that we are going to use, which are mainly those that provided the most stringent constraints at the moment of writing, and some other experiments to provide an idea of the variety of existing experiments.

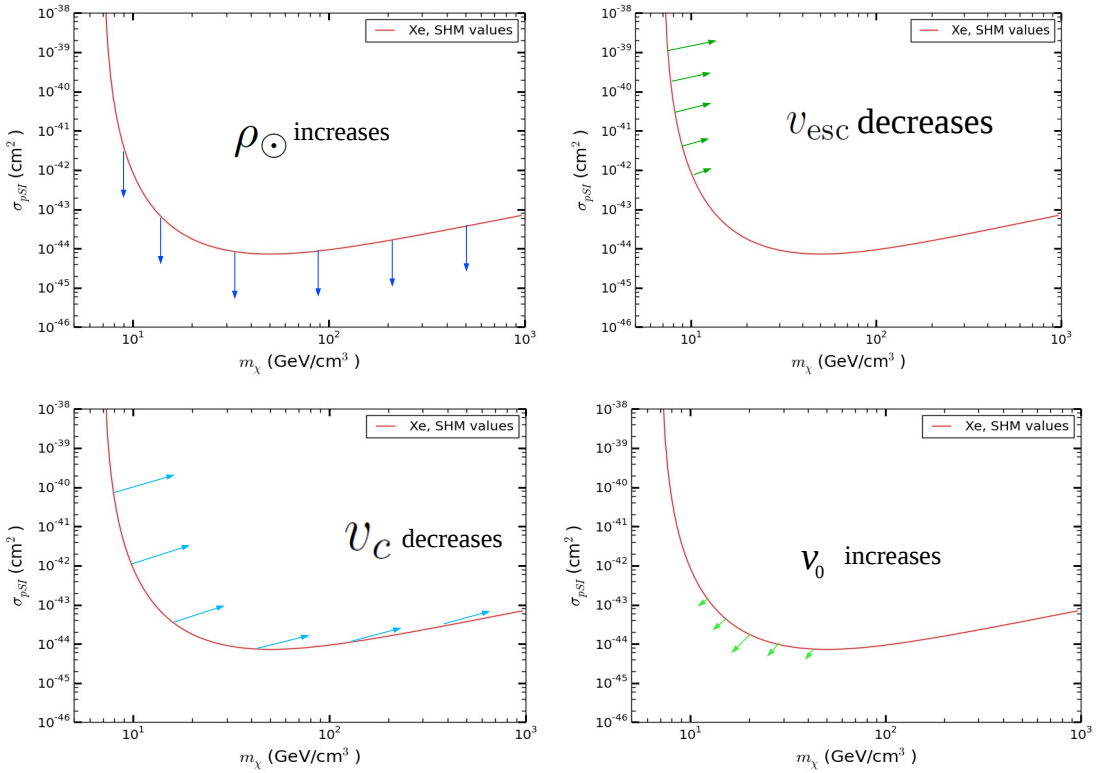

Figure 2.4: The impact of variations in the parameters of the SHM on DMDD exclusion curves, illustrated at a qualitative level using the reference curve for a xenon target nucleus reported in figure 2.3. Top left: the local dark matter density. Top right: the escape speed. Bottom left: the circular speed. Bottom right: the most probable speed (which is related to the velocity dispersion).

are listed in table 2.4. In order to extract the limits that we show in figure 2.5 from every experiment we apply the MGM to the data.

Unless otherwise stated, no quenching factor need to be taken into account for the above-mentioned experiments. As in any of the references from which the data are extracted, the SHM is assumed and we use the Helm form factor to model effects of the nuclear shape. We verified that the upper limits we obtained using the MGM for each experiment reasonably match those obtained (often with different methods) by the corresponding official analysis. These limits are shown in figure 2.5.

2.5.1 XENON10

XENON10 is an experiment located at the Gran Sasso National Laboratory (Italy), which uses a dual phase (liquid and gaseous) detector filled with xenon to search for WIMPs. Dual phase operation enables simultaneous measurement of direct scintillation (called the $S1$ signal) in the liquid, and of ionization via proportional

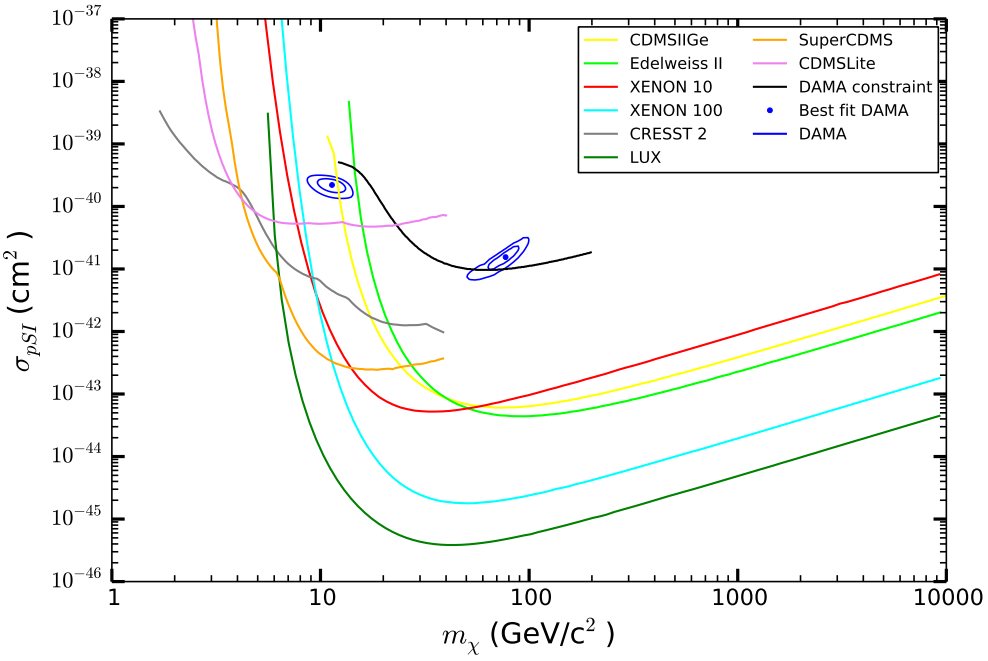

Figure 2.5: The parameter space σ_{pSI},m_χ that one wants to constrain for the spin independent interpretation of the DMDD experimental results. We show the upper limit on σ_{pSI} for the null experiments presented in this section, computed using the MGM. Also shown are the regions associated to the interpretation of the DAMA annual modulated signal as a SI elastic scattering of WIMPs off nuclei. For all the curves, the SHM (which has $v_{esc} = 544$ km/s, $\varrho_\odot = 0.3$ GeV/cm^3 and a Maxwell-Boltzmann distribution with $v_0 = 220$ km/s, see section 1.8) has been assumed.

scintillation[12] (called the $S2$ signal) in the gas. The ratio of the two signals is different for *nuclear recoil events* (from WIMPs and neutrons) and from *electron recoil events* (from gamma and beta background), which allows an event-to-event discrimination.

This can be understood by looking at the upper part of figure 2.1. Electron recoil events distribute in a band in the upper part of the shown plane (the dense gathering of events in figure 2.1), while nuclear recoil events in the lower part (this is determined via calibration). The two bands are mostly separated (even if partially superposed), and this allows to define a band in which almost all events are expected to be from nuclear recoils. This (with additional cuts in the energy range) is used to define the signal region, shown in blue in figure 2.1. Only events falling inside this region are considered as possible WIMP candidates in the data analysis.

We focused on the analysis [28] of data taken between 2006 and 2007, where a total exposure of 577 kg×days was analyzed. The live-time of the experiment was

[12]Scintillation light triggered by the ionization electrons that drifted from the hit nucleus upward to the xenon gaseous phase.

58.6 days and the detector fiducial mass (after cuts) used for the data analysis was 5.4 kg.

The threshold energy employed for the analysis is $E_T = 4.5$ keV, and the recoil energy window extends up to $E_{max} = 26.9$ keV. In the studied energy window, the observed number of events is 10 (without background subtraction), while a background of 7 events was expected in the same window. To obtain for XENON10 the 90% C.L. upper limit on the WIMP parameter space for spin-independent WIMP-nucleon scattering, we used the maximum gap method [30], as done in the original analysis [28] by the XENON collaboration. The boundaries of the maximum gap interval are $E_1 = 4.5$ keV and $E_2 = 15.5$ keV.

In our analysis of the XENON10 data, we also took into account the energy dependent experimental efficiency of the experiment as done in [25], i.e. with the approximated expression:

$$\varepsilon\left(E\right) = 0.46\left(1 - \frac{E}{135\text{keV}}\right) \ . \tag{2.22}$$

As in [25] we used a Gaussian energy resolution (2.5) with

$$\sigma\left(E\right) = (0.579\text{keV})\sqrt{(E/\text{keV})} + 0.021E \ . \tag{2.23}$$

The nuclear recoil scintillation efficiency $\mathcal{L}_{eff}$

The nuclear recoil energy reconstruction in dual phase xenon detectors has been widely discussed and improved over time. The main point is that the XENON10 and XENON100 detectors do not measure directly nuclear recoil energies E_{nr}, but they measure instead the signals $S1$ and $S2$. While the ratio between the two is used for event-to-event background discrimination, only the signal $S1$ is used to compute the nuclear recoil equivalent energy E_{nr} of an event. This is done using the equation

$$E_{nr} = \frac{S1}{L_y \mathcal{L}_{eff}} \frac{S_e}{S_n} \ , \tag{2.24}$$

which can be found for instance in [28], where also the values of the volume averaged light yield L_y and of the scintillation quenching factors for electron recoils S_e and for nuclear recoils S_n for XENON10 are provided.[13] The quantity $\mathcal{L}_{eff}$ is the *nuclear recoil scintillation efficiency* (sometimes called also *scintillation yield for nuclear recoils*), and it has been the subject of an animated debate, see for instance [42].

The value originally used by the XENON collaboration in [28] was the simple constant assumption of $\mathcal{L}_{eff} = 0.19$. Later, the value of $\mathcal{L}_{eff} = 0.14$ was used in [25], based on hints from [43] that $\mathcal{L}_{eff}$ could be lower. A proper approach consists in taking into account the energy dependence of $\mathcal{L}_{eff}\left(E_{nr}\right)$. In our analysis of the XENON10 data we used the form of $\mathcal{L}_{eff}\left(E_{nr}\right)$ obtained from the cubic

[13] These values are $L_y = 3.0 \pm 0.1(syst) \pm 0.1(stat)$, $S_e = 0.54$ and $S_n = 0.93$, at a drift field of 0.73 kV/cm.

spline interpolation of the spline points of figure 3 of [43], which we finally used to recompute updated values of the quantities E_T, E_{max}, E_1 and E_2 (the original values, written above, were obtained by the XENON collaboration with the assumption $\mathcal{L}_{eff} = 0.19$, so we obtained the new ones simply by multiplying the nuclear recoil energy scale by a factor $0.19/\mathcal{L}_{eff}\,(E_{nr})$).[14]

Some recent studies related to the determination of $\mathcal{L}_{eff}$ in liquid xenon, thus particularly relevant for the experiments XENON10, XENON100 and LUX, are [29], [44], [45] and [46]. In [29] constraints and an updated estimate of $\mathcal{L}_{eff}\,(E_{nr})$ with an extrapolation for low energies are proposed, based also on data from [47]. Reference [44] shows that the quenching of electronic excitation from nuclear recoils in liquid xenon is well described by Lindhard theory[15] if the nuclear recoil energy is reconstructed using an energy scale which combines scintillation and ionization. The authors thus argue the adoption of this perspective, whereas usually experiments with liquid xenon as the target medium use only the primary scintillation signal $S1$ to reconstruct E_{nr}. Reference [45] reiterates the idea, and shows that for events falling in the lower left corner of the typical search box (shown in the upper part of figure 2.1), the actual nuclear recoil energies are smaller than the usual energy scale suggests. Reference [46] shows that for very low recoil energies a simplifying approximation of the Lindhard model must be removed, namely the assumption that the atomic binding energy of the electrons is negligible. Removing this hypothesis leads to a modification of the model that reflects on DMDD experiments as a decrease in sensitivity to low mass dark matter, which means less constraining limits in this mass range, as shown in figure 5 of [46].

2.5.2 XENON100

XENON100 is the successor of XENON10, the experimental technique is the same and the main improvement is in size: a total mass of 100 kg of liquid xenon instead of 10 kg. In this work we considered the data of [22] (taken between 2011 and 2012) where a live-time of 224.6 days and a detector fiducial mass of 34.0 kg are considered.

The threshold energy employed for the analysis is $E_T = 6.6$ keV, and the recoil energy window extends up to $E_{max} = 30.5$ keV. In the studied energy window, the observed number of events is 2 (without background subtraction), while a background of 1 event was expected in the same window. To obtain for XENON100 the 90% CL upper limit on the WIMP parameter space for spin-independent WIMP-nucleon scattering shown in figure 2.5, we used the maximum gap method [30], which was used also in the original analysis [22] as a cross-check of the primary

[14] In this way,the original value of $E_T = E_1 = 4.5$ keV, $E_{max} = 26.9$ keV and $E_2 = 15.5$ keV become $E_T = E_1 \approx 5.47$ keV, $E_{max} \approx 23.43$ keV and $E_2 \approx 15.15$ keV.

[15] Lindhard theory is a method of calculating the effects of electric field screening by electrons in a solid, based on quantum mechanics. In this framework, [48] computed a general expression for the expected fraction of nuclear recoil energy that is transferred to electrons, which is of particular interest for DMDD.

analysis, worked out with a profile likelihood. The boundaries of the maximum gap interval are $E_1 = 7.8$ keV (lower boundary) and $E_2 = 30.5$ keV (upper boundary).

For the experimental efficiency we used a second degree polynomial fit to the acceptance shown in figure 1 of [22], which reads $\varepsilon(E) = aE^2 + bE + c$ with $a = 0.00038$, $b = -0.0305$ and $c = 0.818$. For lack of better information we used the same energy resolution that we used for XENON10.

For the XENON100 experiment we do not need any adjustment of the energy values through consideration of an updated $\mathcal{L}_{eff}$ because following the controversy on this quantity that surrounded the interpretation of the XENON10 results, the XENON collaboration improved their $\mathcal{L}_{eff}$ considering an energy dependent $\mathcal{L}_{eff}(E_{nr})$, the one of figure 1 of [49], so that the XENON100 results of [22] already take into account the dependence of $\mathcal{L}_{eff}$ on E_r. A more recent determination of $\mathcal{L}_{eff}$ by the XENON100 collaboration is shown in figure 5 of [50].

2.5.3 LUX

The Large Underground Xenon experiment (LUX) is located at the Sanford underground research facility and aims at detecting WIMPs via their scattering off xenon nuclei. For WIMP masses bigger than around 7 GeV, it represents the more constraining experiment at the moment of writing, for spin-independent WIMP-nucleon interaction. Its data analysis can be found in [24]. The preliminary run described there collected 85.3 days of data, with a detector fiducial xenon mass of 118 kg. In 2014 a 300-days run has started (see [51]), which is supposed to improve the sensitivity by a factor of 5.

Reference [24] does not contain all the information that we need to reproduce the LUX limits. We thus follow the approach detailed in [26]. We use the maximum gap method on an $S1$ range of $2 - 30$ photoelectrons.[16] In this range, 160 events have been observed, all being consistent with the predicted background of electron recoils. Of these events, 24 fall into the calibration nuclear recoil band (see figure 4 of [24]). However, they all fall on the same half of the expected nuclear recoil distribution, while if they would all come from that distribution, they should be with the same probability on one half or on the other half. For this reason, it is unlikely that a significant part of these 24 events would come from nuclear recoils. In [26], the MGM is used to compute five different exclusion curves for LUX, taking into account respectively 0, 1, 3, 5 or all the 24 events. As we can see in figure 1 therein, the official limit obtained by the LUX collaboration, at low WIMP masses, falls between the MGM curve for 0 events, and that for 1 event. We choose to consider, for our MGM analysis, 0 detected events. The obtained curve thus reproduces very well the official curve at low masses, the region on which we are more interested in, while it is more constraining at high masses.[17]

[16] The same range is used for the MGM analysis in [26], and for a likelihood analysis in [24].

[17] We obtained also the curve for 1 event, not shown here; at high masses this curve too is more constraining than the official one.

We have considered the experimental efficiency after cuts of LUX, that can be found in figure 9 of [24] (shown as the black crosses). As in [26], we set the counting efficiency to 0 below 3 keV$_{nr}$.

We use a Gaussian energy resolution, with standard deviation

$$\sigma\left(E_{nr}\right) = \sigma_{PMT} \times Q\left(E_{nr}\right) \ , \tag{2.25}$$

with $Q\left(E_{nr}\right) = \frac{4.131}{E_{nr}/\mathrm{keV}} + 0.690$ and an S1 single photoelectron resolution of $\sigma_{PMT} = 0.37$ photoelectrons (see [26]).

An indicative conversion from $S1$ and $S2$ signals to E_{nr} can be inferred from the contour lines in figure 4 of [24]. To convert $S1$ into E_{nr}, we have used the relation $E_{nr} = \frac{S1}{L_y \mathcal{L}_{eff}} \frac{S_e}{S_n}$ with the *Light yield* $L_y = 3$ photo-electrons/keV$_{ee}$ and the *scintillation quenching* $S_e = 0.54$ for electron recoils and $S_n = 0.93$ for nuclear recoils, from [43]. Even if the value of the *Lindhard factor* $\mathcal{L}_{eff}$ in liquid xenon is the subject of an animated debate, for our analysis of the LUX data we simply assumed the value $\mathcal{L}_{eff} = 0.14$, considering this approximation sufficient for our purposes.

2.5.4 EDELWEISS-II

EDELWEISS-II is an experiment located at the Laboratoire Souterrain de Modane (France) at a depth of 4800 m water equivalent, which aims at detecting WIMPs using Ge crystals as targets. EDELWEISS II uses interleaved detectors that measure both phonons and ionization. In the final data analysis [33] an exposure of 384 kg×days was reported.

The threshold energy employed for the analysis is $E_T = 20$ keV, and the recoil energy window extends up to 200 keV. In the studied energy window, 5 candidate events have been observed, while a background of 3 events was expected in the same window.

To obtain for EDELWEISS-II the 90% C.L. upper limit on the WIMP parameter space for spin-independent WIMP-nucleon scattering, we used the maximum gap method [30], while the original analysis employs the optimum interval method without background subtraction. The boundaries of the maximum gap interval are $E_1 = 23.2$ keV and $E_2 = 172$ keV.

2.5.5 CDMS-II

The Cryogenic Dark Matter Search experiment *CDMS-II* at the Soudan Underground Laboratory (USA) is an experiment which aims at detecting WIMPs using germanium crystals as targets. The detector also contains silicone crystals, but those have been excluded from the analysis [23] that we consider here because of their lower sensitivity to coherent nuclear elastic scattering (they are instead considered in dedicated analysis like [52]). An exposure of 612 kg×days has been analyzed.

The threshold energy employed for the analysis is $E_T = 10$ keV, and the recoil energy window extends up to 100 keV. To obtain for CDMSII the 90% CL upper limit on the WIMP parameter space for spin-independent WIMP-nucleon scattering, we used the maximum gap method [30], while the original analysis employs the optimum interval method (also presented in [30]) without background subtraction. The boundaries of the maximum gap interval are $E_1 = 15.5$ keV and $E_2 = 100$ keV.

We take into account the experimental efficiency, which we obtained from a fit but can be found also in [25].

2.5.6 SuperCDMS

SuperCDMS is an upgrade to the CDMSII experiment with new detector hardware which aims at detecting WIMPs using Ge crystals as targets. We consider a recent data analysis focused on low mass WIMPs that has been released in [32], in which an exposure of 577 kg×days has been analyzed.

The threshold energy employed for the analysis is $E_T = 1.6$ keV$_{nr}$, and the recoil energy window extends up to 10 keV$_{nr}$. In the studied energy window, 11 candidate events have been observed, while a background of 6.198 events was expected in the same window. Their energies are listed in table I of [32].

To obtain for SuperCDMS the 90% CL upper limit on the WIMP parameter space for spin-independent WIMP-nucleon scattering, we used the maximum gap method [30], while the original analysis employs the optimum interval method without background subtraction. We take into account the experimental efficiency, which we obtain from the red curve of figure 1 of [32], and which is an interpolation of data representing the exposure-weighted sum of the measured efficiency for each detector and period. We assumed a Gaussian energy resolution, and for lack of better information we used the same σ as CDMSLite.

2.5.7 CDMSLite

CDMSLite is the name of a calorimetric technique employed to work out a low WIMP mass analysis based on data taken from one single detector of the SuperCDMS experiment. This analysis makes use of data which correspond to an exposure of 10.3×0.6 kg×days, and can be found in [27].

The threshold energy employed for this analysis is 0.170 keV$_{ee}$, and the analysis extends up to energies of 7 keV$_{ee}$. In the CDMSLite analysis, the phonon energy is measured in units of keV$_{ee}$,[18] while in practice in our analysis we use nuclear recoil energies, which are expressed in keV$_{nr}$. The conversion between the two in CDMSLite can be understood from the below dedicated subsection 2.5.7.

We read off the recoil energy spectrum data from figure 1 of [27], using the histogram with bins of 10 eV$_{ee}$ for measured energies between 0.10 keV$_{ee}$ and

[18] In the CDMSLite analysis the phonon energy is calibrated w.r.t. the electron recoils, and because of this it is labeled in electron-equivalent units, see [27].

1.60 keV_{ee}, and the histogram with bins of 75 eV_{ee} above 1.60 keV_{ee}. We can deduce that in the recoil energy window chosen for this analysis 162 candidate events have been observed. Since the maximum gap method requires unbinned data, we have to construct these data. Following the procedure of [26], which uses the maximum gap method as well, we construct them by dividing each bin with multiple events into enough bins of equal width so that in the end we have one event per bin; we then assign to each event the middle energy of the bin containing it.

To obtain for CDMSLite the 90% CL upper limit on the WIMP parameter space for spin-independent WIMP-nucleon scattering, we used the maximum gap method [30], while the original analysis employs the optimum interval method without background subtraction. We take into account the experimental efficiency, which we take to be 98.5% for every energy, as stated in [26] and as can be deduced from the inset of figure 1 of [27]. We assumed a Gaussian energy resolution, with the same value $\sigma = 0.014$ keV_{ee} of [26] and [27].

Energy conversions in CDMSLite

The quantity measured by the detector is the *phonon energy* E_{ee} (measured in keV_{ee}). This energy can be converted into a nuclear recoil equivalent energy E_{nr} (whose unit is denoted keV_{nr}) using the equation

$$E_{nr} = E_{ee} Q^{-1}\left(E_{nr}\right) \ , \tag{2.26}$$

where $Q\left(E_{nr}\right)$ is the quenching factor. This quantity has been introduced in 2.2.1, and depends on the material.

For the CDMSLite experiment, we used the same quenching factor used by the SuperCDMS collaboration in [27].[19] This quenching factor is:

$$Q(E_{nr}, A, Z) = \frac{1 + \frac{e \times V_b}{\varepsilon_\gamma} Y\left(E_{nr}, A, Z\right)}{1 + \frac{e \times V_b}{\varepsilon_\gamma}} \ , \tag{2.28}$$

where e is the charge of the electron, V_b is the bias voltage applied between the two surfaces of the detector, and it was chosen to be $V_b = 69$ V (so $e \times V_b = 69$ eV), ε_γ is the average excitation energy per charge pair, and it takes the value $\varepsilon_\gamma = 3$ eV in Ge, and $Y\left(E_{nr}, A, Z\right)$ is the *ionization yield* (all these values are from [27]).

[19] Note that this choice is not the only possible one. For the same material (Ge) and experiment (CDMSLite) the authors of [26] use, for coherence with the analysis of the CoGeNT experiment, the quenching factor

$$Q_{Ge} = 0.2 E_{nr}^{0.12} \ . \tag{2.27}$$

The effects of changing the quenching factor are shown in Figure 4 of [27]. These effects mostly consist in a shift of the limit curve along the WIMP mass axis. Thus, for masses above ≈ 6 GeV/c^2, where the curve is relatively flat, the effect is rather small. On the other hand, for lighter WIMP masses the systematic uncertainty in yield produces a noticeable effect on the derived limits.

The ionization yield used in the CDMSLite analysis by the SuperCDMS collaboration is the one modeled by Lindhard, which reads

$$Y\left(E_{nr}, A, Z\right) = k\frac{g\left(\varepsilon\right)}{1+kg\left(\varepsilon\right)}\ , \tag{2.29}$$

where A is the mass number, Z the atomic number,

$$\begin{aligned} g\left(E_{nr}, Z\right) &= 3\varepsilon^{0.15} + 0.7\varepsilon^{0.6} + \varepsilon\ , \\ \varepsilon\left(E_{nr}, Z\right) &= 11.5\left(\frac{E_{nr}}{\text{keV}}\right)Z^{-\frac{7}{3}} \quad \text{and} \\ k\left(A, Z\right) &= 0.133Z^{2/3}A^{-0.5}. \end{aligned} \tag{2.30}$$

For a Ge target, this gives $k \approx 0.157$.

In the table below we report some quantities that are relevant for the CDMSLite analysis, with their values in keV_{ee}, and their conversions into keV_{nr} obtained using the quenching factor of equation (2.28) and that of CoGeNT.

	E_T	E_{max}	σ
Original value in keV_{ee}	0.170	7.00	0.014
Converted to keV_{nr} using (2.28)	0.8426	23.61	0.08746
Converted to keV_{nr} using (2.27)	0.8649	23.91	0.09308

Table 2.3: Some quantities that are relevant for the CDMSLite analysis, with their values in keV_{ee}, and their conversions into keV_{nr}. Note that also all the energies at which events occur had to be translated from keV_{ee} to keV_{nr}, but since there are 162 candidate events, we have not listed those values here.

2.5.8 CRESST-II

The cryogenic dark matter search *CRESST-II*, located at the Laboratori Nazionali del Gran Sasso (Italy), is an experiment which aims at detecting WIMPs via elastic scattering off nuclei in $CaWO_4$ crystals. Its most recent data analysis focused on low mass WIMPs can be found in [34]. The exposure (before cuts) is 29.35 $kg \times days$ and it has been collected in 2013.

The threshold energy is set at $E_T = 0.6$ keV, and the upper bound on the recoil energy of the analysis is set at 40 keV. All the events which fall into this recoil energy window, and which have a light yield below the center of the oxygen band (see figure 1 of [34]), are accepted as WIMP recoil candidates. This gives a number of candidate events which is 77. The energies of these events can be inferred from figure 1 of [34], with the help also of the histogram in the inset of figure 2 therein.

To obtain from CRESST-II the 90% C.L. upper limit on the WIMP parameter space for spin-independent WIMP-nucleon scattering, we used the maximum gap method [30], while the original analysis employs the optimum interval method.

Since three different target nuclei are present, to calculate the total rate we have used equation (2.8) with the weights of equation (2.9) being $h_{Ca} = 1/6$, $h_O = 4/6$ and $h_W = 1/6$. We took into account the energy resolution, which according to [34] is Gaussian with $\sigma = 0.107$ keV, and the experimental efficiency after cuts, which we obtain from the blue curve in figure 3 of [34] (where it is called "final nuclear recoil efficiency").

Experiment [reference]	Exposure (days × kg)	N_{obs}	Material	E_r range (keV)	E_1 (keV)	E_2 (keV)	90% CL up. lim. σ_{pSI} (cm^2 (GeV/c^2))	Tecnique	Background (events)
XENON10 (MGM) [28]	58.6×5.4	10	LXe	$4.5 - 26.9$	4.5	15.5	4.5×10^{-44} ($m_\chi^{min} \approx 30$)	sci/ion	$7.0 * *$
XENON100 (PL) [22]	224.6×34	2	LXe	$6.6 - 43.3$			2×10^{-45} ($m_\chi^{min} \approx 55$)	sci/ion	$1.0 * *$
XENON100 (MGM) [22]	2323.7	2	LXe	$6.6 - 30.5$	7.8	30.5	in agreement with PL		
CDMS II (OIM)* [23]	194.1	2	Ge	$10 - 100$	15.5	100	7.0×10^{-44} ($m_\chi^{min} \approx 70$)	pho/ion	$0.7 * *$
CDMS II (all data) [23]		2	Ge/Si				3.8×10^{-44} ($m_\chi^{min} \approx 70$)	pho/ion	
CDMS II (OIM) [53]	19.7	0	Si	$7 - 100$			1.7×10^{-41} ($m_\chi^{min} \approx 10$)	pho/ion	
CDMS II (OIM, all data) [**?**]	23.4	3	Si	$7 - 100$	12.3	100	2.4×10^{-41} ($m_\chi^{min} \approx 10$)	pho/ion	
SuperCDMS (OIM, low mass) [32]	577	11	Ge	$1.6 - 10$	$* * * *$	$* * * *$	1.2×10^{-42} ($m_\chi^{min} \approx 8$)	pho/ion	6.198
CDMSLite (OIM) [27]	10.3×0.6	162	Ge	$0.84 - 23.61 * **$		$* * * *$		pho/ion	
EDELWEISS-II (OIM) [33]	384	5	Ge	$20 - 200$	23.2	172	4.4×10^{-44} ($m_\chi^{min} \approx 85$)	ion/heat	$3 * *$
CRESST-II (OIM) [34]	29.35	77	$CaWO_4$	$0.6 - 40$	$* * * *$	$* * * *$		pho/sci	

Table 2.4: This table summarizes the information on the experiments described in this section, with particular emphasis on the quantities necessary to extract upper limits using the MGM. We also report the method of analysis originally employed by the experimental collaborations, together with the corresponding couple of values (σ_{pSI}, m_χ) that corresponds to the most severe exclusion. Some remarks are in order. *This analysis of CDMSII has been worked out with the latest data only, while the results of the analysis worked out combining all data are reported in the subsequent line of the table. **CDMSLite, SuperCDMS, CRESSTII, XENON10 and EDELWEISS-II specify that they employ no background subtraction in the reported analysis, which results in a more conservative exclusion curve. XENON100 and CDMS do not specify if they consider it or not in their analysis. To reproduce the limits coming from each experiment, we use the MGM with no background subtraction, which gives exclusion curves more conservatives than if we would have taken the expected background into account. ***Energies in the experimental papers are given in keV$_{ee}$, here we report the values converted in keV$_{nr}$, obtained as explained in the text. ****For these experiments, many events are present, and the energies corresponding to the boundaries of the maximum gap interval are different in different regions of the parameter space. The abbreviations used in this table stand for: MGM = Maximum Gap Method (Yellin, [30]), PL = Profile Likelihood, OIM = Optimum Interval Method (Yellin, [30]), sci = scintillation, ion = ionization, pho = phonons, LXe = Liquid Xenon.

2.6 The DAMA experiment

The DAMA experiment, located at the Gran Sasso National Laboratory (Italy), consists of 250 kg of radio pure NaI(Tl) scintillator. It has undergone two phases: DAMA/NaI between 1995 and 2003, and DAMA/LIBRA between 2003 and today.

The DAMA collaboration claims evidence for an annual modulation in the event rate (in the energy range from 2 to 6 keV_{ee}) of 8.9σ [54]. Such modulated signal is compatible with the one expected for WIMPs, that we have presented in section 1.7.

As we have seen, the main features expected for such a WIMP signal (in the absence of non thermalized components in the halo) are a modulation which follows a cosine function, with a period of one year and a phase around June the 2nd, and the modulation must be present only in a well-defined low energy range, where WIMPs can induce signals.[20] These features are clearly present in the DAMA signal, as we will see. In addition, the modulation amplitude of the rate of events in the region of maximal sensitivity has to be, as we have seen, of order $\sim 1\% - 10\%$ of the average rate in the same region. For the DAMA experiment, we can compare the modulation amplitude reported in figure 2.7 with the average rate reported in figure 2.8. It should be noticed that part of the rate in figure 2.8 is due to unknown background, while the modulation amplitude should not be affected by this background. Thus, the ratio between the amplitude of the modulation and the average rate in the DAMA experiment fulfill the above condition, but the presence of this unknown background makes difficult a more quantitative statement.

On the other hand, as we will see the interpretation of the DAMA signal as a spin-independent elastic scattering of WIMPs off nuclei is in contrast with the interpretation of the results of many of the most recent experiments described in the previous section, as it is evident from figure 2.5.[21]

A recent review of the experiment can be found in [54]. We based our reconstruction of the model independent interpretation of the DAMA results mainly on the strategy employed by [55],[22] which is based on data that can be found for instance in [56]. Similar or alternative approaches can be found in the literature,

[20] Moreover, the modulation must be present only in "single hit" events, i.e. those events for which only a single detector, among all the available ones in the experimental setup, "fires", because in fact the probability for a single WIMP of interacting more than once in the same experiment is negligible.

[21] Of course, spin-dependent interpretations can be considered, or even more general approaches, in which cases it is sometimes possible for the tension to be mitigated, see for instance [25], which anyway was published before some of the experimental results leading to the most constraining limits presented in this chapter.

[22] However, as we will discuss later the fractions of channeled events employed in [55] have been superseeded by most recent estimates, which basically imply that channeling for the DAMA experiment is negligible. We thus reproduce the DAMA analysis using the procedure of [55] but neglectin the channelling. How the channeling is implemented in [55] is discussed in section 2.6.2 and we recompute the corresponding DAMA regions and provide the best fit values in section 2.6.4. We compare these DAMA regions obtained with the old fractions of channeling with those resulting from neglecting channeling in figure 2.9.

for instance in [57].

In this section we review the main results of the DAMA experiment and we present the strategy that we employ to provide the interpretation of these results in terms of spin-independent elastic scattering of WIMPs off nuclei, based on a χ^2 analysis, that we show in figure 2.5. We also discuss the issues of quenching, channeling and energy resolution related to the DAMA experiment. We finally present how to derive (following [55]) an upper limit on σ_{pSI} (as a function of m_χ) from the DAMA data.

2.6.1 The annual modulation of the DAMA signal

The first phase of the DAMA experiment, DAMA/NaI, collected over six annual cycles a total exposure of 0.82 ton×year, while the second one, DAMA/LIBRA, collected over seven annual cycles a total exposure of 0.29 ton×year. Thus the total exposure collected by the DAMA experiment over 13 years was 1.17 ton×year, orders of magnitude bigger than the exposure usually collected in the field.

Figure 2.6 shows the time behavior of the experimental residual rate (residual means that the average over time of the signal is subtracted from the total signal, so that only the modulated part of the signal is left) of the single-hit[23] events collected by DAMA/NaI and DAMA/LIBRA in the energy range from 2 to 6 keV$_{ee}$. The experimental data are taken from Fig.1 of [54].

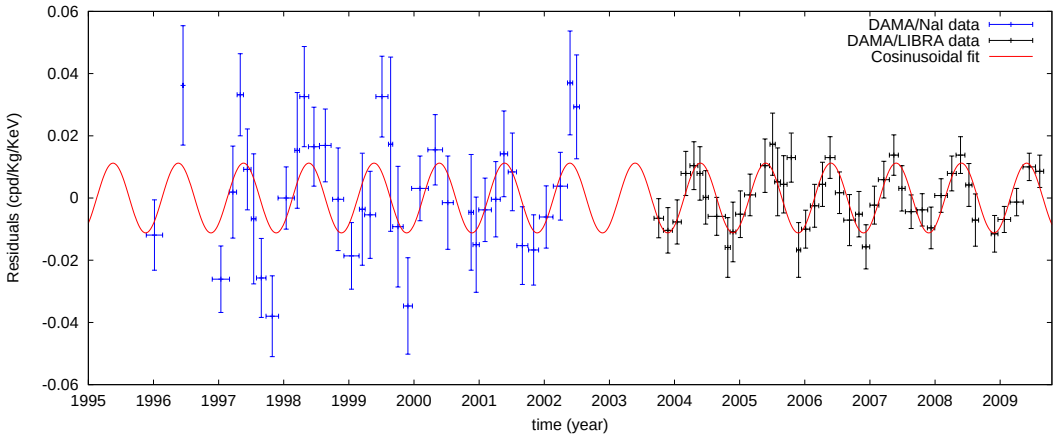

Figure 2.6: The time behavior of the experimental residual rates of the single-hit events collected by DAMA/NaI and DAMA/LIBRA in the energy range from 2 to 6 keV$_{ee}$. The experimental data are taken from figure 1 of [54]. The superimposed curve shows a cosinusoidal fit to the data, described in the text. The ticks on the horizontal axis are placed at the 1st of January of the corresponding year.

The curve superimposed represents the result obtained by fitting a cosinusoidal

[23]In DMDD only single-hit events are considered, i.e. those for which only one single detector among the many presents in an experiment "triggers", because the probability for a WIMP to experience multiple interactions is negligible.

function

$$f(t) = A\cos\left[2\pi\left(t - t_0\right)/T\right] \tag{2.31}$$

to the data (relative to the 13 annual cycles), using as free parameters A, t_0 and T. Doing the fit, we have obtained as final values of the parameters an amplitude of $A = (0.0112 \pm 0.0012)$ day^{-1} kg^{-1} keV^{-1} (sometimes reported as cpd/kg/keV, where cpd means counts per day), a period of $T = (365.7 \pm 1.8)$ days and a phase of $t_0 = (138 \pm 20)$ days (from January the 1st). We obtain a chi square of $\chi^2 = 64.3$ with a number of degrees of freedom[24] $d.o.f. = 77$, thus giving a reduced chi square of $\chi^2/d.o.f. = 0.83$ (which means that the model used to fit the data can be accepted).

The fit was originally performed in [54], with the result $A = (0.0116 \pm 0.0013)$ day^{-1} kg^{-1} keV^{-1}, $T = (0.999 \pm 0.002)$ yr and $t_0 = (146 \pm 7)$ days, which signs the presence of a modulated signal at the level of 8.9σ [54].

We remark that both fits are compatible within errors with the characteristics of the modulated signal expected for WIMPs, which has $T = 365.25$ days and $t_0 = 152$ days as we have seen in section 1.6.3.

2.6.2 Quenching and channeling in DAMA

In the DAMA experiment, in addition to the effect of quenching, one can also take into account that of channeling. Including this effect in the interpretation of the DAMA results has received particular attention in the past, mainly in relation with attempts of mitigating the tension between these results and those of other direct detection experiments. Nevertheless, the recent results of [58] imply that the fraction of channeling is much smaller than assumed previously (for instance in [55], on which our procedure is based), and thus it is practically negligible in the analysis of the DAMA results.[25] For completeness in this section we explain how the channeling effect can be taken into account, but we neglect it in producing figures

[24] The number of 77 $d.o.f.$ is obtained subtracting the number of fitting parameters equal to 3 from the total number of data points, 80.

[25] In [58] the fraction of channeled recoiling ions in NaI(Tl) crystals is studied using analytical models related to Lindhard theory. The channeling of lattice ions recoiling after a collision with a WIMP is found to be very different (in particular, the fraction is smaller) from the channeling of incident ions. This is the reason because of the old estimates of the channeling fraction for the DAMA experiment, presented in the reminder of this section, are ways larger than those of [58]: they apply to atoms which start their motion close to the middle of a channel, but not to the case of lattice ions recoiling after a collision with a WIMP, which is the one relevant for DMDD. Moreover, in [58] the fractions for lattice ions are found to be function not only of the recoil energy, but also of the temperature. The nuclei ejected from their lattice sites by a WIMP are initially part of a row or plane so they start from or very close to lattice sites, thus blocking effects are important and the probability for them of being channeled would be zero. Nevertheless, any departure of the actual lattice from a perfect one due to vibrations of the atom allow for some of the recoiling lattice nuclei to be channeled, because ibrations displace them from the lattice sites. Vibrations are related to the temperature, which explains way the channeling fraction of recoiling ions is very temperature dependent. [58] provides upper limits on the channeling fractions for NaI crystals, for instance in their figure 14.

2.5, 2.7 and 2.8. In figure 2.9 we show the difference between the interpretation of the DAMA results obtained by considering the recent estimates of the channeling in NaI christals (thus practically neglecting it, i.e. setting $f_{Na}(E_r) \approx f_I(E_r) \approx 0$ in equation (2.32)) and that obtained by considering the old values described in this section. More details will be provided at the end of section 2.6.4, but let us anticipate that the results of [58] move the DAMA region at low WIMP masses to cross sections larger by an order of magnitude.

For what concerns the quenching, while the recoiling nucleus loses its energy both via electromagnetic interactions and via nuclear force interactions, the detector measures scintillation light, which comes mainly from the electromagnetic part. So as for (2.1), the observed energy E_{obs} (in keV_{ee}) is smaller than the actual energy E_r (in keV_{nr}) by a factor Q, that for the elements used in the DAMA experiment is respectively $Q_{Na} = 0.3$ and $Q_I = 0.09$ (see for instance [55]).

Because of the crystalline structure of the target, for certain angles and energies of the particles no nuclear force interaction takes place, and the entire energy is lost electromagnetically. These are the so-called channeled events, for which $Q \approx 1$. For the fraction of channeled events in the DAMA experiment, in the past the parameterization e.g. of [55] has been used:

$$f_{Na}(E_r) \approx \frac{\exp(-E_r/18)}{1+0.75E_r} \qquad \text{and} \qquad f_I(E_r) \approx \frac{\exp(-E_r/40)}{1+0.65E_r} \ , \tag{2.32}$$

where E_r is meant in keV_{nr}. This parameterization has been obtained in [55] by fitting figure 4 of [59].

Using the above equations together with equations (2.1), (2.9) and (2.8),[26] we can now write the differential event rate expected for the DAMA experiment as

$$\frac{dR}{dE_r}^{DAMA}(E_{obs}) = \tag{2.33}$$
$$= \sum_{i=Na,I} \frac{m_i}{m_{Na}+m_I} \left\{ \left[1 - f_i(E_{obs}/Q_i)\right] \frac{1}{Q_i} \frac{dR_i}{dE_r}(E_{obs}/Q_i) + f_i(E_{obs}) \frac{dR_i}{dE_r}(E_{obs}) \right\} \ ,$$

where the first term corresponds to quenched events and the second to channeled (so unquenched) ones.

2.6.3 The DAMA energy resolution

To obtain the actual event rate, we still need to take into account the energy resolution of the DAMA experiment, that can be introduced as in equation (2.4), where we are directly computing the total event rate. The total event rate for the i-th energy bin $\left[E_i^+, E_i^-\right]$ centered around the observed energy E_i (and of width

[26] Note that equation (2.8) holds not only for the total event rate, but also for the differential event rate.

ΔE_i), can thus be written as:[27]

$$R^{DAMA}_{[E_i^+,E_i^-]}(t) = \int_0^\infty dE \frac{dR}{dE}(E,t) \int_{E_i^+}^{E_i^-} dE' G(E,E') \ . \tag{2.34}$$

We assume for DAMA a Gaussian energy resolution of the type of (2.5), with energy dependent standard deviation

$$\sigma^{DAMA}(E) = 0.45\sqrt{E/\text{keV}_{ee}} + 0.0091\,(E/\text{keV}_{ee}) \tag{2.35}$$

as in [55].

In our numerical implementation we have taken this energy resolution into account using the energy response function of (2.7).

2.6.4 Fitting the DAMA spectral data

As we have seen in section 1.7.3, the differential event rate can be approximated as in equation (1.103) with a part which is time-independent, plus a part which presents a cosinusoidal variation with time. So, for the model independent analysis of DAMA, the DAMA signal as a function of energy and time can be parametrized as:[28]

$$S(E,t) = S_0(E) + A(E)\cos\left[\frac{2\pi}{T}(t-t_0)\right] \ , \tag{2.36}$$

where $S_0(E)$ is the part of the signal which do not depend on time, $A(E)$ is the amplitude of the modulation, T its period, t_0 its phase, and t is time measured in days from the beginning of the year. Since we are going to provide an interpretation of the DAMA data in terms of WIMPs scattering off nuclei, we assume $T = 1$ year and $t_0 = 152$ days which is what you would expect for WIMPs. As we can see these values are compatible, within errors, with those obtained from the fits in section 2.6.1 to the residual rate measured by the DAMA experiment.

For our analysis we consider the data on the modulation amplitude $A(E)$ relative to the DAMA exposure (first results of DAMA/NaI combined with the final results of DAMA/LIBRA), provided in figure 9 of [56]. In the original DAMA data analysis a software energy threshold of $E_T = 2$ keV$_{ee}$ is considered (see for instance [54]), the above data extend up to $E_{max} = 20$ keV$_{ee}$ and they are presented in $N^{DAMA}_{bins} = 36$ bins of width $\Delta E = 0.5$ keV$_{ee}$ each. We indicate them as A_i^{obs}, where the index i runs over the number of bins, from 1 to N^{DAMA}_{bins}.

For every point of the parameter space σ_{pSI},m_χ the predicted amplitude of the modulation of the scattering rate can be computed as

$$A_i^{pred}(m_\chi, \sigma_{pSI}) \doteq \frac{1}{2\Delta E}\left(R^{DAMA}_{[E_i,E_i+\Delta E]}(t=152) - R^{DAMA}_{[E_i,E_i+\Delta E]}(t=335)\right) \ , \tag{2.37}$$

[27] Note that in this section, to avoid heavy notation, we drop the subscript for observed energies, thus using E instead of E_{obs}.

[28] Note that this corresponds to a differential event rate, not to a total event rate.

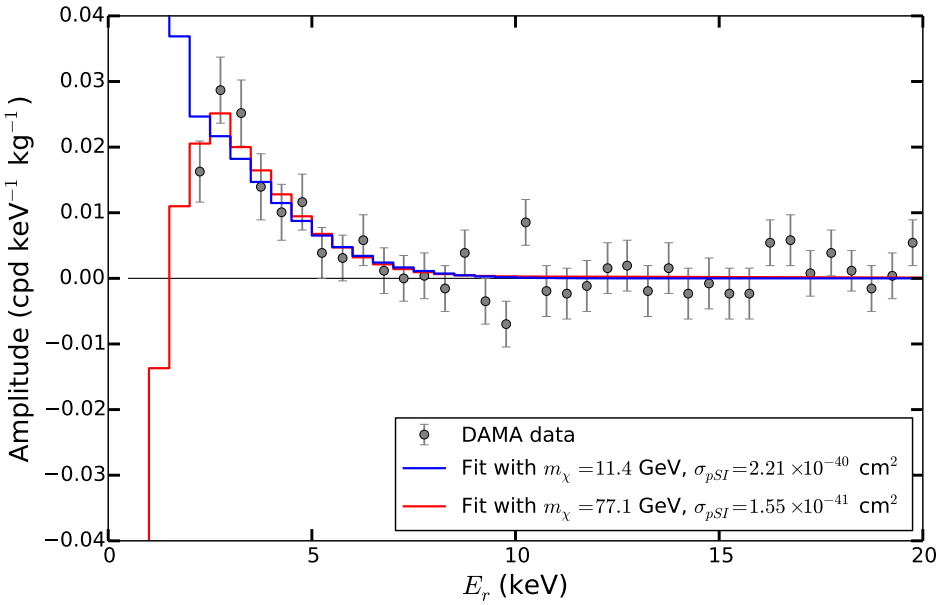

Figure 2.7: The plot shows the data on the modulation amplitude $A(E)$ relative to the DAMA exposure (DAMA/NaI and DAMA/LIBRA) provided in figure 9 of [56]. Superimposed are the two best fitting modulation amplitudes, computed as explained in the text, i.e. the two modulation amplitudes corresponding to the points in the parameter space m_χ, σ_{pSI} which provide the two minima of the χ^2. We recall that the point corresponding to the red curve is already excluded by the constraint obtained from the DAMA data on the average rate, as explained in the text. Due mainly to the presence of two target nuclei and of the channeling effect, the shape of the fitted modulation amplitudes is more complex than the simple one shown for illustration in figure 1.11 (and moreover here we are computing it for each bin of energy used to bin the data). We can see from this figure that only one of the two fitted curves present a phase inversion.

with $R^{DAMA}_{[E_i^+, E_i^-]}(t)$ given by equation (2.34).

To compare the theoretical prediction with the data, a χ^2 function can be used, because as stated by [55] the A_i^{obs} can be considered Gaussianly distributed. It reads:

$$\chi^2_{DAMA}(m_\chi, \sigma_{pSI}) = \sum_{i=1}^{N_{bins}^{DAMA}} \left(\frac{\left(A_i^{pred}(m_\chi, \sigma_{pSI}) - A_i^{obs} \right)}{\sigma_i^{obs}} \right)^2 , \tag{2.38}$$

where $A_i^{pred}(m_\chi, \sigma_{pSI})$ is the predicted amplitude of the modulation of the energy dependent signal in the i-th bin (given a point in the plane σ_{pSI}, m_χ), A_i^{obs} is the amplitude observed by the actual experiment for the i-th bin, and σ_i^{obs} is the associated error (standard deviation).

We thus compute the χ^2 for every point of the parameter space σ_{pSI}, m_χ identifying the points where it presents a local or global minimum χ^2_{min} (i.e. we minimize the χ^2), and we select allowed regions by looking for the contours

corresponding to $\chi^2(\sigma_{pSI}, m_\chi) = \chi^2_{min} + \Delta\chi^2(CL)$, where $\Delta\chi^2(CL)$ is evaluated for 2 degrees of freedom. In particular as in [55] we select the levels corresponding to 90% CL and to 3σ (i.e. 99.73% CL), which for 2 degrees of freedom correspond to $\Delta\chi^2(90\%) = 4.6$ and $\Delta\chi^2(99.73\%) = 11.8$.

We obtain (neglecting channeling) two minima that are shown together with the associated contours in figure 2.5, assuming for the analysis the SHM. We obtain a first minimum at the point $m_\chi = 11.35$ GeV, $\sigma_{pSI} = 2.2 \times 10^{-40}$ cm^2 corresponding to the value $\chi^2_{min} = 33.2$, and a second minimum at the point $m_\chi = 77.2$ GeV, $\sigma_{pSI} = 1.55 \times 10^{-41}$ cm^2 corresponding to $\chi^2_{min} = 28.5$, for 34 degrees of freedom (the number of d.o.f. being given by N^{DAMA}_{bins} minus the number of free parameters). Let us remark that the major part of the 99.73% CL region around the second minimum, including the best fit point, is excluded by the DAMA data presented in the following section.[29]

To test our code w.r.t. values found in literature, and for the comparison shown in figure 2.9, we computed also the best fit points (and the corresponding regions) corresponding to the outdated values for the channeling effect presented in section 2.6.2. They are a first minimum at the point $m_\chi = 12.1$ GeV, $\sigma_{pSI} = 1.26 \times 10^{-41}$ cm^2 corresponding to the value $\chi^2_{min} = 33.3$, and a second minimum at the point $m_\chi = 77.9$ GeV, $\sigma_{pSI} = 2.31 \times 10^{-41}$ cm^2 corresponding to $\chi^2_{min} = 26.5$, for 34 degrees of freedom.[30]

Figure **??** shows the comparison between the DAMA regions obtained by neglecting the channeling (as suggested by the recent estimates of this effect) and those obtained using the out-dated values for the channeling that we presented in section 2.6.2. As we can see from the figure and from the above mentioned values of the best fit points, the low mass region for DAMA corresponding to the old values for the channelling is located at cross sections about a factor ten smaller than those corresponding to the recent estimates of this effect. The second region is just slightly affected, and the significance of the fit (provided by the values of the chi square quoted above) does not change significantly.

[29] The best fit points and the corresponding regions we obtained are quite similar to those that can be found in the recent literature, e.g. [60].

[30] The values that we obtain for the first minimum are very similar to those obtained by [55], which found $m_\chi = 12$ GeV and $\sigma_{pSI} = 1.3 \times 10^{-41}$ cm^2 with $\chi^2_{min} = 36.8$. We cannot directly compare the values we obtain for the second minimum with those of [55], because therein the second minimum is obtained after excluding part of the parameter space using the DAMA data in the way explained in the following section. We report instead the values we get for the second minimum without taking these additional constraint into account. The second minimum we report is thus excluded by the constraint from DAMA, so we report it only for the sake of illustration. Note however that the value we found for this second minimum is similar to the one in table IV of [25], which employs anyway different assumptions, for instance for the parameterization of the fraction of channeled and quenched events.

2.6.5 Constraints from DAMA

Here we follow again the strategy of [55]. The constant part of the detected spectrum $S_0(E)$ (see equation (2.36)) should consist of the time average $\left\langle \frac{dR}{dE}(E) \right\rangle$ of the differential event rate plus an unknown background $BG(E)$, so it can be written as

$$S_0(E) = \left\langle \frac{dR}{dE}(E) \right\rangle + BG(E) \ . \tag{2.39}$$

For any given WIMP model, the annual modulation amplitude $A(E)$ and the averaged differential rate $\left\langle \frac{dR}{dE}(E) \right\rangle$ are not independent. The latter can be computed using (2.34), and for every energy bin it is given by

$$\left\langle \frac{dR}{dE}(E) \right\rangle = \frac{1}{2\Delta E_{cons}} \left(R^{DAMA}_{[E_j, E_j+\Delta E_{cons}]}(t=152) + R^{DAMA}_{[E_j, E_j+\Delta E_{cons}]}(t=335) \right) \ . \tag{2.40}$$

This additional information can be taken into account by using the figure 1 of [56] which shows precisely the signal $S_0(E)$ in 32 bins of width $\Delta E_{cons} = 0.25$ keV$_{ee}$ in the energy range from 2 keV$_{ee}$ to 10 keV$_{ee}$, as measured by the DAMA/LIBRA detectors.

For each value of m_χ we increase σ_{pSI}, computing for every value of σ_{pSI} the expected signal from WIMPs $\left\langle \frac{dR}{dE}(E) \right\rangle$ in each of these energy bins. Whenever $\left\langle \frac{dR}{dE}(E) \right\rangle$ exceeds the observed rate in at least one of the bins, that particular value of (m_χ, σ_{pSI}) is not consistent with the data and has to be excluded. All the values corresponding to the same m_χ and higher σ_{pSI} will provide higher values too, and so can be excluded as well. The exclusion curve that we obtain is plotted in figure 2.5 and clearly exclude the DAMA best fit point at high masses.

2.7 Current and future experiments and expected sensitivities

At the moment, in almost all the mass range apart from low WIMP masses, LUX is the most constraining experiment (in particular, LUX puts the stronger limit from ≈ 6 GeV, value below which the low mass analysis of SuperCDMS is more constraining, up to 5 TeV, where the published LUX limit of [24] ends). The low WIMP mass region is instead dominated by the limits of CRESSTII, CDMSLite and SuperCDMS. Anyway, since many experiments are currently analyzing data, taking data or are under development, the situation is constantly evolving. Some of the experiments described in this chapter are still running, for instance XENON100, LUX, SuperCMDS, EDELWEISS. Several large-scale direct detection experiments are in their planning phase and will start science runs within this decade. A recent review of the current status and perspectives of experiments employing noble gases can be found for instance in [61] or in [62]. Let us remark that so many direct

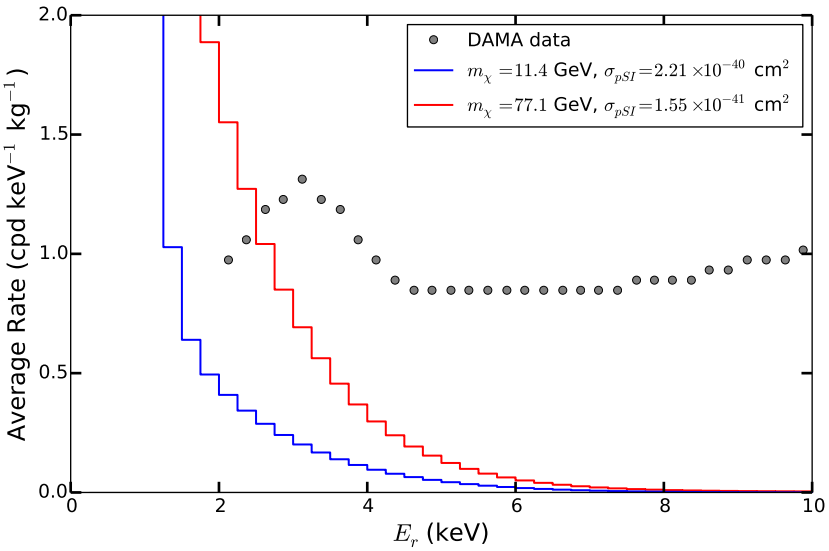

Figure 2.8: We report the average rate measured by the DAMA experiment, as a function of the recoil energy. The data are those from figure 1 of [56]. Superimposed are the two curves representing the average rate (computed as explained in the text) associated to the points in the parameter space m_χ, σ_{pSI} which provide the two minima of the χ^2. We recall that the data points are supposed to come from the signal plus an unknown background, while the superimposed curves are those that would be originated from WIMPs only. As we can see, the average rate represented by the red curve exceed the observed rate in the DAMA experiment (the gray points in the plot), so the associated best fit point is already excluded (see discussion in the text).

detection experiments exist or are planned, that reviewing them all is behind the scope of this work. Here we thus provide only an incomplete presentation of some of these experiments.

The LUX experiment will continue throughout 2015 to take data which will allow it to reach its sensitivity goal with a blinded 300 live-days search [24]. The next phase in the LUX program is called LUX-ZEPLIN and foresees a 7 ton liquid xenon detector. Operation is expected to start in 2016, with the goal of reaching a sensitivity of 2×10^{-48} cm^2 after three years of data taking ([63]).

The next step of the XENON program is called XENON1T and plan to employ an active mass of ≈ 2 tons of xenon. The underground construction of this new phase started in 2013, completion and commissioning are expected for 2015. After two years of continuous data taking, a sensitivity of 2×10^{-47} cm^2 is expected. The upgrade of XENON1T, XENONnT, has the goal of improving the sensitivity of another order of magnitude, thus reaching 2×10^{-48} cm^2.

The SuperCDMS experiment is currently taking data. The next phase of the project is called the SuperCDMS SNOLAB [64], based on a 110 kg target. The baseline design calls for a combination of germanium and silicone detectors that would be operated in both the standard SuperCDMS mode and the new CDMSLite

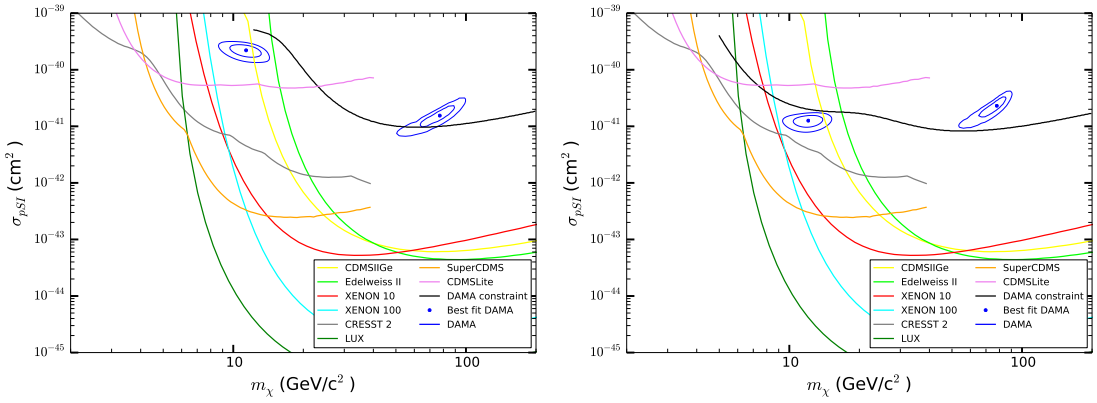

Figure 2.9: We compare the DAMA regions obtained by neglecting the channeling (as suggested by the recent estimates of this effect quoted in the text), on the left panel, with those obtained using the out-dated values for the channeling that we presented in section 2.6.2, on the right panel. As we can see the low mass region for DAMA corresponding to the old values for the channelling is located at cross sections about a factor ten smaller than those corresponding to the recent estimates of this effect (practically implemented by negleting it). This is particularly important because channeling has in the past been invoked to mitigate the tension between the DAMA regions (in particular the low WIMP mass one) and the limits set by other experiments, and due to the above mentioned recent estimates thit role for the channeling effect is even less appropriate nowadays, as it is clear from the figure. The values corresponding to the best fit points shown in the figures are specified at the end of section 2.6.4.

mode.

The next phase of the EDELWEISS project is called EDELWEISS-III, a 24 kg fiducial mass experiment, that has now started to take data. In 2012 and 2013, a substantial upgrade of the setup was undertaken to significantly improve the sensitivity. Several improvements have been made over EDELWEISS-II including a lower detector threshold and an improved energy resolution. Special attention was made to reduce backgrounds through additional shielding and improved radiopurity in several detector components. Finally, improvements are also being made in the discrimination of background events, including surface events. The EDELWEISS-III setup, its physics prospects and first data recorded are described in [65].

DarkSide-50 is a dual-phase argon detector employing 50 kg of active mass, developed inside the Borexino Counting Test facility at the Laboratori Nazionali del Gran Sasso. the collaboration has recently presented results of a run with natural argon. The projected sensitivity considering an energy threshold of 35 keV$_{nr}$ and a data taking period of 3 years is $\approx 10^{-45}$ cm^2 for a 100 GeV WIMP. The DarkSide collaboration plans a 5 ton liquid argon dual-phase detector, with 3.3 tons as active target mass, with an aimed sensitivity of 10^{-47} cm^2.

The DARk matter WImp search with noble liquids (DARWIN) [66] is an initiative to build an ultimate, multi-ton dark matter detector at the Laboratori

Nazionali del Gran Sasso. Its primary goal is to probe the spin-independent WIMP-nucleon cross section down to the 10^{-49} cm^2 region for ≈ 50 GeV/c^2 WIMPs, so it aims at exploring the experimentally accessible parameter space, which will be finally limited by the irreducible neutrino backgrounds.[31]

[31] The effect of neutrino backgrounds on the discovery potential of WIMPs of DMDD experiments is explored in detail in [67].

CHAPTER 3

Galactic dynamics and the dark halo: from Milky Way mass models to the WIMPs phase space

Contents

3.1 Introduction

In the previous chapters we have been looking in detail at how experiments aim at detecting WIMPs via their scattering off nuclei. As we have seen, a lot of astrophysics enters the interpretation of the results of such experiments. In particular, we have seen that a crucial role is played by the velocity distribution of the dark matter, together with quantities like the local dark matter density $\varrho_\odot$, the Galactic escape speed v_{esc} at the position of the Sun and the velocity of the Sun in the Galactic frame.

In chapter 1 we have introduced them by explaining how and where we use them in direct detection, but without specifying the underlying theory from which they come from. If at that moment this choice appeared justified by the necessity of focusing first on the formalism of direct detection, which has provided the initial motivation for this work, now the time has come to provide the theoretical framework on which these astrophysical quantities rely.

This chapter presents a review of the concepts of galactic dynamics that are relevant for the subject of this work. For a full guide to the subject, we refer the reader to the bible of that domain, [17], from which this chapter is inspired. Let us remark that, even if the majority of the laws, definitions, quantities and principles treated in this chapter hold (and are used) in general in the study not only of the Milky Way, but also and especially of any galaxy or cluster of galaxies, here we will obviously focus on their application to our own galaxy. Moreover, we will mostly introduce the physical concepts from the viewpoint of a dark matter particle hunter.

A top-down approach to the subject of galactic dynamics would have probably implied to start by introducing the phase-space distribution of stars, i.e. the distribution in the 6-dimensional space of position and velocity of the stars (which, if the system is not in a steady state, is a function also of time, so 7-dimensional), and deriving from that the spatial distribution and the velocity distributions. Though this approach is more elegant, we follow instead a bottom-up approach to the subject, having already introduced the velocity distribution and going now to introduce the spatial distribution. This is thought to be more suited to drive the reader from the issues concerning direct detection presented in the previous chapters, to the concepts of galactic dynamics described here.

We will start by discussing the mass distribution of the dark matter and of baryons inside the Milky Way, and the construction of mass models. Then we will

provide definitions and illustrations to quantities like the escape speed and the circular speed, assuming Newtonian dynamics. We will then discuss systems in equilibrium, the collisionless Boltzmann equation and the Jeans equations. The next section will be dedicated to an overview of the isothermal sphere, the mass distribution upon which the Maxwell-Boltzmann velocity distribution relies. We will then explain how in spherically symmetric systems the velocity distribution can be computed (under certain conditions) from the mass distribution, both for systems which are isotropic and for anisotropic ones.

3.2 The spatial distribution of mass in the Milky Way

The distribution of mass in the Milky Way is to a big extent still unknown. Stars and gas form the luminous band that we can see at night crossing the sky (we will refer to them as *baryons*), and in modern day standard cosmology this baryonic matter is tought to lie in a cold *dark matter halo*.

The baryons are mainly distributed inside a flattened structure, *the disk*, which contains the majority of the visible mass, and presents spiral arms and a central bar. A part of the baryons lies in a structure located at the center of the Galaxy and less extended than the disk, the *bulge*. The dark matter halo is instead considered to be rather spherical, even if a certain degree of triaxiality is probably present, and in addition substructures like subhaloes should be present (at least, if dark matter is made of WIMPs). Anyway, the structure of the dominant components, the baryonic disk and the dark matter halo, remains to some extent uncertain. More precisely, many reliable models exists, and there is a plethora of data that allows to describe the kinematics of stars in the Milky Way and to constrain the components, but how accurately depends on the physical quantity under scrutiny.

The majority of the mass is contained in the dark matter halo, observable only through its gravitational effect on the luminous components of the Galaxy.

In this chapter we deal with the issue of modeling the Milky Way. It is important to distinguish among three types of models of the Galaxy (see [68]): *mass models*, *kinematic models* and *dynamical models*. Mass models are the simplest ones and simply attempt to describe the density distribution of the various Galactic components, and thus the Galactic potential. Kinematic models describe the density and the velocity distributions of the luminous components of the Galaxy, but do not inspect if they are consistent with a steady state in any Galactic potential. Dynamical models describe systems which are in steady state in a given potential because their phase-space density depends only on integrals of motion.

In next section we deal with mass models only, while we will introduce the dynamics in the following sections. We start by presenting the most common density profiles that are used to describe the dark matter halo. We thus go on and present some interesting density profiles used to describe the baryonic content of

the Milky Way. Then, we discuss how a Milky Way mass model (MWMM) is built up.

3.2.1 The dark matter mass distribution in space

We are now going to introduce some of the most common density profiles used to describe dark matter halos. They span a wide range of shapes. Let us clarify one point about the terminology used, in relation with the behavior of such profiles toward the center of the halo. The two extremes are represented by the so called *core* or *cusp* behaviors. A cusped profile means one for which the density of matter increases as a power law when approaching the center (for instance the NFW profile), while a cored profile is one for which this power law behavior disappear at a certain distance when we approach the center of the halo (for instance the cored isothermal sphere) see figure 3.1.

The singular isothermal sphere profile

The *singular isothermal sphere* (SIS) profile is the simplest parameterization of the spatial distribution of matter in an astronomical system (e.g. galaxies, clusters of galaxies, etc.). It reads:

$$\varrho^{SIS}(r) \doteq \frac{\sigma^2}{2\pi G_N r^2} \ , \tag{3.1}$$

where r is the distance from the center of the sphere and σ^2 is the variance of the corresponding speed distribution, as we will see in section 3.4 where we will study this profile in more detail.

This profile represents one of the standard assumptions used in DMDD on which the Maxwell-Boltzmann velocity distribution for the dark matter relies, as we will see.

The cored isothermal sphere profile

One interesting variant of the singular isothermal sphere profile often considered in the literature is the *cored isothermal sphere*, which reads:

$$\varrho(r) = \varrho_s \frac{a^2 + r_s^2}{a^2 + r^2} \ , \tag{3.2}$$

where r_s is the *scale radius*, ϱ_s is the matter density at the position r_s, and a is a parameter which gives the radius of the transition between the inner part of the halo (the so called core), and the outer one. Clearly, the cored isothermal sphere profile tends toward the singular isothermal sphere profile when $a \ll r$. An example of a cored isothermal sphere profile is shown in figure 3.1.

The Navarro Frenk and White profile

The profile most commonly used to describe dark matter halos is the *Navarro Frenk and White density profile* (NFW hereafter). It was originally derived by analytically fitting N-body simulations (see [69]), and it is used to describe the DM halo of the Milky Way as well as the ones of other galaxies.

The NFW profile is the spherically symmetric density profile of the form (see for instance [69] or [70]):[1]

$$\varrho^{NFW}(r) = \frac{\delta_c \varrho_{crit}}{\frac{r}{r_s}\left(1+\frac{r}{r_s}\right)^2} , \tag{3.3}$$

where r is the *distance from the center of the system*, r_s is the *scale radius*, ϱ_{crit} is the *present critical density for closure of the universe*[2] and δ_c is the (adimensional) *characteristic density constrast*.

The scale radius is defined as

$$r_s \doteq \frac{r_v}{c_\Delta} , \tag{3.4}$$

where c_Δ is the (adimensional) *concentration parameter* and r_v is the *virial radius*. This quantity is defined as the distance from the center of the halo within which the mean density is Δ times the present critical density. The parameter Δ is called the *virial overdensity parameter*.[3]

The characteristic density contrast δ_c is related to the concentration parameter c_Δ by the above mentioned requirement that the mean density within r_v should be $\Delta\varrho_{crit}$,[4] so

$$\delta_c \doteq \frac{v c_\Delta^3 g(c_\Delta)}{3} , \tag{3.5}$$

where

$$g(c_\Delta) = \frac{1}{ln(1+c_\Delta) - c_\Delta/(1+c_\Delta)} . \tag{3.6}$$

In practice, the profile has only two free parameters: the scale radius r_s which determines its scale, and the concentration parameter c_Δ which describes its shape.[5]

[1] Note that often this profile is written in terms of the *scale density* $\varrho_s \doteq \delta_c \varrho_{crit}$, thus reading $\varrho(r) = \frac{\varrho_s}{\frac{r}{r_s}\left(1+\frac{r}{r_s}\right)^2}$.

[2] Remember that $\varrho_{crit} = \frac{3H^2}{8\pi G_N}$, where $H(z)$ is the *Hubble parameter*, for which at $z = 0$ (today) we will consider in the following chapter the same value used by [1] of $H = 73$ (km/s)/Mpc.

[3] Different choices of the value of Δ are possible; some values often used in the literature are 178, 200 (see for instance [17]) and 340 (which is not common, but it is used in the study [1] on which we will rely in the next chapter).

[4] This is equivalent to write that $\Delta\varrho_{crit} = M_{int}^{NFW}(r_v)/\frac{4}{3}\pi r_v^3$, which allows to demonstrate equation (3.5). Note that $M_{int}^{NFW}(r)$ is given in equation (A.1).

[5] The concentration parameter is a general structure parameter not necessarily restricted to the NFW profile. In cosmology, the concentration is related to the time of gravitational collapse, and a cosmological scenario is usually associated with a halo concentration-mass relation; small

Let us remark that the quantity Δ, necessary to define c_Δ, can be fixed freely, but then c_Δ should transform accordingly such that the profile remains unchanged, so Δ does not represent an additional degree of freedom.[6]

Some of the interesting astrophysical quantities that can be computed from the mass density can be obtained analytically for this profile. Their expressions are listed in appendix A. An example of a NFW profile is shown in figure 3.1.

The Zhao profile

The *Zhao profile* (or $\alpha\beta\gamma$ *profile*) reads:

$$\varrho^{\alpha\beta\gamma}(r) = \frac{\varrho_s}{(r/a)^\gamma \left[1 + (r/a)^\alpha\right]^{\frac{\beta-\gamma}{\alpha}}} \ , \tag{3.7}$$

where ϱ_s is the scale density and r_s the scale radius. The parameter γ gives the slope of the profile in the central region (i.e. at small r), β gives the slope of the profile in the outern region (i.e. at large r), and α specifies how fast the slope changes from γ to β. [7] It represents a generalization of the NFW profile of (3.3), which can be recovered with the choices: $(\alpha, \beta, \gamma) = (1, 3, 1)$. It can be used to describe cusp profiles (like the NFW) as well as cored profiles (obtained in general for $\gamma = 0$). In practice it provides a usefull way to parameterize many different profiles in one single equation.

The Einasto profile

The *Einasto* profile [72] reads:

$$\varrho^{Ein}(r) = \varrho_s \exp\left\{-\frac{2}{\alpha}\left[\left(\frac{r}{a}\right)^\alpha - 1\right]\right\} \ , \tag{3.8}$$

where ϱ_s is the scale density and a the scale radius. The parameter α controls the slope of the profile, which thus can be seen as a generalization of a power law (which has a constant slope on a log-log plot). Einasto's profile has the same form as Sersic's law, which is used to describe the surface brightness (i.e. the projected density) profile of galaxies.

For what concerns its use to describe dark matter, this profile seems to better catch the behavior of the dark matter profile of galaxies in N-body simulations w.r.t. broken power-law models like the NFW profile (with the same number of free parameters), see [73]. An example of an Einasto profile is shown in figure 3.1.

---

mass haloes are more concentrated because they typically collapse earlier than haloes of larger masses. These issues are discussed for instance in [71], where the dependence of the concentration parameter on mass of the halo, on redshift and on the environment (halos or subhaloes) is studied using cosmological simulations.

[6] Alternative choices of the two free parameters can be done, for instance r_v and r_s, or r_v and c_Δ. Moreover, if we write the profile in terms of the parameter ϱ_s we can use as free parameters the quantities r_s and ϱ_s, and in this case we do not need to define the concentration parameter so we do not need to fix Δ.

[7] Actually, β and γ are the slopes of the profile in a log-log plot.

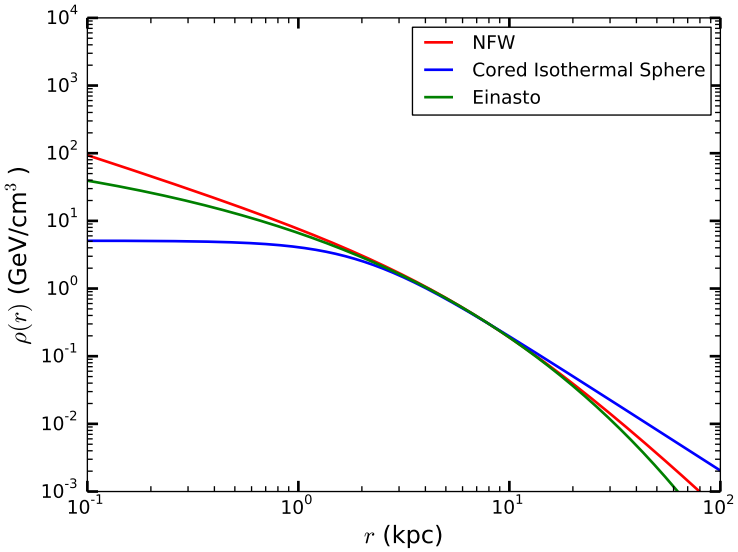

Figure 3.1: Different dark matter profiles, normalized such that they all provide the same value for the dark matter density at the position of the Sun, which we fixed at $\varrho_\odot = 0.3$ GeV/cm^3 (as in the SHM) at $r_\odot = 8$ kpc. They are an NFW profile (3.3) with $r_s = 8$ kpc and $\varrho_s = 1.2$ GeV/cm^3, a cored isothermal sphere (3.2) with $r_s = 8$ kpc, $a = 2$ kpc and $\varrho_s = 0.3$ GeV/cm^3, and an Einasto profile (3.8) with $a = 8$ kpc, $\alpha = 0.3$ and $\varrho_s = 0.3$ GeV/cm^3.

The Burkert profile

The *Burkert* profile [74] reads:

$$\varrho^{Bur}(r) = \frac{c}{(r+a)\,(a^2+r^2)}\ , \tag{3.9}$$

and it is motivated as a fit to observed rotation curves.

3.2.2 The baryons mass distribution in space

Usually, the baryonic content of the Galaxy is modeled by the superposition of different distinct components. In general at least an axisymmetric profile for the disk and a spherically symmetric profile for the bulge, located in the central part of the Galaxy and containing a smaller amount of mass than the disk, are used.[8]

In addition, other components can be taken into account. In particular, often two disks are used, a thin and a thick disk (as e.g. in [68]), and sometimes also a gaseous disk component (separated from the stellar disk). In addition, sometimes axisymmetric (as e.g. in [68]) or triaxial bulges (as e.g. in [75]) with a bar are

[8] This is the case for instance for the simple MWMM employed in [1], that we will use in chapter 4.

considered.[9]

For much of the information contained in this section, we rely on [17].

Stellar disk/s

Most of the stars in the Galaxy lie in a flattened, roughly axisymmetric structure known as the Galactic disk. The disk is a fundamental component of any mass model which aims at describing the Milky Way globally. On clear, dark nights the cumulative light of the faint stars of the disk is visible as a luminous band stretching across the sky, which is where the name Milky Way for our galaxy comes from.

Exponential Disk. Observations of other disk galaxies suggest that the surface brightness is approximatively an exponential function of R, and in the direction perpendicular to the Galactic plane the density of stars fall off exponentially. Thus, an axially symmetric density profile commonly employed in the description of the disk of the Milky Way (as for instance in [68], see also [17]) is the so called *exponential disk*. Its most common form is:

$$\varrho^{ED}(R,z) = \frac{M_d}{4\pi z_d R_d^2} \exp\left(-\frac{|z|}{z_d} - \frac{|R|}{R_d}\right) , \tag{3.10}$$

where M_d is the *total mass of the disk*, z_d is the *scale height* and R_d is the *scale lenght*.[10] In the above equation, z is the distance from the midplane.

The thin and thick disks of the Milky Way. Even if in simple models a single disk is taken into account, more complex ones consider (at least) two populations of stars, described by two different disks, a thin one, and a thick one. Even tough different density profiles for the disks exist, usually a double exponential profile (3.10) is considered for each of the disk components, thin and thick, as done for instance in [68]. The populations of stars described by the two different disks are different (see [17, sec. 1.1]). The stars of the thick disk are older and have a different chemical composition from those of the thin disk, to which the Sun belong. More precisely, the stars of the thick disk have lower metallicities, and for a given metallicity they have higher abundances of the α nuclides (^{16}O, ^{20}Ne, ^{24}Mg, ^{28}Si, etc.) w.r.t. ^{56}Fe (so the thick disk is said to be metal-poor), which are a signature of stars formed early in the history of the disk.

[9] Let us remark that, even if the real Galaxy has spiral arms, for certain purposes (e.g. the determination of quantities on which we are mainly interested in this work, like for instance the local Galactic escape speed) the mass modelling description discussed above is the most suitable one, so a spiral arm description will not be discussed here.

[10] A spherically symmetric approximation of this profile, which provides the same potential in the disk an thus is useful in DMDD related computations, can be found in [76]

Miyamoto-Nagai disk. This axisymmetric density profile can be found in [77], and is used to describe the disk of the Milky Way for instance in [1]. It has the form:

$$\varrho\left(R,z\right)=\frac{b^{2}M_{MN}}{4\pi}\frac{a_{MN}R^{2}+\left[a_{MN}+3\left(z^{2}+b_{MN}^{2}\right)^{1/2}\right]\left[a_{MN}+\left(z^{2}+b_{MN}^{2}\right)^{1/2}\right]^{2}}{\left[R^{2}+\left[a_{MN}+\left(z^{2}+b_{MN}^{2}\right)^{1/2}\right]^{2}\right]^{5/2}\left(z^{2}+b_{MN}^{2}\right)^{3/2}}\ , \tag{3.11}$$

where M_{MN} is the *total mass* of the system described by this profile, while a_{MN} and b_{MN} are non-zero parameters with the dimension of length. Depending on the choice of the parameters, the Miyamoto-Nagai profile can represent anything from an infinitesimally thin disk to a spherical system (see [17, sec. 2.3]). For instance, [78] employs a Miyamoto-Nagai profile to describe both the disk and the bulge.

Stellar bulge

In addition to the disks, the Galaxy contains a small, amorphous, stellar system, located at its center, thicker than the disk, and comprising the 15% of the total luminosity. The bulge stars are tought to date from near the time of formation of the Galaxy, while the stars of the disks have a wide range of ages (stars formation being an ongoing process in the disks). While the stars in the Solar neighborhood are found on nearly circular orbits, the velocity vectors of bulge stars are randomly oriented. In the therminology of statistical mechanics, where temperature is proportional to mean-square velocity, a stellar population like the disk in which the random velocities are much smaller then the mean velocity is said to be cold, while the bulge population, in which the random velocities are larger than the mean velocity, is said to be hot.

Hernqvist profile. This spherically symmetric density profile is presented in [79], and it has been used to describe the bulge of the Milky Way for instance in [1]. Its form is:

$$\varrho^{H}\left(r\right)=\frac{M_{H}}{2\pi}\frac{a_{H}}{r\left(r+a_{H}\right)^{3}}\ , \tag{3.12}$$

where M_H is the mass of the system described by this profile and a_H is the *scale length*. One of the nice features of this profile is that almost all of the interesting quantities that can be computed from the mass density can be obtained analytically. Some of them are listed in appendix A.

Oblate ellipsoidal bulge. The *oblate ellipsoidal bulge* is an axisymmetric density profile which can be used (as in [68]) to provide an approximated description of the stellar bulge of the Milky Way. Its form is:

$$\varrho^{OEB}\left(R,z\right)=\frac{\varrho_{b,0}}{\left(1+m/r_{0}\right)^{\alpha}}\exp\left[-\left(\frac{m}{r_{cut}}\right)^{2}\right]\ , \tag{3.13}$$

where, in cylindrical coordinates, $m \doteq \sqrt{R^2 + (z/q)^2}$, and q is the *axis ratio*. Note that because of its dependence on m only, this density profile is of the form associated with equation (A.10). The properties of oblate ellipsoidal bulges are described in details in appendix A. Let us remark that an alternative form for the stellar bulge, also of an oblate ellipsoidal shape, is presented in [17, sec. 2.7].

Triaxial bulge. Even if spherical (or axial) symmetry can be already a good approximation for the stellar bulge of the Milky Way, the Galactic bulge is actually triaxial. The lenghts of the two principal axes that lie in the Galactic plane are in the ratio 3:3:1, and the triaxial structure extends to about 3 kpc from the center. Its longest axis is inclined by about 20 degrees w.r.t. the line from the Sun to the Galactic center. An example of a triaxial profile for the bulge can be found in [80].

Density profile with a bar. Since the Galactic bulge is triaxial, it is also sometimes called "a bar", and thus the Milky Way is considered to be a barred galaxy. Roughly speaking, a bar is a higly elongated, rapidly rotating stellar system. A recent model for the Milky Way bar can be found in [78]. That work employs the well established bar model of [81], which contains both a bar and a spheroidal nucleus with a steep inner power low behavior and an exponential outern profile.

Gaseous disk

The gas component is sometimes omitted in making models of the Milky Way, but it is particularly relevant for MOND models, as those considered in [82]. A mass model for the gas in the Milky Way can be found in [83].

3.2.3 Mass models for the Milky Way

To describe an astrophysical system, like for instance a galaxy, a cluster of galaxies, the Milky Way, etc., as we already stated different types of models can be used. In this section we focus on the simplest type, i.e. (analytical or semi-analytical) mass models. A mass model is simply a model where we describe a system using a *density profile* $\varrho(\vec{x})$, i.e. a function which, for every point of the physical space, specifies the density of matter for every component of the system (dark matter, baryons,...).

The density profiles that we have seen up to now represent generic models that can be used to describe many different astrophysical systems, like clusters of galaxies, spheroidal galaxies, the different components of our own galaxy, etc. In this section, we aim at describing the mass distribution of the Milky Way, i.e. we consider Milky Way mass models.

A Milky Way mass model usually is obtained adding multiple profiles, each of them describing one component of the Milky Way. How many components one model takes into account, and which degree of symmetry every component

has, depends on the purpose for which one wants to use the MWMM, and on the accuracy with which one wants to describe the Galaxy.[11] In general, a Milky Way mass model can contain the following components: the stellar bulge, the stellar disk (possibly two components, thin and thick), the baryonic gas and the dark matter halo.[12] Anyway, usually simpler mass models are employed (depending on the purposes), which do not contain all of these components.

So, in general a MWMM could read:

$$\varrho^{MWMM}\left(\vec{r}\right) = \varrho^{DM}\left(\vec{r}\right) + \varrho^{Bulge}\left(\vec{r}\right) + \varrho^{ThinDisk}\left(R,z\right) + \varrho^{ThickDisk}\left(R,z\right) + \varrho^{Gas}\left(\vec{r}\right) \ , \tag{3.14}$$

where (R, ϑ, z) indicate cylindrical coordinates (so that $r = \sqrt{R^2 + z^2}$). Usually each of the above profiles will have a certain degree of symmetry, so they will not be all functions of $\vec{r}$.

From the density profile it is straightforward to derive, analytically or numerically, the gravitational potential $\Phi\left(\vec{r}\right)$ using equation (3.16) or equation (3.22), as will be explained in the next section.

Since the Newtonian gravitational potential is additive, we can calculate the potential of this system as the sum of the potentials of the individual terms. This gives:

$$\Phi^{MWMM}\left(\vec{r}\right) = \Phi^{DM}\left(\vec{r}\right) + \Phi^{Bulge}\left(\vec{r}\right) + \Phi^{ThinDisk}\left(R,z\right) + \Phi^{ThickDisk}\left(R,z\right) + \Phi^{Gas}\left(\vec{r}\right) \ , \tag{3.15}$$

where the individual potentials are those computed from the respective profiles.

In the next sections we will introduce some of the basic quantities related to the Galactic dynamics that are more relevant for this work. To illustrate[13] them, we will use two examples of MWMM. The first example that we will employ is inspired from [68] and based on a MWMM calibrated on recent data. The second one, taken from [1], is simpler and it is not meant to be a good Milky Way mass model, but we will show it mainly because we will employ it in the next chapter.

Mass model of the Galaxy from [68]

To illustrate the quantities introduced in the next sections, we will use a MWMM inspired from one calibrated on recent data, the best fit mass model determined in [68]. This model has been obtained by [68] with a Bayesian approach employed to take into account photometric and kinematic data. It contains a NFW dark matter

[11] For instance, a very simple mass model of the Milky Way can include a dark matter spherically symmetric halo, a spherically symmetric bulge and an axially symmetric disk, as it is the case for the mass model employed by [1], on which we will rely in chapter 4. Even though with a high degree of simplification, when constrained from observational kinematic data, such a simple model can already capture the main dynamical features of the Milky Way.

[12] Let us remark that sometimes also other components are considered, like for instance an hot gas halo.

[13] Let us remark that we produced the figures used to illustrate the next sections using analytic expressions where possible, and numerical computations otherwise.

spherically symmetric halo (3.3), combined with an axisymmetric baryonic bulge (the oblate ellipsoid provided in equation (3.13)) and two different populations of baryons in the disk, described through two different axisymmetric disks of different thickness, the thin disk and the thick disk, modeled with two exponential disks of the form (3.10).

The parameters of the model have the following values.[14] The NFW halo has $\varrho_s = 0.00846$ $\mathrm{M}_\odot$ pc^{-3} and $r_s = 20.2$ kpc. The oblate ellipsoidal bulge has $\varrho_0 = 95.6$ $\mathrm{M}_\odot$ pc^{-3}, $r_0 = 0.075$ kpc, $r_{cut} = 2.1$ kpc, $\alpha = 1.8$ and $q = 0.5$. The thick disk is an exponential disk with $R_d = 3.31$ kpc, $\Sigma_0 = 209.5$ $\mathrm{M}_\odot$ pc^{-2} (from which the total mass of the disk can be obtained as $M_d = 2\pi\Sigma_0 R_d^2$), and $z_d = 0.9$ kpc. The thin disk is an exponential disk with $R_d = 2.90$ kpc, $\Sigma_0 = 816.6$ $\mathrm{M}_\odot$ pc^{-2} and $z_d = 0.3$ kpc. These profiles, individaully and summed up to make the full MWMM, are shown in figure 3.2.

To compute the gravitational potential and related quantities shown in the illustrative plots, we neglect the axisymmetry of the bulge and use instead a spherical approximation (as done for instance in [82]) which gives the same run of mass with radius, and consists in substituting in equation (3.13) m/r_0 with $r/q^{1/3}r_0$ and m/r_{cut} with $r/q^{1/3}r_{cut}$. For the same purposes we represent each exponential disk by a spherical distribution (provided for instance in [76]) that approximates the mass and circular velocity of the exponential disk: $\Phi(r) = -M_d G_N \left[1 - \exp\left(-r/b\right)\right]/r$, with $b \doteq \sqrt{R_d^2 + z_d^2}$. Altough the Galactic disk is certainly flattened, this equation provides the same amount of mass interior to r as an exponential disk, and matches its circular speed with error no more than $\sim 15\%$ (see [17, sec. 2.6]). Anyway, we remark that these approximations are only employed in producing some of the figures used in the next sections, which have just an illustrative purpose.

Mass model of the Galaxy from [1]

In chapter 4 we will make use of the MWMM employed by [1], so in this chapter, together with the MWMM presented in the previous section, we show the behavior of the physical quantities introduced in the next sections also for this MWMM. Let us point out that this one is not meant to be a good Milky Way mass model, it was not calibrated for that. We mainly present it because we will use it in the next chapter. Anyway, even though with a high degree of simplification, when constrained from observational kinematic data, such a simple model can already capture the main dynamical features of the Milky Way.

The density profiles and the parameters for the baryonic components are fixed in [1], and we employ the values of the parameters of the dark matter halo corresponding to the best fit obtained therein. This MWMM employs a NFW profile (3.3) for the dark matter, an Hernquist profile (3.12) for the baryonic bulge, and a Miyamoto Nagai profile (3.11) for the baryonic disk.

[14] A more detailed discussion on the different estimates of the above quantities present in the literature and on the associated uncertanties will be done in chapter 5.

The NFW halo has $r_s = 7.8$ kpc and $\varrho_s = 1.92$ GeV/cm^3. The parameters of the baryonic components of the model have the following values, determined by [84]. The Hernqvist bulge has $a_H = 0.6$ kpc and $M_H = 1.5 \times 10^{10}$ M$_\odot$. The Miyamoto-Nagai disk has $a_{MN} = 4$ kpc, $b_{MN} = 0.3$ kpc and $M_{MN} = 5 \times 10^{10}$ M$_\odot$. These profiles, individaully and summed up to make the full MWMM, are shown in figure 3.2.

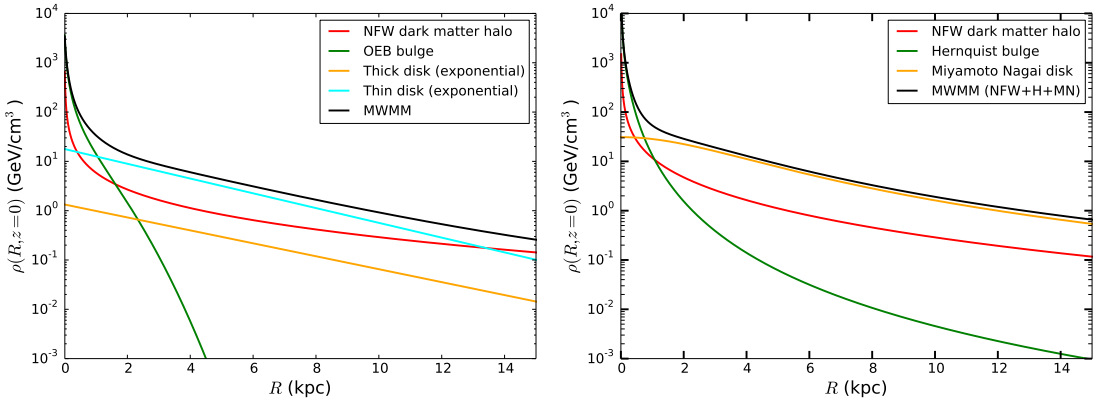

Figure 3.2: Density profiles (in the plane of the disk) for the Milky Way mass models that we use to illustrate this chapter, as a function of the cylindrical coordinate R. Left: MWMM from [68]. Right: MWMM from [1]. The different components of each MWMM are shown together with the total density of the model. The values of the parameters have been fixed as specified in the text, see section 3.2.3.

3.3 Galactic dynamics, the basic ingredients

A Milky Way mass model specifies the mass distribution of the various components of our Galaxy, dark matter and baryons, through the density of mass, and Poisson equation associates to this density the corresponding gravitational potential.

From the quantities above it is then possible to derive other useful quantities like the total mass contained in a sphere of a certain radius centered on the center of the system and, most important for DMDD, to define the escape speed from the system and the speed of a body on a circular orbit, as we are now going to see.

We report in appendix A the analytic expressions of the quantities defined below for some of the density profiles quoted above.

3.3.1 The gravitational potential and the internal mass

Following [17, sec 2.1] we define the *Newtonian gravitational potential* $\Phi(\vec{x})$ as

$$\Phi(\vec{x}) \doteq -G_N \int \frac{\varrho(\vec{x}')}{|\vec{x}' - \vec{x}|} d^3x' \ . \tag{3.16}$$

In Newtonian gravity, the density of mass $\varrho(\vec{x})$ of a system generates its gravitational potential $\Phi(\vec{x})$ as described by *Poisson's equation*:

$$\nabla^2\Phi(\vec{x}) = 4\pi G_N \varrho(\vec{x}) \ . \tag{3.17}$$

Poisson's equation is a differential equation which can be solved for $\Phi(\vec{x})$ given $\varrho(\vec{x})$ and an appropriate boundary condition. The boundary conditions to impose to Poisson equation depend on the physical system under study. For an isolated system the boundary condition is $\Phi \to 0$ as $|\vec{x}| \to \infty$.

The gravitational potential derives from the gravitational force $\vec{F}(\vec{x})$, acting on a point mass m situated at position $\vec{x}$, and generated by the Newtonian gravitational attraction of a distribution of mass $\varrho(\vec{x})$:

$$\vec{F}(\vec{x}) = -m\vec{\nabla}\Phi(\vec{x}) \ . \tag{3.18}$$

For spherically symmetric systems we have that $\varrho(\vec{x}) = \varrho(r)$, so $\Phi(\vec{x}) = \Phi(r)$, and thus[15]

$$\vec{F}(r) = -m\frac{d\Phi}{dr}\hat{e}_r = -G_N\frac{mM_{int}(r)}{r^2}\hat{e}_r \ , \tag{3.19}$$

where

$$M_{int}(r) \doteq \int d\Omega \int_0^r r'^2 dr' \varrho(r', \vartheta, \varphi) = 4\pi \int_0^r \varrho(r')\, r'^2 dr' \tag{3.20}$$

is the *mass interior to a radius r*. Using the second equality of (3.19), and recalling that (for an isolated system) the potential $\Phi(r)$ is assumed to be zero at infinity and negative otherwise, we can write

$$\Phi(r) = -\int_r^\infty dr' \frac{d\Phi}{dr'} = -\int_r^\infty dr' \frac{G_N M_{int}(r')}{r'^2} \ . \tag{3.21}$$

The interior masses associated to some dark matter profiles are reported in figure 3.3.

We can take the above equality (3.21) and insert the expression of $M_{int}(r)$, given in equation (3.20). We can integrate by parts the obtained expression, taking the derivative of $M_{int}(r)$ and the primitive of r^{-2}, and we thus obtain that the Newtonian potential arising from a spherically symmetric density profile $\varrho(r)$ can be written also as:

$$\Phi(r) = -4\pi G_N \left[\frac{1}{r}\int_0^r \varrho(r')\, r'^2 dr' + \int_r^\infty \varrho(r')\, r' dr'\right] \ , \tag{3.22}$$

which is found also in [17, pag. 36] and reflects the fact that the Newtonian gravitational potentials add linearly.

The gravitational potentials arising from such dark matter profiles are reported in figure 3.4. Those arising from the different components of the MWMMs introduced in section 3.2.3 are reported in figure 3.5.

[15] The second equality follows from Newton's second theorem, [17, pag. 34].

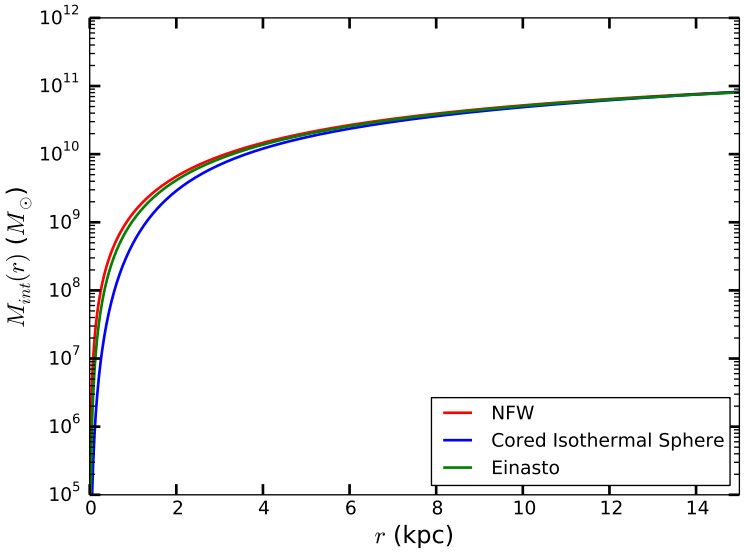

Figure 3.3: Examples of the mass interior to a certain radius r, as a function of r, for the dark matter halo profiles of figure 3.1. The different profiles are normalized such that they all provide the same value for the dark matter density at the position of the Sun, which we fixed at $\varrho_\odot = 0.3$ GeV/cm^3 (as in the SHM) at $r_\odot = 8$ kpc. The values of the parameters for each profile are specified in the caption of figure 3.1.

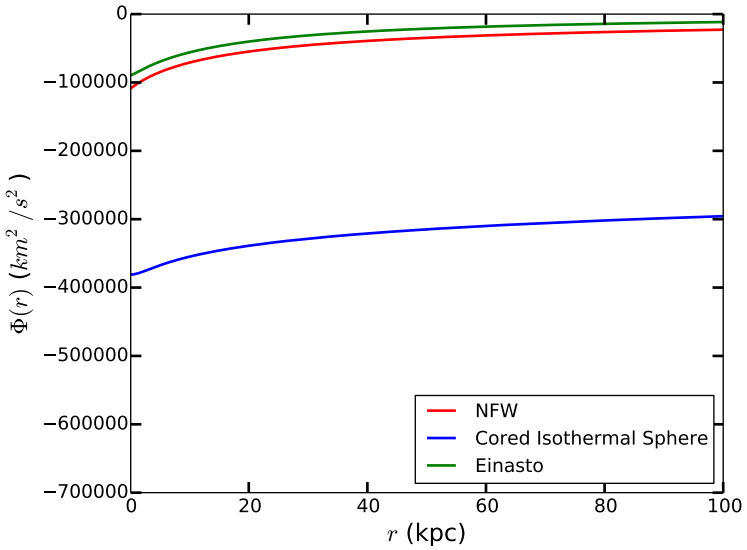

Figure 3.4: The gravitational potential of the dark matter halo profiles of figure 3.1. The different profiles are normalized such that they all provide the same value for the dark matter density at the position of the Sun, which we fixed at $\varrho_\odot = 0.3$ GeV/cm^3 (as in the SHM) at $r_\odot = 8$ kpc. The values of the parameters for each profile are specified in the caption of figure 3.1.

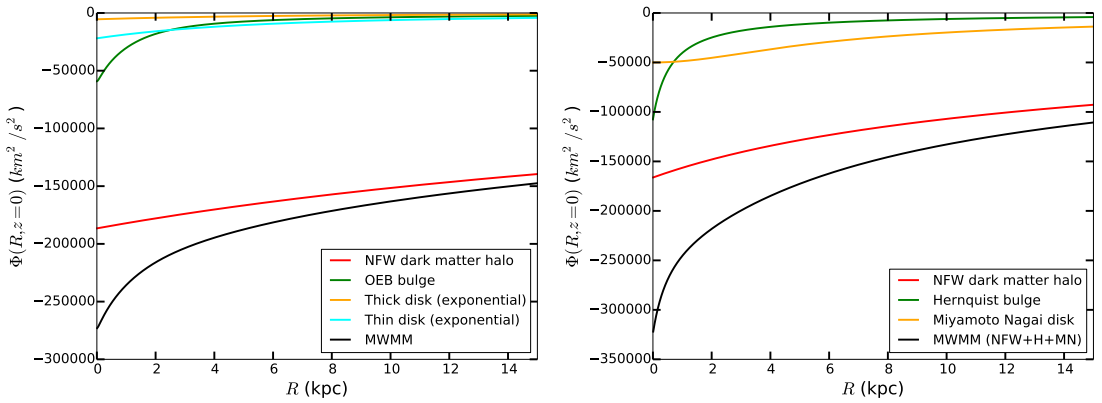

Figure 3.5: Gravitational potential (in the plane of the disk) for the Milky Way mass models that we use to illustrate this chapter, as a function of the cylindrical coordinate R. Left: MWMM from [68]. Right: MWMM from [1]. The different components of each MWMM are shown together with the total density of the model. The values of the parameters have been fixed as specified in the text, see section 3.2.3.

3.3.2 The circular speed

An important property of a spherical matter distribution, in particular in the light of the subject of this work, is its *circular speed* $v_c(r)$, which is defined as the speed of a test particle in a circular orbit at radius r and reads

$$v_c^2(r) \doteq r a_c = r\frac{\left|\vec{F}\right|}{m} = r\frac{d\Phi}{dr} = \frac{G_N M_{int}(r)}{r}\ , \tag{3.23}$$

where a_c is the *centripetal acceleration*, and we have used equation (3.19).

We now want to determine the speed of a body moving on a circular orbit in the axial plane of an axisymmetric system. Recalling that $\vec{F} = -\vec{\nabla}\Phi$, we can see that the square of this quantity is given by the radial component of the gravitational force multiplied by the distance from the center, i.e. for an axisymmetric system:

$$v_c^2(R, z=0) \doteq R a_c = R\frac{\left|\vec{F}_R\right|}{m} = R\left(\left|\frac{d\Phi(R,z)}{dR}\right|\right)_{z=0}\ , \tag{3.24}$$

where we have used cylindrical coordinates, which we indicate as (R, ϑ, z). The circular speed associated with some dark matter profiles is reported in figure 3.6.

The circular speed of a MWMM

We now want to calculate the circular speed of a body orbiting along a circular orbit in the plane of the disk of a mass model. We have already calculated the circular velocities for the three individual density profiles which compose it. From equation (3.24) we can easily see that the square of the circular velocity for any Milky Way

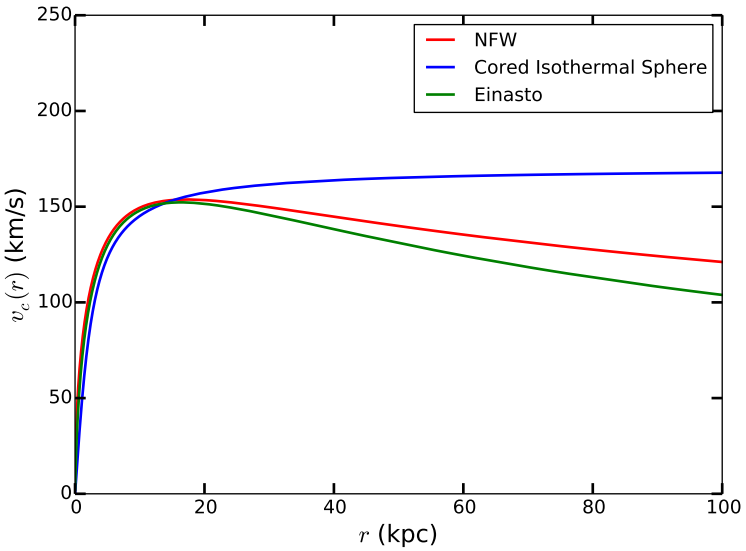

Figure 3.6: The circular speed of the dark matter halo profiles of figure 3.1. The different profiles are normalized such that they all provide the same value for the dark matter density at the position of the Sun, which we fixed at $\varrho_\odot = 0.3$ GeV/cm^3 (as in the SHM) at $r_\odot = 8$ kpc. The values of the parameters for each profile are specified in the caption of figure 3.1.

mass model will simply be the sum of the squares of the circular velocities of the individual components, so

$$\left(v_c^{MWMM}(R, z=0)\right)^2 = \left(v_c^{DM}(r)\right)^2 + \left(v_c^{Bulge}(r)\right)^2 + \left(v_c^{Disk}(R, z=0)\right)^2 , \quad (3.25)$$

with the addition of other components (e.g. a second disk or the gas) if present.

Figure 3.7 illustrates the contribution to the total circular speed of the different components of the two MWMMs presented in section 3.2.3.

3.3.3 The escape speed

For an object of mass m at a position r (for instance a star or a dark matter particle) in a spherically symmetric potential $\Phi(r)$ we can write the potential gravitational energy as $U(r) = m\Phi(r) < 0$, and the kinetic energy as $K(r) = \frac{1}{2}mv^2(r) > 0$. The object can escape the potential which is in only when its kinetic energy exceeds the module of its potential energy, i.e. when $v(r) \geqslant \sqrt{2|\Phi(r)|}$. So, following [17, sec. 2.2] we can define the *escape speed* $v_{esc}(r)$ as

$$v_{esc}(r) \doteq \sqrt{2|\Phi(r)|} , \quad (3.26)$$

i.e. as the minimum velocity that an object need to have in order to be able to escape the gravitational potential represented by $\Phi(r)$.

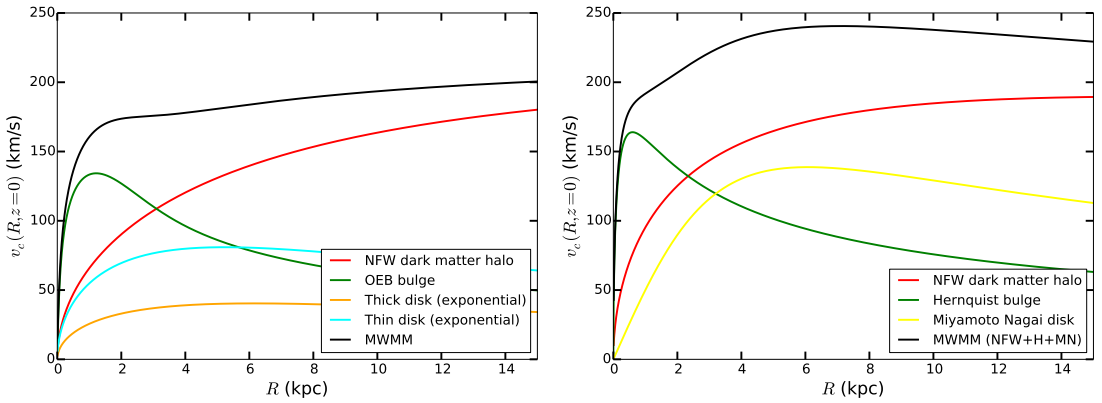

Figure 3.7: The circular speed (for objects in the plane of the disk) for the Milky Way mass models that we use to illustrate this chapter, as a function of the cylindrical coordinate R. Left: MWMM from [68]. Right: MWMM from [1]. The different components of each MWMM are shown together with the curve for the MWMM. The values of the parameters have been fixed as specified in the text, see section 3.2.3. We remark that in the inner part of the Galaxy the baryonic bulge contributes more than the disk, while in the outer the converse happens. The contribution of the dark matter is very small in the inner Galaxy, while it dominates going toward higher R. This are the so called *rotation curves* for a spiral Galaxy, i.e. the curves providing the circular speed as a function of R in the disk. As we can clearly see from the figure, the effect of adding to the baryons the dark matter component is to enhance the values of the circular speed at R outside the inner part of the Galaxy. In particular, the impact of the dark matter is such that the rotation curve is almost flat at every R outside the inner Galaxy, while it would have had a Keplerian behavior if only the baryons would have been present. Flat rotation curves are usually what is observed either for other spiral galaxies and for the Milky Way (usually with bigger uncertainties). This has historically been one of the first and most invoked arguments for the need of dark matter in galaxies.

The above definition of the escape speed would be the speed that a body should have in order to be able to arrive at an infinite distance from the Milky Way. Anyway, sometimes we can use another definition of the escape speed, namely:

$$v_{esc}(r) \doteq \sqrt{2\left|\Phi(r) - \Phi(r_{max})\right|}\,, \tag{3.27}$$

where r_{max} is the distance from the center of the potential at which a body is considered to be unbound. This is more appropriate when we do not consider an isolated system, to describe the fact that an object can escape the gravitational potential of such a system once it is sufficently far away from it to be "captured" by the gravitational potential of a nearby object. While equation (3.26) well represents the escape speed necessary for escaping for instance a star, since the Milky Way is not an isolated system, the escape speed from the Galaxy can more appropriately be described using equation (3.27). This will describe the fact that, though $\Phi(r_{max})$ is not necessarily 0, the body could escape the gravitational potential of the Milky

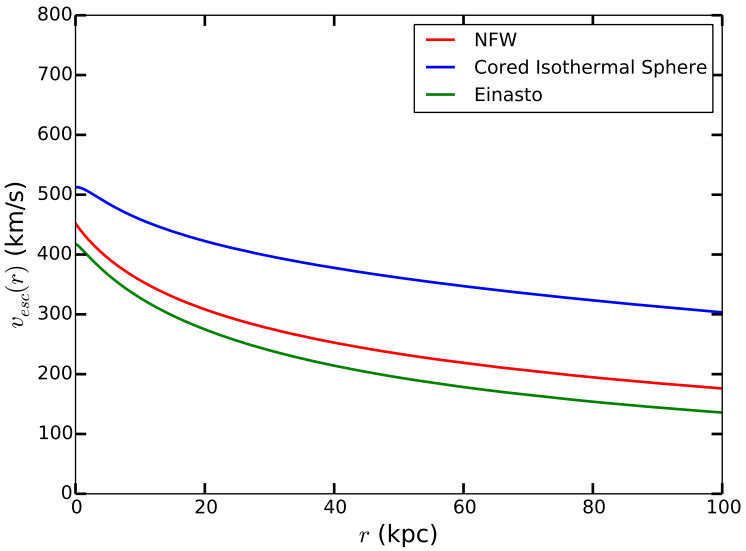

Figure 3.8: The escape speed of the dark matter halo profiles of figure 3.1. The different profiles are normalized such that they all provide the same value for the dark matter density at the position of the Sun, which we fixed at $\varrho_\odot = 0.3$ GeV/cm^3 (as in the SHM) at $r_\odot = 8$ kpc. The values of the parameters for each profile are specified in the caption of figure 3.1.

Way because of e.g. the presence of other nearby galaxies. This definition is used for instance in [1].

The escape speed of some dark matter profiles is shown in figure 3.8, while that of the MWMM presented in section 3.2.3 is shown in figure 3.9.

For a point which lies in the plane of the disk, we can write:

$$v_{esc}^{MWMM}\left(R, z=0\right) = \sqrt{2\left|\Phi^{MWMM}\left(R, z=0\right) - \Phi^{MWMM}\left(R_{max}, z=0\right)\right|}\ , \quad (3.28)$$

where the potential is that of the MWMM under consideration.

The escape speed for every component of the MWMMs presented in the beginning of this chapter, as well as the ones for the total, are shown in figure 3.9.

3.4 The isothermal sphere

This section provides an overview of the isothermal sphere, the mass distribution upon which the Maxwell-Boltzmann velocity distribution relies. The discussion is mainly based on [17, sec. 2.1, sec. 4.3].

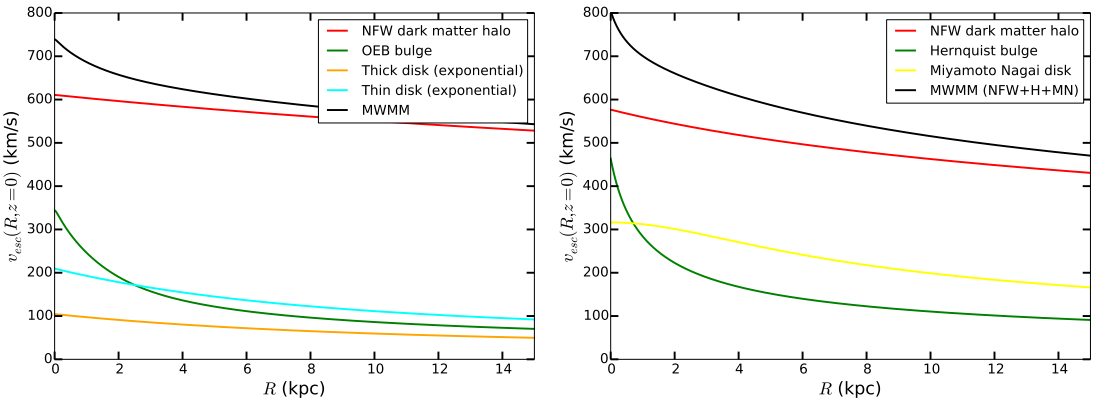

Figure 3.9: The escape speed (in the plane of the disk) for the Milky Way mass models that we use to illustrate this chapter, as a function of the cylindrical coordinate R. Left: MWMM from [68]. Right: MWMM from [1]. The different components of each MWMM are shown together with the curve for the MWMM. The values of the parameters have been fixed as specified in the text, see section 3.2.3. The escape speed of this figure is defined as in equation (3.27), with $R_{max} = 500$ kpc.

3.4.1 Power-law density profiles

We can consider a system whose mass density drops off as a certain power α of the radius:

$$\varrho^{PL}(r) = \varrho_0 \left(\frac{r}{r_0}\right)^{-\alpha} , \tag{3.29}$$

i.e. a *power law density profile*.

Using equation (3.20) we obtain that the above profile corresponds to an internal mass of

$$M_{int}(r) = \frac{4\pi\varrho_0 r_0^{\alpha}}{3-\alpha} r^{(3-\alpha)} , \tag{3.30}$$

and we see that we have to assume $\alpha < 3$ in order to have a finite interior mass.

Using equations (3.23) and (3.30), we obtain

$$v_c^2(r) = \frac{4\pi G_N \varrho_0 r_0^{\alpha}}{3-\alpha} r^{(2-\alpha)} . \tag{3.31}$$

When $\alpha > 2$ the potential difference in these models between radius r and infinity is finite. Thus, the escape speed $v_{esc}(r)$ from radius r, using its definition (3.26) and equation (3.21), is given by

$$v_{esc}^2(r) = 2\int_r^{\infty} \frac{G_N M_{int}(m)}{m^2} dm = 2\frac{v_c^2(r)}{\alpha - 2} \quad (\alpha > 2) . \tag{3.32}$$

So we see that, for this family of models with the above mentioned assumptions, v_{esc}, v_c and α are related (this is not the case for the majority of the density profiles). Anyway, over the range $3 > \alpha > 2$, (v_{esc}/v_c) rises from the value of 2, characteristic of a point mass, toward infinity.

Observations tell us that the circular-speed curves of many galaxies are remarkably flat, so we see from equation (3.31) that an interesting case is $\alpha = 2$. This is actually the profile of the model called *singular isothermal sphere*, treated in detail in the following subsection.

Let us remark that the light distributions in elliptical galaxies suggest $\alpha = 3$ (see [17]) and the flat rotation curves of spiral galaxies suggest $\alpha = 2$, so it is evident that the escape speed of galaxies is in general a very uncertain quantity.

3.4.2 The singular isothermal sphere

The *singular isothermal sphere* has already been introduced in section 3.2.1, and it is the spherically symmetric density profile of the form:[16]

$$\varrho^{SIS}(r) \doteq \frac{\sigma^2}{2\pi G_N r^2} \ , \tag{3.33}$$

where r is the distance from the center of the sphere and σ is the dispersion in any one component of the velocity. The mean square speed of the objects described by this profile is $3\sigma^2$, as we are going to see in the next subsection.

The mass contained in a sphere of radius r concentric with the isothermal sphere can be computed from (3.20) and reads:

$$M_{int}^{SIS}(r) = \frac{2\sigma^2 r}{G_N} \ . \tag{3.34}$$

The speed of a body which is on a circular orbit in a system whose density profile is that of a singular isothermal sphere can be calculated from (3.23) and turns out to be:

$$v_{circ}^{SIS}(r) = \sqrt{2}\sigma \ . \tag{3.35}$$

The density profile (3.33) diverges for $r \to 0$ (i.e. the density at the center of the sphere is infinite). Moreover, it has a serious defect: its total mass is infinite, as can be seen by taking the limit of (3.34) for $r \to \infty$. No real astrophysical system can thus be modeled with such a profile over more than a limited range of radii. The Newtonian gravitational potential corresponding to this profile can be computed from equation (3.22), but the integral in the second term of that equation diverges. To get rid of this problem it is possible to limit the use of this model up to only a certain distance from the center of the system, r_{cut}. This means to redefine the profile in (3.33) as being equal to zero for every $r > r_{cut}$.

[16]The singular isothermal sphere profile can be alternatively written as $\varrho^{SIS}(r) \doteq \varrho_s (r_s/r)^2$, where r_s is some *scale radius* and ϱ_s is the *matter density at the position* r_s. This form makes clear that it is a particular case of the power law profile of equation (3.29), obtained with the choice $\alpha = 2$.

3.4.3 The phase-space distribution associated with the SIS, and the analogy with an isothermal gas

We now want to point out which are the phase-space distribution and velocity distribution associated with a SIS profile, and why this profile is called isothermal.

Taking Φ_0 to be a constant, let us define the *relative potential* Ψ and the *relative energy per unit mass* $\mathcal{E}$ as

$$\Psi = -\Phi + \Phi_0 \tag{3.36}$$

and

$$\mathcal{E} = -E + \Phi_0 = \Psi - \frac{v^2}{2} \ , \tag{3.37}$$

where $E = \Phi + \frac{1}{2}v^2$.

The SIS density profile from the phase-space distribution

Let us consider a dynamical system (made of stars, or of dark matter particles), whose phase-space distribution is

$$f\left(\mathcal{E}\right) = \frac{\varrho_1}{\left(2\pi\sigma^2\right)^{3/2}} \exp\left(\frac{\mathcal{E}}{\sigma^2}\right) \ . \tag{3.38}$$

Integrating over all velocities we find

$$\varrho = \varrho_1 e^{\Psi/\sigma^2} \ . \tag{3.39}$$

We can write Poisson's equation (3.17) for this system, which turns out to be

$$\frac{1}{r^2}\frac{d}{dr}\left(r^2\frac{d\Psi}{dr}\right) = -4\pi G_N \varrho \ , \tag{3.40}$$

or using (3.39)

$$\frac{d}{dr}\left(r^2\frac{d\ln\varrho}{dr}\right) = -\frac{4\pi G_N}{\sigma^2} r^2 \varrho \ . \tag{3.41}$$

We can easily find one solution of equation (3.41), namely

$$\varrho\left(r\right) \doteq \frac{\sigma^2}{2\pi G_N r^2} \ , \tag{3.42}$$

which is exactly the singular isothermal sphere presented in equation (3.33).

The analogy with an isothermal gas

Consider an isothermal gas. Its equation of state is

$$p = \frac{k_B T}{m}\varrho \ , \tag{3.43}$$

where k_B is Boltzmann's constant, p and T the pressure and temperature of the gas, m the mass of a gas particle and ϱ the density. The equation of hydrostatic equilibrium reads

$$\frac{dp}{dr} = -\varrho \frac{d\Phi}{dr} \tag{3.44}$$

and can be easily rewritten as

$$\frac{k_B T}{m} \frac{d\varrho}{dr} = -\varrho \frac{G_N M_{int}(r)}{r^2} \ . \tag{3.45}$$

Multiplying this equation by $r^2 m/\varrho k_B T$ and then differentiating it w.r.t. r one obtains

$$\frac{d}{dr}\left(r^2 \frac{d\ln\varrho}{dr}\right) = -\frac{4\pi G_N m}{k_B T} r^2 \varrho \ . \tag{3.46}$$

If we compare equation (3.46) with equation (3.41), we see that they are identical if we set

$$\sigma^2 = \frac{k_B T}{m} \ . \tag{3.47}$$

Therefore, the structure of an isothermal self-gravitating sphere of gas is identical with the structure of a collisionless system of objects (stars or dark matter particles) whose phase-space distribution is given by equation (3.38).

The velocity distribution associated with a SIS

We can easily obtain the distribution for the velocities of the particles described by (3.38) at a given radius r as

$$f(v;r) = \frac{f\left(\psi(r) - \frac{v^2}{2}\right)}{\varrho(r)} \ , \tag{3.48}$$

and we find that it is a Maxwell-Boltzmann distribution

$$f_v(v) = \frac{1}{(2\pi\sigma^2)^{3/2}} \exp\left(-\frac{v^2}{2\sigma^2}\right) \ . \tag{3.49}$$

The mean square speed of the objects of this system can be easily computed from (3.38) and is $3\sigma^2$, and the dispersion in any one component of the velocity is σ^2.

3.5 Systems in equilibrium and the Jeans equations

In this section we review some of the bases of the dynamics of a galaxy, which will be useful in the sequel. They hold of course for stellar systems as well as for dark matter halos.

We introduce the collisionless Boltzmann equation and we present how the Jeans equations can be obtained. We then focus on particular results holding for spherically symmetric systems only. We discuss the anisotropy in velocity space, introducing the useful anisotropy parameter. We summarize the Jeans theorems and we recall the relationship among integrals of motion and the phase-space distribution of a system. This section is mainly based on [17, sec. 4.1, sec. 4.8 and 7.2].

3.5.1 The collisionless Boltzmann equation

Consider an Hamiltonian dynamical system with canonical coordinates q_i and conjugate momenta p_i, $i = 1, \ldots, n$ where $2n$ is the number of degrees of freedom of the system[17], and $f^{(n)}(p, q)$ is the *phase-space distribution*. The *Liouville theorem* is a fundamental result which tells us that the flow of points trough the phase space is incompressible. This theorem follows directly from the continuity equation satisfied by $f^{(n)}(p, q)$. It reads:

$$\frac{df^{(n)}}{dt} \doteq \frac{\partial f^{(n)}}{\partial t} + \sum_{i=1}^{n} \left(\frac{\partial f^{(n)}}{\partial q_i} \dot{q}_i + \frac{\partial f^{(n)}}{\partial p_i} \dot{p}_i \right) = 0 \ . \tag{3.50}$$

Now imagine a large number of stars (or dark matter particles) moving under the influence of a *smooth potential* $\Phi(\vec{x}, t)$. At any time t, a full description of the state of any collisionless system is given by specifying the *phase-space density* (called also *distribution function*) $f(\vec{x}, \vec{p}, t)$.[18]

A particular case of Liouville's theorem, the one that we obtain for $n = 3$, is the *collisionless Boltzmann equation*, which reads:

$$\frac{df}{dt} \doteq \frac{\partial f}{\partial t} + \sum_{i=1}^{3} \left(\frac{\partial f}{\partial x_i} \dot{x}_i + \frac{\partial f}{\partial v_i} \dot{v}_i \right) = \frac{\partial f}{\partial t} + \sum_{\alpha=1}^{6} \left(\frac{\partial f}{\partial w_\alpha} \dot{w}_\alpha \right) = 0 \ , \tag{3.51}$$

where $\vec{x}$ is the position in three-dimensional space, $\vec{v} \doteq \dot{\vec{x}}$ and $\vec{w} \doteq (\vec{x}, \vec{v}) = (w_1, \ldots, w_6)$.

Recalling the relations $\vec{F} = m\dot{\vec{v}}$ and $\vec{F} = -\vec{\nabla}(m\Phi(\vec{x}, t))$, we can make the substitution $\dot{\vec{v}} = -\vec{\nabla}\Phi(\vec{x}, t)$, so we can rewrite the above equation as:

$$\frac{df}{dt} \doteq \frac{\partial f}{\partial t} + \sum_{i=1}^{3} \left(\frac{\partial f}{\partial x_i} v_i - \frac{\partial f}{\partial v_i} \frac{\partial \Phi}{\partial x_i} \right) = 0 \ , \tag{3.52}$$

This is the fundamental equation of stellar dynamics, and it means that the flow of stellar phase points in the phase space is incompressible. The quantity

[17] Note that if the system is constituted of particles, as for instance the molecules of a gas, or the stars of a galaxy, or the particles of the dark matter halo, $n = Nd$, where N is the number of particles and d is the number of spatial dimensions of the system (for instance $d = 3$ for a system in three-dimensional space).

[18] Let us remark that using the velocities as in $f(\vec{x}, \vec{v}, t)$, instead of the momenta as in $f(\vec{x}, \vec{p}, t)$, relies on the assumption that all the stars or particles of the system have the same mass.

$f(\vec{x}, \vec{p}, t)$, i.e. the phase-space distribution, is defined to be the *number of stars per unit volume of phase space*, but the same equation holds also when interpreting it as the *mass density* or the *luminosity density in phase space*.

This equation, here reported in Cartesian coordinates, can easily be rewritten in any coordinate system, and the corresponding expressions can be found in [17].

3.5.2 The Jeans equations

It is possible to gain valuable insights by taking "moments" of the collisionless Boltzmann equation. We need to define some quantities: the *spatial number density* (of stars or dark matter particles)[19]

$$\nu(\vec{x}, t) \doteq \int f(\vec{x}, \vec{v}, t)\, d^3v \ ; \tag{3.53}$$

the *mean velocity*

$$\overline{v}_i(\vec{x}, t) \doteq \frac{1}{\nu} \int v_i f(\vec{x}, \vec{v}, t)\, d^3v \ ; \tag{3.54}$$

the quantity

$$\overline{v_i v_j}(\vec{x}, t) \doteq \frac{1}{\nu} \int v_i v_j f(\vec{x}, \vec{v}, t)\, d^3v \tag{3.55}$$

and the *stress tensor* $-\nu\sigma_{ij}^2$ (which is symmetric), of components

$$\sigma_{ij}^2(\vec{x}, t) \doteq \overline{(v_i - \overline{v}_i)(v_j - \overline{v}_j)} = \overline{v_i v_j} - \overline{v}_i \overline{v}_j \ . \tag{3.56}$$

The second equality tells us that the mean value of $v_i v_j$ may be separated in two parts, a part $\overline{v}_i \overline{v}_j$ which is due to streaming motion, and the part $\overline{v_i v_j}$ which arises because the stars near any given point $\vec{x}$ do all have the same velocity.

From the collisionless Boltzmann equation we can derive the *Jeans equations*:

$$\frac{\partial \nu}{\partial t} + \frac{\partial (\nu \overline{v}_i)}{\partial x_i} = 0 \ , \tag{3.57}$$

$$\frac{\partial (\nu \overline{v}_j)}{\partial t} + \frac{\partial (\nu \overline{v_i v_j})}{\partial x_i} + \nu \frac{\partial \Phi}{\partial x_j} = 0 \tag{3.58}$$

$$\frac{\partial \overline{v}_j}{\partial t} + \overline{v}_i \frac{\partial \overline{v}_j}{\partial x_i} = -\frac{\partial \Phi}{\partial x_j} - \frac{1}{\nu} \frac{\partial \left(\nu \sigma_{ij}^2\right)}{\partial x_i} \ . \tag{3.59}$$

The first equation is clearly a *continuity equation*.

The above set of equations is written in Cartesian coordinates. With an analogous procedure it is possible to derive the Jeans equations in cylindrical and in spherical coordinates.

[19] Let us remark that the spatial number density $\nu(\vec{x}, t)$ is related to the mass density $\varrho(\vec{x}, t)$ by the relation $m\nu(\vec{x}, t) = \varrho(\vec{x}, t)$, under the assumption that all the objects of the system have the same mass m.

From the collisionless Boltzmann equation in cylindrical coordinates we obtain the *Jeans equations in cylindrical coordinates*:

$$\frac{\partial \nu}{\partial t} + \frac{1}{R}\frac{\partial \left(R\nu\overline{v}_R\right)}{\partial R} + \frac{\partial \left(\nu\overline{v}_z\right)}{\partial z} = 0 \ , \tag{3.60}$$

$$\frac{\partial \left(\nu\overline{v}_R\right)}{\partial t} + \frac{\partial \left(\nu\overline{v_R^2}\right)}{\partial R} + \frac{\partial \left(\nu\overline{v_R v_z}\right)}{\partial z} + \nu\left(\frac{\overline{v_R^2} - \overline{v_\varphi^2}}{R} + \frac{\partial \Phi}{\partial R}\right) = 0 \ , \tag{3.61}$$

$$\frac{\partial \left(\nu\overline{v}_\varphi\right)}{\partial t} + \frac{\partial \left(\nu\overline{v_R v_\varphi}\right)}{\partial R} + \frac{\partial \left(\nu\overline{v_\varphi v_z}\right)}{\partial z} + \frac{2\nu}{R}\overline{v_\varphi v_R} = 0 \ , \tag{3.62}$$

$$\frac{\partial \left(\nu\overline{v}_z\right)}{\partial t} + \frac{\partial \left(\nu\overline{v_R v_z}\right)}{\partial R} + \frac{\partial \left(\nu\overline{v_z^2}\right)}{\partial z} + \frac{\nu\overline{v_R v_z}}{R} + \nu\frac{\partial \Phi}{\partial z} = 0 \ . \tag{3.63}$$

In *spherical coordinates*,[20] the case of greatest importance is when the system is in steady state and $\overline{v}_r = \overline{v}_\vartheta = 0$, in which case we find:

$$\frac{d\left(\nu\overline{v_r^2}\right)}{dr} + \frac{\nu}{r}\left[2\overline{v_r^2} - \left(\overline{v_\vartheta^2} + \overline{v_\varphi^2}\right)\right] = -\nu\frac{d\Phi}{dr} \ . \tag{3.64}$$

Jeans equations in spherically symmetric systems

Consider a system (for instance a galaxy, or a naive approximation of the dark matter halo surrounding our Galaxy [21]) in which both the density and the velocity structures are invariant under rotations about the galactic center. Thus the system (galaxy or halo) does not rotate, and

$$\overline{v_\vartheta^2} = \overline{v_\varphi^2} \ . \tag{3.65}$$

We can now define the *anisotropy parameter* $\beta(r)$ as

$$\beta(r) \doteq 1 - \frac{\overline{v_\vartheta^2}(r)}{\overline{v_r^2}(r)} \ . \tag{3.66}$$

where $\overline{v_r^2}(r)$ is the *radial velocity dispersion*. This parameter describes the degree of anisotropy of the velocity distribution at each point. Note that it can be rewritten

[20] We will decompose here the velocity vector $\vec{v}$ in the components v_r along the radial direction (the same as $\vec{r}$), v_φ and v_ϑ. These can be expressed in terms of the polar coordinates for the velocity space as (we use the same notation as [17, pag. 295]) $v_r = v\cos\eta$, $v_\vartheta = v\sin\eta\cos\psi$, and $v_\varphi = v\sin\eta\sin\psi$, where $v^2 = v_r^2 + v_\varphi^2 + v_\vartheta^2$ is the square of the modulus of the velocity, η is the polar angle and ψ the azimuthal angle. Let us finally remark that $v_T^2 = v_\varphi^2 + v_\vartheta^2$.

[21] This approximation is considered for a galaxy in [17, sec. 4.8], on which this section mostly relies, and used also for the dark matter halo of our Galaxy in [55].

in terms of the *tangential velocity dispersion* recalling that $\overline{v_T^2}(r) \doteq \overline{v_\vartheta^2}(r) + \overline{v_\varphi^2}(r) = 2\overline{v_\vartheta^2}(r)$. Its values have the following meanings:

$$\begin{aligned} \beta = 1 &\iff \overline{v_\vartheta^2} = 0 \\ 0 < \beta < 1 &\iff \overline{v_\vartheta^2} < \overline{v_r^2} \\ \beta = 0 &\iff \overline{v_\vartheta^2} = \overline{v_r^2} \quad \text{(isotropic case)} \\ \beta < 0 &\iff \overline{v_\vartheta^2} > \overline{v_r^2} \end{aligned}$$

The configuration in which $\beta = 0$ corresponds to the isotropic case, the one in which $\overline{v_T^2} \ll \overline{v_r^2}$ which implies $\beta(r) \approx 1$ corresponds to *radial anisotropy*, while the opposite limit, in which $\overline{v_T^2} \gg \overline{v_r^2}$ and so $\beta \to -\infty$, is referred to as *tangential anisotropy*.

Even though this formalism holds in general for stellar systems as well for the dark matter, either for the Milky Way and for other galaxies, in the framework of this work we are mostly interested in the value of β for the dark matter halo of our Galaxy. Numerical models and observations suggest (see [17, sec. 4.8]) that for the dark matter halo of the Milky Way $\overline{v_\vartheta^2} \leqslant \overline{v_r^2}$, and thus $\beta \geqslant 0$. More precisely, N-body simulations of the Galaxy suggest that it grows from approximately zero at the center of the halo (isotropic) up to a value of about $0.2 - 0.4$ for r larger than the Sun's position (up to [60]), or even 0.5 (up to [85]) and then it remains constant or mildly decreases approaching the edge of the Galaxy, see [60] and references therein. Note anyway that there are of course no direct measures from observations of β for the dark matter, and also those of β for stars are few and unclear because the real stars populations are ways more anisotropic than what can be described through β.

With the above assumptions, equation (3.64) becomes

$$\frac{1}{\nu}\frac{d\left(\nu\overline{v_r^2}\right)}{dr} + 2\frac{\beta\overline{v_r^2}}{r} = -\frac{d\Phi}{dr} \ . \tag{3.67}$$

Isotropic velocity dispersion

To solve the Jeans equations, we usually need some assumptions on the form of the velocity dispersion tensor $\boldsymbol{\sigma^2}$ of equation (3.56).

The simplest assumption we can make is to suppose that $\boldsymbol{\sigma^2}$ takes the special isotropic form:

$$\sigma_{ij}^2 \doteq \overline{(v_i - \overline{v}_i)(v_j - \overline{v}_j)} = \sigma^2\delta_{ij} \ . \tag{3.68}$$

In general there is no reason to assume that the dispersion tensor is isotropic, but this can be a useful starting/reference point.

Then, the Jeans equations in the particular case of a 1) steady state 2) axisymmetric system in which 3) $\boldsymbol{\sigma^2}$ is isotropic and 4) the only streaming motion is in the azimutal direction become:

$$\frac{\partial(\nu\sigma^2)}{R} - \nu\left(\frac{\overline{v_\varphi}^2}{R} - \frac{\partial\Phi}{\partial R}\right) = 0 \ , \tag{3.69}$$

obtained from (3.61), and

$$\frac{\partial\left(\nu\sigma^2\right)}{\partial z}+\nu\frac{\partial\Phi}{\partial z}=0 \tag{3.70}$$

obtained from (3.63).

3.5.3 Integrals of motion and the Jeans theorems

A *constant of motion* in a given force field is any function $C\left(\vec{x}\left(t\right),\vec{v}\left(t\right),t\right)$ that is constant along any orbit, i.e.:

$$\frac{dC\left(\vec{x}\left(t\right),\vec{v}\left(t\right),t\right)}{dt}=0\ . \tag{3.71}$$

An *integral of motion* in a given force field is any function of the phase-space coordinates alone $I\left(\vec{x}\left(t\right),\vec{v}\left(t\right)\right)$ that is constant along any orbit, i.e.:

$$\frac{dI\left(\vec{x}\left(t\right),\vec{v}\left(t\right)\right)}{dt}=0\ . \tag{3.72}$$

While every integral of motion is a constant of motion, the converse is not true.

According to [17, sec. 3.1.1], any orbit in any force field has at least 6 constants of motion. The coordinates $\left(\vec{x}\left(0\right),\vec{v}\left(0\right)\right)$ can be regarded as such. In any static potential $\Phi\left(\vec{x}\right)$, the total energy is an integral of motion. In any axysymmetric potential $\Phi\left(R,z,t\right)$ (where we took the z axis to be parallel to the axis of symmetry) the component of the angular momentum along the z axis is an integral of motion. In any spherical potential $\Phi\left(r,t\right)$, the three components of the angular momentum are three integrals of motion. In a spherically symmetric potential $\Phi\left(r\right)$, i.e. one which is static and spherical, both the total energy and the three components of the angular momentum are integrals of motions; there is also a fifth integral of motion, which has a more complicated form.[22] So orbits in any time-independent potential necessarily admit five independent integrals of motion.

Jeans Theorems

We report here two results, taken from [17, sec. 4.2], that are useful for the sequel.

Jeans Theorem. Any steady-state solution of the collisionless Boltzmann equation depends on the phase-space coordinates only through integrals of motion in the galactic potential, and any function of these integrals yields a steady-state solution of the collisionless Boltzmann equation.

The most interesting part of the theorem, the one which will be used in the following, is the second one. The first proposition only tells us that the distribution function, the form of which we do not know a priori, is a function of at least two integrals whose form is likewise a priori unknown to us.

[22] In such a potential, it is usually more practical to consider as integrals of motion the modulus of the angular momentum and the two independent components of $\hat{n}\doteq\vec{L}/L$.

Strong Jeans theorem. The distribution function of a steady-state gravitational system in which almost all orbits are regular with non-resonant frequencies may be presumed to be a function only of three independent isolating integrals, which may be taken to be actions.

In practice, this theorem tells us that, if the potential is regular, for all practical purposes any time-dependent galaxy may be represented by a solution of the form $f(I_1, I_2, I_3)$, where I_1, I_2, I_3 are any three independent isolating integrals.

Jeans Theorems applied to spherical systems

As we have seen, any spherical potential necessarily admits four isolating integrals, the total energy E and the three components of the angular momentum $\vec{L}$. Applying the Jeans theorem we can thus conclude that any non-negative function of these integrals can serve as the distribution function of a spherical stellar system.

There is a simple extension of the strong Jeans theorem which allows to conclude that the distribution function of any steady-state spherical system can be expressed as a function $f\left(E, \vec{L}\right)$. If the system is spherically symmetric in all its properties, f cannot depend on the direction of $\vec{L}$ but only on its magnitude L, and we have that $f = f(E, L)$.

The most interesting and important case is when the stellar system itself provides the potential Φ. If we regard f as the mass density function, then we have

$$\bigtriangledown^2 \Phi = 4\pi G \varrho = 4\pi G \int f d^3\vec{v} \; . \tag{3.73}$$

This equation can be written, using spherical symmetry, as:

$$\frac{1}{r^2}\frac{d}{dr}\left(r^2 \frac{d\Phi}{dr}\right) = 4\pi G \int f\left(\frac{1}{2}v^2 + \Phi, |\vec{r} \times \vec{v}|\right) d^3\vec{v} \; . \tag{3.74}$$

The above equation is the fundamental equation governing spherical equilibrium stellar systems.

3.6 How to derive the phase-space distribution from the density profile

In this section we are going to study the following problem. We have a system, the mass density function of which is described by a function of the position. The system can be composed of one or more components, each of them with its own mass distribution. It is important to remark that the sum of all components features the total gravitational potential that drives the dynamics of each component. We would like to compute the phase-space distribution corresponding to the mass density. This problem was presented and solved by Eddington [86] in the context of globular clusters. This section is mainly based on [17, sec. 4.3].

We are going to consider different degrees of symmetry for the density distribution and for the velocity distribution. We will consider in this section only spherically symmetric density distributions, and we will not consider distributions with lesser spatial symmetries.

For what concerns the velocity part of the phase-space distribution, for systems with spherically symmetric densities we will consider isotropic velocity distributions and anisotropic ones. These latter, due to the spherical symmetry of the density distribution, have the same velocity dispersion in both the angular directions, as in equation (3.65). This allows to define the anisotropy parameter (3.66). We are going to consider cases with constant anisotropy parameter as well as cases with anisotropy parameter which is a function of the spherical coordinate r.

Taking Φ_0 as a constant (sometimes set at $\Phi\left(R_{max}\right)$, which delineates the virial radius of the gravitational system, or the virial radius times some factor, as we will use for example in next chapter) let us define the *relative potential* Ψ and the *relative energy per unit mass* $\mathcal{E}$ (of a star or a dark matter particle) as

$$\Psi = -\Phi + \Phi_0 \tag{3.75}$$

and

$$\mathcal{E} = -E + \Phi_0 = \Psi - \frac{v^2}{2} \ , \tag{3.76}$$

where $E = \Phi + \frac{1}{2}v^2$ is the *total mechanical energy per unit mass* . We generally choose Φ_0 such that $f > 0$ for $\mathcal{E} > 0$ and $f = 0$ for $\mathcal{E} \leq 0$.

Let us remark that, once we have obtained the phase-space distribution, it is enough to evaluate it at the position of the Sun $r_\odot$ and to divide it by the local dark matter density evaluated at $r_\odot$ to get back the velocity distribution at the position of the Sun

$$f\left(v; r_\odot\right) = \frac{f\left(\mathcal{E}\left(r_\odot\right) = \psi\left(r_\odot\right) - \frac{v^2}{2}\right)}{\varrho\left(r_\odot\right)} \ , \tag{3.77}$$

which is what one need in studying dark matter direct detection.

Let us emphasize that, though $f\left(\mathcal{E}\right)$ is the phase-space distribution function of a given species, the gravitational potential $\psi\left(r\right)$ does include the contributions of all other massive components.

3.6.1 Spherically symmetric systems with isotropic dispersion tensors

The simplest spherical models are those with distribution functions that depend on $\mathcal{E}$ only, $f\left(\mathcal{E}\right)$, which are called *ergodic systems*.[23] For those systems, the velocity

[23] In statistical mechanics and chaos theory, the term ergodic denotes a system that unifromly explores its energy surface in phase space, which implies that the phase-space distrbution is uniform on the energy surface. In the usage of this term made here the phase-space distribution is ergodic, but the motion of individual stars generally is not.

dispersions are given by

$$\overline{v_i^2} = \frac{1}{\varrho}\int dv_r dv_\vartheta dv_\varphi v_i^2 f\left[\Psi - \frac{1}{2}\left(v_r^2 + v_\vartheta^2 + v_\varphi^2\right)\right] , \tag{3.78}$$

where $i = r, \vartheta, \varphi$.

It is clear from the dependence on each v_i of the f in the above equation that $\overline{v^2}_r = \overline{v^2}_\vartheta = \overline{v^2}_\varphi$, so the velocity-dispersion tensor is everywhere isotropic.

When $f = f(\mathcal{E})$ and we have chosen the constant involved in the definition of Ψ in such a way that $f(\mathcal{E}) = 0$ for $\mathcal{E} < 0$, equation (3.74) becomes

$$\frac{1}{r^2}\frac{d}{dr}\left(r^2\frac{d\Phi}{dr}\right) = -16\pi^2 G\int_0^\psi f(\mathcal{E})\sqrt{2(\Psi - \mathcal{E})}d\mathcal{E} . \tag{3.79}$$

This equation may be regarded either as a nonlinear equation for $\psi(r)$, or as a linear equation for $f(\mathcal{E})$. We will start by choosing simple forms for f and solving for Ψ (and hence for ϱ).

Eddington Equation

Now we want to find the way to determine the phase-space density $f(\mathcal{E})$ of a spherically symmetric system with isotropic velocity from its mass distribution, $\varrho(r)$, which is only a function of the distance r to the system's center. We will mainly follow [17, sec. 4.3.1]. We can calculate its mass density $\varrho(r)$ from the phase-space distribution function of the system via:

$$\varrho(r) = \int d^3\vec{v} f(r, \vec{v}) . \tag{3.80}$$

Because of the assumed isotropic velocity, we showed before that the phase-space distribution function was a mere function of the energy. By a simple change of variable, we therefore get:

$$\varrho(r) = 4\pi\int_0^\Psi f(\mathcal{E})\sqrt{2(\Psi - \mathcal{E})}d\mathcal{E} . \tag{3.81}$$

Since Ψ is a monotonic function of r, we can regard ϱ as a function of Ψ. We can thus differentiate both sides of the equation with respect to Ψ (taking care of the upper bound of the integral), and the result is an Abel integral equation having solution

$$f(\mathcal{E}) = \frac{1}{\sqrt{8}\pi^2}\frac{d}{d\mathcal{E}}\int_0^\mathcal{E}\frac{d\varrho}{d\Psi}\frac{d\Psi}{\sqrt{\mathcal{E} - \Psi}} . \tag{3.82}$$

This result is due to Eddington [86] and this equation is known as *Eddington's formula* [17]. It can be rewritten as:

$$f(\mathcal{E}) = \frac{1}{\sqrt{8}\pi^2}\left[\int_0^\mathcal{E}\frac{d^2\varrho}{d\Psi^2}\frac{d\Psi}{\sqrt{\mathcal{E} - \Psi}} + \frac{1}{\sqrt{\mathcal{E}}}\left(\frac{d\varrho}{d\Psi}\right)_{\Psi=0}\right] . \tag{3.83}$$

We can also rewrite it in a way which is more suitable for numerical integration because of the absence of the square root at the denominator in the integral term, i.e.:

$$f(\mathcal{E}) = \frac{1}{\sqrt{8}\pi^2}\left[+\frac{1}{\sqrt{\mathcal{E}}}\left(\frac{d\varrho}{d\Psi}\right)_{\Psi=0} + 2\sqrt{\mathcal{E}}\left(\frac{d^2\varrho}{d\Psi^2}\right)_{\Psi=0} + 2\int_0^{\mathcal{E}} d\Psi\sqrt{\mathcal{E}-\Psi}\frac{d^3\varrho}{d\Psi^3}\right] . \tag{3.84}$$

An example of the use of Eddington equation is that from the singular isothermal sphere we are able to recover the phase-space distribution function

$$f(\mathcal{E}) = \frac{\varrho_1}{(2\pi\sigma^2)^{3/2}}\exp\left(\frac{\Psi - \frac{v^2}{2}}{\sigma^2}\right) , \tag{3.85}$$

from which we can easily obtain the distribution for the velocities of dark matter particles at a given radius r, which as we have seen in section 3.4.3 is the Maxwell-Boltzmann distribution.

An illustration of the $f(\mathcal{E})$ associated with the NFW dark matter profile of the MWMMs considered in the first part of this chapter, obtained via Eddington equation, is shown in figure 3.10

3.6.2 Spherically symmetric systems with anisotropic dispersion tensors

N-body simulations show that dark matter do not follow the isothermal sphere density profile. Moreover, their velocity distribution turns out to anisotropic [60].

Let us now consider procedures generalized from the Eddington equation that allow us to determine the phase-space density functions with an anisotropic velocity dispersion tensor, associated to spherically symmetric density distributions.

When f depends on L as well as on $\mathcal{E}$, $\overline{v}_\varphi^2 = \overline{v}_\vartheta^2 \neq \overline{v}_r^2$. The essential distinction between systems with $f = f(\mathcal{E})$ and those with $f(\mathcal{E}, L)$ is that the former have isotropic velocity-dispersion tensors and the latter do not.

Let us recall that from such an $f(\mathcal{E}, L)$ we can recover the density distribution as

$$\nu(r) = \int d^3\vec{v} f(\mathcal{E}, L) = 2\pi\int_0^\pi d\eta \sin\eta \int_0^{\sqrt{2\Psi}} dv v^2 f\left(\Psi - \frac{1}{2}v^2, rv\sin\eta\right) . \tag{3.86}$$

Constant anisotropy parameter

Constant anisotropy parameter and ansatz for the functional shape. The simplest way to introduce anisotropy is to take distributions of the kind considered in the previous section, and to multiply them by functions of L.[24] For

[24] The distributions obtained in this way will still be solutions of the Boltzmann equation thanks to the second part of Jeans theorem.

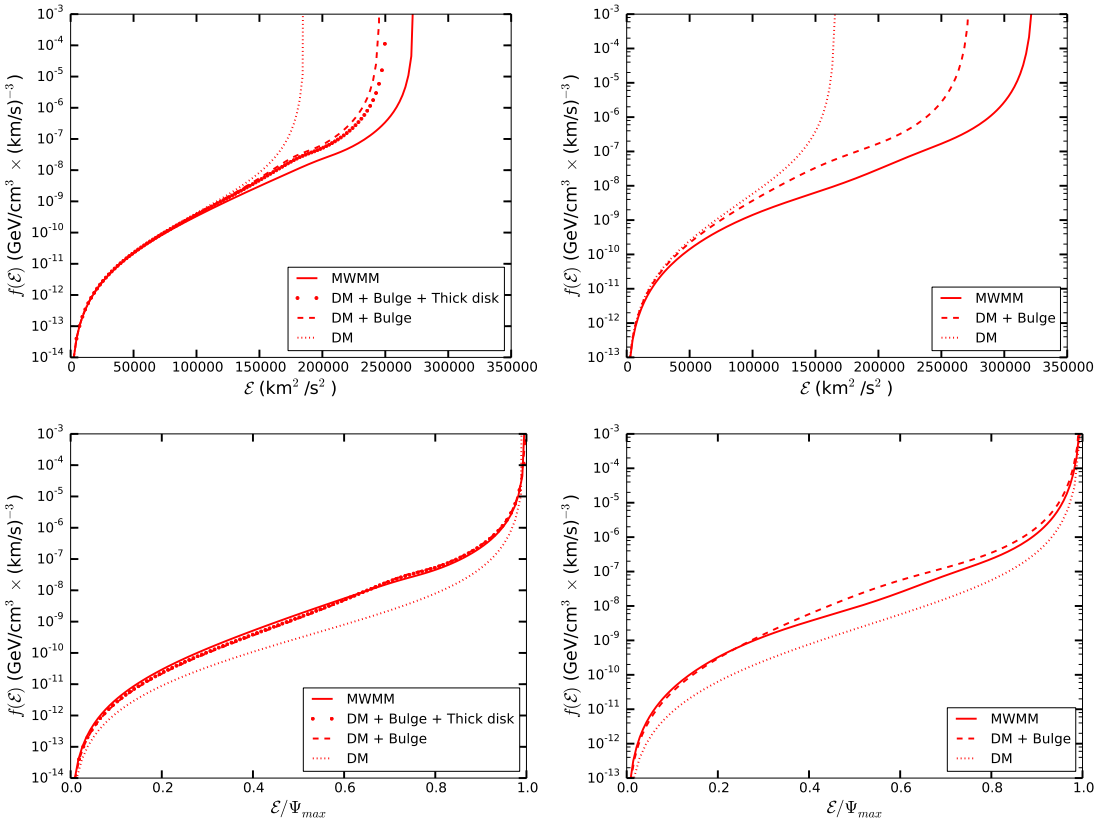

Figure 3.10: Upper panel: the $f(\mathcal{E})$ associated with the NFW dark matter profiles of the MWMMs used to illustrate the first part of this chapter. These phase-space distributions have been obtained applying Eddington equation to the NFW density profiles. Different cases are considered: the $f(\mathcal{E})$ associated to the NFW dark matter profile first in the presence of its gravitational potential only, then in the presence of the potential generated by itself (dark matter) plus the stellar bulge, and finally in the presence of the potential generated by the whole MWMM, i.e. dark matter plus baryons (bulge and two disks components, or bulge and disk, depending on the MWMM). Left: MWMM from [68]. Right: MWMM from [1]. Lower panel: the same quantities, but this time as functions of $\mathcal{E}/\Psi_{max}$. For every curve, the corresponding Ψ_{max} is the maximum value of the gravitational potential of the system changed in sign Ψ. It is simply the value attained by Ψ at the center of the system.

instance, we can construct a phase-space distribution with constant anisotropy parameter $\beta(r) = \beta$ assuming for its functional form the ansatz

$$f(\mathcal{E}, L) = L^{-2\beta} G(\mathcal{E}) \ , \tag{3.87}$$

where $L = |\vec{r} \times \vec{v}| = rv \sin(\eta) = rv_T$ is the modulus of the angular momentum per unit mass.

The above form is justified because it allows to consistently recover $\varrho(r)$ from $f(\mathcal{E}, L)$ using (3.80).

The function $G(\mathcal{E})$ can be computed from the following formula [25] used in [85]

$$G(\mathcal{E}) = \frac{2^{\beta}(2\pi)^{-3/2}}{\Gamma(1-\lambda)\Gamma(1-\beta)} \frac{d}{d\mathcal{E}} \int_0^{\mathcal{E}} \frac{d\Psi}{(\mathcal{E}-\Psi)^{\lambda}} \frac{d^n \varrho_{\beta}}{d\psi^n} , \tag{3.88}$$

where $\varrho_{\beta} \doteq r^{2\beta}\varrho$ is expressed as a function of ψ and $n \doteq \lfloor (3/2-\beta) \rfloor$ and $\lambda \doteq 3/2-\beta-n$ are the integer floor and the fractional part of $3/2-\beta$.

Let's note that the convergence of the above integral requires $\beta < 1$. This equation is a generalization of the Eddington formula, which one can recover in the particular case of $\beta = 0$ (isotropic case).

There are particular cases in which computing the phase-space distribution function from the potential-density pair becomes trivial, since the above equation reduces to equations in which only differentiations enter (see [85]).

For half-integer values of β, i.e. $\beta = 1/2, -1/2, \ldots$, the above expression reduces to

$$f(\mathcal{E}, L) = \frac{1}{2\pi^2} \frac{L^{-2\beta}}{(-2\beta)!!} \frac{d^{3/2-\beta}\varrho_{\beta}}{d\psi^{3/2-\beta}}|_{\psi=\mathcal{E}} . \tag{3.89}$$

For the simplest case of $\beta = 1/2$, it becomes simply

$$f(\mathcal{E}, L) = \frac{1}{2\pi^2 L} \frac{\varrho + r(d\varrho/dr)}{(d\psi/dr)}|_{r=r_E} , \tag{3.90}$$

where r_E is the radius of the largest orbit of a particle with energy $\mathcal{E}$, i.e. $\Psi(r_E) = \mathcal{E}$.

Particular case from generalized NFW, with anisotropy parameter 1/2. Let us consider a family of centrally cusped spherically symmetric density profiles which reads

$$\varrho(r) = \frac{(b-2)\Psi_0}{4\pi G} \frac{a^{b-2}}{r(r+a)^{b-1}} , \tag{3.91}$$

where $b > 2$ is the asymptotic density power index at large radii, and Ψ_0 is the depth of the central potential well. This family of profiles contains the Hernquist profile for $b = 4$ and the NFW profile for $b = 3$.

The corresponding phase-space distribution can be computed using equation (3.88), but for the particular case of $\beta = 1/2$ equation (3.90) allows to write down the phase-space distribution for all the family using r_E written in terms of the *q-logarithm* function defined in [85] (so $r_E = Ln_{b-2}(1+r_E)$). One obtains

$$f(\mathcal{E}, L) = \frac{b-2}{(2\pi)^3 L} \frac{(b-1)r_E}{(1+r_E)^b E - (1+r_E)^2} . \tag{3.92}$$

Note that $f(\mathcal{E}, L)$ for some particular values of β can be found again in [85].

[25] An equivalent but slightly different way of writing this equation can be found in [60].

Anisotropy parameter dependent on r

Osipkov-Merrit models. Let us consider now a phase-space distribution which is associated with an anisotropy factor $\beta(r)$ growing with the galactocentric distance r, called the *Osipkov-Merritt* family of models.[26] It consists in considering $f(\mathcal{E}, L)$ depending on $\mathcal{E}$ and L only through the variable

$$Q \doteq \mathcal{E} - \frac{L^2}{2r_a^2} \ , \tag{3.93}$$

where r_a is the *anisotropy radius*.

For $r \ll r_a$, $Q \to \mathcal{E}$ and the OM distribution is isotropic, while for r larger than r_a the distribution exhibits a radial anisotropy which grows with r approaching the value $\beta(r) \approx 1$ for large values of r_a. It can be shown [60] that the anisotropy parameter takes the form:

$$\beta(r) = \frac{r^2}{r^2 + r_a^2} \ . \tag{3.94}$$

Recalling that $L = rv_T$, we can rewrite the above variable Q as

$$Q = \Psi(r) - \frac{1}{2}\left[v_r^2 + \left(1 + \frac{r^2}{r_a^2}\right) v_T^2\right] = \Psi(r) - \frac{1}{2}\left[v_r^2 + \frac{1}{1-\beta(r)} v_T^2\right] \tag{3.95}$$

One finds that [17, pag. 298]

$$f(Q) = \frac{1}{\sqrt{8}\pi^2}\left[\int_0^Q \frac{d^2\varrho_Q}{d\psi^2}\frac{d\psi}{\sqrt{Q-\psi}} + \frac{1}{\sqrt{Q}}\left(\frac{d\varrho_Q}{d\Psi}\right)_{\Psi=0}\right] \ , \tag{3.96}$$

where

$$\varrho_Q(r) \doteq \left(1 + \frac{r^2}{r_a^2}\right)\varrho(r) = \frac{1}{1-\beta(r)}\varrho(r) \ . \tag{3.97}$$

Notice that this is another generalization of Eddington equation, because in the limit $r \ll r_a$, $Q \to \mathcal{E}$ so the above equation goes back to the Eddington formula.

Linear combination. In order to provide a better fit to the behavior of $\beta(r)$ found in N-body simulations, which is not captured by the anisotropy coefficient of the Osipkov-Merrit models who grows too fast, [60] considers the linear combination[27] of a distribution associated with a fixed β and one of the Osipkov-Merrit type:

$$f(\mathcal{E}, L) = w f_{OM}(Q) + (1-w) f_\beta(\mathcal{E}, L) \ , \tag{3.98}$$

[26] Let us remark that the *Osipkov-Merritt* family of models is a subclass of the *Michie models*, which are themselves a subclass of the *King models*.

[27] Note that this is not the only solution: some authors have considered simplest ways to combine different asymptotic values for β in the center of the halo, and in the outskirts of the halo (see e.g. [87])

where w is a real constant which weights the contribution of the two terms, $f_{OM}(Q)$ is a distribution of the type of equation (3.96), and $f_\gamma(\mathcal{E}, L)$ is of the type (3.87).

As shown in [60], the associated anisotropy parameter turns out to be

$$\beta(r) = [1 - w\frac{\overline{v_T^2}(r; f_{OM})}{\overline{v_r^2}(r; f)}] - [(1-w)\frac{\overline{v_T^2}(r; f_\gamma)}{\overline{v_r^2}(r; f)}] \tag{3.99}$$

This model has the 3 free parameters w, r_a and γ which allows to fit the anisotropy parameter to reproduce the results of N-body simulations.

Product. Of course alternative distributions can be considered. To recover the behavior of the anisotropy parameter found in N-body simulations, one possibility is to consider as in [60] the phase-space distribution of the form

$$f(\mathcal{E}, L) = k(\mathcal{E})\, h(\mathcal{E}, L) \ . \tag{3.100}$$

We can make two different ansatz for $h(\mathcal{E}, L)$:

$$h_A(\mathcal{E}, L) = (1+k)^{-b/a} \tag{3.101}$$

and

$$h_B(\mathcal{E}, L) = (1 + k - k\exp(-10/k))^{-b/a} \ , \tag{3.102}$$

where $\mathcal{E}$ and L enters only via the particular dimensionless combination

$$k = \left(\frac{L^2}{2r_k^2\mathcal{E}}\right) \tag{3.103}$$

with r_k a constant characteristic radius.

On the other hand, $k(\mathcal{E})$ must be determined by numerically solving an integral equation containing Ψ and ϱ.

3.6.3 A remark on the applicability of Eddington equation

We would like to make an important remark concerning the applicability of Eddington equation. As we know, in order to be physically meaningful (as a phase-space distribution function), the function $f(\mathcal{E})$ obtained via Eddington equation needs to be non-negative everywhere (more precisely, non-negative for every $\mathcal{E}$ between 0 and the maximum value of Ψ associated to the studied system). Unfortunately, nothing in the derivation of the Eddington formula guarantees that the obtained $f(\mathcal{E})$ would be non-negative everywhere in such domain.

The condition for the applicability of Eddington equation

As we have seen in equation (3.82), we can write the phase-space distribution computed via Eddington equation as the derivative w.r.t $\mathcal{E}$ of a function $I(\mathcal{E})$ defined as:

$$I(\mathcal{E}) \doteq \int_0^{\mathcal{E}} \frac{d\varrho}{d\Psi} \frac{d\Psi}{\sqrt{\mathcal{E}-\Psi}} \ . \tag{3.104}$$

Since the $f(\mathcal{E})$ obtained is related to $I(\mathcal{E})$ through a derivative w.r.t $\mathcal{E}$, it is easy to see that the function $f(\mathcal{E})$ is everywhere non-negative if and only if the function $I(\mathcal{E})$ is monotonous and increasing, or at most constant (but not decreasing). As a consequence, as [17] points out, a spherical density distribution $\varrho(r)$ in the (positive) potential $\Psi(r)$ can arise from an ergodic phase-space distribution if and only if the couple $\varrho(r)$, $\Psi(r)$ is such that the above condition is satisfied.

We could wonder if, in those cases where the above condition is not satisfied, it is still possible to use the $f(\mathcal{E})$ obtained via Eddington equation only in the limited range of $\mathcal{E}$ where $f(\mathcal{E})$ is positive. From the above discussion we can conclude that this would not be correct, because a phase-space distribution $f(\mathcal{E})$ that is somewhere negative is not a physically meaningful object, and thus even the positive part of it would not represent anything meaningful.

In this section we would like to gain some insights on how to deal with the problem of which are the conditions for the applicability of Eddington equation. We will illustrate some examples of cases where this procedure can be applied, and cases where this procedure cannot. We will thus adopt a more general point of view, and specify a sufficient condition for the Eddington procedure to be applicable. We will finally recall a theorem which deals with the same issue in the more general case of anisotropic systems of the Osipkov-Merrit type, that we encountered in the literature while writing this section.

Examples of MWMMs to which Eddington equation can be applied

We show in figure 3.11 three examples of cases where the condition for the applicability of Eddington equation (i.e. $\frac{dI(\mathcal{E})}{d\mathcal{E}} \geq 0$, equivalent to the condition $f(\mathcal{E}) \geq 0$) is satisfied. Those curves represent the function $I(\mathcal{E})$ corresponding to the dark matter profile lying in the MWMM used in [1], respectively for the three cases where we consider only the dark matter halo, dark matter plus baryonic bulge and dark matter plus baryonic bulge and disk. We see that for both cases the above condition for the applicability of Eddington equation is fulfilled, and in fact from the application of Eddington equation we obtain a positive $f(\mathcal{E})$.

Examples of MWMMs to which Eddington equation cannot be applied

The question of the applicability of Eddington equation arose from the fact that we came across cases for which $f(\mathcal{E})$ is somewhere negative. This always corresponds to a violation of the condition $\frac{dI(\mathcal{E})}{d\mathcal{E}} \geq 0$.

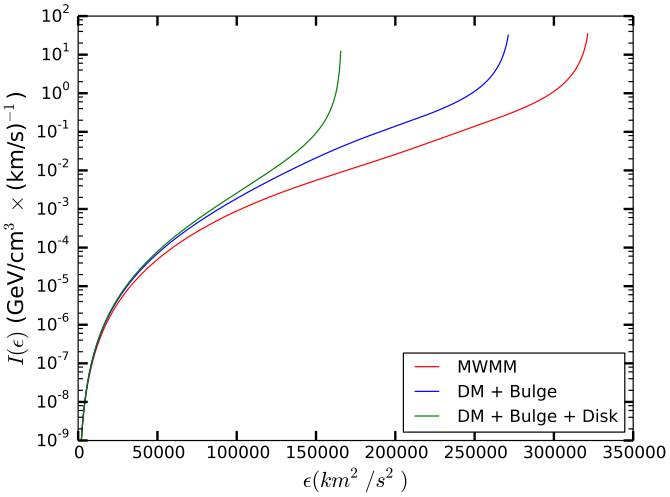

Figure 3.11: We show three examples of couples $\varrho(r)$, $\psi(r)$ for which Eddington equation is applicable, those corresponding to the dark matter NFW profile $\varrho(r)$ associated to the MWMM of [1] introduced in section 3.2.3, respectively with dark matter halo only, dark matter halo and baryonic bulge, and dark matter halo with baryonic bulge and disk.

We illustrate this with an example. For instance, in figure 3.12 we show that if we consider the same mass model as in figure 3.11, but with a cored profile specified in the caption instead of the NFW used above (and using the same baryonic component), we incur in the situation where $I(\mathcal{E})$ is decreasing, so $f(\mathcal{E})$ is not everywhere positive. For the model of figure 3.12 this occurs only when baryons are added to the dark matter in the gravitational potential, while when both $\varrho(r)$ and $\psi(r)$ are those associated to the dark matter only, $I(\mathcal{E})$ is monotonous increasing and we can apply Eddington equation.

We also kept the same baryonic content and the same dark matter profile used above, but varying the parameter γ from 0 (core) to 1 (cusp). We saw that increasing the value of γ from 0 gradually leads from non-monotonous to monotonous increasing $I(\mathcal{E})$; we show the situation for a slightly increased value of $\gamma = 0.2$ in figure 3.13.

Since we came across this issue while trying to apply the Eddington equation to a cored profile, we have been wondering if it was the cored nature of the profile to be at the origin of the non applicability of the Eddington procedure as one might think by looking at the figures above. As we can see from figure 3.12, when the cored dark matter profile is considered lying in the gravitational potential associated to itself plus the baryonic content used in this section, it gives a $I(\mathcal{E})$ not monotonous. However, we also see from figure 3.12 that, when we remove all the additional components (so that the cored dark matter profile is left alone in the gravitational potential generated by itself), it provides a monotonous and increasing $I(\mathcal{E})$. We can thus conclude that considering a cored profile is not enough to end up in the situation where the Eddington procedure is not applicable.

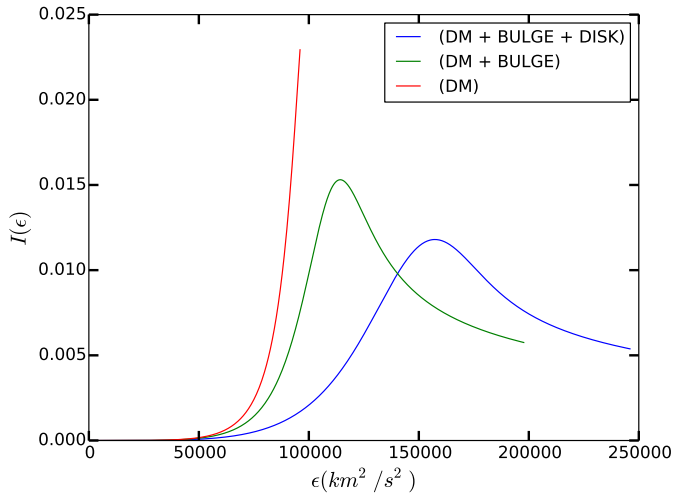

Figure 3.12: Same as figure 3.11, but now the NFW profile describing the dark matter halo has been replaced by a cored profile obtained from the $\alpha\beta\gamma$ parameterization by setting $\alpha = 2.9$, $\beta = 2.5$, $\gamma = 0$, $r_s = 4.4$ kpc and $\varrho_s = 1.75$ GeV/cm^3. For the cases with dark matter halo plus baryons (both bulge and disk or bulge only) the function $I(\mathcal{E})$ is clearly not monotonous, thus providing via Eddington equation a phase-space distribution not positively defined.

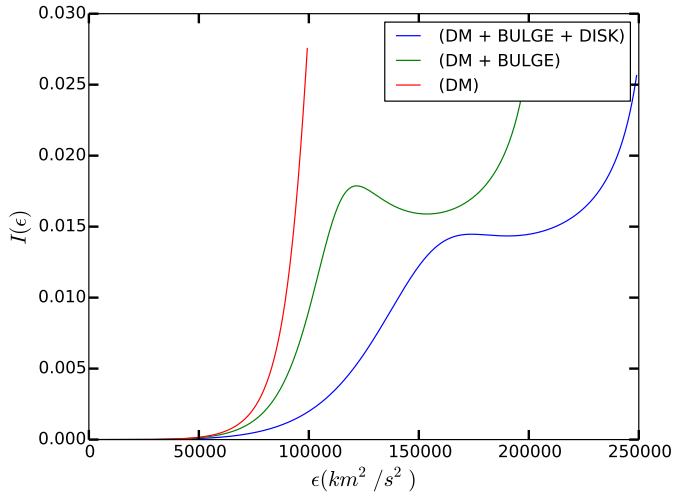

Figure 3.13: The same as figure 3.12, but now the parameter γ of the dark matter profile has been set to $\gamma = 0.2$, i.e. a less cored profile.

Some questions could be raised, for instance is the cored nature of the dark matter profile which originates the violation of the above condition? Or is it the fact that we take into account additional components which originates it? Actually, no one of this facts is directly responsible, in the sense that considering a cored profile is not enough for the condition of applicability to be violated (as we have just

seen), and neither it is summing additional components (that in our case describe baryons) to the $\varrho(r)$ for which we want to compute the phase-space distribution.

Actually, we will see that the problem could be better approached from another point of view: in general, only conditions on generic $\varrho(r)$ and $\psi(r)$ could be cast. Only once a particular model (i.e. a couple of $\varrho(r)$, $\psi(r)$) is specified, these conditions might be translated into conditions on the parameters that have a physical meaning in the model like the baryonic mass.

A sufficient condition on $\frac{d^2\varrho}{d\Psi^2}$ for the applicability of Eddington equation

We will now approach the problem from a different point of view. Instead of concentrating on a particular feature (as the cored nature or the baryonic content) of a particular couple $\varrho(r)$, $\psi(r)$, we will look for a condition on generic $\varrho(r)$ and $\psi(r)$. In this section we would like to provide a sufficient condition which, once verified, ensures the applicability of Eddington equation, and to explain why it is so. This corresponds to a necessary condition for the non-applicability of Eddington equation.

As we said, Eddington equation provides a non-negative phase-space distribution if and only if $I(\mathcal{E})$ defined in equation (3.104) is not decreasing, which is equivalent to say that $\frac{dI(\mathcal{E})}{d\mathcal{E}} \geq 0$. Recalling the form of Eddington equation (3.82), we can write this condition as:

$$\frac{dI(\mathcal{E})}{d\mathcal{E}} = \frac{1}{\sqrt{\mathcal{E}}}\left(\frac{d\varrho}{d\Psi}\right)_{\Psi=0} + \int_0^{\mathcal{E}} d\Psi\, \frac{d^2\varrho}{d\Psi^2}\, \frac{1}{\sqrt{\mathcal{E}-\Psi}} \geq 0\ . \tag{3.105}$$

For every physically interesting couple $\varrho(r)$, $\psi(r)$, the first term is positive or equal to zero. Thus, the condition

$$\int_0^{\mathcal{E}} d\Psi\, \frac{d^2\varrho}{d\Psi^2}\, \frac{1}{\sqrt{\mathcal{E}-\Psi}} \geq 0 \tag{3.106}$$

ensures the applicability of Eddington equation. It is clear that the integrand in the above equation is always positive if $\frac{d^2\varrho(\Psi)}{d\Psi^2} \geq 0$ for all Ψ between 0 and $\mathcal{E}$, so $\frac{d^2\varrho(\Psi)}{d\Psi^2} \geq 0$ is sufficient for the above inequality to be verified. Thus $\frac{d^2\varrho(\Psi)}{d\Psi^2} \geq 0$ is a sufficient condition for the applicability of Eddington equation to the couple ϱ, Ψ (where we remind that ϱ is the one of any component of a mass model, and Ψ is the collective one, i.e. the one arising from the sum of all the components). This means that, when we want to obtain via Eddington equation the phase-space distribution of a particular ϱ in a particular gravitational potential Ψ, we can check if the above condition is verified, and in the affirmative case we are sure that the phase-space distribution obtained using Eddington equation will be everywhere non-negative. We can also rephrase this by saying that $\frac{d^2\varrho(\Psi)}{d\Psi^2} < 0$ is a necessary condition for the non-applicability of Eddington equation.

Let us rewrite this necessary condition for the non-applicability of Eddington equation in a more convenient way, in terms of derivatives w.r.t. r. Both ϱ and ψ

are actually functions of r, and to take derivatives w.r.t. Ψ one has to express the former as a function of the latter eliminating r, which can always be done because both are monotonous functions of r, but which in practice is rarely trivial (or even possible) to do analytically. To circumvent it, one can express the condition as the following.

Since

$$\frac{d^2\varrho}{d\Psi^2} = \left(\frac{d\Psi}{dr}\right)^{-2} \left[\frac{d^2\varrho}{dr^2} - \frac{d\varrho}{dr}\left(\frac{d\Psi}{dr}\right)^{-1}\frac{d^2\Psi}{dr^2}\right], \tag{3.107}$$

we thus have that the condition $\frac{d^2\varrho}{d\Psi^2} < 0$, necessary for the non-applicability of Eddington equation, is equivalent to the condition

$$\frac{d\varrho}{dr}\left(\frac{d\Psi}{dr}\right)^{-1}\frac{d^2\Psi}{dr^2} > \frac{d^2\varrho}{dr^2}\ , \tag{3.108}$$

which can be rewritten as

$$\frac{d^2\Psi}{dr^2}\Big/\frac{d\Psi}{dr} < \frac{d^2\varrho}{dr^2}\Big/\frac{d\varrho}{dr}\ , \tag{3.109}$$

where we flipped the versus of the inequality because $\frac{d\varrho}{dr} < 0$. Written in this fashon, the condition is easier to be checked.

Examples of MWMMs which fulfill the above necessary condition for the failure of the Eddington procedure

As we have seen in section 3.6.3, $\frac{d^2\varrho(\Psi)}{d\Psi^2} < 0$ is a necessary condition for the non-applicability of Eddington equation. In figure 3.14, we show three examples of a dark matter profile ϱ in a potential Ψ, two of which correspond to a decreasing $I(\mathcal{E})$. We also show the corresponding $\varrho(\Psi)$, $\frac{d\varrho(\Psi)}{d\Psi}$ and $\frac{d^2\varrho(\Psi)}{d\Psi^2}$. As we can see, as expected for the cases which correspond to the non applicability of the Eddington procedure, the second derivative occurs to be negative from a certain value of Ψ on.

The three examples of figure 3.14 are a dark matter profile ϱ in a potential Ψ generated by itself, then by itself plus a bulge, and finally by itself plus a bulge with twice the mass of the previous one.

Here we have been obtaining the failure of the Eddington procedure by progressively adding baryonic mass, while in a previous section we have obtained the same result by shifting from a cusped to a cored dark matter profile. It is very important to remark that in the case of a generic mass model only generic conditions on the behavior of ϱ as a function of Ψ can be cast, as for instance the necessary condition for the non-applicability $\frac{d^2\varrho}{d\Psi^2} < 0$. Only when applied to a couple of ϱ, Ψ of which we specify the functional shapes, such conditions for the applicability of Eddington equation can thus be translated on particular conditions on the values that the parameters of the model can assume without braking them.

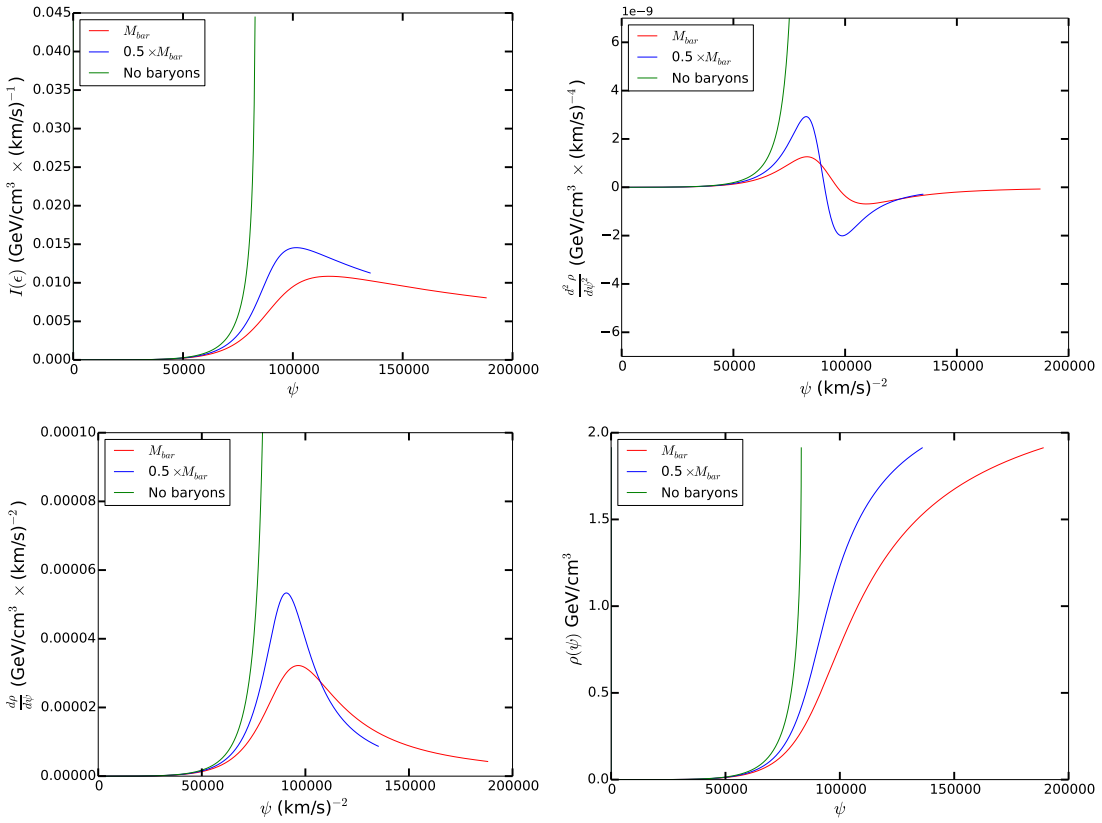

Figure 3.14: Illustration. The dark matter is described using the $\alpha\beta\gamma$ parameterization for the density profile, by setting $\alpha = 1$, $\beta = 3$, $\gamma = 0$, $r_s = 7.8$ kpc and $\varrho_s = 1.92$ GeV/cm^3. The baryonic component is represented by an Hernqvist profile (3.12) with $a_H = 0.6$ kpc, and various values for the mass $M_H = M_b, 0.5 \times M_b, 0$, with $M_b = 1.5 \times 10^{10}$ $M_\odot$.

We can finally wonder what happens when generalized Eddington procedures (with velocity anisoropy) are considered. For anisotropic models of the Osipkov-Merrit type (which includes the Eddington procedure as a particular case), the answer is provided by a theorem that we report in the next section.

A general theorem on the consistency of mass models, for phase-space distributions of the Osipkov-Merrit type

In this section we state a theorem, originally derived in [88] and formulated in a more suitable way in [89], which investigates precisely the so called *consistency* of a mass model. A mass model is said to be consistent when the distribution function f which describes it is everywhere non-negative.

More precisely, this theorem provides conditions to check the non-negativity of the distribution function of a multi-component (i.e. composed by more than one density profile) spherical system where the orbital anisotropy of each component

is described by the Osipkov-Merrit anisotropy presented in section 3.6.2 (i.e. for which the distribution function is of the type described in that section). As we have seen, the distribution function for each component ϱ_k (where k enumerates the components, while T will stand for total) can be obtained with equation (3.96), which is a generalization of Eddington equation that we can recover in the limit of $r_a \to \infty$, which means velocity isotropy. We recall that the gravitational potential which enters in that equation is the total one, i.e. the one which arises from the sum of all the components.

The theorem is valid for untruncated systems with a finite total mass, for which the second term in equation (3.96) is zero. An example of such a system, studied in [89], is constituted by the sum of two Hernquist profiles.

The theorem, as reported in [89], states that a *necessary condition* for the non negativity of the distribution function f_k of the Osipkov-Merrit type (associated to the component described by $\varrho_{Q,k}$ defined from ϱ_k in equation (3.97)) is:

$$\frac{d\varrho_{Q,k}}{d\Psi_k} \geq 0 \text{ , for } 0 \leq \Psi_k \leq \Psi_k(0) \text{ .} \tag{3.110}$$

If this necessary condition is satisfied, a *strong sufficient condition* for the non negativity of f_k is

$$\frac{d}{d\Psi_k}\left[\frac{d\varrho_{Q,k}}{d\Psi_k}\left(\frac{d\Psi_T}{d\Psi_k}\right)^{-1}\sqrt{\Psi_T}\right] \geq 0 \text{ , for } 0 \leq \Psi_k \leq \Psi_k(0) \text{ .} \tag{3.111}$$

The proof can be found in [88]. A *weak sufficient condition* is

$$\frac{d}{d\Psi_k}\left[\frac{d\varrho_{Q,k}}{d\Psi_k}\left(\frac{d\Psi_T}{d\Psi_k}\right)^{-1}\right] \geq 0 \text{ ,} \tag{3.112}$$

obtained by requiring that $\frac{d^2\varrho_{Q,k}}{d\Psi_T^2} \geq 0$ in equation (3.96) (after having eliminated the second term).

The first thing to remark is that the necessary condition (3.110) depends only on $\varrho_{Q,k}$ and thus it is valid independently of any other interacting component added to the model.

Then, even when the necessary condition is satisfied, f_k can be negative, because of the radial behavior of the integrand in equation (3.96), which depends on the total potential, on the particular $\varrho_{Q,k}$, and on the anisotropy radius r_a.

This theorem, that we encountered in the literature while writing this section, addresses thus a more general issue w.r.t. the one addressed by this section, i.e. under which conditions the distribution function obtained via the generalization of the Eddington procedure for anisotropic Osipkov-Merrit models is non negative. It does so focusing on untruncated systems with a finite total mass. Since Eddington equation is a particular case of (3.96), obtained in the limit $r_a \to \infty$, which means velocity isotropy, the results of the theorem apply directly to the Eddington procedure, for which $\varrho_{Q,k}$ in the conditions above becomes ϱ_k.

CHAPTER 4

On the use of the estimates of the local Galactic escape speed in computing dark matter direct detection limits

Contents

4.1 Introduction

Astrophysical quantities enter in the computation of DMDD limits from experimental results, and the uncertainties on these quantities translate into uncertainties on the limits. Moreover, relevant astrophysical quantities are usually determined from observations by making assumptions which should be taken into account while using them to compute DMDD limits. In addition, often these quantities arise from a mass model, which induces correlations among them.

In this chapter, after introducing these problems (that have already been discussed in section 2.4), we are going to focus on the recent estimate of the local Galactic escape speed that has been published recently (2014) by [1], and on its implications for dark matter direct detection. This quantity matters in particular at low WIMP masses, where the results of the experiments are more controversial. Moreover, it serves as a case study to outline the issues related to the use of the estimates of astrophysical quantities in DMDD.

We are thus also going to briefly summarize in section 4.2 the work that has been done by the RAVE collaboration in [1], because the results of this chapter highly rely on the results and procedure employed therein.

To translate the results of that study into DMDD we consider in section 4.5 either the standard assumption of a Maxwell-Boltzmann speed distribution for the dark matter, and alternatively an ergodic distribution arising from the application

of the Eddington procedure to the mass model employed by [1], that we are going to describe in detail in section 4.3.

We are then going to present in detail in sections 4.4 and 4.6 the impact of the RAVE estimate of the escape speed on DMDD limits, with a particular attention to the correlations induced by the assumed mass model and to the uncertainties associated to this estimate. We conclude in section 4.7.

4.1.1 Astrophysical uncertainties

Considering the SHM as a starting point, we can now try to understand which are the facts that should be taken into account to improve the description of the astrophysics involved in DMDD.

We will proceed as follows. The first step is to focus on the different estimates present in the literature for the parameters of the SHM, and on the associated uncertainties. We briefly did so in section 2.4, and we will go into more details in next chapter. Here, we just recall few facts about the escape speed, on which this chapter mainly relies. The second step is to take into account the hypothesis on which such estimates rely upon, and the correlations among the parameters. The third step is to relax the hypothesis of a Maxwell-Boltzmann speed distribution for the dark matter, and consider instead other ergodic phase-space distributions for the dark matter.

We have worked out a detailed analysis of these topics focusing on the case study of the escape speed, which we present in the reminder of this chapter.

Let us remark that other studies on the impact of astrophysical uncertainties in DMDD exist, for instance [90], but they follow a pretty different approach.

4.1.2 The local Galactic escape speed

The escape speed measures the depth of the potential well of the Milky Way and therefore contains information about the mass distributed exterior to the radius for which it is estimated.

Methods to estimate this quantity were introduced in [91], where a sample of high-velocity stars was analyzed. It was pointed out that the determination of the escape speed required, due to the reduced sample dimension, prior knowledge of the form of the high-velocity distribution. This prior is assumed also by [1], as we will see in section 4.2.1.

The value of the local Galactic escape speed assumed in the SHM is $v_{esc} = 544$ km/s. This value was estimated by the RAVE collaboration in [41] in 2007. In particular, the result of that study was the range 498 km/s $< v_{\rm esc} <$ 608 km/s at 90% confidence level, with 544 km/s as a median likelihood. The median values of the two studies are very similar, while the uncertainties at 90% confidence level are reduced to a factor of 0.6 (0.7) for the upper (lower) margin respectively, mainly

due to the augment number of stars considered.[1]

A new estimate of this quantity was published in 2014 by the RAVE collaboration in [1], providing the result of 533^{+54}_{-41} km/s at 90% confidence level, with an additional 4% of systematic uncertainty.[2] This is the estimate on which we will focus in this chapter, so a detailed description of it will be provided in the following sections.

The main differences among [41] and [1] will be summarized in section 4.2.6.

4.1.3 Working plan to evaluate the impact of the local Galactic escape speed estimates on dark matter direct detection limits

We conclude this introductory part by presenting the motivations and the working plan for this chapter.

The knowledge of the high velocity tail of the WIMP velocity distribution has a strong impact on the way dark matter direct detection may constrain or discover light WIMPs in the GeV mass range. A careful investigation of the physics affecting the low WIMP mass region of the parameter space for the spin-independent interpretation of this scattering is fundamental, because at around 10 GeV signal-like events reported by some experiments (e.g. the DAMA experiment [54]), are at odds with limits from other experiences. Different effects impact DMDD limits at low WIMP masses. Those related to the detector are the energy threshold and the energy resolution of the detector, while those of astrophysical origin are related to the high velocity tail of the dark matter speed distribution and to the local dark matter density. In this respect, particularly relevant are the local escape speed from the Milky Way, and the local circular speed, as the sum of both defines the maximum speed in the observer's frame.

While the latter has been studied in depth by many authors, this is not the case for the former. Recently, there have been important observational efforts to estimate it. A method to measure it is to use nearby high-velocity stars, that are supposed to trace the high-velocity tail of the stars speed distribution, which should vanish at the escape speed as well. Following this approach, the RAVE collaboration published in 2014 the latest estimate of this quantity [1] (P14 from now on), while its previous estimate, again from the same collaboration, dates back to 2007 [41].

In this chapter we focus our attention on the estimates of the escape speed published by P14, which rely on the assumption, among others, of a particular Milky Way mass model. Because of this, these new estimates cannot be used blindly as they rely on assumptions which induce tight correlations between the escape speed and other local astrophysical parameters (e.g. the local circular speed, the local dark matter density and the distance of the Sun to the Galactic center).

[1] A comparison between the two works of [41] and [1] is briefly worked out in section 4.2.6.

[2] See the following sections for the other results obtained in that study.

Directly using those results to compute DMDD limits is straightforward, but this would lead to inconsistent results because neglecting the hypotheses these estimates rely upon, and the induced correlations, which should instead be taken into account in the computation of such limits. In this chapter we analyze these assumptions and derive a self-consistent model for the local phase-space distribution of the dark matter, which consistently takes into account the correlations between the astrophysical parameters.

We consider isotropic dark matter velocity distributions. We initially consider the standard Maxwell-Boltzmann speed distribution for the dark matter. We then go beyond the Maxwell-Boltzmann approximation computing by means of Eddington equation (thus assuming spherical symmetry of the gravitational potential) the phase-space distribution of the dark matter (still ergodic in this case), wherein the previously mentioned correlations are automatically taken into account.

We take as reference the experimental sensitivities currently achieved by the most constraining experiments at the moment of writing: LUX [24], SuperCDMS [32] and CRESST2 [34], and we compute the corresponding exclusion curves with associated uncertainties (focusing on the spin-independent interpretation of DMDD, with no isospin violation). We have found that a treatment which implements the RAVE results on the escape speed by consistently correlating all relevant parameters leads to more constraining exclusion curves with respect to the standard ones, and to moderate uncertainties (that we quantify later).

The procedure that we employ and the results that we obtain in this study are contained in our paper [2] that has recently been published in the journal Physical Review D.

4.2 Summary of the estimates of the local Galactic escape speed worked out by the RAVE collaboration in P14

This section briefly summarizes the work done in P14 to estimate the local Galactic escape speed. In particular, we recall their methods and assumptions in order to emphasize that their results should not be used with other arbitrary assumptions.

P14 uses data mainly taken from the Radial Velocity Experiment (RAVE DR4) to estimate the local escape speed from the Galaxy, and tests its method using a suite of cosmological simulations of the formation of Milky Way-sized galaxies. Its best estimate of the local Galactic escape speed is 533^{+54}_{-41} km/s, at 90% C.L. with an additional 4% of statistical uncertainties. P14 defines $v_{\rm esc}$ as the minimum speed required to reach $3 \times R_{340}$, three times the Galactocentric radius encompassing a mean overdensity of 340 times the critical density for closure in the Universe. Then it estimates the mass of the Galaxy starting from the escape speed, and assuming as mass model for the halo two versions of the NFW profile. Its best estimate of M_{340} (mass interior to R_{340}, dark matter and baryons) is $1.6^{+0.5}_{-0.4} \times 10^{12}\ M_\odot$.

4.2.1 The Likelihood analysis

In many equilibrium models of stellar systems there are stars with velocities up to the escape speed, but in others all stars have velocities considerably smaller than the escape speed. To obtain a credible relationship between the densities of fast stars and the escape speed one must engage oneself with processes that place stars in the marginally bound part of the phase space. The simulations on which P14 tests its method give velocity distributions that are compatible with the law

$$n_{||}\left(v_{||}|\vec{r},k\right) \propto \left(v_{\rm esc}\left(\vec{r}\right)-\left|v_{||}\right|\right)^{k+1} \ , \tag{4.1}$$

where $v_{||}$ is the line-of-sight velocity expressed in a Galactocentric rest frame, and k is an index (this ansatz was originally used in [91], work from which also the method employed in [1] was proposed, later being extended by [41]).

Let us remember the definition of likelihood function (from [92, pag. 324]):

$$L\left(\boldsymbol{\vartheta}|\underline{\boldsymbol{x}}\right)=\prod_{i=1}^{n}p\left(\boldsymbol{x}_i|\boldsymbol{\vartheta}\right) \ , \tag{4.2}$$

where $\boldsymbol{\vartheta}$ is a set of parameters, $\boldsymbol{x}_i$ is one of the n experimental realizations of the multidimensional stochastic variable $\boldsymbol{X}$, and $p\left(\boldsymbol{x}_i|\boldsymbol{\vartheta}\right)$ is the probability that an experiment could give as result the values $\boldsymbol{x}_i$, if the parameters have the values $\boldsymbol{\vartheta}$.

So P14 adopts as likelihood function the function

$$L\left(v_{||}\right)=\frac{\left(v_{\rm esc}\left(\vec{r}\right)-\left|v_{||}\right|\right)^{k+1}}{\displaystyle\int_{v_{\rm min}}^{v_{\rm esc}}dv\left(v_{\rm esc}\left(\vec{r}\right)-\left|v_{||}\right|\right)^{k+1}} \ , \tag{4.3}$$

We can see that this likelihood is simply defined as the probability distribution $n_{||}\left(v_{||}|\vec{r},k\right)$, which has been normalized by means of the denominator.

4.2.2 The employed procedure

Given the observational data for $v_{||}$, they calculate the above likelihood for a wide range of values of the two parameters v_{esc} and k. Then they marginalize over the nuisance parameter k. Finally they find out the best estimate of v_{esc} as the value which maximizes the marginalized likelihood.

Since the stars of the data set do not reside all near the Sun's location, it is necessary to take into account their individual positions. They do this in two alternative ways: 1) by binning the data in Galactocentric radial distance bins or 2) by correcting the measured parallel speeds by the ratio of the distant to local gravitational field.

Calculating the gravitational potential relies on a Galactic mass model that includes both the baryons and dark matter. They use 1) a Miyamoto & Nagai disk, 2) an Hernqvist bulge and 3) an original or (alternatively) an adiabatically

contracted NFW profile for the dark matter halo. In the NFW profile the free parameters are the total mass M_{340} inside R_{340} and the concentration parameter c_{340}, one of which can be set by imposing a fixed value for $v_{\rm circ}\,(r_\odot)$.

P14 uses a set of simulations to create fake data, to study how the employed likelihood analysis behave, and to extract from them the values of some parameters. In this way P14 found that its likelihood analysis gives a strong degeneracy between $v_{\rm esc}$ and k, and tends to give too low values of the escape speed. In order to be able to obtain information on $v_{\rm esc}$, they need to acquire more information on k. They do this using cosmological simulations, and they finally select the interval on k which gives the better reconstruction of the true $v_{\rm esc}$ put as input from the simulation. The adopted interval is finally $2.3 < k < 3.7$. They also adopt a threshold of $v_{\rm min} = 200$ km/s and, alternatively, 300 km/s. P14 also concludes that, corrected in this way, the method yields a non negligible systematic scatter, but not a bias in the estimated escape speed.

4.2.3 The analysis on real data: sample selection

The majority of the observational data for P14's study comes from the fourth data release (DR4) of the Radial Velocity Experiment (RAVE). The survey determines from the spectra of the stars very precise line-of-sight velocities $v_{\rm los}$, plus several other stellar properties. The DR4 contains information about more than 420000 individual stars (of which after selection P14 actually uses only around one hundred, see section 4.2.4, so the sample employed is very small compared to the the full catalog).

The data give precise measurements of v_{los}, which P14 converts into Galactic rest frame $v_{||,i}$ adopting the values $(U_\odot, V_\odot, W_\odot) = (11.1, 12.24, 7.25)$ km/s (from [19]). P14 then computes the rotational velocities of all stars in Galactocentric cylindrical coordinates v_φ, using the line-of sight velocities, proper motions, distances and the angular coordinates of the stars. It assumes $r_\odot = 8.28$ kpc as the distance from Sun to Galactic Center (from [93]) and discards all the stars that 1) have positive v_φ (i.e. they select only counter rotating (halo) population), or 2) those for which the upper end of the 95% confidence interval on v_φ reaches above 100 km/s. This is important because a contamination from stars from the rapidly rotating disk (P14 wants only stars from the stellar halo) could jeopardize the procedure. Also other publicly available data sets are considered (the sample of metal-poor dwarf stars collected by [94], from which respectively 17 and 14 stars for the two different velocity selections described below are considered).

4.2.4 P14 results

For all stars in the catalog it can be estimated what their radial velocity would be if they were situated at the position of the Sun. Then they create two samples using the new velocities :

- **V300**: stars with rescaled velocities $v'_{||} > 300$ km/s, which are predominantly halo stars (51 stars, 34 from RAVE).
- **V200**: stars with rescaled velocities $v'_{||} > 200$ km/s, preselecting only stars classified as "halo" (83 stars, 69 from RAVE).

Then P14 makes the likelihood analysis in the plane k,$v_{\rm esc}$. All but one of the maximum likelihood pairs agree very well. In all cases a clear degeneracy between k and $v_{\rm esc}$ is visible. Then P14 marginalizes over the optimized k-interval obtained above, and computes the median of every distribution, obtaining a higher value of $v_{\rm esc}$ than the maximum likelihood value for all samples. This behavior is consistent with the test P14 performed on the simulations, which yield the conclusion that the likelihood method underestimates $v_{\rm esc}$.

For halo stars with original $|v_{||}| > 200$ km/s P14 does a second analysis, binning in Galactocentric distance (6 overlapped bins, only 3 used for analysis), and thereby performs a spatially resolved analysis.

4.2.5 Discussion

Estimating the mass of the Milky Way

P14 also wants to determine the mass of the Milky Way from the estimate of the local escape speed. It uses the fact that the escape speed is a measure of the local depth of the potential well $\Phi(r_\odot) = -\frac{1}{2}v_{\rm esc}^2$. A critical point in P14's analysis is whether the velocity distribution reaches up to $v_{\rm esc}$, or it is truncated at some lower values.

It is not a conceptual problem to define the escape speed as the high end of the velocity distribution in disregard of the potential profile outside the corresponding limiting radius. However, then it is important to use the same limiting radius while deriving the total mass of the system using an analytic profile. This means P14 had to redefine the escape speed as:

$$v_{esc}(r, R_{max}) = \sqrt{2\left|\Phi(r) - \Phi(R_{max})\right|}\ . \tag{4.4}$$

$R_{max} = 3R_{340}$ was assumed being considered an appropriate value by [1].[3] This leads to somewhat higher estimates, for similar escape speeds w.r.t. other studies.

[3] To give an idea of the values assumed by $R_{\rm max}$, we can provide two values which are representative of those occurring in the RAVE analysis: for the best fit analysis which assumed $v_{\rm c} = 220$ km/s and obtained 533^{+54}_{-41} km/s, the corresponding $R_{\rm max}$ is ≈ 490 kpc, while for the best fit analysis which assumed $v_{\rm c} = 240$ km/s and obtained 511^{+48}_{-35} km/s, the corresponding $R_{\rm max}$ is ≈ 427 kpc. The meaning of defining the escape speed as the speed necessary to reach $R_{\rm max}$, from the physical point of view, is to consider an object unbound when it reaches that distance from the center of the Galaxy. Even tough this choice is somewhat arbitrary, we should recall that the Andromeda Galaxy (also known as M31), the nearest major galaxy to the Milky Way, is located at approximately 780 kpc from the Earth, and it has a mass of the same order of magnitude of the Milky Way. Thus, the above values of $R_{\rm max}$ are around half way between M31 and us, so it is meaningful to think that an object which reaches such a distance could leave the Milky Way because captured by the gravitational potential of another galaxy.

For instance, [41] found an escape speed of 544 km/s and derived a halo mass of $0.85 \times 10^{12} M_{\odot}$ for an NFW profile, using in practice $R_{\max} = \infty$. If the value $R_{max} = 3R_{340}$ is used instead, the resulting halo mass is $1.05 \times 10^{12} M_{\odot}$, an increase by more than 20% (see [1]). This explains why the mass estimates of [1] are higher then those of [41] even if the values obtained for the escape speed are similar. Keeping this in mind, it should be straightforward to compute the virial mass of the Milky Way, given a certain local escape speed value, assuming the simple mass model presented above.

Fitting the halo concentration parameter

The previous analysis have been repeated by P14 using two fixed values of $v_{\rm c}$: the standard value of $v_{\rm c} = 220$ km/s, and the value of $v_{\rm c} = 240$ km/s toward which the most recent estimates point (as we have seen in chapter 2).

Up to now the value of $v_{\rm c}$ was fixed, but there are many different estimates of it. To deal with this P14 reparametrizes the NFW and leaves the concentration of the halo c_{340} as a free parameter. So P14 repeats the likelihood analysis following the same procedure, but in the plane M_{340}, c_{340}. Because the concentration parameter is strongly related to the mass and the formation time of a dark matter halo, additional constraints on this space can be put from the results of some simulations. The maximum likelihood points, for the NFW and contracted NFW, are respectively $M_{340} = 1.37 \times 10^{12} M_{\odot}$, $c_{340} = 5$ and $M_{340} = 1.22 \times 10^{12} M_{\odot}$, $c_{340} = 5$. These values corresponds respectively to circular speeds of 196 km/s and 236 km/s. Marginalizing the likelihood along the c_{340}-axis, P14 obtains the one-dimensional PDF for the virial mass. The median values obtained are almost identical to the maximum likelihood found above.

To summarize, P14 applies a likelihood analysis on a set of stars selected between those contained in the RAVE survey. First, P14 assumes a value for the $v_{\rm c}$, and once it has marginalized over the nuisance parameter, it ends up with a likelihood for the escape speed $v_{\rm esc}$. Then P14 relaxes the hypothesis on $v_{\rm c}$ (so it has an additional free parameter), and using the mass model of the Milky Way it does a likelihood analysis on the plane c_{340} versus M_{340}. We consider this second analysis to be more interesting, because recent studies (as for instance [40]) suggest a value for $v_{\rm c}$ different from that of the SHM, and this second analysis allows this parameter to vary.

The result of the likelihood analysis worked out by P14 for the plane c_{340} versus M_{340} is shown in figure 4.1. Note that P14 applies the same analysis also using a contracted NFW profile instead of the standard one, but we are not going to consider that part of the analysis.[4] Instead, we are going to consider the content of figure 4.1, focusing in particular on the blue areas.

[4] Note just that the two halo models, the unaltered and the adiabatically contracted NFW halo, are rather extreme cases and the true shape of the Galactic halo is most likely intermediate to these options.

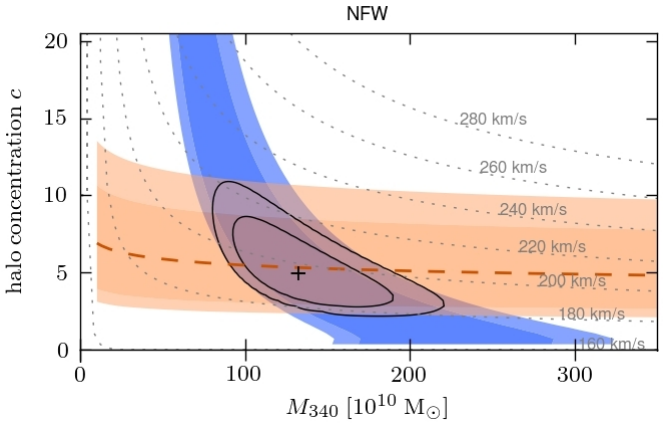

Figure 4.1: The result of the likelihood analysis worked out by P14 in the plane c_{340} versus M_{340}. The likelihood is plotted in blue. The dark blue area marks the region where the value of the likelihood ranges from the maximum to 10% of the maximum. The light blue area marks the regions where the value of the likelihood ranges from 10% of the maximum to 1% of the maximum. This blue areas are those that we are going to consider in the following. The orange area represents a prior from simulations, and we are not going to consider it for the reasons listed in the following sections, The black closed lines arise from applying the prior from the simulation (orange) to the likelihood (blue). Along the gray lines the value of the v_c remains constant. This figure is taken from [1].

4.2.6 Comparison with the escape speed estimates worked out by the RAVE collaboration in 2007

It is important to recall some differences and analogies between the work of P14 [1] on which this chapter focuses, and the work of [41] which provides the standard value for the escape speed assumed by the SHM.[5]

[41] employed data from an earlier version of the RAVE survey. The basic analysis strategy is the same, but [41] used a different ansatz for the high velocity tail of the stars' speed distribution w.r.t. that of equation (4.1) used by [1]. In [41] the assumption was made that the stars considered were from a local sample, i.e. they were located in a volume small enough w.r.t. the Galaxy for the escape speed to be approximately constant over that volume. Thus no rescaling of the projected parallel velocities by means of the gravitational potential was employed, unlike in [1] where such a rescaling is considered. The mass model employed and the values of the baryonic components are the same in [41] and in [1]. The degeneracy between k and v_{esc} was already pointed out by [41] who used priors from simulations as well as [1] does. However, the simulations employed by [1] are much more advanced (because more recent), thus allowing a more detailed analysis. The prior on k used by [41], $2.7-4.7$, is larger than the one of [1], which is nevertheless very close to the lower part of the interval of [41]. The number of stars employed in [1] represents an

[5] For the result of the study [41], see 4.1.2; for the standard halo model, see section 1.8.

increase of a factor of 5 w.r.t. [41] (a factor of 3 if the additional catalogs considered are taken into account). Even though the escape speed found by the two studies is similar, the estimated mass of the Milky May is higher in [1] due to the fact that [41] practically employs $R_{\max} = \infty$.

4.2.7 Conclusions drown by P14

P14 analyzes the data of the RAVE survey and other literature data, to evaluate the local escape speed, and from this the virial mass of our galaxy.

- They have to calibrate their method on cosmological simulations to brake the degeneracy in parameters.
- They define the escape speed as the speed necessary to reach $3R_{340}$. The best estimate (with 90% confidence interval) is 533^{+54}_{-41} km/s. Their estimate is very close to the previous one by [41].
- With their value of $v_{\rm esc}$ they can estimate the virial mass of the Galaxy (dark matter and baryons) by assuming a simple mass model of the baryonic content of the Milky Way and a spherical (original or contracted) NFW halo for the dark matter, and fixing $v_{\rm c} = 220$ km/s and $v_{\rm c} = 240$ km/s.
- Since the quantity $v_{\rm c}$ is under debate, they relax any hypothesis on its value by adding a free parameter, the concentration parameter c_{340}, in the NFW profile. Then they marginalize over c_{340} using simulations results, and find estimates for the mass of the Galaxy.
- Finally they can compare their results with the results of other studies in the literature. Their mass results obtained with unaltered NFW better agree with literature estimates, but imply a value of $v_{\rm c}$ which is in strong disagreement with recent estimates (because too low). The adiabatically contracted NFW pushes toward a value of $v_{\rm c}$ which is in better agreement with recent estimates, but the associated mass value agrees worse with the literature. These circular speeds are highly dependent on the adopted model for the baryonic component, so have to be threaten with caution. An intermediate model could mitigate the tensions.

4.3 The Milky Way mass model employed by P14

P14 analysis is based on a sample of ~ 100 stars mostly from the RAVE catalog. To derive observational constraints on $v_{\rm esc}$ from stellar velocities P14 needed to make an assumption on the shape of the high velocity tail of the stars speed distribution, namely $f_\star(v) \propto (v_{\rm esc} - v)^k$, with k calibrated from cosmological simulations. To

estimate $v_{\rm esc}$ at the position of the Sun, P14 rescaled the $v_{\rm esc}$ of the observed stars using the gravitational potential of the Milky Way, for which a particular Milky Way mass model had to be assumed and where only the dark matter halo parameters were left free. They thus transformed the line of sight velocity $v_{||}\left(\vec{r}\right)$ of each star according to $v'_{||}\left(\vec{r}\right) = v_{||}\left(\vec{r}\right) \times \sqrt{\left|\Phi\left(\vec{r}_{\odot}\right)/\Phi\left(\vec{r}\right)\right|}$ ($\vec{r}_{\odot}$ being the position of the Sun) before performing a likelihood analysis.[6] This introduces a dependence on the assumed Milky Way mass model and thus correlations in the astrophysical parameters relevant to DMDD, that one must take into account when using P14 results.

P14 fixed the Sun's distance from the Galactic center at $r_{\odot} = 8.28$ kpc [93], the peculiar motion of the Sun at the values determined by [19], and repeated the analysis for 3 cases: $v_{\rm c} = 220$ km/s, $v_{\rm c} = 240$ km/s and free $v_{\rm c}$. Their Milky Way mass model is based on a fixed baryonic model (disk and bulge), and on a NFW profile for the dark halo, the parameters of which (the scale density ϱ_s and radius r_s) were left free. The Milky Way mass model assumed in P14 contains a NFW halo [69] for the dark matter, an Hernquist [79] baryonic bulge and a Miyamoto Nagai [77] baryonic disk. Thus it reads:[7]

$$\begin{aligned}\varrho_{MW}\left(R,z\right) = {} & \varrho_s \frac{r_s}{r}\left(1+\frac{r}{r_s}\right)^{-2} + \frac{M_H}{2\pi}\frac{a_H}{r\left(r+a_H\right)^3} \\ & + \frac{b^2 M_{MN}}{4\pi}\frac{a_{MN}R^2 + \left[a_{MN}+3\left(z^2+b_{MN}^2\right)^{1/2}\right]\left[a_{MN}+\left(z^2+b_{MN}^2\right)^{1/2}\right]^2}{\left[R^2+\left[a_{MN}+\left(z^2+b_{MN}^2\right)^{1/2}\right]^2\right]^{5/2}\left(z^2+b_{MN}^2\right)^{3/2}}\,,\end{aligned} \tag{4.5}$$

where R and z are cylindrical coordinates ($r = \sqrt{R^2+z^2}$). It has only two free parameters, the scale density ϱ_s and the scale radius r_s of the NFW profile. The baryonic content is fixed, with the parameters taking the values specified in table 4.1 that were determined by [84].

Disk (Miyamoto Nagai)			Bulge (Hernquist)		
Scale length a_{MN}	4	kpc	Scale radius a_H	0.6	kpc
Scale height b_{MN}	0.3	kpc	Total mass M_H	1.5×10^{10}	$\mathrm{M}_{\odot}$
Total mass M_{MN}	5×10^{10}	$\mathrm{M}_{\odot}$			

Table 4.1: Structural parameters of the baryonic components of the MWMM used by P14, taken from [1].

[6] Remember that the escape speed for a star in $\vec{r}$ is defined as $v_{\rm esc}\left(\vec{r}\right) \doteq \sqrt{2\left|\Phi\left(\vec{r}\right)\right|}$, $\Phi\left(\vec{r}\right)$ being the gravitational potential of the Milky Way.

[7] This expression is simply the sum of the three components, the individual expressions of which are provided respectively by the equations (3.3), (3.12) and (3.11).

The associated Newtonian gravitational potential is:[8]

$$\begin{aligned}\Phi_{MW}(R,z) = &-4\pi G_N \frac{\varrho_s r_s^3}{r} ln\left(1+\frac{r}{r_s}\right) - \frac{G_N M_H}{r+a_H} \\ &- \frac{G_N M_{MN}}{\left[R^2 + \left[a_{MN} + (z^2 + b_{MN}^2)^{1/2}\right]^2\right]^{1/2}} \ .\end{aligned} \tag{4.6}$$

P14 chooses the value of the virial overdensity v to be $v = 340$, thus fixing c_v as c_{340}. P14 assumes $R_{\rm max} = 3R_{340}$ as the distance from the center of the Galaxy at which a body would be considered unbound, where R_{340} is simply the virial radius $r_v = r_s c_v$ of the NFW profile, calculated for $v = 340$. We keep the same choices.
In P14 the above mass model is used to estimate the mass of the Milky Way. In particular, M_{340} is used, which is the total mass (dark matter and baryons) contained inside a sphere of radius R_{340}.
In this model, the total mass inside a spherical shell of any radius r can be calculated simply as

$$M_{\rm int}(r) = M_{\rm int}^{NFW}(r) + M_{\rm int}^{H}(r) + M_{\rm int}^{MN}(r) \ . \tag{4.7}$$

P14 computes this quantity for $r = R_{340}$, thus using

$$M_{340} \doteq M_{\rm int}(R_{340}) = M_{\rm int}^{NFW}(R_{340}) + M_{\rm int}^{H}(R_{340}) + M_{\rm int}^{MN}(R_{340}) \ . \tag{4.8}$$

For the NFW profile, using the definition of R_{340} we have that $M_{\rm int}^{NFW}(R_{340}) = 340\varrho_c \frac{4}{3}\pi R_{340}^3$. For the Miyamoto Nagai disk, since $R_{340} \gg a_{MN}$, one can safely assume that almost all the mass of the disk is contained inside a sphere of radius R_{340}, so that $M_{\rm int}^{MN}(R_{340}) \approx M_{MN}$. Finally, the mass $M_{\rm int}^{H}(r)$ can easily be calculated from (A.5) for any r.

4.4 Converting P14 results into the v_c,v_{esc} plane

As we have already said, P14 repeated its analysis for the 3 cases: $v_c = 220$ km/s, $v_c = 240$ km/s and v_c free, obtaining different results, the main of which (that we are going to use) are summarized in table 4.2 below. Since we want to study the impact of the P14 results on DMDD, we are going to convert those results in the plane v_c,v_{esc}, which is more relevant to DMDD. Since the mass model has only two free parameters, we see that for every couple of values v_c, v_{esc} the local dark matter density $\varrho_\odot$ can be directly computed using the mass model. The correlations among these astrophysical parameters should be properly taken into account while computing DMDD limits. We are also going to consider independent estimates of v_c, in the way explained in the sequel.

[8] Again, this expression is the sum of the three components, given in the equations (A.2), (A.6) and (A.12).

4.4.1 From the constraints on M_{340},c_{340} to those on $v_{\rm esc}$,$v_{\rm c}$

The speed of a body which is on a circular orbit on the Galactic plane can be computed from the gravitational potential of the Milky Way as $v_{\rm c}^2\left(R,0\right)=R\frac{d\Phi(R,z)}{dR}\Big|_{z=0}$, where R and z are cylindrical coordinates. This circular speed in our Milky Way mass model can be computed as in equation (3.25) and reads:[9]

$$\begin{aligned} v_c^2\left(r\right) =& 4r_s^3\pi\varrho_s G_N\left[\frac{\ln\left(1+\frac{r}{r_s}\right)}{r}-\frac{1}{r_s+r}\right]+\frac{G_N M_H r}{\left(r+a_H\right)^2} \\ &+R\left[\frac{G_N M_{MN}}{\left[R^2+\left(a_{MN}+b_{MN}\right)^2\right]^{3/2}}\right] . \end{aligned} \tag{4.9}$$

The escape speed is set by the kinetic energy an object needs to get unbound, i.e. to reach a certain $R_{\rm max}$, it is thus defined as (see also equation (3.28)):

$$v_{\rm esc}\left(r_\odot\right)\doteq\sqrt{2\left|\Phi_{MW}\left(r_\odot\right)-\Phi_{MW}\left(R_{\rm max}\right)\right|} . \tag{4.10}$$

As we stated in section 4.3, the assumed mass model has only two free parameters, and we can recast equations so that the two free parameters are any of the couples of parameters c_{340} and M_{340}, ϱ_s and r_s, or v_c, $v_{\rm esc}$. Thus, a pair of ϱ_s, r_s (or equivalently a pair of M_{340}, c_{340}) converts into a pair of v_c, $v_{\rm esc}$, and viceversa. We thus converted in the v_c, v_{esc} plane, more relevant to DMDD, the P14 results for the 3 cases mentioned above (prior or not on v_c), which are summarized in table 4.2.

P14 assumption	$v_{\rm c}$ (km/s)	$v_{\rm esc}$ (km/s)	r_s (kpc)	ϱ_s (GeV/cm^3)	$\varrho_\odot$ (GeV/cm^3)
$v_{\rm c}=220$km/s	220	$533^{+54+109}_{-41-60}$	$16.4^{+6.6+13.6}_{-4.5-6.4}$	$0.42^{+0.26+0.48}_{-0.16-0.24}$	$0.37^{+0.02+0.04}_{-0.03-0.04}$
$v_{\rm c}=240$km/s	240	511^{+48}_{-35}	$7.8^{+3.8}_{-2.2}$	$1.92^{+1.85}_{-0.82}$	$0.43^{+0.05}_{-0.05}$
Free $v_{\rm c}$	196^{+26}_{-18}	537^{+44}_{-55}	$36.7^{+50.7}_{-19.0}$	$0.08^{+0.31}_{-0.07}$	$0.25^{+0.14}_{-0.12}$

[9] It is instructive to estimate the contribution that each component of the mass model provides to the circular speed at Sun's position ($r_\odot=8.28$ kpc). Using (A.7) and (A.13) we obtain $v_{\rm c}^H\left(r_\odot\right)\approx 82$ km/s, and $v_{\rm c}^{MN}\left(r_\odot\right)\approx 134$ km/s, which give a contribution of 157 km/s from the baryons all together. We can see using equation (3.25) that a circular speed at the position of the Sun of $v_{\rm c}\left(r_\odot\right)=220$ km/s requires $v_{\rm c}^{NFW}\left(r_\odot\right)\approx 153$ km/s. Thus, at the position of the Sun the contribution of the dark matter halo is roughly the same as that of the baryons altogether, and the disk contributes more than the bulge. Clearly the baryons alone are not enough to justify the observed value of the circular speed at Sun's position.

Table 4.2: Main results of the three analysis of P14, the ones with priors on v_c and the one without any prior. Let us remark that once you assume a value for v_c, and you have determined a value for v_{esc}, using the same equations (4.9) (4.10) you can determine the two free parameters of the model, r_s and c_v. We did it numerically, solving the system iteratively.

This is shown in Fig.4.2, where we have translated the constraints of the results of P14, shown in the previous section in figure 4.1, in constraints on the plane v_c, v_{esc}. In addition, we superimpose the two points (with error bars) corresponding to the best fit values obtained by P14 by means of the analysis with v_c fixed a priori.

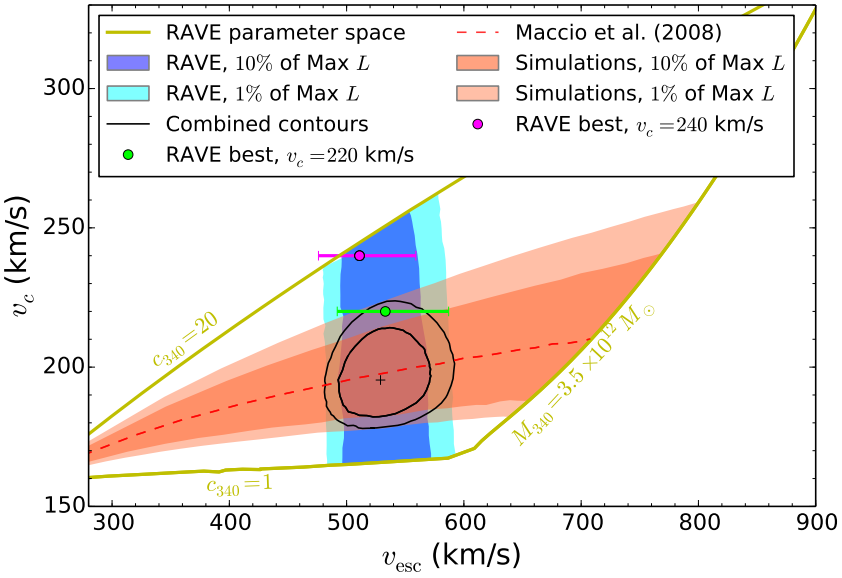

Figure 4.2: P14 parameter space (yellow contours), with the regions where their likelihood for free v_c decreases down to the 10% (blue) and 1% (cyan) of its maximum, and with the best-fit P14 results for fixed $v_c = 220$ km/s and for $v_c = 240$ km/s (with 90% C.L. error bars). Shown in pink are also the priors on the concentration from simulations used by P14, that as discussed below we do not take into account.

The large yellow contours in figure 4.2 encompass the same area encompassed by the whole area of figure 4.1. The dark blue and light blue areas are represented in this plane with the same colors as in the original plane. The constraints that the study in [1] puts on the possible values of v_{esc} and v_c are expressed by the blue (light and dark) areas of figure 4.2. A small (but non negligible) anti-correlation between v_{esc} and v_c is evident from the plot. We also report on the same figure the main results of the P14 analysis obtained with priors on v_c.

4.4.2 The local dark matter density

Since the mass model has only two free parameters, we see that for every couple of values v_c, v_{esc} the local dark matter density $\varrho_\odot$ can be directly computed using the mass model. This is clear from the plane of figure 4.3, where superposed to the same plane of 4.2 we now show (in gray) the curves of constant local dark matter density $\varrho_\odot$. It is clear from this figure that, because of the assumed Milky Way mass model, the results of P14 induce strong correlations among v_c, v_{esc} and the local dark matter density $\varrho_\odot$.

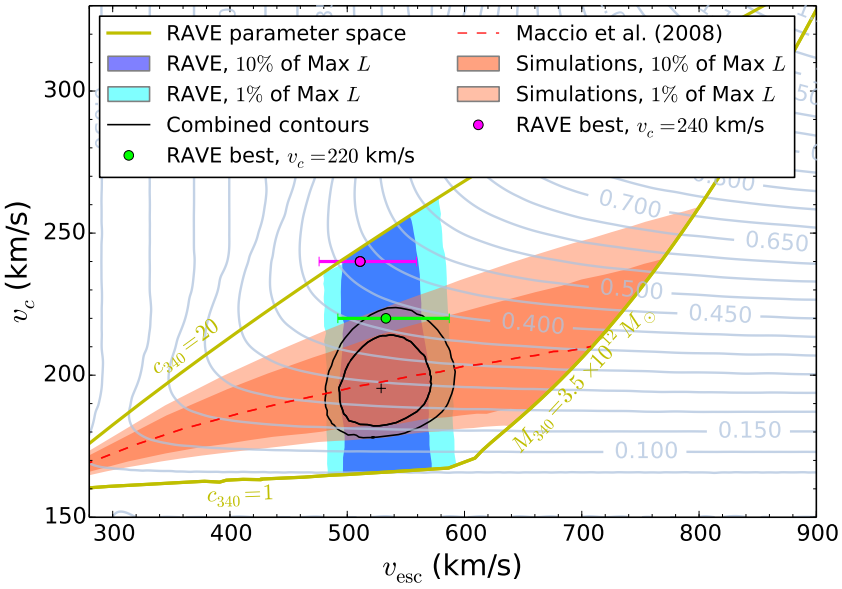

Figure 4.3: Same as figure 4.2 but showing in gray the curves of constant $\varrho_\odot$ (in GeV/cm^3).

4.4.3 Adding other observational constraints

We can see from figure 4.2 that the prior on the concentration (pink band) assumed by P14 forces their global best fit (in black) to a central value of $v_c = 196$ km/s, low w.r.t. observational estimates (see section 2.4.2). Anyway, this prior is based on [95] which studies cosmological simulations without baryonic content. Since we know today that baryons may play an important role in shaping the dark matter distribution on Galactic scales, we are going to relax this prior and thus to consider the entire range provided by the P14 likelihood in the plane of figure 4.2. By doing this we see from figure 4.3 that a strong correlation between $\varrho_\odot$ and v_c is present. Anyway, the circular speed v_c can be constrained independently of any assumption on the MWMM. For instance, as done in [40] it is possible to use measures of trigonometric parallaxes and proper motions of stars to reconstruct the local kinematics, where it is only necessary to consider the distance from the Sun to the

Galactic center, and the circular and peculiar motions of the Sun in the Milky Way rest frame.

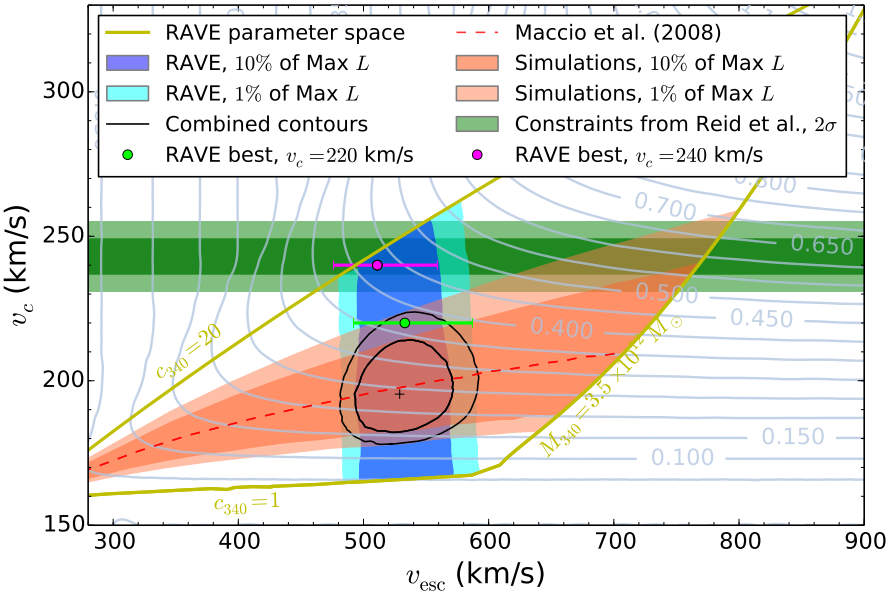

Figure 4.4: Same as 4.3, but showing also the additional constraints on v_c taken from the model B1 of [40].

As we have seen, often the ratio $v_c/r_\odot$ is better constrained than the two quantities separately. We would thus like to use such estimates to identify a range for v_c motivated by observations. We can rely on [40], which is a study based upon parallaxes and proper motions of masers associated with young and massive stars. We can implement its results in our work because some of its priors are similar to those of P14 (the details of [40] will be presented in chapter 4).
We will consider the Bayesian fit model called B1 in [40]. It assumes as a prior on the peculiar velocity of the Sun the same results (from [19]) employed by P14. Moreover, they determine a distance of the Sun from the Galactic center of $r_\odot = 8.33 \pm 0.16$ kpc, consistent with the assumption of $r_\odot = 8.28$ kpc made by P14. We have also verified that the slope of the rotation curve at the position of the Sun for the mass model employed in P14 is compatible with the one obtained for the B1 model in [40], which is

$$\frac{dv_c\,(R,z)}{dR}|_{R=r_\odot,z=0} = -0.2 \pm 0.4 \text{ km s}^{-1} \text{ kpc}^{-1} \,, \tag{4.11}$$

i.e. an almost flat rotation curve.
The estimate on the local circular speed obtained by the B1 model of [40], that we are going to use in our study, gives the result of

$$v_c = 243 \pm 6 \text{ km/s} \tag{4.12}$$

at 1σ, and ± 12 km/s at 2σ, which is the range that we will consider in the following in association with the P14 v_c-free analysis for the study of the astrophysical uncertainties on DMDD. This range is reported as a green band in figure 4.4. We can see that by crossing the v_c, v_{esc} band provided by the result of the P14 v_c-free analysis, this additional constraint defines a region, that we will use for the study of the astrophysical uncertainties on DMDD. Let us remark that this region extend up to values of the local dark matter density of $\varrho_\odot = 0.55$ GeV/cm^3, which is higher than the corresponding value in the SHM but consistent with the tendency found in recent studies as described in section 2.4.2. Anyway, we recall that the MWMM employed has been chosen only for consistency with the procedure employed by P14 (which assumed the same mass model), but it is rather simplistic and not meant to be used to provide precise estimates of the local dark matter density.

4.4.4 Speculating beyond P14

We may also note that the trend of the blue band is in contrast with the claim in P14 that their v_{esc} estimates anticorrelate with v_c as a result of their selection of stars from the RAVE catalog (biased to negative longitudes), which explains why v_{esc} decreases from 533 to 511 km/s as the prior on v_c is increased from 220 to 240 km/s. This anticorrelation is illustrated by the dotted lines in figure 4.5.
This contrast comes from the method used in P14 to extract the likelihood region in the c_{340}-M_{340} plane,[10] shown in their figure 4.1: the authors kept the posterior PDF of v_{esc} frozen to the shape obtained with $v_c = 220$ km/s, while varying only c_{340} and M_{340}. This means that they did not recompute the velocities of their stellar sample according to the changes in v_c induced by those in c_{340} and M_{340}. We remind that in principle the pair v_c, v_{esc} is strictly equivalent to the pair c_{340}-M_{340}, so we may have expected to recover the anticorrelation claimed for the former pair from the contours obtained for the latter.
While the goal of P14 in the v_c-free case was mostly to investigate how to improve the matching between Galactic models and the primary fit results, with a focus on the Milky Way mass, the above procedure somehow breaks the self-consistency of the analysis. This has poor impact on the Galactic mass estimate, which was the main focus in P14, but this affects the true dynamical correlation that v_{esc} should exhibit with the other astrophysical parameters. Unfortunately, improving on this issue would require access to the original data, which are not available to us. Therefore, we will stick to this result in the following, and further comment on potential ways to remedy this limitation at the qualitative level in section 4.6.3.

[10] We thank T. Piffl for having clarified this issue.

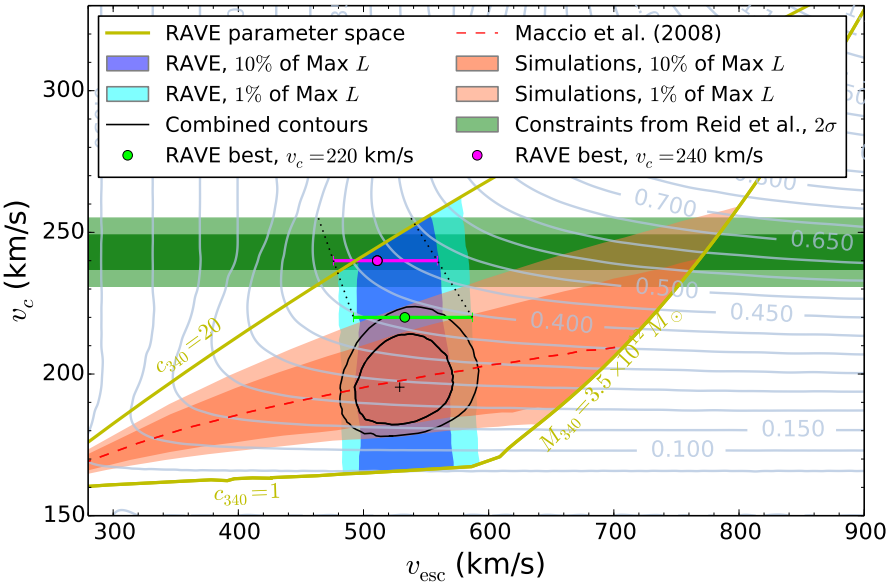

Figure 4.5: Same as figure 4.4, but illustrating through the black dotted lines the anticorrelation between $v_{\rm esc}$ and $v_{\rm c}$ described in this section. We published this figure in [2].

4.5 Ergodic dark matter phase-space distribution from the Eddington equation

Usually, DMDD limits are computed by means of the Standard Halo Model, in which the WIMP speed distribution is assumed to be a Maxwell-Boltzmann truncated at the escape speed as described in section 1.6.1. The more physically meaningful form is the one with the smooth cut-off, equation (1.61), which we recall:

$$f(\vec{v}) \doteq \frac{1}{N_{\rm esc}} \left(\frac{1}{\pi v_{\rm c}^2}\right)^{3/2} \left[e^{-|\vec{v}|^2/v_{\rm c}^2} - e^{-v_{\rm esc}^2/v_{\rm c}^2}\right] \Theta\left(v_{\rm esc} - |\vec{v}|\right) \ , \tag{4.13}$$

where $N_{\rm esc}$ is the normalization and Θ the Heaviside step function.
As we have seen in section 3.4, the Maxwell-Boltzmann distribution corresponds to a dark matter halo which is an isothermal sphere in the Galactic frame. In the Milky Way mass model considered in this chapter, the one fixed by P14, the dark matter profile under consideration is instead an NFW profile. Moreover, because of the by-hand cutoff at the escape speed, the above distribution is no more a solution of the Jeans equation, so it is not even self-consistent.
For these two reasons, we are now going to consider phase-space distributions for the dark matter that do not correspond to the Maxwell-Boltzmann speed distribution.

4.5.1 From the Milky Way mass model to the dark matter speed distribution

As we have seen in section 3.6, in order to build a self-consistent velocity distribution, we can consider as phase-space distributions functions of integrals of motion which automatically satisfy the Jeans equation. The simplest case occurs assuming spherical symmetry (of the total gravitational potential) and velocity isotropy (for the dark matter velocity distribution), so that the phase-space distribution becomes a function of the total energy $E = m\Phi + \frac{1}{2}mv^2$ only, which is an integral of motion. Such systems are called ergodic [17].
Under these assumptions we can use the Eddington equation [96], which allows to compute the phase-space distribution for the dark matter directly from the assumed gravitational potential of the Milky Way and the dark matter density profile. We wrote this equation in different ways as (3.82), (3.83) and (3.84), but let us recall for clarity its most common form:

$$f\left(\mathcal{E}\right) = \frac{1}{\sqrt{8}\pi^2}\left[\int_0^{\mathcal{E}} \frac{d^2\varrho}{d\Psi^2}\frac{d\Psi}{\sqrt{\mathcal{E}-\Psi}} + \frac{1}{\sqrt{\mathcal{E}}}\left(\frac{d\varrho}{d\Psi}\right)_{\Psi=0}\right] , \tag{4.14}$$

where $\Psi = -\Phi + \Phi_0$ is the relative gravitational potential of the Milky Way, $\mathcal{E} = -E/m + \Phi_0$ the relative energy per unit mass and Φ_0 a constant.
The local velocity distribution for the dark matter can then be computed as $f_{\vec{v}}^{\mathrm{erg}}\left(\left|\vec{v}\right|, r\right) = f\left(\mathcal{E}\right)/\varrho\left(r\right)$, which turns out to be actually a function of the modulus of $\vec{v}$ only (a direct consequence of the assumed velocity isotropy). Thus, it is enough to consider the dark matter speed distribution, which reads $f_v^{\mathrm{erg}}\left(v, r\right) = 4\pi v^2 f_{\vec{v}}^{\mathrm{erg}}\left(\left|\vec{v}\right|, r\right)$.
In practice, we solved numerically Eddington equation (easier to solve numerically in the form (3.84)) for the MWMM assumed by P14.
This procedure can be applied only to spherically symmetric systems, and the Milky Way mass model assumed by P14 is not, because of the disk which is instead axisymmetric, see (4.5). Anyway, since it does not dominate the potential at the position of the Sun ($r_\odot, z = 0$), it can be shown that we can force spherical symmetry while not affecting the circular velocity at the Sun's position. In fact, we can consider, instead of the axially symmetric spherical potential $\Phi\left(R, z\right)$ of equation (4.6), a spherically symmetric potential $\Phi'\left(r\right)$ obtained with the same dark matter halo and baryonic bulge as the one above, but with a spherical approximation of the disk. We just need to verify that Φ' gives in the disk (and in particular at Sun's position) the same circular velocity (so $v_{\mathrm{c}}^2\left(r_\odot, z = 0\right) = R\partial_R\Phi'\left(R, z\right)|_{R=r_\odot, z=0}$ must be satisfied) and the same internal mass given by Φ, and we can then apply the above procedure to Φ'. This approximation is valid when we compute the speed distribution for a point which lies in the Galactic disk (as it is the case here, since we are interested in computing this distributions at the position of the Sun).

4.5.2 The impact of baryons

We illustrate here the application of the Eddington procedure to compute the phase-space distribution, and then the speed distribution, of the dark matter that is described by the NFW profile lying in the gravitational potential described by the Milky Way mass model assumed by P14. This is the procedure that we will employ systematically in the next section to compute the speed distributions associated with the ergodic phase-space distributions that we are going to use to go beyond the Maxwell-Boltzmann approximation. We take here the opportunity to outline the modifications induced by the presence of the baryons.

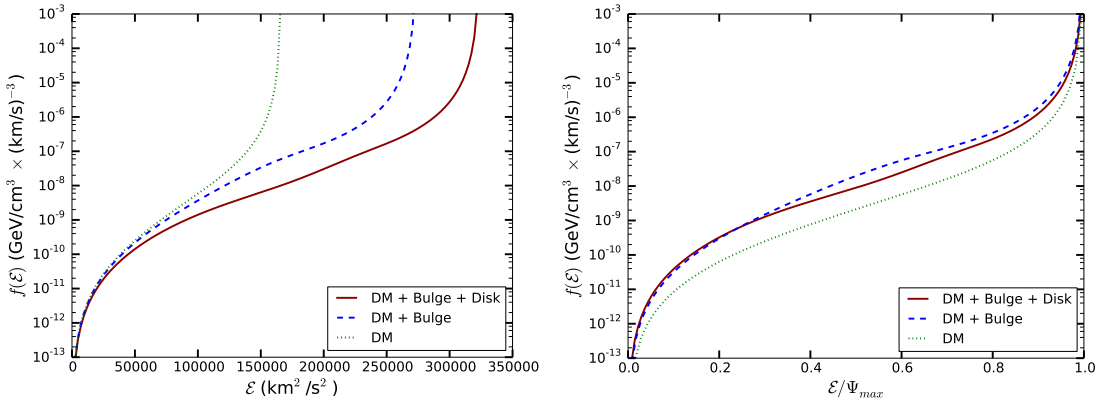

Figure 4.6: The $f(\mathcal{E})$ associated with the NFW dark matter profile of the Milky Way mass model with the parameters fixed at the values associated to the best fit point of the P14 analysis with prior $v_c = 240$ km/s. This phase-space distribution has been obtained applying Eddington equation to the NFW density profile. Three different cases are considered: the $f(\mathcal{E})$ associated to the NFW dark matter profile first in the presence of its gravitational potential only, then in the presence of the potential generated by itself (dark matter) plus the stellar bulge, and finally in the presence of the potential generated by the whole Milky Way mass model, i.e. dark matter plus baryons (bulge and disk). Left panel: the curves as a function of $\mathcal{E}$. Right panel: the same curves as a function of $\mathcal{E}/\Psi_{\rm max}$. The values of $\Psi_{\rm max}$ are 166285 km^2/s^2, 273806 km^2/s^2 and 323815 km^2/s^2, respectively for dark matter only, dark matter plus baryonic bulge and dark matter plus bulge and disk.

Figure 4.6 shows the phase-space distribution associated to the NFW profile with the parameters values associated to the best fit point of the P14 analysis with prior $v_c = 240$ km/s. We show three different cases: the $f(\mathcal{E})$ associated to the NFW dark matter profile in the presence of its gravitational potential only, then the $f(\mathcal{E})$ in the presence of the potential generated by itself (dark matter) plus the stellar bulge, and finally the $f(\mathcal{E})$ in the presence of the potential generated by the whole Milky Way mass model, i.e. dark matter plus baryonic bulge and disk.
As we can see, adding the baryons (i.e. adding the bulge and than the disk) has the effect of shifting the vertical asymptote of the phase-space distribution toward higher values of the relative energy $\mathcal{E}$ (which is positively defined). This can be

easily understood if we think that adding a baryonic component to the mass model means to add mass and thus to deepen the gravitational potential weel. A deeper potential weel allows for more energetic particles in the system, so the values allowed for $\mathcal{E}$ are higher.
It is now important to remark that, when we compute the speed distribution from the phase-space distribution, we do so for a fixed value of the distance from the Galactic center r. On the one hand, the phase-space distribution computed via Eddington equation is by construction a function of only one variable, $\mathcal{E}$. More precisely, The phase-space distribution depends on the phase-space variables, $\vec{r}$ and $\vec{v}$, only through $\mathcal{E}$, which is itself a function of these variables $\mathcal{E} = \mathcal{E}(\vec{r}, \vec{v})$. When we compute the speed distribution from the phase-space we thus reintroduce the dependence on $\vec{r}$ (more precisely r, because the system is spherically symmetric). It is very important to remark that, once we fix r to a certain value r_0 and compute $f_{\rm erg}(v, r_0)$, only a part of the corresponding $f(\mathcal{E})$ is accessible. This happens because the particles described by $f_{\rm erg}(v, r_0)$ have an energy which is $\mathcal{E} = \Psi(r_0) - \frac{1}{2}v^2$, which can thus range between zero and $\Psi(r_0)$. Thus, $\Psi(r_0)$, the depth of the potential well at r_0, defines the maximal allowed value for $\mathcal{E}$. On the other hand, $\mathcal{E} = 0$ corresponds to $v = v_{\rm esc}$, i.e. particles which have a kinetic energy equal (or bigger) than their potential energy can escape the potential weel of the Galaxy so they are no longer present (so the tail of the speed distribution vanishes at $v_{\rm esc}$).
In figure 4.7 we show $f_{\rm erg}(v, r_\odot)$, i.e. the dark matter speed distribution computed at the position of the Sun $r_\odot$ (in the Galactic reference frame), again for the three cases of figure 4.6, i.e. the NFW dark matter profile (with the parameters of the best fit point of the P14 analysis with prior $v_{\rm c} = 240$ km/s) in the presence of its gravitational potential only, then in the presence of the potential generated by itself plus the stellar bulge, and finally in the presence of the potential generated by the whole Milky Way mass model, dark matter plus baryonic bulge and disk. We can remark that, as can be understood from the discussion above on $v_{\rm esc}$, the high velocity tail (and thus $v_{\rm esc}$) of the speed distribution extends toward higher values of the velocity when we add the baryons. The peak of the distribution (and so the most probable speed) as well moves toward higher velocities when we add the baryons. Both facts clearly come from having added mass to the system, and then having deepened the gravitational potential weel.

4.5.3 Comparing the Maxwell-Boltzmann and the ergodic speed distributions

We now want to compare the Maxwell-Boltzmann speed distribution (of which we consider the smoothly cut version of equation (4.13)) and the ergodic speed distribution that we compute using the Eddington formula. We will compare them in the Galactic reference frame, remembering that we need to transform them into the corresponding distributions in the Earth reference frame in order to use them

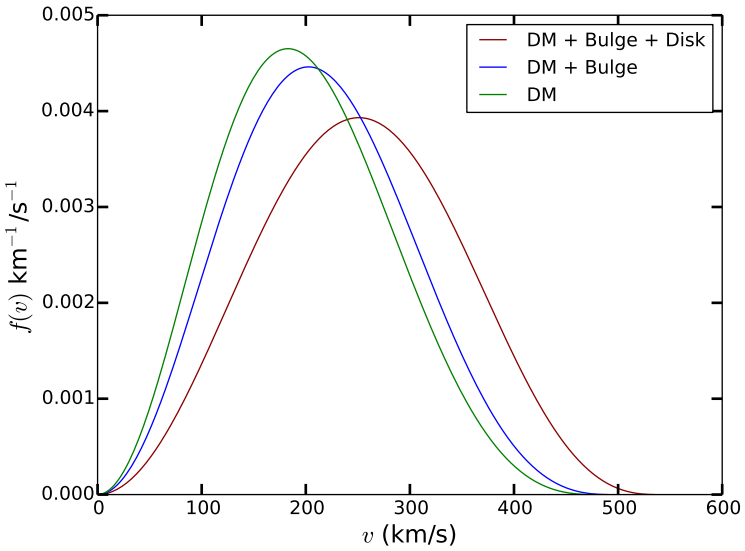

Figure 4.7: The speed distribution $f(v)$ associated with the NFW dark matter profile of the Milky Way mass model with the parameters fixed at the values associated to the best fit point of the P14 analysis with prior $v_c = 240$ km/s. These speed distributions come from the phase-space distributions of figure 4.6. Three different cases are considered: the NFW dark matter profile first in the presence of its gravitational potential only, then in the presence of the potential generated by itself plus the stellar bulge, and finally in the presence of the potential generated by the whole Milky Way mass model, i.e. dark matter plus baryons (bulge and disk).

for the DMDD-related computations we are interested in.
Firstly, we compare the Maxwell-Boltzmann and the ergodic distributions for different values of the distance r from the Galactic center. We use the MWMM already presented in this section, and for illustration we fix the parameters of the dark matter NFW halo at the values of $r_s = 20$ kpc and $c_{340} = 10$ (corresponding to roughly $\varrho_s = 0.25$ GeV/cm^3). The two speed distributions associated to the dark matter halo lying in the gravitational potential of the considered MWMM are shown in figure 4.8 for three different values of the distance from the Galactic center: $r = 0.1$ kpc, $r = 1$ kpc and $r = 10$ kpc. The Maxwell-Boltzmann speed distributions have been computed using the values of $v_c(r)$ and $v_{esc}(r)$ associated to the MWMM in use, and computed at the corresponding distance r from the Galactic center.
As we can appreciate from figure 4.8, the peak of the Maxwell-Boltzmann distribution shifts toward higher values of v when we increase the distance from the Galactic center, due to the behavior of $v_c(r)$, since the most probable speed of the distribution, i.e. the one at which the peak occurs, is given by $v_0 = v_c(r)$. Since as we have shown in equation (1.52) the velocity dispersion of the Maxwell-Boltzmann velocity distribution (i.e. of the vector, while in the figure we are showing the speed distribution, i.e. the distribution of the modulus of $\vec{v}$, the two of them being

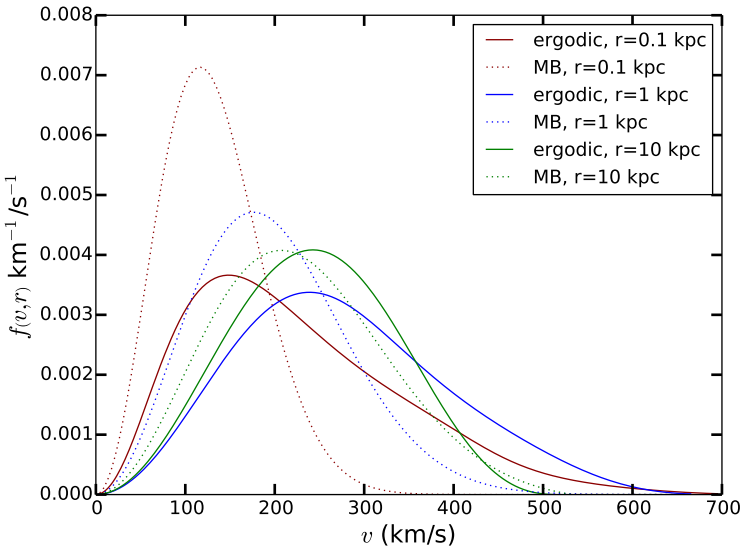

Figure 4.8: Comparing the Maxwell-Boltzmann and the ergodic speed distributions obtained from the Eddington procedure, at different distances from the Galactic center. The MWMM is the one fixed in the beginning of this chapter, and the parameters of the NFW halo are fixed at the values of $r_s = 20$ kpc and $c_{340} = 10$ (corresponding to roughly $\varrho_s = 0.25$ GeV/cm^3).

related by $f_v^{MB} = 4\pi v^2 f_{\vec{v}}^{MB}$) is related to the most probable speed as $v_0 = \sqrt{2/3}\sigma_{\vec{v}}$, also the width of the peak of the Maxwell-Boltzmann increase while increasing r.[11] Finally, we remark that the high-velocity tail of the Maxwell-Boltzmann extends toward higher velocities while r increases, as v_{esc} does. However, it should be remarked that, due to the above relation between the most probable speed and the width of the peak, these tails are quite thin.

On the other hand, it is clear from figure 4.8 that the behavior of the ergodic distributions obtained from the Eddington procedure is less simple to guess. The high velocity tail, which by construction ends at the escape speed, extends to lower values of v when increasing r, because the escape speed has the same behavior. On the other hand, the position of the peak does not follow from the circular speed, and neither does the width of the peak. The high velocity tails are this time considerably fatter and elongated w.r.t the low velocity ones, especially at low r. We can clearly see that the ergodic speed distribution at low r is very different from the corresponding Maxwell-Boltzmann, while the similarity between the two increases while augmenting r. In particular, we can see that at $r = 10$ kpc, i.e. at distances from the Galactic center similar to the distance of the Sun, the two

[11] Actually, the relations $v_0 = v_c(r)$ and $v_0 = \sqrt{2/3}\sigma_{\vec{v}}$ are exact for a Maxwell-Boltzmann without truncation. Since here we are truncating the Maxwell-Boltzmann at the escape speed, these relations have to be considered in our case just indicative. Even if quantitatively the difference is small, this shows that the Maxwell-Boltzmann, once truncated, is no more self-consistent, and so the SHM neither.

distributions are much more similar, which tells us that the use of the Maxwell-Boltzmann for direct detection is in practice a viable approximation. However, we see that some differences are still there, and they will have a non-negligible impact.

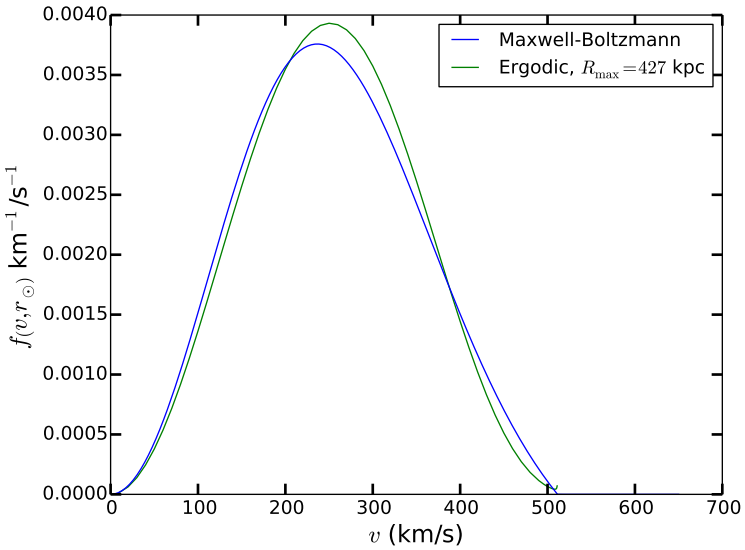

Figure 4.9: Comparing the Maxwell-Boltzmann speed distribution and the ergodic speed distribution obtained from the Eddington procedure. The MWMM is the one fixed in the beginning of this chapter. The parameters of the Maxwell-Boltzmann are those corresponding to the best fit point of P14 with prior on $v_c = 240$ km/s, and correspondingly $v_{esc} = 511$ km/s. Those of the ergodic distribution are the ones corresponding to the same best fit point, i.e. the values of r_s and of ϱ_s from table 4.2. We remind that the ergodic speed distribution has been computed using $R_{max} = 427$ kpc, the effect of which is widely discussed in section 4.5.4.

Figure 4.9 shows a comparison between the Maxwell-Boltzmann speed distribution and the ergodic speed distribution obtained from the Eddington procedure. The parameters of the Maxwell-Boltzmann are those corresponding to the best fit point of P14 with prior on $v_c = 240$ km/s, and correspondingly $v_{esc} = 511$ km/s, while those of the ergodic distribution are the ones corresponding to the same best fit point, i.e. the values of r_s and of ϱ_s from table 4.2. We can notice that the peaks of the two distributions are different, as the widths of the distributions themselves. As already stated, while for the Maxwell-Boltzmann the most probable speed is related to the circular speed and to the velocity dispersion, this is not the case for the ergodic speed distribution. Also the high velocity tails are different, with a fatter tail for the Maxwell-Boltzmann w.r.t the ergodic one. Moreover, as we have seen the peak of the Maxwell-Boltzmann varies a lot with the circular speed, while the one of the ergodic distribution is almost unaffected.

4.5.4 The role of $R_{\rm max}$

As we have seen, P14 defines in (4.4) the escape speed as the speed necessary to reach a distance from the Galactic center of $R_{\rm max}$. We presented the same definition in chapter 2 as (3.27), and at that time we pointed out that, while the usual definition of the escape speed (3.26) is suitable for isolated systems, like for instance a star, the definition which includes $R_{\rm max}$ is more appropriate for systems like the Galaxy, which are not isolated because surrounded by other galaxies.
The choice made by P14 is to set the value of the distance from the Galactic center at which an object is considered to be unbound $R_{\rm max}$ to the value of $3R_{340}$, as an educated guess.[12] This provides values of $R_{\rm max}$ that are between 430 kpc and 530 kpc in the simulations considered by P14. For the real Galaxy, the best fit of the analysis worked out by P14 assuming $v_{\rm c} = 220$ km/s (which obtained 533^{+54}_{-41} km/s) corresponds to an $R_{\rm max}$ of ≈ 490 kpc, while the best fit of the analysis worked out by P14 assuming $v_{\rm c} = 240$ km/s (which obtained 511^{+48}_{-35} km/s) corresponds to $R_{\rm max} \approx 427$ kpc.
The nearest major galaxy to the Milky Way, the Andromeda Galaxy (also known as M31), is located at approximately 780 kpc from the Earth, and it has a mass of the same order of magnitude of the Milky Way. Thus, the choice of P14 of taking $R_{\rm max} = 3R_{340}$ provides values of $R_{\rm max}$ that are around half way between M31 and us: an object which could reach such a distance could leave the Milky Way for instance because captured by the gravitational potential of M31. We recall anyway that the potential slowly changes with radius, so the results of P14 are rather insensitive to small changes in the above definition.
For consistence with the analysis worked out by P14, in the work presented in this chapter we took into account the same definition of the escape speed including R_{max}. Even if it does not play a major role in the analysis worked out in this chapter, in this section[13] we want to briefly outline which is the impact of including this $R_{\rm max}$ in the definition of the escape speed on the phase-space distributions obtained from the Eddington equation for the mass model considered by P14, and on the associated speed distributions.
First of all, considering an object unbound at a finite $R_{\rm max}$ provides lower values (in modulus) for the gravitational potential Φ, and thus lower values of Ψ. This can be seen by comparing the values of $\Psi_{\rm max}$ reported in the legend of figure 4.6 with those of figure 4.10. As a consequence, obviously also the values of the escape speed are lower (since they scale as the square root of the modulus of the potential).
The impact of a finite $R_{\rm max}$ on the phase-space distribution $f(\mathcal{E})$ obtained from Eddington equation can be clearly seen comparing figure 4.6 with figure 4.10, where we show the $f(\mathcal{E})$ associated with the NFW dark matter profile of the Milky Way mass model assumed, with the parameters fixed at the values associated to the best fit point of the P14 analysis with prior $v_{\rm c} = 240$ km/s. Adding the cutoff at $R_{\rm max}$

[12] We remember that we can compute R_{340} as $R_{340} = r_s c_{340}$.

[13] We warmly thank Benoit Famaey for useful discussions on the subject of this section, and more in general on the astrophysics involved in this work.

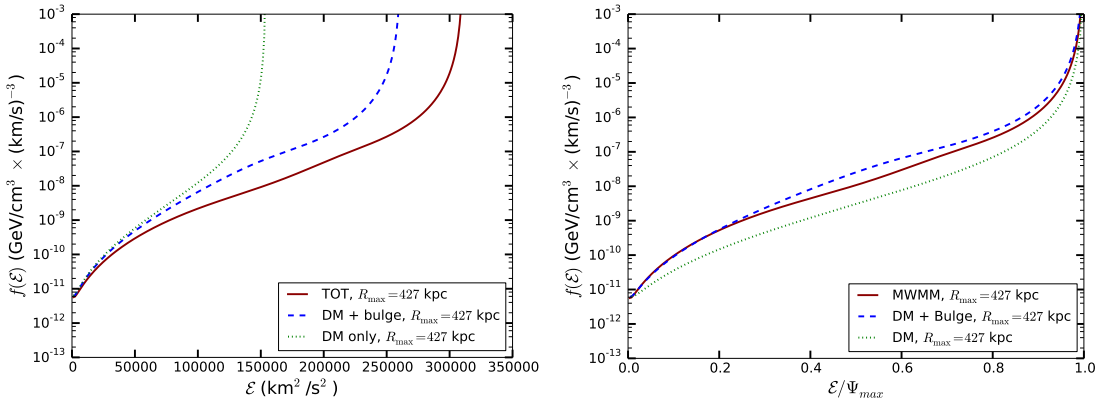

Figure 4.10: The $f(\mathcal{E})$ associated with the NFW dark matter profile of the Milky Way mass model with the parameters fixed at the values associated to the best fit point of the P14 analysis with prior $v_c = 240$ km/s, as in figure 4.6, but with the cutoff at $R_{\rm max}$ in the definition of the escape speed. The value of $R_{\rm max} = 427$ kpc is the one associated with the parameters of the halo for the best fit point with prior $v_c = 240$ km/s, computed as $R_{max} = 3R_{340} = 3r_s c_{340}$. The impact of adding the cutoff at $R_{\rm max}$ in the definition of the escape speed is evident as the fact that the curves do not tend toward zero when approaching $\mathcal{E} = 0$ s^2/km^2. The values of $\Psi_{\rm max}$ are 154072 km^2/s^2, 261442 km^2/s^2 and 310948 km^2/s^2, respectively for dark matter only, dark matter plus baryonic bulge and dark matter plus bulge and disk. As expected these values are slightly decreased w.r.t. the corresponding ones found for the case without $R_{\rm max}$ shown in figure 4.6. Left panel: the curves as a function of $\mathcal{E}$. Right panel: the same curves as a function of $\mathcal{E}/\Psi_{\rm max}$.

in the definition of the escape speed leads to the fact that the curves do not tend toward zero when approaching $\mathcal{E} = 0$, as they do when no $R_{\rm max}$ is considered. The non-zero value of $f(\mathcal{E})$ at $\mathcal{E} = 0$ comes from the second term in Eddington equation (3.83), for which $\Psi = 0$ now means $r = R_{\rm max}$ and not $r = \infty$. This is particularly interesting as that term is sometimes neglected in computing Eddington equation. The impact of $R_{\rm max}$ on the $f(v)$ obtained from Eddington equation can be understood by comparing figure 4.7 with figure 4.11, where we show the speed distributions $f(v)$ associated with the NFW dark matter profile of the Milky Way mass model considered with the parameters fixed at the values associated to the best fit point of the P14 analysis with prior $v_c = 240$ km/s. These speed distributions arise respectively from the phase-space distributions of figure 4.6 (which do not include any $R_{\rm max}$ in the definition of the escape speed) and that of figure 4.10 (which include $R_{\rm max}$). The impact of adding the cutoff at $R_{\rm max}$ in the definition of the escape speed is clearly visible in the high velocity tail of the speed distribution: when $R_{\rm max}$ is considered, the escape speed is lowered, and the speed distribution, instead of decreasing toward zero (and reach it at $v = v_{\rm esc}$, where the escape speed is now the one computed using $R_{\rm max}$), decreases up to a certain value of v close to $v_{\rm esc}$, but then before reaching zero it presents a small increase when approaching

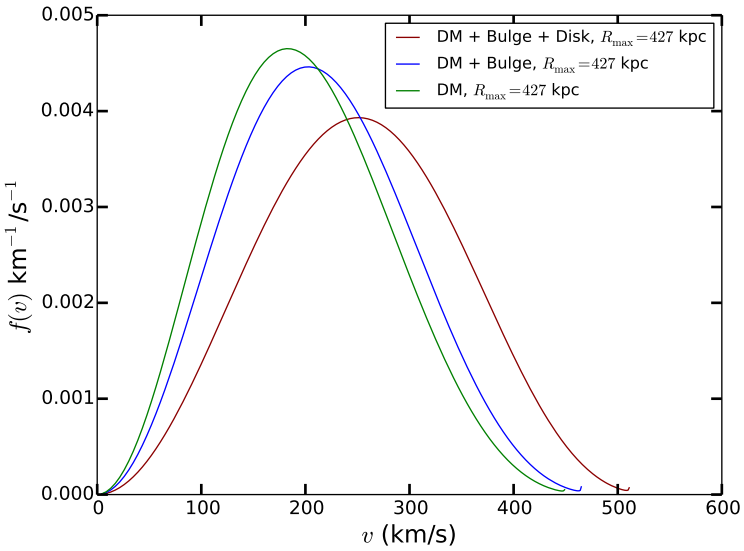

Figure 4.11: The speed distribution $f(v)$ associated with the NFW dark matter profile of the Milky Way mass model with the parameters fixed at the values associated to the best fit point of the P14 analysis with prior $v_c = 240$ km/s, as in figures 4.7 but with the cutoff at $R_{\rm max}$ in the definition of the escape speed. These speed distributions come from the phase-space distributions of figure 4.10. The value of $R_{\rm max} = 427$ kpc is the one associated with the parameters of the halo for the best fit point with prior $v_c = 240$ km/s, computed as $R_{max} = 3R_{340} = 3r_s c_{340}$. The impact of adding the cutoff at $R_{\rm max}$ in the definition of the escape speed is clearly visible in the high velocity tail of the speed distribution: when $R_{\rm max}$ is added, the escape speed is lowered, and the speed distribution, instead of going toward zero, has a small increase when approaching the escape speed.

the new escape speed.[14]

This effect can be more or less prominent depending on the value of $R_{\rm max}$ and the value of r at which the speed distribution is computed. For the values of $R_{\rm max}$ typical of P14 and for $r = r_\odot$, as we can see from figure 4.11 the effect is present, but not very prominent with respect to the size of the whole speed distribution.

Including $R_{\rm max}$ in our procedure is necessary for consistence with the definition of the escape speed employed by P14, and it allows us to obtain ergodic speed distributions that end at the correct escape speed (i.e. the one corresponding to the values of the mass model parameters used to compute it via Eddington equation). On the other hand, the growing of $f(v)$ when it approaches $R_{\rm max}$ is not a physical effect: it is due to the fact that with the definition of the escape speed including $R_{\rm max}$ we are somewhat forcing a part of the population of dark matter particles described by $f(v)$ to have velocities smaller than the v_{esc} computed with $R_{\rm max}$, while they would otherwise occupy the tail extending till the value of $v_{\rm esc}$ computed without $R_{\rm max}$, larger than that with $R_{\rm max}$. Thus, when this effect is present in

[14] Let us remark that, a part from this effect at high velocities, the distributions obtained with and without $R_{\rm max}$ are the same.

the speed distributions that we derive from the mass model employed by P14, we employ an exponential cutoff to obtain an $f(v)$ which decreases and reaches zero at $v_{\rm esc}$ (the one computed with $R_{\rm max}$). We also normalize the distribution so obtained to unity, because this normalization, present in the $f(v)$ obtained from Eddington equation, is lost when using the above cutoff.
Let us conclude by saying that we had to define the escape speed using $R_{\rm max}$ for consistence with P14 (motivated by the fact, as stated above, that the Galaxy is not an isolated system). We thus faced the effect that this has on the very end of the high velocity tail of the speed distribution, we asked ourselves questions about this effect, and we finally dealt with it in the way that appeared to us the most consistent, which we described above.

4.6 DMDD limits from the P14 estimates of $v_{\rm esc}$ and related astrophysical uncertainties

We are now going to translate the P14 estimates into DMDD limits, focusing on the spin-independent interpretation of the elastic scattering of a WIMP (of mass m_χ) off a nucleus (of atomic number A and mass m_A), and no isospin violation. To understand the impact of the above parameters on DMDD limits, we need to recall the master equation (2.21), from which we have that the differential event rate per atomic target mass in an experiment is:

$$\frac{dR}{dE_r}(E_r) = \frac{\varrho_\odot \sigma_{pSI} A^2}{2 m_\chi \mu_{\rm p}^2} F^2(E_r) \int_{|\vec{v}|>v_{min}(E_r)} d^3\vec{v} \frac{f_\oplus(\vec{v},t)}{|\vec{v}|} \ , \tag{4.15}$$

with $\mu_{\rm p}$ the WIMP-proton reduced mass, E_r the recoil energy, σ_p the WIMP-nucleon cross section, $F(E_r)$ the nuclear form factor (assumed of the Helm type), and $v_{min} = \sqrt{m_A E_r/(2\mu_{\rm p})}$ the minimal velocity that a WIMP needs to transfer to a nucleus the recoil energy E_r. $f_\oplus(\vec{v},t)$ is the dark matter velocity distribution in the Earth reference frame obtained from the one in the Galactic frame via a Galilean transformation. Let us remark that, as explained in chapter 2, when computing DMDD limits we also take into account the experimental efficiency, the energy resolution of the detector, the fractions of atomic targets, the isotopic compositions for each target element, and we take the time average of equation 4.15.
For illustration, we will compute the DMDD limits using the results of the most constraining (in different WIMP-mass ranges) experiments at the moment of writing: LUX [24] (a reference for xenon experiments), SuperCDMS [32] (a reference for Germanium experiments), and CRESST II [34] (a reference for multitarget experiments).
Before converting P14 results on $v_{\rm esc}$ in terms of DMDD limits, we recall that they affect the whole WIMP velocity distribution ($v_{\rm c}$, $v_{\rm esc}$, and the velocity dispersion) as well as the local dark matter density $\varrho_\odot$, which will now be different w.r.t the ones of the SHM. Thanks to equation 4.15, we have already outlined in section

2.4.3 how the astrophysical parameters affect the exclusion curves. We just remind that the sum $v_{esc} + v_c$ impacts on the position of the asymptote of the limit at low WIMP mass and v_c on the position of the maximum of sensitivity of the experiment on the m_χ axis, while $\varrho_\odot$ produces a linear vertical translation of the entire curve. Figure 4.3 helps us to notice a few features from P14 results. First, we see that there is a strong correlation between the circular speed v_c and the local dark matter density $\varrho_\odot$, while the latter is poorly correlated with v_{esc}. Second, we note that though the two P14 best-fit points with priors on v_c exhibit an anticorrelation between v_c and v_{esc}, this is no longer the case when v_c is left free. This implies that the v_c-free case would provide constraints on v_{esc} independent of v_c and $\varrho_\odot$.
Since there are different choices in P14 for the priors on v_c as well as for the prior on the concentration of the NFW halo, there could be different ways to investigate how the constraints on v_{esc} affect the DMDD exclusion curves. In this work we will first consider the three P14 results independently before comparing them together.

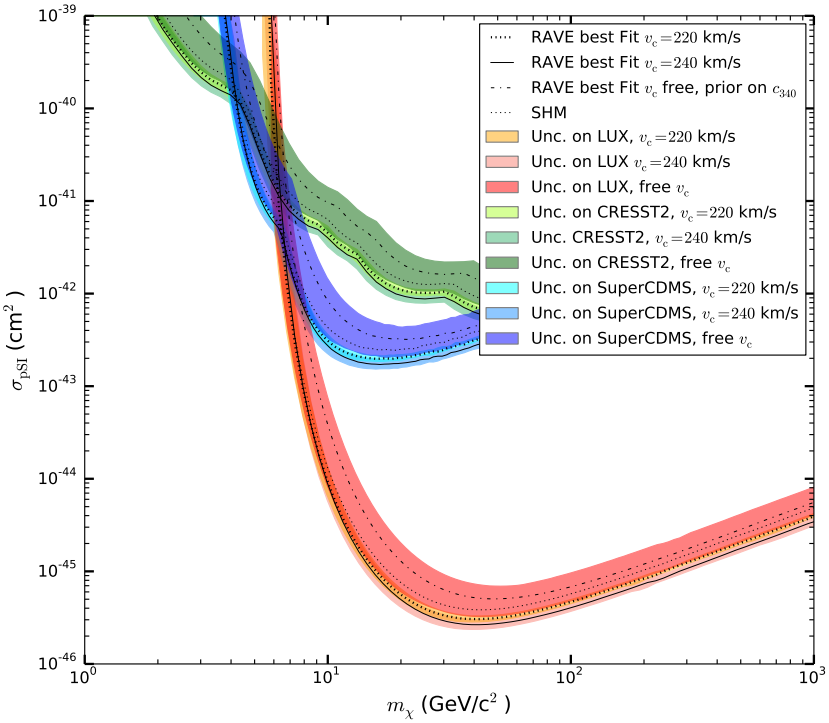

Figure 4.12: Exclusion curves obtained from the uncertainty contours associated with the astrophysical configurations derived from the three P14 best-fit points: the one with prior $v_c = 220$ km/s and associated 90% CL error bar, the one with prior $v_c = 240$ km/s and associated 90% CL error bar, and the one with free v_c (plus an additional prior on the concentration) and associated uncertainty band corresponding to 1% of maximum likelihood in the M_{340}-c_{340} plane. We published this figure in [2].

For illustration, in 4.12, we show the exclusion curves obtained in the σ_{pSI},m_χ plane with the uncertainty contours associated with the astrophysical configurations derived from the three P14 best-fit points:

- the best-fit point with prior $v_c = 220$ km/s and associated 90% CL error bar,
- the best-fit point with prior $v_c = 240$ km/s and associated 90% CL error bar,
- the best-fit point with free $v_{\rm c}$ (plus an additional prior on the concentration) and associated uncertainty band corresponding to 1% of maximum likelihood in the M_{340}-c_{340} plane.

These curves have been derived by using the ergodic speed distribution obtained from Eddington equation in section 4.5, which self-consistently correlates the dark halo parameters with $v_{\rm esc}$ and $v_{\rm c}$. We also report on the same plot the exclusion curves calculated from the SHM (the parameters of which are given in section 1.8). We note that the best-fit points associated with priors on $v_{\rm c}$ lead to similar curves and bands, in particular in the low WIMP mass region. This is due to the anticorrelation between $v_{\rm c}$ and $v_{\rm esc}$, which is such that the sum $v_c + v_{\rm esc}$, relevant to characterize the WIMP mass threshold, remains almost constant. From 4.3, we also see that $\varrho_\odot$ varies over the range of values $\approx [0.35, 0.47]$ GeV/cm^3 for these two points, which leads to less than $\pm 15\%$ of relative difference in the predicted event rate. In contrast, the exclusion curves associated with the $v_{\rm c}$-free case have a slight offset toward larger WIMP masses while lying slightly above the others with a larger uncertainty. This is due to the prior on the concentration that forces small values of $v_{\rm c}$ while not affecting $v_{\rm esc}$, and consequently to the lower values of $\varrho_\odot$ spanning the range $\approx [0.15, 0.35]$ GeV/cm^3. In comparison, the SHM curves (aimed at reproducing the limits published by the experimental collaborations) lie in between, and are less constraining than the P14 parameters with priors on $v_{\rm c}$. We will now describe in detail, one by one, the results obtained firstly for the case with prior $v_{\rm c} = 240$ km/s, secondly for the $v_{\rm c}$-free case, and finally for another case which will bring us to speculate beyond the results of P14.

4.6.1 DMDD limits from the P14 best-fit point with prior $v_{\rm c} = 240$ km/s

We first considered the P14 best-fit point with prior $v_{\rm c} = 240$ km/s, likely the most motivated case given the recent estimates (e.g. [40], see section 2.4.2). Figure 4.13 shows the exclusion curves and the associated 90% C.L. uncertainties for this configuration. The CRESST-II, SuperCDMS and LUX limits are shown respectively in the left, middle and right panels. The absolute and the relative uncertainties are shown in the top and, respectively, in the bottom panels. We compare the limits obtained from the ergodic speed distribution to those calculated from the SHM model on the one hand, and from the Maxwell-Boltzmann with the P14 values for the astrophysical parameters on the other hand.
Comparing our results with those obtained for the SHM, we find that the former are more constraining by $\sim 40\%$ in a wide range of high WIMP masses, due to the value of $\varrho_\odot = 0.43 \pm 0.05$ GeV/cm^3 (inferred from the P14 escape speed estimate

of $v_{\rm esc} = 511^{+48}_{-35}$ at 90% CL), higher than the SHM one ($\varrho_\odot = 0.3$ GeV/cm^3) over a large part of the depicted WIMP mass range.
At very low WIMP masses the SHM beats the ergodic one because $v_{\rm esc}$ itself affects the effective WIMP mass threshold: it is set to 544 km/s in the SHM ($v_c + v_{\rm esc} = 764$ km/s), while the P14 best-fit point (for $v_c = 240$ km/s) corresponds to $v_{\rm esc}$=511 km/s ($v_c + v_{\rm esc} = 751$ km/s).
We also show the effect of using a Maxwell-Boltzmann velocity distribution, instead of a more consistent ergodic one together with the correctly correlated astrophysical parameters. This impacts especially at low WIMP masses, because of significant differences between the high-velocity tail of the two distributions. Comparing on each plot the limits obtained with the same astrophysical parameters, but respectively with a Maxwell-Boltzmann or an ergodic velocity distribution, we see that the shape of the distribution plays a role where its tail (less step for the Maxwell-Boltzmann) does, mainly at low WIMP masses. The Maxwell-Boltzmann is actually more constraining at energy recoils leading to $v_{\rm min}$ larger than the peak velocity of the phase-space distribution. This is because the Maxwell-Boltzmann exhibits a less steep tail at high velocities than the ergodic one. This illustrates why not only is the escape speed important in the low WIMP mass region, but also the high-velocity tail of the speed distribution, and thereby the speed distribution itself.

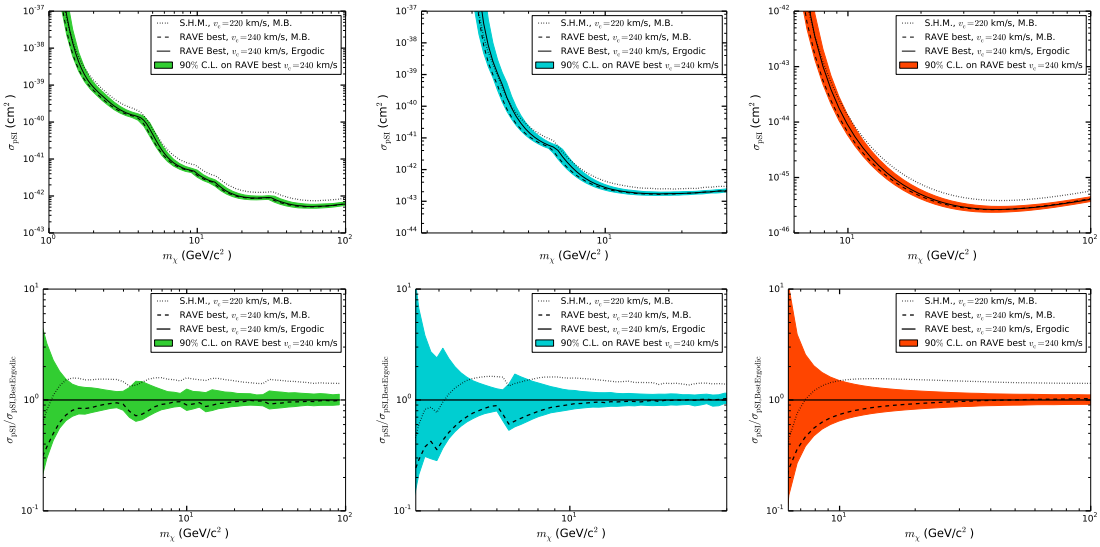

Figure 4.13: Top panels: experimental 90% C.L. exclusion curves, calculated using the P14 result for the $v_{\rm c} = 240$ km/s analysis. Bottom panels: relative uncertainties with respect to the $v_c = 240$ km/s best-fit point of P14. Left panels: CRESST-II data. Middle panels: SuperCDMS data. Right panels: LUX data. See the text for details. We published these figures in [2].

The relative uncertainties in the exclusion curves for this P14 point saturate at $\sim \pm 10\%$ at high WIMP masses, value set by the allowed range in $\varrho_\odot$, and they

degrade toward very low WIMP masses, where the high-velocity tail and $v_{\rm esc}$ come also into play, and the maximum possible recoil energy approaches the threshold energy. This can clearly be observed in the case of LUX, the efficiency of which drops for WIMP masses below ~ 8 GeV (bottom right panel of 4.13).
Some of the bumps in figure 4.14 in the case of CRESST2 come from the presence of more than one target nucleus (the others, similar to those in SuperCDMS, from the impact of the observed nuclear-recoil-like events on the maximum gap method that we used to derive the exclusion curves). This shows that employing different target nuclei in a detector helps to reduce the astrophysical uncertainties (as well as combining different experiments). A similar complementarity arises when considering experiments based on different target nuclei.
It is still difficult to draw strong conclusions on the overall uncertainties in the exclusion curves induced by the P14 results without questioning more carefully the P14 initial assumptions and priors. We will do so in the next subsections. We can already emphasize that a self-consistent use of these estimates of $v_{\rm esc}$ is not straightforward (for instance, one cannot just vary $v_{\rm esc}$ in a given C.L. range irrespective of the other astrophysical parameters). A proper use must take the correlations between all the relevant astrophysical parameters into account. Indeed, we have just seen that not only the WIMP mass threshold is affected (a direct consequence of varying $v_{\rm esc} + v_c$), but also the global event rate is, because $\varrho_\odot$ must be varied accordingly.

4.6.2 DMDD limits from the P14 $v_{\rm c}$-free analysis, with additional constraints

In this section, we are going to examine the P14 results in light of independent constraints on the astrophysical inputs. As we have seen, P14 provided three best-fit configurations each based on different priors. The most conservative approach would be to relax fixed priors as much as possible, as all astrophysical parameters are affected by uncertainties. In this section we will therefore focus on the $v_{\rm c}$-free case.
We do not use the same prior on the concentration of the dark matter halo of P14 (represented by the pink band in figure 4.4) because it is based on cosmological simulations without baryons. Instead, we combine the region provided by the $v_{\rm c}$-free analysis of P14 in the plane of figure 4.4, with the constraint on $v_{\rm c}$ published in [40] and already described in section 4.4.3, which is independent on any Milky Way mass model because based on geometric quantities only (parallaxes and proper motions of masers). For the reasons explained in section 4.4.3, we selected from [40] the results corresponding to the model B1, which are $v_{\rm c} = 243 \pm 12$ km/s at 2σ (shown as a green band in figure 4.4). As already stated, to ensure consistency we have verified that the other quantities estimated in [40], in particular the Sun distance from the Galactic center and the local radial derivative of the circular velocity, have values compatible with those of the Milky Way mass model we use

(which for consistency we had to chose to be the same as the mass model used in P14).

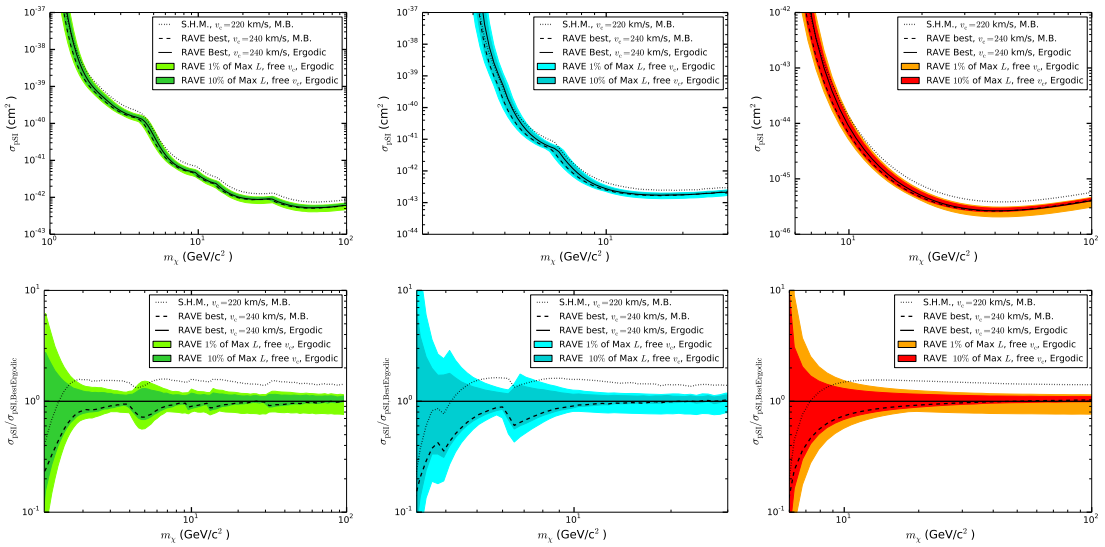

Figure 4.14: Upper panel: Experimental 90% C.L. exclusion curves, calculated using a combination of the P14 v_c-free analysis with the additional constraints on v_c from [40] presented in the text. Lower panel: corresponding relative uncertainties. From left to right: CRESST2, SuperCDMS, LUX. We published these figures in [2].

To compute the DMDD limits associated to the v_c-free analysis of P14, we used the region of the plane in figure 4.4 where the P14 blue band crosses the green band associated with the results of [40]. In the above region the allowed values of the local dark matter density reach up to $\varrho_\odot \approx 0.57$ GeV/cm^3 (as can be understood by looking at the gray contours in figure), i.e. they are higher than those of the SHM, but similar to those found in recent studies [38]. We show in 4.14 the uncertainties obtained when considering the combination of the P14 v_c-free case with the additional constraints on v_c discussed above.
The behavior is qualitatively similar to the one already described for the $v_c = 240$ km/s case in figure 4.13, only the uncertainties change. We also report the exclusion curves obtained with the P14 results with prior $v_c = 240$ km/s, which are shown to lie within the contours of the v_c-free case (plus independent and additional constraints on v_c). This can easily be understood from 4.4. The relative uncertainties saturate at values of $\approx \pm 20\%$ at large WIMP masses, due to the allowed range of $\varrho_\odot \in [0.37, 0.57]$ GeV/cm^3 while they further degrade toward low WIMP masses because of the additional effects from v_{esc} and v_c.

4.6.3 Speculating beyond P14

In the P14 analysis with fixed v_c an anticorrelation is present between v_c and v_{esc}, which is absent in the v_c-free analysis due to the procedure employed, as explained

in section 4.4.4. This anticorrelation is due to the fact that the majority of the stars studied are located at negative Galactic longitudes, so it is consistent to take it into account. Because of the caveats affecting the v_c-free case of P14 (see the discussion in 4.4.4), and in order to try to recover a better consistency in the Galactic mass modeling, we may try to further speculate about what a self-consistent v_c-free band would look like. The P14 argument that v_c and v_{esc} should linearly anticorrelate is sound because it is based on a purely geometrical reasoning (the fact that the stellar sample is biased toward negative longitudes).
We thus "speculate" beyond the P14 analysis, suggesting that the most self-consistent use of the RAVE results would be to consider the region which takes into account this anticorrelation, represented in figure 4.5 by the black dotted lines. As before, we also investigate how the uncertainties export to DMDD limits, using again the additional 2-σ constraints on v_c from [40].

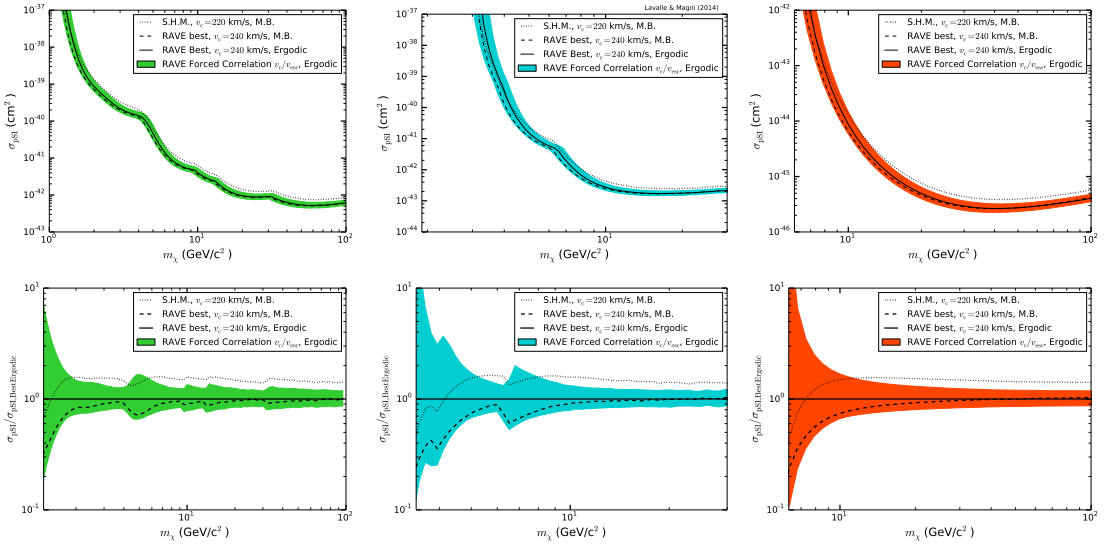

Figure 4.15: Same as 4.14, but for the v_c-v_{esc} range supposed to properly take the anticorrelation (represented by the dotted lines in figure 4.5) into account (upper: absolute, lower: relative). From left to right: CRESST2, SuperCDMS, LUX. We published these figures in [2].

The DMDD limits and uncertainties obtained from this region are shown in figure 4.15. They are similar to those presented in the previous section (v_c-free case), but likely more consistent with the original data used in P14 (because of the supposed anticorrelation between v_{esc} and v_c).
The relative uncertainties improve on the entire mass range. They improve down to $\sim \pm 10\%$ in the large WIMP mass region. This illustrates the importance of accounting for astrophysical correlations in reducing the astrophysical uncertainties that affects DMDD. To quantify this, we show the difference in the relative uncertainty band between the correlated and uncorrelated cases in 4.16, using the LUX results, where the dashed region shows the correlated uncertainty band obtained in

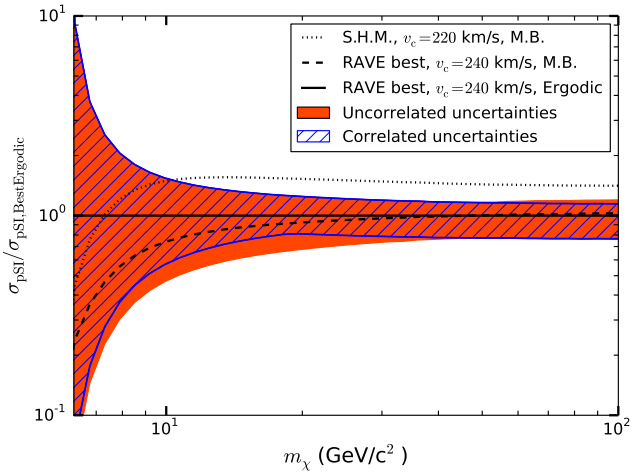

Figure 4.16: Effect of not considering the correlation of the astrophysical parameters (local dark matter density and relevant speeds) in drawing the relative uncertainty in the LUX DMDD exclusion curve. The dashed region is the same as the colored region in the bottom left panel of 4.15. We published this figure in [2].

the bottom left panel of 4.15. The improvement is not as tremendous as one would naively expect, but still clearly visible around the maximum sensitivity region: this is due to the fact that large speeds (v_c and v_{esc}) are dynamically correlated with a large local dark matter density, which tends to maximize the uncertainty in the low WIMP mass region (there is still a gain in the intermediate region). Nevertheless, we stress that accounting for these dynamical correlations would become critical when using direct detection to check a WIMP model that would be invoked to interpret any putative indirect detection signal (the WIMP annihilation rate scales like $\varrho_\odot^2$).

4.7 Conclusions

In this chapter we have studied the impact of the recent estimate of the Galactic escape speed v_{esc} from [1] (P14) on the DMDD exclusion curves. This observable is difficult to reconstruct, and the method used in P14, as recognized by the authors, is potentially subject to systematic errors. Nevertheless, these constraints are independent of those coming from studies of rotation curves, and thereby may provide complementary information on the WIMP phase-space. We have shown that the conversion of these results is nontrivial, as the constraints on v_{esc} are obtained from a series of assumptions that relate each value of v_{esc} to a different set of parameters for the dark halo profile. This implies that one cannot use the different v_{esc} ranges provided by P14 blindly and irrespective of these assumptions. A naive use of these estimates would neglect the underlying assumptions, and thus the correlations they induce among the astrophysical parameters and the dark matter velocity distribution.

We have assumed spherical symmetry and gone beyond the Maxwell-Boltzmann approximation by considering ergodic phase space distributions for the WIMPs. This method ensures a self-consistent physical connection between the phase-space distribution and the underlying Milky Way mass model. In particular, all local variables relevant to DMDD calculations, i.e. the average WIMP speed, the dispersion velocity, and the local dark matter density, are consistently dynamically correlated in this approach.
We have studied the three best-fit configurations provided by P14, two with priors on the circular velocity v_c (220 and 240 km/s), and one with v_c left free. These configurations are shown in the v_c,v_{esc} plane in 4.2. As the first two appeared to us too specific, we concentrated on the latest, which was originally optimized for Milky Way mass estimates (we had to convert the P14 results from the c_{340},M_{340} plane to the v_c,v_{esc} plane). The anticorrelation between v_c and v_{esc} arising from the locations of the stars of the P14 sample extracted from the RAVE catalog, which are biased toward negative longitudes, and found in the $v_c = 220$ km/s and in the $v_c = 240$ km/s cases, was no longer present due to the use of the posterior PDF for v_{esc} with the $v_c = 220$ km/s prior. We therefore further speculated on what a fully self-consistent v_c-free case could look like, and considered this guess as an alternative. Finally, we accounted for independent constraints on v_c from [40], which have the advantage of being almost fully independent of the Galactic mass model. This has driven us to favor large v_c regions, around 240 km/s, which are in principle associated with lower escape speeds in P14.
We have translated these P14 results in terms of DMDD exclusion curves focusing on the LUX, SuperCDMS, and CRESST-II experiments as references. We found that a consistent use of these estimates implies large values for $\varrho_\odot$, so more constraining exclusion curves (up to $\sim 40\%$ more), and evaluated the associated uncertainties. This is anyway consistent with several independent recent results on the local dark matter density (see e.g. references [97], [38] and [98]). This is a good news for direct dark matter searches as it tends to increase their potential of discovery or exclusion. We have also investigated the associated relative uncertainties, and shown that they are highly nontrivial as P14 values of v_{esc} are correlated with other astrophysical parameters, as already stated above. We have shown that taking P14 results at face value (plus eventually additional independent constraints on v_c) converts into moderate uncertainties, down to $\sim \pm 10\%$ in the regime where the experiments can trigger on the whole phase space (large WIMP masses). This is not to be considered as a definitive estimate of the overall astrophysical uncertainties, as both P14 and our phase-space modeling suffer from simplifying assumptions (simplistic baryonic mass model, spherical symmetry, etc.); this is still indicative, and compares to the low-edge estimates of other studies based on rotation curves (see for instance [90]). When getting closer to the high-velocity tail (low WIMP masses), the uncertainties explode as the experimental efficiency drops, but we have illustrated the nice complementarity between the experiments using different target atoms in this regime. This complementarity allows to maintain a moderate

uncertainty of $\sim \pm 20\%$ down to WIMP masses of a few GeV. Nevertheless, since the SHM value for the sum $v_c + v_{\rm esc}$ is 764 km/s, slightly more than the 751 km/s found from the more recent P14 estimate (with the prior $v_c = 240$ km/s), the generic outcome is that we find an effective WIMP mass threshold slightly heavier than in the SHM.

There are several limitations in this analysis, the main of which are the simple Milky Way mass model and its baryonic content, fixed by P14. Unfortunately, we cannot go beyond this choice as this would no longer be consistent with P14 results. Second, we made the assumption that the dark matter phase-space was entirely governed by the total energy, and that the system was spherically symmetric, which led to the derivation of ergodic velocity distribution. While this approach self-consistently correlates the local velocity features and the local dark matter density to the full gravitational potential, it remains to be investigated in detail whether it reliably captures the dynamics at stake in spiral galaxies. Some works do indicate that this approach provides a reasonable description of cosmological simulation results (see for instance [99]), but it is obvious that more studies are necessary to clarify this issue.

Finally, we stress that our study is complementary to those based e.g. on rotation curves, as it relies on different, and independent, observational constraints. Further merging these different sets of constraints would be interesting in the future. Moreover, because of these dynamical correlations arising in the local astrophysical parameters, which was continuously underlined throughout this chapter, several improvements could also be expected in the complementary use of direct and indirect detection constraints in order to exclude or validate some WIMP scenarios.

CHAPTER 5

A review of estimates of the astrophysical quantities relevant to dark matter direct detection

Contents

5.1 Introduction

Studying the astrophysical properties of the Milky Way is of course very interesting in its own, but it is also crucial for the topic of this work, dark matter direct detection. As we have seen in the previous chapters, computing the limits (or signal regions) associated to dark matter direct detection experiments requires to fix the astrophysical framework. We have seen in section 2.4 which are the main astrophysical quantities that are directly relevant for direct detection, in section 1.8 we have presented the standard assumptions employed (the Standard Halo Model)

and in section 2.4 we have shown which is the impact on the exclusion curves of variations in some of these parameters.
Chapter 4 has been dedicated to study in particular the impact on dark matter direct detection limits of the recent estimates of the local Galactic escape speed published by the RAVE collaboration. We have seen that the procedure employed to determine the escape speed relies on certain hypothesis (among which the particular Milky Way mass model assumed), which induces correlations among the astrophysical parameters, that we have tried to take into account at our best in computing the direct detection exclusion curves.
The goal of this chapter is to attempt a review of some of the up to date estimates of the astrophysical quantities that matters for direct detection, briefly summarizing the methods employed to determine these quantities from the observations. We will try to focus on the results of these studies, but also on the underlying assumptions, on the compatibility among them, and on the correlations between different astrophysical quantities present in the assumptions or in the results. This review thus expands without any claim of completeness the discussion already outlined in section 2.4.
Quantities like the distance from the Sun to the Galactic center $r_\odot$ are usually determined via geometric methods, which are usually based on few hypothesis. On the other hand, quantities like the circular velocity at Sun's position are evaluated via dynamical methods, by assuming models for the gravitational potential or for the mass distribution of the Milky Way. Some studies use local models (valid only in the surroundings of the Sun), while others employ global models (e.g. Milky Way mass models).
Since often models of the Milky Way are employed (e.g. mass models), we aim at summarizing which are some among the most up to date theoretical and observational achievements on this topic present in the literature.[1]
This review of the main estimates for the astrophysical quantities relevant for direct detection, and those characterizing the mass models involved in the description of our Galaxy, is meant to complete the picture outlined in this work providing complementary information on many of the astrophysical quantities that we have encountered. This also represents an opening toward possible generalizations to other astrophysical quantities of the work done in this thesis on the impact of the escape speed estimates on dark matter direct detection limits.
For a major readability of this section we will recall the author's names when making citations, unlike we did in the rest of this work.

[1]For very useful discussions about this and other topics discussed in this manuscript, we warmly thank Benoit Famaey who also provided us the most up to date references that we will consider in this chapter.

5.2 The astrophysical quantities more relevant for direct detection: review of some estimates in the recent literature

As we have seen, the astrophysical parameters most relevant for dark matter direct detection are: the Galactic escape speed at the position of the Sun $v_{\rm esc}$, the Sun's distance from the Galactic center $r_\odot$, the local dark matter density $\varrho_\odot$ and the velocity of the Sun in the Galactic frame, $\vec{v}_{\rm pec} = (U_\odot, v_{\rm c} + V_\odot, W_\odot)$, where $v_{\rm c}$ is the circular speed at the position of the Sun. Since the whole chapter 4 has been dedicated to the escape speed, we will not threat it again here.

5.2.1 The distance from the Galactic center, the circular velocity and the peculiar velocity of the Sun

Let us first focus on the distance from the Galactic center $r_\odot$, the circular velocity at the position of the Sun v_c, and the peculiar velocity of the Sun $\vec{v}_{\rm pec} = (U_\odot, V_\odot, W_\odot)$. We discuss these quantities together because, as we will see, their measures are related. In particular, the measures of $r_\odot$ do not depend on the others, but conversely the measures of the others depend on those of $r_\odot$, and on each others.

The distance of the Sun from the Galactic center $r_\odot$

The best available estimate of the Sun's distance from the Galactic center $r_\odot$ dates to 2009 and can be found in Gillessen et al. (2008) [93], which provides the value $r_\odot = 8.28 \pm 0.15$ (stat.) ± 0.29 (sys.). This is also the value that we employed in chapter 4, as it was assumed by Pifflet al. in [1] to estimate the escape speed.
Previously on the same year, two other estimates appeared in the literature: $r_\odot = 8.4 \pm 0.4$ kpc from Ghez et al. (2008) [100] and $r_\odot = 8.33 \pm 0.35$ kpc from Gillessen et al. (2008) [101]. They both contained measures of the mass of and the distance from the supermassive black hole in the center of the Galaxy, coincident with the radio source Sagittarius A* (this being the operational definition of $r_\odot$). For the two studies of Ghez et al. (2008) [100] and Gillessen et al. (2008) [101] above, astrometric and radial data were collected. Those data were relative to the star S2 closely orbiting on an elliptical orbit around the supermassive black hole at the center of the Galaxy, with a period of 15.9 years which allowed the observation of one full orbit. Such a star is a good tracer of the gravitational potential in that region. The data consist in observations of the position of the star S2 at different instants of time (astrometric data), and of its radial velocity.
The sets of data used by the two studies were taken respectively with the Keck telescope (the one of Ghez et al. (2008) [100]), and with the NTT/VLT telescope (the one of Gillessen et al. (2008) [101]).
The two sets of data on the position of S2 employed by these two studies were initially thought to be incompatible, but Gillessen et al. (2008) [93] have shown

that, allowing an offset in the definition of the reference frames used, the two sets of data can be brought to agreement, and Gillenssen et al. (2008) [93] thus used the combination of the two dataset to obtain the above estimate, which has slightly reduced uncertainties.
The method is purely geometrical: it consists in taking the above mentioned data and fitting an ellipsoidal orbit, performing a χ^2 test. The distance from the Galactic center $r_\odot$ is one of the parameters of the fit.
The above method does not rely on any assumption concerning other astrophysical parameters. The other quantities that are estimated in Gillessen et al. (2008) [93], like for instance the mass of the central black hole, are not relevant for direct detection. No Milky Way mass model has been assumed.

The circular velocity v_c and its combination with other quantities, $v_c+V_\odot$ and $(v_c+V_\odot)/r_\odot$

The most recent study, on which we are going to focus, is the one by Reid et al. (2014) [40], which used the measurements of trigonometric parallaxes and proper motions for over 100 masers associated with young, high-mass stars. This study is particularly interesting to us also because we have used some of its results in chapter 4.

Summary. In Reid et al. (2014) [40], axially symmetric models of the Milky Way have been fit to the data. The main results are that the distance to the Galactic center $r_\odot$ has been estimated to be 8.34 ± 0.16 kpc, the circular rotation speed at the Sun $v_c = 240 \pm 8$ km/s, and the rotation curve has been found to be almost flat at Sun's position (with a slope of -0.2 ± 0.4 km s^{-1} kpc^{-1}).
Since the dataset is large, the parameters $r_\odot$ and v_c are no longer highly correlated. The component of the peculiar Solar motion in the direction of the Galactic center is found to be $V_\odot = 14.6 \pm 5.0$ km s^{-1}. $V_\odot$ and v_c are significantly correlated, but the sum of these parameters is well constrained, $V_\odot + v_c = 255.2 \pm 5.1$ km s^{-1}, as well as the angular speed of the Sun in its orbit around the Galactic center $(v_c + V_\odot)/r_\odot = 30.57 \pm 0.43$ km s^{-1} kpc^{-1}.
The work of Reid et al. (2014) [40] is the first one which uses fully three-dimensional data to strongly constrain all three parameters $r_\odot$, $U_\odot$ and $v_c + V_\odot$.

Methodology employed. The measurements used by Reid et al. (2014) [40] are relative to position, parallax, proper motion and Doppler shift, and they allow a complete reconstruction of the velocity vectors of observed objects, which are masers located in high mass star forming regions (HMSFR). Then, a model for the Milky Way is assumed, which consists in modeling the Galaxy as a disk rotating with circular speed given by[2] $v_c(R) = v_c(r_\odot) + \frac{dv_c}{dR}(R - r_\odot)$.

[2] Let us remark that the sensitivity of the fundamental Galactic parameters $r_\odot$ and v_c to alternative rotation curves has been investigated by substituting (when fitting) the simple linear

A Bayesian fitting approach is employed,[3] with the posterior estimated using a MCMC based on the Metropolis-Hastings algorithm. The data were fitted with a least-square fitting (i.e. assuming Gaussian data uncertainties). Priors on $(U_\odot, V_\odot, W_\odot)$ were necessary, and particularly important is $V_\odot$, the motion of the Sun in the direction of the Galactic center, because the average peculiar motion of the sources is correlated to it. Because of the range of values found in the literature (which ranges up to $V_\odot = 26$ km/s in Bovy et al. (2012) [102], see next section), the prior assumed is $V_\odot = 15 \pm 10$ km/s.
Note that to model the observations, two kinds of motion are relevant: the peculiar motion of the Sun (important since all measurements are relative to it, and parameterized as usual as $(U_\odot, V_\odot, W_\odot)$), and that of the sources being measured. Here we report on the latter only few details, because it is beyond the scope of this chapter, but let us remark that in Reid et al. (2014) [40] these movements are taken into account and extensively described.
Four different sets of priors were considered, assuming the values and obtaining the results described below. Let us remark that the set called A is the most relevant one, and in particular the model A5 is considered to be the reference fit, because its priors are those least restrictive while in keeping with current knowledge. In order to test the sensitivity of the procedure to the priors, other sets of priors have been considered (B,C,D). The complete results of the Bayesian fitting associated with the various models are shown in table 4 of Reid et al. (2014) [40].

Set-A: The priors assumed are: $U_\odot = 11.1 \pm 1.2$ km/s, $V_\odot = 7.2 \pm 1.1$ km/s and $W_\odot = 7.2 \pm 1.1$ km/s, and priors on the average peculiar motion of the HMSFR of $\overline{U}_s = 3 \pm 10$ km/s and $\overline{V}_s = -3 \pm 10$ km/s.
The data contain some outliers, namely sources with anomalous kinematics, probably due to the effect of supernovae in the spiral arms. The method employed for set-A represents an outlier-tolerant approach, because it initially keeps all the sources, only removing some of them in subsequent repetitions of the analysis with prior A, giving rise to sets A1 to A4. The 95 initial sources are thus reduced to 80, which are used for the fit with less outliers, A5.
This fit has a good $\chi^2 = 224.9$ for 232 d.o.f., and provides $r_\odot = 8.34 \pm 0.16$ kpc, $v_c = 240 \pm 8$ km/s and almost flat rotation curve at Sun's position ($dv_c/dR = -0.2 \pm 0.4$ km s^{-1} kpc^{-1}).
Thanks to the higher number of sources and better distribution across the Galaxy, v_c and $r_\odot$ are significantly less correlated than in previous studies (marginalized and joint PDF are shown in figure 3 of Reid et al. (2014) [40]).
Anyway, a strong anti-correlation is present between $V_\odot$ and v_c. Circular velocity

form above with alternative forms. The conclusion is that these two parameters are reasonably insensitive to a wide variety of rotation curve shapes. Anyway, the authors report that some of the sources clearly cannot be modeled by an axisymmetric rotation curve.

[3]The procedure involves a transformation between heliocentric and Galactocentric frames, which requires accurate values for $r_\odot$, $U_\odot$ and, in particular, for $v_c + V_\odot$, which has been subtracted in the heliocentric frame.

parameters are still correlated but linear combinations of them are well determined: $v_c + V_\odot = 255.2 \pm 5.1$ km/s and $(v_c + V_\odot)/r_\odot = 30.57 \pm 0.43$ km s^{-1} kpc^{-1}. Moreover, $V_\odot = 15.6 \pm 6.8$ km s^{-1} (consistent with Bovy et al. (2012) [102]). We remind that A5 is considered to be the reference fit, because its priors are those least restrictive while compatible with current knowledge.

Set-B: Sets B, C, and D are based on the same selection of 80 stars as model A5 (thus without those that are kinetically anomalous). Tighter priors for the Solar motion (from Schönrich et al. (2010) [19]) are used: $U_\odot = 11.1 \pm 1.2$ km/s, $V_\odot = 12.2 \pm 2.1$ km/s and $W_\odot = 7.2 \pm 1.1$ km/s, and no priors for the average peculiar motion of the HMSFR is assumed. The main results are: $r_\odot = 8.33 \pm 0.16$ kpc and $v_c = 243 \pm 6$ km s^{-1}, with a χ^2 comparably good to the one of set A.

Set-C: No priors for the Solar motion are assumed (because of the big uncertainties found in the literature, see next section) but tighter priors on the peculiar motion of the HMSFRs are considered: $\overline{U}_s = 3 \pm 5$ km/s and $\overline{V}_s = -3 \pm 5$ km/s. The main results are: $r_\odot = 8.30 \pm 0.19$ kpc, $v_c = 239 \pm 8$ km s^{-1} and $V_\odot = 14.6 \pm 5.0$ km s^{-1}.

Set-D: No priors are assumed on both the Solar motion and the average peculiar motion of the HMSFR, a part from bounding $V_\odot$ and $\overline{V}_s$ with equal probability within ± 20 km/s of the Set A initial values and zero probability outside that range. This is motivated by the aim of facilitating the use of the associated results together with other literature estimates. Main results are: $r_\odot = 8.29 \pm 0.21$ kpc and $v_c = 238 \pm 15$ km s^{-1}.

Comparison with other estimates. The value for $V_\odot$ obtained with Set-C priors is consistent with that of Schönrich et al. (2010) [19], while it presents some contrast w.r.t. that of Bovy et al. (2012) [102], anyway in the sets where the prior that the peculiar motions of the HMSFR are small are relaxed, the results lose significance.
The values found for the Sun's motion toward the Galactic center are in agreement with other estimates, as for instance 11.1 ± 1.2 km/s in Schönrich et al. (2010) [19], or 10 ± 1 km/s in Bovy et al. (2012) [102], while those for the Solar motion component perpendicular to the Galactic plane $W_\odot$ differ only slightly from for instance the 7.2 km/s in Schönrich et al. (2010) [19].
The results obtained for $r_\odot$ (for model A5) are compatible with those obtained by Gillessen et al. [93], and are claimed to be likely the most accurate to date.
The estimates of v_c in the last decade have been ranging over a range of values 100 km/s wide. Comparing the result associated with the model A5, 240 ± 8 km/s, to the one obtained by Bovy et al. (2012) [102] of 218 ± 6 km/s, we see that the values differ, but in Bovy et al. (2012) [102] a high value of $V_\odot = 26 \pm 3$ km/s is obtained (see the details below). Since the full tangential speed in these two works,

$v_c + V_\odot = 252.2 \pm 4.8$ km/s in A5 of Reid et al. (2014) [40] and $v_c + V_\odot = 242^{+10}_{-3}$ km/s in Bovy et al. (2012) [102] are consistent, probably the differences on v_c come from the differences on $V_\odot$, as explained in the section dedicated to Bovy et al. (2012) [102].
The model A5 of Reid et al. (2014) [40] strongly constrains $(v_c + V_\odot)/r_\odot = 30.57 \pm 0.43$ km s^{-1} kpc^{-1}. This value can be compared with the one in Reid et al. (2004) [103] of $(v_c + V_\odot)/r_\odot = 30.24 \pm 0.12$ km s^{-1} kpc^{-1}. This last is an estimate based on the proper motion of Sgr A*, interpreted as the reflex motion from the Sun's Galactic orbit. This gives, by using $r_\odot = 8.34 \pm 0.16$ kpc, a value of $v_c + V_\odot = 252.2 \pm 4.8$ km/s, in good agreement with the results obtained in Reid et al. (2014) [40] from parallaxes.
Up to Reid et al. (2014) [40], it can be concluded that v_c exceed the IAU recommended value of 220 km/s with $> 95\%$ probability provided that $V_\odot < 23$ km/s. Changing the value of this quantity would have an impact on a wide range of astrophysical estimates. Let us remark in particular that higly affected would be the estimates of the total mass (dark matter dominated) of the Milky Way. Interestingly for dark matter direct detection, this would lead also to a higher value of the local dark matter density $\varrho_\odot$, as we have seen already in the previous chapter when considering the assumption of $v_c = 240$ km/s.

The peculiar velocity of the Sun $\vec{v}_{pec}$ and its component in the direction of the disk's rotation $V_\odot$

We are now going to summarize which are the main results in the literature about Sun's peculiar motion (w.r.t the Local Standard of Rest, LSR), and in particular its component in the direction of Galactic rotation $V_\odot$. Let us remark that knowing with high precision the proper motion of the Sun w.r.t. the Local Standard of Rest is of fundamental importance to convert any astrophysical measure from the heliocentric reference frame in which it is worked out, to the Galactic reference frame. While the radial and azimutal components $U_\odot$ and $W_\odot$ are simpler to determine from the movements of Solar-neighborhood stars, the determination of $V_\odot$ is more involved, and thus its estimates are spread over a wider range of values. In particular, they range between approximately 5 and 25 km/s. The above range is inferred from the following values estimated in the literature: $V_\odot = 5.23 \pm 0.62$ km/s in Dehnen et al. (1997) [104], $V_\odot = 12.24 \pm 0.47$ km/s in Schönrich et al. (2010) [19] and $V_\odot = 26 \pm 3$ km/s in Bovy et al. (2012) [102].

The estimate of Dehnen et al. (1997) [104]. The value of $V_\odot$ had a low value (compared to the other components of the peculiar velocity) since few years ago, due to estimates as the one from Dehnen et al. (1997) [104], which provided a value of $V_\odot = 5.23 \pm 0.62$ km/s (together with $U_\odot = 10.00 \pm 0.36$ km/s and $W_\odot = 7.17 \pm 0.38$ km/s for the other components, and with a value of $r_\odot/R_d \approx 3$ to 3.5, where R_d is the scale length of the disk).
This estimate was based on stellar kinematics, and used data relative to parallaxes

and proper motions of a subsample of the Hipparcos catalog. The velocity dispersion tensor was determined as a function of the color of the main sequence stars observed. As a side note, let us quote that the data seemed to indicate that the Galactic gravitational potential is significantly non-axisymmetric at the Solar radius, which could be due to the spiral structure of the Milky Way.
The numerical values obtained were based on the assumption of $r_\odot = 8$ kpc, and of other quantities not relevant for this discussion.

The work of McMillan et al. (2009) [39]. McMillan and Binney (2009) [39] analyze observations of parallax, proper motion and line-of-sight velocity for 18 masers to investigate the distance of the Sun from the Galactic center $r_\odot$, the rotational speed of the local standard of rest v_c and the peculiar velocity of the Sun $\vec{v}_{pec}$.
Various models of the rotation curve and models allowing for a peculiar motion of the HMSFR are considered. They obtain that the data are best fit by either assuming a higher value of $V_\odot$ than the usual one presented above, or by a net peculiar motion of the HMSFR. They argue that a correction in $V_\odot$ would be much more likely, and that the data support the conclusion that the value of $V_\odot$ should be revised upward from 5.23 to 11 km/s.
They also found out that the value of the ratio $v_c/r_\odot$ is better constrained than the two quantities considered independently. In particular, McMillan and Binney (2009) [39] estimate ranges from $v_c/r_\odot = 29.9 \pm 1.7$ km s^{-1} kpc^{-1} to $v_c/r_\odot = 31.6 \pm 1.7$ km s^{-1} kpc^{-1}. On the other hand, the estimates of the two separate quantities highly depend on the model assumed, and range between 6.7 ± 0.5 kpc and 8.9 ± 0.9 kpc for $r_\odot$, and between 200 ± 20 km/s and 279 ± 33 km/s for v_c.
This is particularly important, because it points out that an important correlation in the measured values of v_c and $r_\odot$ is present, as it is clearly shown by figure 2 of McMillan and Binney (2009) [39]. This should be kept in mind when using this or similar estimates in computing DMDD limits. Anyway, the more recent estimate provided by Reid et al. (2014) [40] has found that, since the dataset employed therein is large, the parameters $r_\odot$ and v_c are no longer higly correlated in their work.

The estimate of Schönrich et al. (2010) [19]. The value determined in Dehnen et al. (1997) [104] has been largely used, but McMillan and Binney (2009) [39] argued that a more plausible interpretation of the data (w.r.t. assuming an unexpected lag in the HMSFR on which that study relies upon) is obtained if $V_\odot$ exceeds the value of Dehnen et al. (1997) [104] by ≈ 6 km/s.
Thus, a subsequent analysis was worked out by Schönrich et al. (2010) [19], obtaining the following values: $V_\odot = 12.24^{+0.47}_{-0.47}$ km/s (together with $U_\odot = 11.1^{+0.69}_{-0.75}$ km/s and $W_\odot = 7.25^{+0.37}_{-0.36}$ km/s), with additional systematic uncertainties on $(U_\odot, V_\odot, W_\odot)$ of $\sim (1, 2, 0.5)$ km/s. In particular, this estimate provides a value of $V_\odot$ which is higher than the previously estimated one by 7 km/s.

The work of Schönrich et al. (2010) [19] is based on stellar kinematics. It applies an analysis based on similar data, but on a different methodology w.r.t the standard one employed in Dehnen et al. (1997) [104], namely using a particular chemo-dynamical model of the Galaxy (which in turn allows to compute the phase-space distribution for the stars). It should be noted that, up to the authors, the critics moved to the standard procedure are beyond doubt, while the result on $V_\odot$ has some sensitivity to the dynamical approximations used in deriving the Galaxy model, so that improvements on the model to fit more datasets could lead to small variations in the value of $V_\odot$.

The estimate of Bovy et al. (2012) [102]. Bovy et al. (2012) [102] determine the local value of the circular velocity to be $v_c = 218 \pm 6$ km/s (at 68% confidence), and marginalizing over all the systematics considered they find that $v_c < 235$ km/s at $> 99\%$ confidence. On the other hand, they find that the Sun's rotational velocity is $V_{\varphi,\odot} = 242^{+10}_{-3}$ km/s.[4] As can be seen, an offset between the Sun's rotational velocity and the local circular velocity $V_\odot = 26 \pm 3$ km/s is found, which is larger than the locally-measured Solar motion of 12 km/s. This larger offset reconciles the value of v_c found with the recent claims that $v_c \lesssim 240$ km/s. Also the Solar distance to the Galactic center is determined, with values in the range 8 kpc $< r_\odot <$ 9 kpc with the best fit at the lower hand.[5]
The analysis is based on measuring the rotation curve of the Milky Way over the Galactocentric range 4 kpc $\lesssim R \lesssim$ 14 kpc from the data taken by the SDSS III's Apache Point Observatory Galactic Evolution Experiment (APOGEE). The line-of-sight velocities of 3365 stars out to heliocentric distances of 10 kpc are modeled using an axisymmetric kinematical model. While warm stellar-disk tracers do not on average rotate at the circular velocity, their off-set from v_c, the so-called asymmetric drift, is a dynamical effect that can be calculated from their observed velocity dispersion.
A model is fit to the data. A flat rotation curve and alternatively a power low rotation curve are considered. For the distribution of velocities in Galactocentric rest frame, it consists of a single biaxial Gaussian, with a mean radial velocity of zero because of the assumption of axisymmetry, and a mean rotational velocity given by the local circular velocity v_c, adjusted for the local axisymmetric drift. Velocity anisotropy between the radial and the rotational directions is present in the model, described by the rotational velocity variance σ^2_φ and by the radial velocity variance σ^2_R. Their ratio comes from an axisymmetric equilibrium model for the distribution function $f(\mathcal{E}, L)$ in a disk with a circular velocity constant with radius. For this a Dehnen distribution function is used (see Dehnen (1999) [105]).

[4] The most robust measurements on the local circular velocity are those based on the observed proper motion of Sag A*, but this requires an estimate of $r_\odot$. Other measurements are based for instance on samples of halo stars or on globular cluster systems, but what such measurements actually measure is Sun's rotational velocity, $V_{\varphi,\odot}$. To obtain v_c, these measurements depend on a highly uncertain correction for the Sun's motion w.r.t v_c.

[5] Note that more detailed results are summarized in table 2 of [102].

No assumptions on $r_\odot$ are made. The systematics of the analysis are studied, with the conclusion that they do not significantly bias the results for the Galactic parameters.
The value obtained for v_c in this study is considered compatible with the other estimates in the literature (as for instance those of McMillan et al. (2009) [39]) by the authors, because differences are explained by the different peculiar motion of the Sun w.r.t. v_c, and because their work takes into account the theoretically well motivated corrections due to the axisymmetric drift.
A crucial point is that the Galactocentric motion of the Sun is approximately $V_{R,\odot} = -10.5 \pm 1.0$ km/s, but the difference $v_c - V_{\varphi,\odot}$ turns out around 26 ± 3 km/s. This difference must be understood in the following terms. Usually the peculiar motion of the Sun is defined w.r.t. the Local Standard of Rest (LSR). The LSR itself is assumed to rotate around the Galactic center with velocity given by $(0, v_c, 0)$. This is the case, roughly speaking, only if the stars surrounding the Sun are on average rotating with that velocity. Anyway, the model used in Bovy et al. (2012) [102] calls Rotational Standard of Rest (RSR) the reference frame moving with $(0, v_c, 0)$, and find a difference between the motions of LSR and RSR: the LSL seems to rotate ~ 12 km/s faster than the RSR.[6] A difference in the motion of the two should be understood as the fact that the LSR would not be on a circular orbit around the Galactic center.
The implication of this result on dark matter direct detection is, as explained in Bovy et al. (2012) [102], that decomposing the motion of the Sun in the usual way, i.e. with v_c and $V_\odot$ kept separate (instead of considering only the rotational velocity $V_{\varphi,\odot}$), is dangerous because it can lead in taking into account high values of v_c as 240 km/s together with the standard value (or higher values) for $V_\odot$, which would be incorrect if this difference in rotation between LSR and RSR is really present.

5.2.2 The local dark matter density $\varrho_\odot$

The standard value of the local dark matter density is considered to be $\varrho_\odot = 0.3$ GeV/c^2 cm^{-3}. This is for instance the "canonical value" reported in the reviews of particle physics [36] and [35], where it is reported to be correct within a factor of 2 or 3.
In the recent years, anyway, there has been a tendency to consider higher values, somewhat around $\varrho_\odot \approx 0.4$ GeV/c^2 cm^{-3}. For instance in Ling et al. (2010) [37] it is reported that, even if the commonly used value is the one above, a recent determination suggests $\varrho_\odot = 0.39$ GeV/c^2 cm^{-3} and this is also what the authors found in their simulation.

[6] Note that the measure of the Solar motion w.r.t. the LSR is then local, while the one w.r.t. the RSR is global.

The recent estimate of Bovy and Tremaine (2012) [97]. The work of Bovy and Tremaine (2012) [97] considers the same measures employed by Moni Bidin et al. (2014) [106][7] of the vertical motion of stars situated 1 to 4 kpc from the Galactic mid-plane. Using the same procedure of Moni Bidin et al. (2012) [107], based on Jeans equation, but assuming instead the approximation that the circular velocity curve is flat in the mid-plane (i.e. that the circular speed is therein independent of radius) Bovy and Tremaine (2012) [97] ends up with an estimate of the local dark matter density which is $\varrho_\odot = 0.3 \pm 0.1$ GeV/c^2 cm^{-3}, consistent with the standard estimates, and which they consider to be the most robust direct measurement of this quantity to date.
It should be noticed that the above estimate relies on the additional assumptions of $r_\odot = 8$ kpc, and of $v_c = 220$ km s^{-1}, consistent for instance with the results of Bovy et al. (2012) [102], but with the standard value of v_c that many recent estimates suggest should be increased.
Moreover the authors notice that the dark matter density they estimate is the average at $R = r_\odot$, but at a height from the disk mid-plane of 1 to 4 kpc. For two reasons the local dark matter density at $z = 0$, the one important for dark matter direct detection, should thus be enhanced. First, for the pure geometrical reason that for instance an NFW profile gives a higher ϱ at $z = 0$ than at $z = 2.5$ kpc. Second, the gravitational influence of the disk should further increase the mid-plane dark matter density. Thus the value of the local dark matter density reported above should be enhanced by about thirty percent.

The recent estimate of Bienaymé et al. (2014) [38]. The work of Bienaymé et al. (2014) [38] employs a model for the local (i.e. in the Solar neighborhood) Galactic potential applied to the data from the observations worked out by the RAVE collaboration, already described in the previous chapter, combined with data from the 2MASS and UCAC catalogs.
The observed stars are red clump stars for which distances, radial velocities and metallicities have been measured, located in a cylinder of 500 pc of radius extending from 200 to 2000 pc in the direction of the South Galactic Pole. The procedure employed consists in assuming a distribution function depending on three integrals of motion in a separable potential which locally represents the one of the Milky Way, with four free parameters. The distribution is fit to the data and allows to deduce the vertical force and the total mass density distribution up to 2 kpc away from the Galactic plane.
The value of $\varrho_\odot = 0.542 \pm 0.042$ GeV/c^2 cm^{-3} is then determined, considerably higher than the standard one. This value is obtained assuming $r_\odot = 8.5$ kpc. Such a high local density, in combination with a circular velocity of 240 km/s, could be produced by a flattening of the halo of order 0.8. Another possibility, which would also provide a lower circular velocity, would be the presence of a secondary dark

[7] Moni Bidin et al. (2014) [106] provided an estimate of $\varrho_\odot$ pointing toward values one order of magnitude smaller than the standard one.

matter component, a very thick disk.

The recent estimate of Piffl et al. (2014) [98]. The work of Piffl et al. (2014) [98] makes use of the kinematics of ~ 200000 giant stars lying within ~ 1.5 kpc of the Galactic plane. They are primarily used to determine the vertical profile of mass density near the Sun.
The employed procedure is based on the assumption of mass models made of three double exponential disks, an oblate bulge and a NFW dark matter halo. The dynamics of RAVE stars in the gravitational potential is modeled by assuming phase-space distributions that are functions of three integrals of motion.
Piffl et al. (2014) [98] provides an estimate of the local dark matter density which depends on the axis ratio of the dark matter halo q, $\varrho_\odot = 0.48 q^{-0.89}$ GeV cm^{-3}. Once combined with the value for this ratio provided by observations, $q \approx 0.8$, it provides as a result a value of $\varrho_\odot$ higher than the one of the SHM. This value is bigger than the one usually found in dark matter only simulations, but in good agreement with the one of simulations which include baryons.
Statistical errors are significantly smaller than systematics effects. Those other than the flattening of the dark halo yield overall uncertainties of $\sim 15\%$.

The detailed study on the dark halo of Piffl et al. (2015) [108]. As we have seen in the previous paragraph, Piffl et al. (2014) [98] estimated the local dark matter density by modeling the Galaxy by combining dynamical models of the stellar disc with star counts and the kinematics of RAVE stars. The major uncertainty of their model was the flattening q of the dark halo. The best-fitting local dark matter density in that study increased with the assumed halo axis ratio as $q^{-0.89}$. In Piffl et al. (2015) [108] it has been found that, even if the dark halo were originally spherical, it must be flattened inside the solar radius $r_\odot$ with $q = 0.7$ to 0.9. Even though q varies with radius, this variation is modest within $r_\odot$. As we have previously seen, from a subset of the data used by Piffl et al. (2015) [108] and employing a very different procedure, Bienaymé et al. (2014) [38] determined as well the local dark matter density. Piffl et al. (2015) [108] points out that the local dark matter densities of these two studies (Piffl et al. (2014) [98] and Bienaymé et al. (2014) [38]) agree for halo axis ratio q in the range 0.79 to 0.94. Interestingly, this is just the range of axis ratios that Piffl et al. (2015) [108] leads to expect if the dark halo were spherical before the baryonic disk was added (more precisely, the final minor-major axis ratios found are $q = 0.75$ to 0.95).
For completness, let us report the procedure employed by Piffl et al. (2015) [108] and some of the additional results found therein, which even tought not directly related to the local dark matter density discussed in this section, are interesting as well for DMDD. The reader interested only in the local dark matter density can skip this part and go directly to the conclusions of the section.
The study of Piffl et al. (2015) [108] shows how to construct fully self-consistent multi-component equilibrium Galaxy models with axisymmetric distribution func-

tions $f(J_r, J_\varphi, J_z)$ which depends on phase-space position only through action coordinates. The goal is to study how the dark matter halo is distorted when baryonic disks and bulge are adiabatically added to the system (i.e. with $f(J_r, J_\varphi, J_z)$ left unchanged). A dark halo will respond to the quiescent accumulation of baryons in the disk by distorting adiabatically. This means that the three action integrals J_r, J_φ, J_z of which the phase-space distribution is function will be constants, and thus $f(J_r, J_\varphi, J_z)$ will be unaffected by the accumulation of baryons. This is an enormous advantage because $f(J_r, J_\varphi, J_z)$ can thus be inferred by dark matter only simulations, and then adding baryons will leave it unchanged. Only the velocity distribution and density distribution will change.
As working example, Piffl et al. (2015) [108] employs the Galaxy model inspired from the model presented in Piffl et al. (2014) [98] (for which the axis ratio q in the dark matter halo is the less constrained parameter) and makes its dark matter halo a fully dynamical object. The employed reference mass model contain a thin, a thick and a gaseous disks, a dark matter halo and a bulge, with functional forms described in appendix A and main parameters described in table 4 of Piffl et al. (2015) [108]. Its parameters were obtained in Piffl et al. (2014) [98] by reproducing a variety of observational constraints such as gas kinematics, the proper motion of Sagittarius A*, maser sources in the disk and the kinematics of around 200000 stars taken from the RAVE survey. Piffl et al. (2014) [98] originally considers a NFW dark matter halo, good only for dark matter only simulations, and Piffl et al. (2015) [108] study how this halo modifies when the bryonic disks of Piffl et al. (2014) [98] are adiabatically added.
Through an iterative procedure, the gravitational potential that is generated by the dark matter halo and the stellar disk in presence of predefined contributions from a gas disc and an axisymmetric bulge is determined.
A new family of phase-space distributions is introduced, in which only the functional form for the phase-space distribution for disks is fixed. No phase-space distribution is used for the gaseous disk and for the bulge (which are taken into account only via fixed density distributions). A phase-space distribution with the functional form f(J) is fixed for the dark matter, which i) generates a halo which is NFW when isolated, and ii) presents a flattenng internal to the Sun's orbit when disks and bulge are added. The velocity anisotropy for the dark matter phase-space distribution must be fixed. Piffl et al. (2015) [108] considers three different sets of parameters in order to have isotropy, radial anisotropy and tangential anisotropy. The main change in the final model is the adiabatic compression of the dark halo by the flattened potential of the discs. This contraction has two components. The first component of the contraction is a spherical shrinkage, the second component is a pinching towards the plane at distances from the Galactic center inferior to around 10 kpc, which flattens the halo. The extent to which the halo flattens depends on the velocity anisotropy, in the sense that radial bias maximises the flattening. In the case of a radially biased halo (the most likely case according to cosmological simulations) the compressed halo obtained after introducing the baryons looks very

much like a "dark disc" (superimposed to a spherical halo). Such a disc would be non-rotating, in contrast to a dark disc formed by the capture of satellite halos. The models worked out in Piffl et al. (2015) [108] yield the velocity distribution of dark matter particles at Sun's position, which is of crucial importance for dark matter direct detection. The distributions of speeds with respect to the Sun are clearly not Maxwellian, and triaxial. They are more sharply peaked in the radially biased model, and less sharply peaked in the tangentially biased model. Since the detectors employed in DMDD have a threshold speed for detection, the radially biased model offers significantly better chances of detecting dark matter.

Conclusion. We can basically conclude this section by stating that recent estimates of the local dark matter density are pointing (apart from few exceptions) toward values higher than the standard one, but the uncertainties on each individual measure and especially the differences among the results of different studies are still very important.

5.3 Global studies and constraints on the parameters of Milky Way mass models

As we have seen, the estimates of the astrophysical quantities directly relevant for dark matter direct detection, as $v_{\rm esc}$, $r_\odot$, $\varrho_\odot$ and $\vec{v}_{\rm pec} = (U_\odot, v_{\rm c} + V_\odot, W_\odot)$, are obtained from the observations through procedures that usually rely on certain assumptions. Some of these studies need to assume a particular mass model for the Milky Way.
In this section we aim at summarizing some among the most updated or robust estimates[8] of the parameters associated to the components of Milky Way mass models more realistic than e.g. the one employed in chapter 4.
We extensively discussed in section 3.2.2 which are the components usually employed in a Milky Way mass model, which are their main characteristics, and which are the functional shapes of the most commonly employed density profiles. In this section we will instead deal with estimates of the values that the parameters of such components assume when Milky Way mass models are constrained using data from observations.

5.3.1 Baryons

Let us first focus on the baryonic content of the Milky Way. We already provided two sets of parameters describing the baryonic component of the Milky Way. The first one represents a recent determination of the values of these quantities that has been worked out in McMillan (2011) [68], which we discussed in section 3.2.3.

[8] We warmly thank Benoit Famaey for providing us with the references that we will consider in this section.

The second one is an old determination of the parameters of the Galactic bulge and disk that was originally worked out in Xue et al. (2008) [84] and successively employed in Piffl et al. (2014) [1], so we have discussed it in sections 3.2.3 and 4.3.

The thin and thick disks of the Milky Way

The disk is a fundamental component of any mass model which aims at describing the Milky Way globally. Even if in simple models a single disk is taken into account, more complex ones consider (at least) two populations of stars, described by two different disks, a thin one, and a thick one. Even though different density profiles for the disks exist, usually a double exponential profile (3.10) is considered for each of the disk components, thin and thick.

The parameters of the baryonic components obtained by McMillan (2011) [68]. As we already stated, McMillan (2011) [68] employs a Bayesian approach to take into account input from photometric and kinematic data. For the disks, he considers a thick and a thin component. We report here the values corresponding to the best fit model of McMillan (2011) [68]. The thick disk is an exponential disk with $R_d = 3.31 \pm 0.56$ kpc and $\Sigma_0 = 209.5 \pm 110$ $M_\odot$ pc^{-2} (from which the total mass of the disk can be obtained as $M_d = 2\pi\Sigma_0 R_d^2$), for which $z_d = 0.9$ kpc is assumed. The thin disk is an exponential disk with $R_d = 2.90 \pm 0.22$ kpc and $\Sigma_0 = 816.6 \pm 123$ $M_\odot$ pc^{-2} for which $z_d = 0.3$ kpc is assumed.

More on the scale lengths of the thin and thick disks. A recent estimate of the scale length of the thin disk can be found in Bovy et al. (2013) [109], which provides the value of $R_d = 2.15 \pm 0.14$ kpc. That estimate is based on fitting a parameterized Milky Way potential and a phase-space distribution depending on three integrals of motion to the data relative to the dynamics of G-type dwarfs from SEGUE. It should be noticed that purely photometric constraints are usually less strong, thus allowing values of R_d up to 3 kpc. The length scale of the thick disk can be taken approximately equal to the one of the thin disk, as explained by Binney and Tremaine [17].

More on the scale heights of the thin and thick disks. For the values of the scale heights we can consider $\sim 0.3 \pm 0.05$ kpc for the thin disk and $\sim 1.35 \pm 0.4$ kpc for the thick disk. The central values are the traditional one obtained by Gilmore and Read (1983) [110]. The values of the associated uncertainties are subject to a certain debate in the literature, thus it is not simple to provide a recent reference value. We thus report the error bars above, suggested by B. Famaey and which arise from taking into account the concurrent estimates appeared in the literature in the last thirty years.

Bulges and MWMM

We are now going to discuss two works in which one can find the values of the parameters of the components describing the baryonic content of the Milky Way, interesting in particular for the bulges employed.

The parameters of the oblate ellipsoidal bulge determined in McMillan (2011) [68]. For the oblate ellipsoidal bulge of his best fit model, McMillan (2011) [68] finds $\varrho_0 = 95.6 \pm 6.9$ $M_\odot$ pc^{-3}, assuming $r_0 = 0.075$ kpc, $r_{cut} = 2.1$ kpc, $\alpha = 1.8$ and $q = 0.5$.

The MWMM with a triaxial bulge used in McGaugh (2008) [82]. McGaugh (2008) [82] employed a mass model which includes an exponential stellar disk, the triaxial bulge originally determined by Binney et al. (1997) [80] and a gas disk following the distribution of Merrifield and Olling [83] described in detail in next section.[9] Particularly interesting are the values of the parameters associated to the triaxial bulge, in particular the azimuthal mean density of the bulb/bar, originally determined in Binney et al. (1997) [80], which can be found also in section 3 of McGaugh (2008) [82], together with the values for the other baryonic components (which anyway miss a thick disk).

The MWMM with a bar of Wang et al. (2012) [78]. A recent model for the Milky Way bar can be found in Wang et al. (2012) [78], where data from the BRAVA survey have been fit with a χ^2 minimization to determine the relevant parameters of the model.[10] That work employs the well established bar model of Dwek et al. (1995) [81], which contains both a bar and a spheroidal nucleus with a steep inner power low behavior and an exponential outer profile. For the gravitational potential Wang et al. (2012) [78] employs a Miyamoto-Nagai profile for both the disk and the bulge, with no explicit component for the dark matter contribution, considered very low in mass in the central part of the halo under investigation.

The mass model for the gas of Olling and Merrifield

A mass model for the gas in the Milky Way can be found in Olling and Merrifield (2001) [83], where the surface gas density at the position of the Sun (assumed to be $r_\odot = 8.5$ kpc) is determined to be $\Sigma_{HI} + \Sigma_{H_2} \approx 11$ $M_\odot/pc^2$, summing atomic and molecular hydrogen.[11]
The local scale height of the gas is found to be $h_{z0,gas} = 150$ pc in Karlberla et al. (2009) [111], while Olling and Merrifield (2001) [83] point toward $h_{z0,gas} = 240$ pc.

[9] The gas component is sometimes omitted in making models of the Milky Way, but it is particularly relevant for MOND models, as those considered in McGaugh (2008) [82].

[10] The values of these parameters can be found in Wang et al. (2012) [78].

[11] See table D1 of Olling and Merrifield (2001) [83].

In Karlberla et al. (2009) [111], also a radial dependence of the scale height of the gas density profile is proposed. This dependence has the behaviour $h_z(R) = h_{z0,gas} \exp[(R - R_\odot)/R_{gas}]$, with $R_{gas} = 9.8$ kpc.
Karlberla et al. (2009) [111] provides an estimate of $\Sigma_{HI,local} \sim 10$ $M_\odot/pc^2$, approximately in agreement with the one of Olling and Merrifield (2001) [83] for which Σ_{HI} alone was ~ 9.25 $M_\odot/pc^2$. In Karlberla et al. (2009) [111, pag. 37] also a radial distribution of the surface density is proposed, with saturation at ~ 10 $M_\odot/pc^2$ below 12.5 kpc.
The value of $\Sigma_{gas,local} = 13$ $M_\odot/pc^2$ is obtained in Bovy and Rix (2013) [109]. The same value is obtained by Flynn et al. (2006) [112] in the so-called Tuorla model.[12]
To summarize, taking into account the different values presented above, we guess that a reasonable interval could be represented by $\Sigma_{gas,local} = 12 \pm 1$ $M_\odot/pc^2$.

Hot gas component

Finally, an additional component of hot gas (distributed in a halo) can be considered. This gas has been proposed to account for the missing baryons in the Milky Way. One such model is presented in Fang et al. (2012) [113, sec. 2]. Observational constraints on such a hot gas corona, from dwarf satellites, can be found in Gatto et al. (2013) [114].

5.3.2 Milky Way total mass and surface densities

In this section we consider the total mass content of the Milky Way (baryons and dark matter), and the surface densities relative to the luminous components only, and to the total.

Milky Way total mass estimates from observations of Leo I

The most updated estimate of the mass of the Milky Way (more precisely, the virial mass), is the one obtained by Boylan-Kolchin et al. (2013) [115], which provides a median value of $M_{vir,MW} = 1.6 \times 10^{12}$ $M_\odot$, with a 90% confidence interval of $[1.0 - 2.4] \times 10^{12}$ $M_\odot$. This estimate is based on measurements of the proper motion of the Leo I dwarf spheroidal galaxy obtained with the Hubble Space Telescope, combined with numerical simulations of Galaxy-size dark matter halos.

The total mean surface density within 1.1 kpc: a recent estimate by the Strasbourg's group

The value recently obtained by the group of Strasbourg formally is 68.5 ± 1 $M_\odot/pc^2$. Anyway, the error bars describing the systematic errors are larger than those above, so that taking them into account would lead to a value of 68.5 ± 10 $M_\odot/pc^2$.

[12] The name comes from that of the observatory where part of the study is carried out.

In addition, a surface density of 97 ± 2.2 $M_\odot/pc^2$ at $z = 2$ kpc has been obtained by the same group, where again the errors are statistical ones and not systematic ones. Because of this reason, a value of 97 ± 15 $M_\odot/pc^2$ would be more safe and representative of both the systematic and statistical errors.
Bovy and Rix (2013) [109] found a value of 68 ± 4 $M_\odot/pc^2$ for the total mean surface density at $z = 1.1$ kpc, where again uncertainties of ± 10 kpc would be more representative of the statistical plus systematic uncertainties. These values are courtesy of B. Famaey.

The local surface density corresponding to the visible components: recent estimates by the Strasbourg's group

The value obtained for the baryons (all together) in 1 kpc is 44.5 ± 4.1 $M_\odot/pc^2$, of which ~ 11 $M_\odot/pc^2$ for the gas and so $\sim 33.5 \pm 4$ $M_\odot/pc^2$ for the stars. The Tuorla model of Flynn et al. (2006) [112] provides the value 35.5 $M_\odot/pc^2$ for the stellar component (without error bars).
Bovy and Rix (2013) [109] provides the value of 38 ± 4 $M_\odot/pc^2$ for the stars and fixes 13 $M_\odot/pc^2$ for the gas. Olling and Merrifield (2001) [83] should be better for the gas, so one could consider instead the value of 11 $M_\odot/pc^2$ for the gas. Bovy et al. (2012) [116] constrained $\Sigma_{stars} = 30\pm$ $M_\odot/pc^2$ at $r_\odot$, more or less in agreement with their estimate of $\sim 33.5 \pm 4$ $M_\odot/pc^2$. Otherwise, Binney and Tremaine [17] state that the local gas is $\sim 25\%$ of the surface baryonic density of the disk, which would provide something around ~ 33 $M_\odot/$ pc^2 for the stars (thin plus thick disks) if the density of gas is 11 $M_\odot/$ pc^2.
To summarize, combining the different local estimates in $z = \pm 1.1$ kpc: $\Sigma_{gas} = 11$ $M_\odot/pc^2$ (or 12 ± 1 $M_\odot/pc^2$), $\Sigma_{stars} = 33.5 \pm 4$ $M_\odot/pc^2$ (but values up to 42 can be considered if one wants to follow Bovy et al. (2012) [116]). These values are courtesy of B. Famaey.

Conclusions

This thesis deals with the astrophysical aspects related to the direct detection of WIMPs. In the first part of this work we described the formalism of DMDD, as well as the results obtained by experimental collaborations and the statistical techniques related to the interpretation of their data. We have then outlined the main concepts of the dynamics of our galaxy that allow to put the astrophysics related to DMDD in a wider framework, and reviewed some of the main determinations present in the literature of the astrophysical quantities relevant for DMDD.
The main results that we have obtained are described in chapter 4, where we have focused on the recent estimates of the local Galactic escape speed published by the RAVE collaboration [1]. We have studied in detail the implications of these results for the spin-independent interpretation of DMDD experimental results.
We have focused on the exclusion curves associated with the three most constraining experiments at the moment of writing: LUX (representative of xenon experiments), SuperCDMS (representative of germanium experiments) and CRESST-II (representative of multi-target experiments).
A naive use of these estimates would neglect the underlying assumptions, and thus the correlations they induce among the astrophysical parameters and between them and the dark matter velocity distribution.
We have gone beyond the Maxwell-Boltzmann approximation (usually assumed in the framework of the Standard Halo Model), computing from the mass model assumed by means of Eddington equation the phase-space distribution of the dark matter. This provides a self-consistent physical connection between the phase-space distribution and the underlying Milky Way mass model. Moreover, in this approach dynamical correlations among the astrophysical parameters relevant for DMDD calculations are automatically taken into account.
We have shown that taking into account the RAVE results on the escape speed by consistently correlating all the relevant parameters leads to more constraining exclusion curves with respect to the standard ones, due to the higher values of the associated local dark matter density, and we have evaluated the uncertainties

associated to each experiment. These uncertainties, moderate at large WIMP masses, grow as the experimental efficiency drops, i.e. at low WIMP masses, and we have illustrated the nice complementarity between the experiments using different target nuclei in this regime.
These results are the object of our paper [2] that has been published in the journal Physical Review D during the final year of this thesis.
The main limitations of this analysis are the simple Milky Way mass model and its fixed baryonic content, which we employed for consistency with the assumptions of the RAVE collaboration, and the assumption for the dark matter phase space to be governed by the total energy only. For these reasons in this thesis we complemented the picture by reviewing more realistic mass models and more complex phase-space distributions.

The work presented in this document has been carried out over a period of three years. During these three years, a part of the working time has been dedicated to learn the formalism of DMDD and the statistical methods used to extract information from the data, and to understand and reproduce the interpretation of the experimental results. A part of the time has been used to learn the basics of the dynamics of our Galaxy, and to implement the associated numerical computations. A significant part of the time has been spent to learn and implement the numerical solutions used to reproduce the interpretation of the data from DMDD experiments and the computations related to the Galactic dynamics (e.g. solving Eddington equation), and to learn the programming languages used, mainly C, C++ and python. Another significant part of the time has been dedicated to study the impact of the RAVE estimates of the escape speed on DMDD limits. Even if never enough widened, bibliographic searches has received a certain attention too.
During the preparation of this thesis, I have also had the chance to experience the teaching of Newtonian mechanics to first year university students for two consecutive years.

APPENDIX A

Additional details on some interesting mass density profiles

In this section we provide additional information on some of the dark matter and baryonic mass density profiles introduced in chapter 3. We also present the analytic expressions of some useful quantities like the gravitational potential Φ, the Galactic escape speed $v_{esc}(r)$, the mass $M_{int}(r)$ interior to radius r, etc. for some of these profiles.

A.1 NFW profile

The mass contained within a sphere of radius r in a NFW profile (3.3) can be computed from (3.20) and reads:

$$M_{int}^{NFW}(r) = 4\pi\varrho_{crit}\delta_c r_s^3 \left[\ln\left(1+\frac{r}{r_s}\right) - \frac{\frac{r}{r_s}}{\left(1+\frac{r}{r_s}\right)}\right] . \tag{A.1}$$

As we can see, the above mass exhibits a logarithmic divergence for $r \to \infty$, which means that the NFW halo profile should come with a finite extent, i.e. it can be useful to define the edge of the halo up to which we describe the density of matter with equation (3.3) and assume that outside it there is no more matter. Sometimes the edge of the halo is assumed to occur at r_v.
The Newtonian gravitational potential corresponding to this profile can be computed from equation (3.22), and it reads:

$$\Phi^{NFW}(r) = -4\pi G_N \varrho_{crit}\delta_c r_s^3 \frac{ln\left(1+\frac{r}{r_s}\right)}{r} . \tag{A.2}$$

The limit for $r \to 0$ of $\Phi^{NFW}(r)$ is finite and has the value $-4\pi G_N \varrho_{crit}\delta_c r_s^2$.

The speed of a body which is on a circular orbit in a NFW profile can be calculated from (3.23) and turns out to be:

$$v_c^{NFW}(r) = \sqrt{4r_s^3 \pi \varrho_{crit} \delta_c G_N \left[\frac{\ln\left(1+\frac{r}{r_s}\right)}{r} - \frac{1}{r_s + r} \right]} \,. \tag{A.3}$$

From the above result, using equation (3.26) we can obtain the escape speed of a body inside a NFW profile, which is:

$$v_{esc}^{NFW}(r) = \sqrt{8\pi G_N \varrho_{crit} \delta_c r_s^3 \frac{\ln\left(1+\frac{r}{r_s}\right)}{r}} \,, \tag{A.4}$$

A.2 Hernqvist profile

Using equation (3.20), we can calculate the mass contained in a spherical shell of radius r for the Hernqvist profile (3.12), which reads:

$$M_{int}^H(r) = \frac{M_H r^2}{(r + a_H)^2} \,. \tag{A.5}$$

From (3.22) we deduce that the Newtonian potential generated by the Herquist profile is:

$$\Phi^H(r) = -\frac{G_N M_H}{r + a_H} \,. \tag{A.6}$$

Using equations (3.23) and (A.5), we can calculate the speed of a body on a circular orbit inside an Hernqvist profile, which is:

$$v_c^H(r) = \frac{\sqrt{G_N M_H r}}{r + a_H} \,, \tag{A.7}$$

and using (3.26) we can calculate the escape speed for the Hernquist profile, which reads:

$$v_{esc}^H(r) = \sqrt{\frac{2G_N M_H}{r + a_H}} \,. \tag{A.8}$$

A.3 Oblate ellipsoids

The dark matter halo of the Milky Way can be considered spherical as a first approximation. Nevertheless, if we would like to consider the baryons, we should take into account that in a typical spiral galaxy they are not spherically symmetric distributed, but instead they lie mainly in the Galactic disk, so at least axial symmetry is required.
The bulge can be approximated as being spherically symmetric, but it would be better to describe it with an oblate ellipsoid. Finally, it can also be interesting to

consider axially symmetric (or even triaxial) dark matter halos. In this section we then recall some results about ellipsoidal systems (oblate ellipsoids in particular), which can be found in [17, sec. 2.5].
An *axisymmetric ellipsoid* has two semi-axis of equal lenght, and the third one of a different lenght, which can be bigger or smaller than the previous ones. If the two semiaxes which are equal between each others are the minor ones, we have a *prolate ellipsoid*. If the two semiaxes which are equal between each others are the major ones, we have an *oblate ellipsoid*.
We now consider the case of an oblate spheroid. The lengths of the principal semi-axis will be denoted by a and b, with $b \leq a$.[1] The *eccentricity* e is defined as:

$$e \doteq \sqrt{1 - \frac{b^2}{a^2}} \ , \tag{A.9}$$

and $q \doteq b/a$ is the *axis ratio*. The volume of an oblate spheroid is $V = \frac{4}{3}\pi a^2 b = \frac{4}{3}\pi a^3 \sqrt{1-e^2}$.
Let us now define the quantity $m^2 \doteq R^2 + \frac{z^2}{1-e^2}$ and consider a body in which $\varrho = \varrho\left(m^2\right)$, i.e. a body whose isodensity surfaces are the similar spheroids

$$constant = m^2 \doteq R^2 + \frac{z^2}{1-e^2} \ . \tag{A.10}$$

Following [17, sec. 2.5] one can calculate its gravitational potential $\Phi\left(R_0, z_0\right)$ at any point (R_0, z_0).
It is now possible to find the radial component of the force exerted at point (R_0, z_0) by the distribution of mass $\varrho\left(m\right)$ considered. Using (3.24), we can then calculate the *circular speed* $v_c\left(R, z=0\right)$ *in the equatorial plane of an oblate spheroidal mass distribution*, which reads:

$$v_c^2\left(R, z=0\right) = 4\pi G_N \sqrt{1-e^2} \int_0^R \frac{\varrho\left(m^2\right) m^2 dm}{\sqrt{R^2 - m^2 e^2}} \ . \tag{A.11}$$

A.4 Miyamoto-Nagai disk

The gravitational potential that is generated via Poisson equation by the Miyamoto-Nagai density profile (3.11) can be found in [77] and reads

$$\Phi^{MN}\left(R, z\right) = -\frac{G_N M_{MN}}{\left[R^2 + \left[a_{NM} + \left(z^2 + b_{NM}^2\right)^{1/2}\right]^2\right]^{1/2}} \ . \tag{A.12}$$

From equations (3.24) and (A.12), it is easy to compute the circular velocity of a body in a circular orbit inside the plane $z = 0$ of the Miyamoto-Nagai potential,

[1] Note that in an oblate spheroid by definition two semiaxes will be of lenght a, and one of lenght b.

which is:

$$v_c^{MN}\left(R, z=0\right) = R\left[\frac{G_N M_{MN}}{\left[R^2 + \left(a_{MN} + b_{MN}\right)^2\right]^{3/2}}\right]^{1/2} . \tag{A.13}$$

Acknowledgments

I would like to thank all the people that has played an important role during the three years of my Ph.D..
First of all, my advisor Julien Lavalle who has guided me during my Ph.D., taught me a lot about research and shared his scientific knowledge with me. He has always encouraged me and his support has been fundamental for the successful completion of my Ph.D..
My scientific growth has benefited from him, and from all my colleagues. The collaborators with whom I interacted in Marseille, Pol Mollitor, Christian Torrero, Emmanuel Nezri and Laurent Lellouche, working together made me learn a lot. I am grateful to Benoit Famaey for very useful discussions about key astrophysical aspects of my work. The members of my research group, Gilbert Moultaka, Michele Frigerio, Felix Bruemmer, Cyril Hugonie, Jean-Loïc Kneur, Karsten Jedamzik, Michel Capdequi-Peyranere and all the others, that I thank for the discussions about physics and otherwise. The ambiance at the University has been made pleasant also by other people: Jean-Charles Walter, Jerome Dorignac, Andrea Parmeggiani, Nicolas Crampé, Pronob Mitter, André Niveu, Vladimir Lorman, Maxim Clusel and many others. A big thank goes to Dominique Caron, who has been there any time I needed an informatics support, always ready to answer to my questions and to share a smile.
The PhD students of my laboratory, Johanna, Pierre, Rana, Louis, Thibaut, Diane, and especially Lola, who shared with me a Ph.D. at the LUPM. I thank the administrative and technical members of the LUPM for providing very efficient practical support. Financial support to my work for the entire duration of my Ph.D. has been provided by the University of Montpellier, that I acknowledge.
A special thank goes to the students who attended the TD that I directed, for having given me the possibility to learn how to teach.
Definitively, it would have not been the same without the friends with whom I shared the office, Nicolas who has been discussing with me about science and otherwise during so many lunches, Pablo, my Ph.D. mentor, from whom I learned

a lot, and with whom I enjoyed to discuss about life and our common interests, and Sibasish, for sharing with me so many working times at unusual hours, for the coffee brakes, and for our dinners, that I will miss. I thank Michele, Luca and Rachele for having been always available to discuss with me, and for having been there in these three years.
I am also grateful to my longtime friends from whom I have been far away in these three years, but that I bears with me: Marta, Erika, Lorenzo, Sere, Matteo, Paolo, Giada, Roberto, Luigi, Matteo, Alice, Miki, Roberto, Luigi, Ale and all the others.
I warmly thank my family, Ugo, Pierangela, Sara, and all the others, who always unconditionally support me. A very special thank goes to my girlfriend Cecilia. We walked this path together, she stands by me and inspires me to grow.

Bibliography

[1] T. Piffl, C. Scannapieco, J. Binney, M. Steinmetz, R.-D. Scholz, *et al.*, "The RAVE survey: the Galactic escape speed and the mass of the Milky Way," *Astron.Astrophys.* **562** (2014) A91, arXiv:1309.4293 [astro-ph.GA]. x, 58, 88, 90, 92, 94, 95, 96, 99, 101, 102, 103, 116, 120, 121, 128, 129, 130, 132, 134, 135, 136, 137, 138, 141, 162, 167, 179, 183

[2] J. Lavalle and S. Magni, "Making sense of the local Galactic escape speed estimates in direct dark matter searches," *Phys.Rev.* **D91** no. 2, (2015) 023510, arXiv:1411.1325 [astro-ph.CO]. x, 131, 145, 156, 158, 160, 161, 162, 184

[3] F. Zwicky, "On the Masses of Nebulae and of Clusters of Nebulae," *Astrophys. J.* **86** (1937) 217–246. 2

[4] H. W. Babcock, "The Rotation of the Andromeda Nebula," *Lick Observatory Bulletin* **19** (1939) 41. 2

[5] V. C. Rubin and W. K. Ford, Jr., "Rotation of the Andromeda Nebula from a Spectroscopic Survey of Emission Regions," *Astrophys. J.* **159** (1970) 379–403. 2

[6] M. S. Roberts and R. N. Whitehurst, "The Rotation Curves of Galaxies," *Astrophys. J.* **201** (1975) 327. 2

[7] B. Famaey and S. McGaugh, "Modified Newtonian Dynamics (MOND): Observational Phenomenology and Relativistic Extensions," *Living Rev. Rel.* **15** (2012) 10, arXiv:1112.3960 [astro-ph.CO]. 2

[8] G. Jungman, M. Kamionkowski, and K. Griest, "Supersymmetric dark matter," *Phys.Rept.* **267** (1996) 195–373, arXiv:hep-ph/9506380 [hep-ph]. 3, 10, 12, 14, 15, 16, 17

[9] A. Drukier and L. Stodolsky, "Principles and Applications of a Neutral Current Detector for Neutrino Physics and Astronomy," *Phys. Rev.* **D30** (1984) 2295. 4

[10] M. W. Goodman and E. Witten, "Detectability of Certain Dark Matter Candidates," *Phys. Rev.* **D31** (1985) 3059. 4

[11] A. K. Drukier, K. Freese, and D. N. Spergel, "Detecting Cold Dark Matter Candidates," *Phys. Rev.* **D33** (1986) 3495–3508. 4

[12] K. Freese, M. Lisanti, and C. Savage, "Colloquium: Annual modulation of dark matter," *Rev.Mod.Phys.* **85** (2013) 1561–1581, `arXiv:1209.3339 [astro-ph.CO]`. 4, 8, 12, 17, 18, 22, 27, 28, 31, 32, 33, 38, 57

[13] J. Lewin and P. Smith, "Review of mathematics, numerical factors, and corrections for dark matter experiments based on elastic nuclear recoil," *Astropart.Phys.* **6** (1996) 87–112. 4, 42

[14] A. Kurylov and M. Kamionkowski, "Generalized analysis of weakly interacting massive particle searches," *Phys. Rev.* **D69** (2004) 063503, `arXiv:hep-ph/0307185 [hep-ph]`. 12

[15] J. R. Ellis, K. A. Olive, and C. Savage, "Hadronic Uncertainties in the Elastic Scattering of Supersymmetric Dark Matter," *Phys.Rev.* **D77** (2008) 065026, `arXiv:0801.3656 [hep-ph]`. 12, 14, 15, 17

[16] G. Duda, A. Kemper, and P. Gondolo, "Model Independent Form Factors for Spin Independent Neutralino-Nucleon Scattering from Elastic Electron Scattering Data," *JCAP* **0704** (2007) 012, `arXiv:hep-ph/0608035 [hep-ph]`. 17

[17] J. Binney and S. Tremaine, *Galactic dynamics*. Princeton University Press, 2nd ed., 2008. 21, 85, 88, 91, 92, 93, 95, 96, 97, 100, 102, 104, 107, 108, 109, 110, 111, 112, 114, 118, 120, 146, 179, 182, 187

[18] L. Bergstrom, "Saas-Fee Lecture Notes: Multi-messenger Astronomy and Dark Matter," `arXiv:1202.1170 [astro-ph.CO]`. 24

[19] R. Schoenrich, J. Binney, and W. Dehnen, "Local Kinematics and the Local Standard of Rest," *Mon.Not.Roy.Astron.Soc.* **403** (2010) 1829, `arXiv:0912.3693 [astro-ph.GA]`. 27, 133, 138, 143, 170, 171, 172, 173

[20] A. M. Green, "Effect of realistic astrophysical inputs on the phase and shape of the WIMP annual modulation signal," *Phys. Rev.* **D68** (2003) 023004, `arXiv:astro-ph/0304446 [astro-ph]`. [Erratum: Phys. Rev.D69,109902(2004)]. 27

[21] C. McCabe, "The Earth's velocity for direct detection experiments," *JCAP* **1402** (2014) 027, arXiv:1312.1355 [astro-ph.CO]. 27

[22] **XENON100** Collaboration, E. Aprile *et al.*, "Dark Matter Results from 225 Live Days of XENON100 Data," *Phys.Rev.Lett.* **109** (2012) 181301, arXiv:1207.5988 [astro-ph.CO]. 39, 49, 64, 65, 71

[23] **CDMS-II** Collaboration, Z. Ahmed *et al.*, "Dark Matter Search Results from the CDMS II Experiment," *Science* **327** (2010) 1619–1621, arXiv:0912.3592 [astro-ph.CO]. 39, 43, 53, 66, 71

[24] **LUX** Collaboration, D. Akerib *et al.*, "First results from the LUX dark matter experiment at the Sanford Underground Research Facility," *Phys.Rev.Lett.* **112** (2014) 091303, arXiv:1310.8214 [astro-ph.CO]. 39, 65, 66, 80, 81, 131, 155

[25] C. Savage, G. Gelmini, P. Gondolo, and K. Freese, "Compatibility of DAMA/LIBRA dark matter detection with other searches," *JCAP* **0904** (2009) 010, arXiv:0808.3607 [astro-ph]. 42, 43, 63, 67, 73, 79

[26] E. Del Nobile, G. B. Gelmini, P. Gondolo, and J.-H. Huh, "Update on Light WIMP Limits: LUX, lite and Light," *JCAP* **1403** (2014) 014, arXiv:1311.4247 [hep-ph]. 42, 43, 49, 65, 66, 68

[27] **SuperCDMS** Collaboration, R. Agnese *et al.*, "Search for Low-Mass Weakly Interacting Massive Particles Using Voltage-Assisted Calorimetric Ionization Detection in the SuperCDMS Experiment," *Phys.Rev.Lett.* **112** no. 4, (2014) 041302, arXiv:1309.3259 [physics.ins-det]. 42, 53, 67, 68, 71

[28] **XENON** Collaboration, J. Angle *et al.*, "First Results from the XENON10 Dark Matter Experiment at the Gran Sasso National Laboratory," *Phys.Rev.Lett.* **100** (2008) 021303, arXiv:0706.0039 [astro-ph]. 43, 49, 51, 62, 63, 71

[29] P. Sorensen, "A coherent understanding of low-energy nuclear recoils in liquid xenon," *JCAP* **1009** (2010) 033, arXiv:1007.3549 [astro-ph.IM]. 44, 64

[30] S. Yellin, "Finding an upper limit in the presence of unknown background," *Phys.Rev.* **D66** (2002) 032005, arXiv:physics/0203002 [physics]. 49, 50, 51, 52, 53, 54, 63, 64, 66, 67, 68, 69, 72

[31] G. J. Feldman and R. D. Cousins, "A Unified approach to the classical statistical analysis of small signals," *Phys.Rev.* **D57** (1998) 3873–3889, arXiv:physics/9711021 [physics.data-an]. 49

[32] **SuperCDMS** Collaboration, R. Agnese *et al.*, "Search for Low-Mass Weakly Interacting Massive Particles with SuperCDMS," *Phys.Rev.Lett.* **112** no. 24, (2014) 241302, arXiv:1402.7137 [hep-ex]. 53, 67, 71, 131, 155

[33] **EDELWEISS** Collaboration, E. Armengaud *et al.*, "Final results of the EDELWEISS-II WIMP search using a 4-kg array of cryogenic germanium detectors with interleaved electrodes," *Phys.Lett.* **B702** (2011) 329–335, arXiv:1103.4070 [astro-ph.CO]. 53, 66, 71

[34] **CRESST-II** Collaboration, G. Angloher *et al.*, "Results on low mass WIMPs using an upgraded CRESST-II detector," *Eur.Phys.J.* **C74** no. 12, (2014) 3184, arXiv:1407.3146 [astro-ph.CO]. 53, 69, 70, 71, 131, 155

[35] **Particle Data Group** Collaboration, K. Olive *et al.*, "Review of Particle Physics," *Chin.Phys.* **C38** (2014) 090001. 57, 174

[36] **Particle Data Group** Collaboration, J. Beringer *et al.*, "Review of Particle Physics (RPP)," *Phys.Rev.* **D86** (2012) 010001. 57, 174

[37] F. Ling, E. Nezri, E. Athanassoula, and R. Teyssier, "Dark Matter Direct Detection Signals inferred from a Cosmological N-body Simulation with Baryons," *JCAP* **1002** (2010) 012, arXiv:0909.2028 [astro-ph.GA]. 57, 174

[38] O. Bienaymé, B. Famaey, A. Siebert, K. Freeman, B. Gibson, *et al.*, "Weighing the local dark matter with RAVE red clump stars," *Astron.Astrophys.* **571** (2014) A92, arXiv:1406.6896 [astro-ph.GA]. 57, 160, 163, 175, 176

[39] P. J. McMillan and J. J. Binney, "The uncertainty in Galactic parameters," *Mon.Not.Roy.Astron.Soc.* **402** (2010) 934, arXiv:0907.4685 [astro-ph.GA]. 57, 58, 172, 174

[40] M. Reid, K. Menten, A. Brunthaler, X. Zheng, T. Dame, *et al.*, "Trigonometric Parallaxes of High Mass Star Forming Regions: the Structure and Kinematics of the Milky Way," *Astrophys.J.* **783** (2014) 130, arXiv:1401.5377 [astro-ph.GA]. 58, 135, 142, 143, 157, 159, 160, 161, 163, 168, 169, 171, 172

[41] M. C. Smith, G. Ruchti, A. Helmi, R. Wyse, J. Fulbright, *et al.*, "The RAVE Survey: Constraining the Local Galactic Escape Speed," *Mon.Not.Roy.Astron.Soc.* **379** (2007) 755–772, arXiv:astro-ph/0611671 [astro-ph]. 58, 129, 130, 132, 135, 136, 137

[42] C. Savage, G. Gelmini, P. Gondolo, and K. Freese, "XENON10/100 dark matter constraints in comparison with CoGeNT and DAMA: examining the Leff dependence," *Phys.Rev.* **D83** (2011) 055002, arXiv:1006.0972 [astro-ph.CO]. 63

[43] P. Sorensen, A. Manzur, C. Dahl, J. Angle, E. Aprile, *et al.*, "The scintillation and ionization yield of liquid xenon for nuclear recoils," *Nucl.Instrum.Meth.* **A601** (2009) 339–346, arXiv:0807.0459 [astro-ph]. 63, 64, 66

[44] P. Sorensen and C. E. Dahl, "Nuclear recoil energy scale in liquid xenon with application to the direct detection of dark matter," *Phys.Rev.* **D83** (2011) 063501, arXiv:1101.6080 [astro-ph.IM]. 64

[45] P. Sorensen, "Importance of upgraded energy reconstruction for direct dark matter searches with liquid xenon detectors," *Phys.Rev.* **D86** (2012) 101301, arXiv:1208.5046 [astro-ph.CO]. 64

[46] P. Sorensen, "Atomic limits in the search for galactic dark matter," *Phys.Rev.* **D91** no. 8, (2015) 083509, arXiv:1412.3028 [astro-ph.IM]. 64

[47] A. Manzur, A. Curioni, L. Kastens, D. N. McKinsey, K. Ni, and T. Wongjirad, "Scintillation efficiency and ionization yield of liquid xenon for mono-energetic nuclear recoils down to 4 keV," *Phys. Rev.* **C81** (2010) 025808, arXiv:0909.1063 [physics.ins-det]. 64

[48] J. Lindhard, V. Nielsen, M. Scharff, and P. V. Thomsen, "Integral Equations Governing Radiation Effects," *Mat. Fys. Medd. Dan. Vid. Selsk* **33** (1963) 10. 64

[49] **XENON100** Collaboration, E. Aprile *et al.*, "Dark Matter Results from 100 Live Days of XENON100 Data," *Phys.Rev.Lett.* **107** (2011) 131302, arXiv:1104.2549 [astro-ph.CO]. 65

[50] **XENON100** Collaboration, E. Aprile *et al.*, "Response of the XENON100 Dark Matter Detector to Nuclear Recoils," *Phys.Rev.* **D88** (2013) 012006, arXiv:1304.1427 [astro-ph.IM]. 65

[51] **LUX** Collaboration, C. Faham, "First Dark Matter Search Results from the Large Underground Xenon (LUX) Experiment," arXiv:1405.5906 [hep-ex]. 65

[52] **CDMS** Collaboration, R. Agnese *et al.*, "Silicon Detector Dark Matter Results from the Final Exposure of CDMS II," *Phys.Rev.Lett.* **111** no. 25, (2013) 251301, arXiv:1304.4279 [hep-ex]. 66

[53] **CDMS** Collaboration, R. Agnese *et al.*, "Silicon detector results from the first five-tower run of CDMS II," *Phys.Rev.* **D88** no. 5, (2013) 031104, arXiv:1304.3706 [astro-ph.CO]. 71

[54] R. Bernabei, P. Belli, A. Di Marco, F. Cappella, A. d'Angelo, *et al.*, "DAMA/LIBRA results and perspectives," arXiv:1301.6243 [astro-ph.GA]. 73, 74, 75, 77, 130

[55] M. Fairbairn and T. Schwetz, "Spin-independent elastic WIMP scattering and the DAMA annual modulation signal," *JCAP* **0901** (2009) 037, arXiv:0808.0704 [hep-ph]. 73, 74, 75, 76, 77, 78, 79, 80, 109

[56] **DAMA** Collaboration, R. Bernabei *et al.*, "First results from DAMA/LIBRA and the combined results with DAMA/NaI," *Eur.Phys.J.* **C56** (2008) 333–355, arXiv:0804.2741 [astro-ph]. 73, 77, 78, 80, 81

[57] M. Farina, D. Pappadopulo, A. Strumia, and T. Volansky, "Can CoGeNT and DAMA Modulations Be Due to Dark Matter?," *JCAP* **1111** (2011) 010, arXiv:1107.0715 [hep-ph]. 74

[58] N. Bozorgnia, G. B. Gelmini, and P. Gondolo, "Channeling in direct dark matter detection I: channeling fraction in NaI (Tl) crystals," *JCAP* **1011** (2010) 019, arXiv:1006.3110 [astro-ph.CO]. 75, 76

[59] R. Bernabei *et al.*, "Possible implications of the channeling effect in NaI(Tl) crystals," *Eur. Phys. J.* **C53** (2008) 205–213, arXiv:0710.0288 [astro-ph]. 76

[60] N. Bozorgnia, R. Catena, and T. Schwetz, "Anisotropic dark matter distribution functions and impact on WIMP direct detection," *JCAP* **1312** (2013) 050, arXiv:1310.0468 [astro-ph.CO]. 79, 110, 115, 117, 118, 119

[61] L. Baudis, "WIMP Dark Matter Direct-Detection Searches in Noble Gases," *Phys.Dark Univ.* **4** (2014) 50–59, arXiv:1408.4371 [astro-ph.IM]. 80

[62] P. Cushman *et al.*, "Working Group Report: WIMP Dark Matter Direct Detection," in *Community Summer Study 2013: Snowmass on the Mississippi (CSS2013) Minneapolis, MN, USA, July 29-August 6, 2013.* 2013. arXiv:1310.8327 [hep-ex]. https://inspirehep.net/record/1262767/files/arXiv:1310.8327.pdf. 80

[63] D. Malling, D. Akerib, H. Araujo, X. Bai, S. Bedikian, *et al.*, "After LUX: The LZ Program," arXiv:1110.0103 [astro-ph.IM]. 81

[64] **SuperCDMS** Collaboration, P. Brink, "Conceptual Design for SuperCDMS SNOLAB," *J.Low.Temp.Phys.* **167** (2012) 1093–1098. 81

[65] **EDELWEISS** Collaboration, K. Eitel, "The EDELWEISS Dark Matter Search: Status and Perspectives," *Phys.Procedia* **61** (2015) 61–66. 82

[66] **DARWIN Consortium** Collaboration, L. Baudis, "DARWIN: dark matter WIMP search with noble liquids," *J.Phys.Conf.Ser.* **375** (2012) 012028, arXiv:1201.2402 [astro-ph.IM]. 82

[67] J. Billard, L. Strigari, and E. Figueroa-Feliciano, "Implication of neutrino backgrounds on the reach of next generation dark matter direct detection experiments," *Phys.Rev.* **D89** no. 2, (2014) 023524, arXiv:1307.5458 [hep-ph]. 83

[68] P. J. McMillan, "Mass models of the Milky Way," *Mon.Not.Roy.Astron.Soc.* **414** (2011) 2446–2457, arXiv:1102.4340 [astro-ph.GA]. 86, 90, 91, 92, 94, 96, 99, 101, 103, 116, 178, 179, 180

[69] J. F. Navarro, C. S. Frenk, and S. D. White, "The Structure of cold dark matter halos," *Astrophys.J.* **462** (1996) 563–575, arXiv:astro-ph/9508025 [astro-ph]. 88, 138

[70] E. L. Lokas and G. A. Mamon, "Properties of spherical galaxies and clusters with an nfw density profile," *Mon.Not.Roy.Astron.Soc.* **321** (2001) 155, arXiv:astro-ph/0002395 [astro-ph]. 88

[71] J. S. Bullock, T. S. Kolatt, Y. Sigad, R. S. Somerville, A. V. Kravtsov, A. A. Klypin, J. R. Primack, and A. Dekel, "Profiles of dark haloes. Evolution, scatter, and environment," *Mon. Not. Roy. Astron. Soc.* **321** (2001) 559–575, arXiv:astro-ph/9908159 [astro-ph]. 89

[72] J. Einasto, "Kinematics and dynamics of stellar systems," *Trudy Inst. Astrofiz. Alma-Ata* **5** (1965) 87. 89

[73] A. W. Graham, D. Merritt, B. Moore, J. Diemand, and B. Terzic, "Empirical models for Dark Matter Halos. I. Nonparametric Construction of Density Profiles and Comparison with Parametric Models," *Astron. J.* **132** (2006) 2685–2700, arXiv:astro-ph/0509417 [astro-ph]. 89

[74] A. Burkert, "The Structure of dark matter halos in dwarf galaxies," *IAU Symp.* **171** (1996) 175, arXiv:astro-ph/9504041 [astro-ph]. [Astrophys. J.447,L25(1995)]. 90

[75] R. Catena and P. Ullio, "A novel determination of the local dark matter density," *JCAP* **1008** (2010) 004, arXiv:0907.0018 [astro-ph.CO]. 90

[76] F. Ferrer and D. R. Hunter, "The impact of the phase-space density on the indirect detection of dark matter," *JCAP* **1309** (2013) 005, arXiv:1306.6586 [astro-ph.HE]. 91, 95

[77] M. Miyamoto and R. Nagai, "Three-dimensional models for the distribution of mass in galaxies," *Publ.Astron.Soc.Jap.* **27** (1975) 533–543. 92, 138, 187

[78] Y. Wang, H. Zhao, S. Mao, and R. Rich, "A New Model for the Milky Way Bar," *Mon.Not.Roy.Astron.Soc.* **427** (2012) 1429, arXiv:1209.0963 [astro-ph.GA]. 92, 93, 180

[79] L. Hernquist, "An Analytical Model for Spherical Galaxies and Bulges," *Astrophys.J.* **356** (1990) 359. 92, 138

[80] J. Binney, O. Gerhard, and D. Spergel, "The photometric structure of the inner galaxy," *Mon. Not. Roy. Astron. Soc.* **288** (1997) 365–374, arXiv:astro-ph/9609066 [astro-ph]. 93, 180

[81] E. Dwek, R. G. Arendt, M. G. Hauser, T. Kelsall, C. M. Lisse, S. H. Moseley, R. F. Silverberg, T. J. Sodroski, and J. L. Weiland, "Morphology, near infrared luminosity, and mass of the galactic bulge from Cobe dirbe observations," *Astrophys. J.* **445** (1995) 716. 93, 180

[82] S. McGaugh, "Milky Way Mass Models and MOND," *Astrophys.J.* **683** (2008) 137–148, arXiv:0804.1314 [astro-ph]. 93, 95, 180

[83] R. Olling and M. Merrifield, "Luminous and dark matter in the milky way," *Mon.Not.Roy.Astron.Soc.* **326** (2001) 164, arXiv:astro-ph/0104465 [astro-ph]. 93, 180, 181, 182

[84] **SDSS** Collaboration, X. X. Xue *et al.*, "The Milky Way's Circular Velocity Curve to 60 kpc and an Estimate of the Dark Matter Halo Mass from Kinematics of 2400 SDSS Blue Horizontal Branch Stars," *Astrophys. J.* **684** (2008) 1143–1158, arXiv:0801.1232 [astro-ph]. 96, 138, 179

[85] N. W. Evans and J. H. An, "Distribution function of the dark matter," *Phys.Rev.* **D73** (2006) 023524, arXiv:astro-ph/0511687 [astro-ph]. 110, 117

[86] A. Eddington, "The Kinetic Energy of a Star Cluster," *MNRAS* **76** (1916) 525. 112, 114

[87] R. Wojtak, E. L. Lokas, G. A. Mamon, S. Gottloeber, A. Klypin, and Y. Hoffman, "The distribution function of dark matter in massive haloes," *Mon. Not. Roy. Astron. Soc.* **388** (2008) 815, arXiv:0802.0429 [astro-ph]. 118

[88] L. Ciotti and S. Pellegrini, "Self-consistent two-component models of elliptical galaxies," *M.N.R.A.S.* **255** (1992) 561–571. 125, 126

[89] L. Ciotti, "The analytical distribution function of anisotropic hernquist+hernquist models," *Astrophys. J.* **471** (1996) 68, arXiv:astro-ph/9605084 [astro-ph]. 125, 126

[90] M. Fairbairn, T. Douce, and J. Swift, "Quantifying Astrophysical Uncertainties on Dark Matter Direct Detection Results," *Astropart.Phys.* **47** (2013) 45–53, arXiv:1206.2693 [astro-ph.CO]. 129, 163

[91] P. Leonard and S. Tremaine, "The local Galactic escape speed," *ApJ* **353** (1990) 486. 129, 132

[92] A. P. A. Rotondi, P. Pedroni, *Probabilitá, Statistica e Simulazione*. Springer, seconda edizione ed. 132

[93] S. Gillessen, F. Eisenhauer, T. Fritz, H. Bartko, K. Dodds-Eden, *et al.*, "The orbit of the star S2 around SgrA* from VLT and Keck data," *Astrophys.J.* **707** (2009) L114–L117, `arXiv:0910.3069 [astro-ph.GA]`. 133, 138, 167, 168, 170

[94] T. C. Beers, M. Chiba, Y. Yoshii, I. Platais, R. B. Hanson, B. Fuchs, and S. Rossi, "Kinematics of metal-poor stars in the galaxy. 2. Proper motions for a large non-kinematically selected sample," *Astron. J.* **119** (2000) 2866–2881, `arXiv:astro-ph/0003103 [astro-ph]`. 133

[95] A. V. Maccio', A. A. Dutton, and F. C. d. Bosch, "Concentration, Spin and Shape of Dark Matter Haloes as a Function of the Cosmological Model: WMAP1, WMAP3 and WMAP5 results," *Mon.Not.Roy.Astron.Soc.* **391** (2008) 1940–1954, `arXiv:0805.1926 [astro-ph]`. 142

[96] P. Ullio and M. Kamionkowski, "Velocity distributions and annual modulation signatures of weakly interacting massive particles," *JHEP* **0103** (2001) 049, `arXiv:hep-ph/0006183 [hep-ph]`. 146

[97] J. Bovy and S. Tremaine, "On the local dark matter density," *Astrophys.J.* **756** (2012) 89, `arXiv:1205.4033 [astro-ph.GA]`. 163, 175

[98] T. Piffl, J. Binney, P. McMillan, O. Bienaymé, J. Bland-Hawthorn, *et al.*, "Constraining the Galaxy's dark halo with RAVE stars," *Mon.Not.Roy.Astron.Soc.* **445** no. 3, (2014) 3133–3151, `arXiv:1406.4130 [astro-ph.GA]`. 163, 176, 177

[99] M. Lisanti, L. E. Strigari, J. G. Wacker, and R. H. Wechsler, "The Dark Matter at the End of the Galaxy," *Phys.Rev.* **D83** (2011) 023519, `arXiv:1010.4300 [astro-ph.CO]`. 164

[100] A. Ghez, S. Salim, N. Weinberg, J. Lu, T. Do, *et al.*, "Measuring Distance and Properties of the Milky Way's Central Supermassive Black Hole with Stellar Orbits," *Astrophys.J.* **689** (2008) 1044–1062, `arXiv:0808.2870 [astro-ph]`. 167

[101] S. Gillessen, F. Eisenhauer, S. Trippe, T. Alexander, R. Genzel, *et al.*, "Monitoring stellar orbits around the Massive Black Hole in the Galactic Center," *Astrophys.J.* **692** (2009) 1075–1109, `arXiv:0810.4674 [astro-ph]`. 167

[102] J. Bovy, C. A. Prieto, T. C. Beers, D. Bizyaev, L. N. da Costa, *et al.*, "The Milky Way's circular velocity curve between 4 and 14 kpc from APOGEE data," *Astrophys.J.* **759** (2012) 131, arXiv:1209.0759 [astro-ph.GA]. 169, 170, 171, 173, 174, 175

[103] M. J. Reid and A. Brunthaler, "The Proper motion of Sgr A*. 2. The Mass of Sgr A*," *Astrophys.J.* **616** (2004) 872–884, arXiv:astro-ph/0408107 [astro-ph]. 171

[104] W. Dehnen and J. Binney, "Local stellar kinematics from hipparcos data," *Mon.Not.Roy.Astron.Soc.* **298** (1998) 387–394, arXiv:astro-ph/9710077 [astro-ph]. 171, 172, 173

[105] W. Dehnen, "Simple distribution functions for stellar disks," *Astron. J.* **118** (1999) 1201, arXiv:astro-ph/9906082 [astro-ph]. 173

[106] C. M. Bidin, R. Smith, G. Carraro, R. Mendez, and M. Moyano, "On the local dark matter density," *Astron.Astrophys.* **573** (2015) A91, arXiv:1411.2625 [astro-ph.GA]. 175

[107] C. M. Bidin, G. Carraro, R. Mendez, and R. Smith, "Kinematical and chemical vertical structure of the Galactic thick disk II. A lack of dark matter in the solar neighborhood," *Astrophys.J.* **751** (2012) 30, arXiv:1204.3924 [astro-ph.GA]. 175

[108] T. Piffl, Z. Penoyre, and J. Binney, "Bringing the Galaxy's dark halo to life," *Mon. Not. Roy. Astron. Soc.* **451** no. 1, (2015) 639–650, arXiv:1502.02916 [astro-ph.GA]. 176, 177, 178

[109] J. Bovy and H.-W. Rix, "A Direct Dynamical Measurement of the Milky Way's Disk Surface Density Profile, Disk Scale Length, and Dark Matter Profile at 4 kpc $\lesssim$ R $\lesssim$ 9 kpc," *Astrophys.J.* **779** (2013) 115, arXiv:1309.0809 [astro-ph.GA]. 179, 181, 182

[110] G. Gilmore and N. Reid, "New light on faint stars. III - Galactic structure towards the South Pole and the Galactic thick disc," *Mon. Not. Roy. Astron. Soc.* **202** (1983) 1025–1047. 179

[111] P. Kalberla and J. Kerp, "The Hi Distribution of the Milky Way," *nnu. Rev. Astron. Astrophys.* **47** (2009) 27–61. 180, 181

[112] C. Flynn, J. Holmberg, L. Portinari, B. Fuchs, and H. Jahreiss, "On the mass-to-light ratio of the local Galactic disc and the optical luminosity of the Galaxy," *Mon.Not.Roy.Astron.Soc.* **372** (2006) 1149–1160, arXiv:astro-ph/0608193 [astro-ph]. 181, 182

[113] T. Fang, J. S. Bullock, and M. Boylan-Kolchin, "On the Hot Gas Content of the Milky Way Halo," *Astrophys.J.* **762** (2013) 20, arXiv:1211.0758 [astro-ph.CO]. 181

[114] A. Gatto, F. Fraternali, J. Read, F. Marinacci, H. Lux, *et al.*, "Unveiling the corona of the Milky Way via ram-pressure stripping of dwarf satellites," arXiv:1305.4176 [astro-ph.GA]. 181

[115] M. Boylan-Kolchin, J. S. Bullock, S. T. Sohn, G. Besla, and R. P. van der Marel, "The Space Motion of Leo I: The Mass of the Milky Way's Dark Matter Halo," *Astrophys.J.* **768** (2013) 140, arXiv:1210.6046 [astro-ph.CO]. 181

[116] J. Bovy, H.-W. Rix, and D. W. Hogg, "The Milky Way has no thick disk," *Astrophys.J.* **751** (2012) 131, arXiv:1111.6585 [astro-ph.GA]. 182

Abstract

This thesis deals with the astrophysical aspects of the direct detection of WIMP dark matter (DMDD). In particular, it focuses on the observational constraints on the astrophysical quantities relevant for DMDD, which impact on the interpretation of the experimental results.

We review the formalism of DMDD and we summarize some of the main experimental results in this domain and the statistical methods usually employed to interpret the data, reproducing the associated constraints on the parameter space relevant for spin-independent WIMP-nucleon interaction. We summarize the set of astrophysical assumptions usually employed, the Standard Halo Model, and we point out the impact of variations in its parameters on such limits.

We outline the main concepts of the dynamics of our galaxy that allow to put the astrophysics related to DMDD in a wider framework. In particular, we review the description of the Galaxy through Milky Way mass models (MWMM), pointing out how the astrophysical quantities are related. We describe some procedures to obtain dark matter phase-space distributions consistent with given dark matter profile and Galactic potential, the simplest being Eddington equation, of which we discuss the limits of applicability. We review in detail the recent literature on the main determinations and uncertainties of the astrophysical quantities relevant for DMDD and of the fundamental Galactic parameters.

In the most original part of this thesis we focus on the recent estimates of the local Galactic escape speed published by the RAVE collaboration. We study in detail the implications of these results for the spin-independent interpretation of DMDD experiments. We take into account the correlations between the astrophysical quantities relevant for DMDD calculations, and from the assumed MWMM we compute the dark matter phase-space distribution using Eddington equation, which provides a self-consistent physical connection between the two. This procedure leads to more constraining exclusion curves with respect to the standard ones, due to higher values of the local dark matter density.

Résumé

Cette thèse traite des aspects astrophysiques de la détection directe (DD) de matière noire sous forme de WIMPs. On se concentre sur les contraintes observationnelles des quantités astrophysiques qui influent sur l'interprétation des résultats expérimentaux de DD.

On revoit tout d'abord le formalisme de la DD et on résume les résultats expérimentaux les plus importants ainsi que les méthodes statistiques généralement utilisés pour interpréter les données. On reproduit ensuite les limites expérimentales sur la section efficace spin-indépendante. On résume l'ensemble des hypothèses astrophysiques couramment utilisées dans le modèle de halo standard et on décrit l'influence de ses paramètres sur les limites.

Pour inscrire la DD dans un cadre plus général, on résume les concepts les plus importants de la dynamique Galactique. En particulier, on revoit comment modéliser la Galaxie avec des modèles de masse, tout en soulignant les relations entre les différentes quantités astrophysiques. On décrit des procédures qui permettent d'obtenir des distributions dans l'espace des phases de la matière noire qui soient consistantes avec un profil de matière noire et un potentiel Galactique donné. La plus simple procédure étant basée sur l'équation d'Eddington, on discute ses limites d'applicabilité. On revoit dans les détails la littérature récente concernant les déterminations et les incertitudes des quantités astrophysiques liées à la DD et des paramètres Galactiques fondamentaux.

Dans la derniere partie de la thèse on s'intéresse aux estimations récentes de la vitesse d'échappement publiées par la collaboration RAVE. On étudie dans les détails les implications de ces résultats sur les expériences de DD. Pour cela on prends en compte les corrélations entre les quantités astrophysiques importantes pour la DD, et en assumant le modèles de masse de RAVE on calcule la distribution de matière noire dans l'espace des phases avec l'équation d'Eddington. Du fait des valeurs plus élevés de la densité locale de matière noire, cette procédure conduit à des limites plus contraignantes par rapport a celles standards.